REPORT DOCUMENTATION PAGE

Public reporting burden for this collection of information is estimated to average 1 hour per response, inc sources,
gathering and maintaining the data needed, and completing and reviewing the collection of information. t of this
collection of information, including suggestions for reducing this burden, to Washington Headquarters Sei efferson
Davis Highway, Suite 1204, Arlington, VA 22202-4302, and to the Office of Management and Budget, Pa

AFRL-SR-AR-TR-03-
0188

1. AGENCY USE ONLY *(Leave blank)*	**2. REPORT DATE** 14-APR-2003	**3. REI** FINAL (01-MAY-1999 TO 31-DEC-2002

4. TITLE AND SUBTITLE
MATERIALS CHARACTERIZATION BY ATOMIC FORCE MICROSCOPY

5. FUNDING NUMBERS
F49620-99-1-0254

6. AUTHOR(S)
JOSEPH A. TURNER

7. PERFORMING ORGANIZATION NAME(S) AND ADDRESS(ES)
DEPARTMENT OF ENGINEERING MECHANICS
UNIVVERSITY OF NEBRASKA-LINCOLN
LINCOLN, NEBRASKA 68588

8. PERFORMING ORGANIZATION REPORT NUMBER

9. SPONSORING/MONITORING AGENCY NAME(S) AND ADDRESS(ES)
AFOSR/NA
4015 WILSON BOULVARD
ARLINGTON, VA 22203

10. SPONSORING/MONITORING AGENCY REPORT NUMBER

11. SUPPLEMENTARY NOTES

12a. DISTRIBUTION AVAILABILITY STATEMENT

Approved for public release;
distribution unlimited.

20030602 127

13. ABSTRACT *(Maximum 200 words)*

During this project, the development of AFM experimental expertise was undertaken. An AFM was purchased and modified for the dynamic AFM measurements. The system allows the cantilever resonance frequencies to be determined both in and ou of contact with a specimen. In addition, the dynamic implementation allows the surface topography and material stiffness to b mapped simultaneously. During this project, several aspects of this research were explored. One focus was on comparison of ATM methods with other experimental measurement techniques using thin films as a test base. Improved modeling of the AFM cantilevers was undertaken as it became apparent that simpler methods were not sufficient for experimental analysis. Finite element models are being constructed to include observed variations in cantilever width, thickness, and tip location. The analytical modeling has been focused on the nonlinear vibrations of ATM cantilevers with nonlinear boundary conditions. The studies of nonlinear vibrations have been extended for contact boundary conditions of a general nature such that both soft and hard contacts may be analyzed. The method of multiple scales is the primary method used for these studies. Finally, the coupling of flexural and torsional vibration modes has been examined. The coupling is the result of the specific geometry of certain ATM cantilevers. Both experimental and analytical studies have been conducted.

14. SUBJECT TERMS

15. NUMBER OF PAGES
112

16. PRICE CODE

17. SECURITY CLASSIFICATION OF REPORT UNCLASSIFIED	**18. SECURITY CLASSIFICATION OF THIS PAGE** UNCLASSIFIED	**19. SECURITY CLASSIFICATION OF ABSTRACT** UNCLASSIFIED	**20. LIMITATION OF ABSTRACT**

APR 15 2003

FINAL REPORT

MATERIALS CHARACTERIZATION BY ATOMIC FORCE MICROSCOPY

AFOSR GRANT NO. F49620-99-1-0254

Joseph A. Turner, Associate Professor
Department of Engineering Mechanics
University of Nebraska-Lincoln
Lincoln, Nebraska 68588
phone: 402-472-8856
fax: 402-472-8292
e-mail: **jaturner@unl.edu**
web-site: http://em-jaturner.unl.edu

MATERIALS CHARACTERIZATION BY ATOMIC FORCE MICROSCOPY
AFOSR GRANT NO. F49620-99-1-0254

Joseph A. Turner
Department of Engineering Mechanics
University of Nebraska-Lincoln
Lincoln, Nebraska 68588
phone: 402-472-8856
fax: 402-472-8292
e-mail: **jaturner@unl.edu**

Objectives

This research program is focused on the study of the atomic force microscope (AFM) as an instrument for quantitative measuring and imaging material properties with nanoscale resolution. More specific to this research are the dynamic modes of AFM, in which the specimen moves relative to the AFM cantilever tip while in contact. Particular emphases include the higher-order vibration modes and the nonlinear vibration response. In addition to the original objective, improved modeling of AFM cantilevers has been undertaken. The use of simplified beam models with uniform cross section does not reflect the AFM cantilevers that are often used in experiments. High resolution cantilever measurements with a scanning electron microscope (SEM) and modeling with finite element analysis have been used to improve the comparisons between experiments and numerical models.

Description of Effort

During this project, the development of AFM experimental expertise was undertaken. An AFM was purchased and modified for the dynamic AFM measurements. The system allows the cantilever resonance frequencies to be determined both in and out of contact with a specimen. In addition, the dynamic implementation allows the surface topography and material stiffness to be mapped simultaneously. During this project, several aspects of this research were explored. One focus was on comparison of AFM methods with other experimental measurement techniques using thin films as a test base. Improved modeling of the AFM cantilevers was undertaken as it became apparent that simpler methods were not sufficient for experimental analysis. Finite element models are being constructed to include observed variations in cantilever width, thickness, and tip location. The analytical modeling has been focused on the nonlinear vibrations of AFM cantilevers with nonlinear boundary conditions. The studies of nonlinear vibrations have been extended for contact boundary conditions of a general nature such that both soft and hard contacts may be analyzed. The method of multiple scales is the primary method used for these studies. Finally, the coupling of flexural and torsional vibration modes has been examined. The coupling is the result of the specific geometry of certain AFM cantilevers. Both experimental and analytical studies have been conducted.

Accomplishments

Comparisons with other Techniques. The experimental setup for the dynamic AFM experiments (also known as atomic force acoustic microscopy or AFAM) is shown schematically in Fig. 1. A commercial AFM (Thermomicroscopes Autoprobe CP) was modified for these experiments. A reference specimen and an unknown specimen are placed on a broadband ultrasonic transducer (2.25 MHz center frequency). The transducer is mounted on the AFM stage and is excited by the function generator. The output from the AFM photodiode is mixed with the driving signal in the lock-in amplifier. The lock-in output and the photodiode output are both used by the AFM for imaging. The function generator is controlled by Labview software.

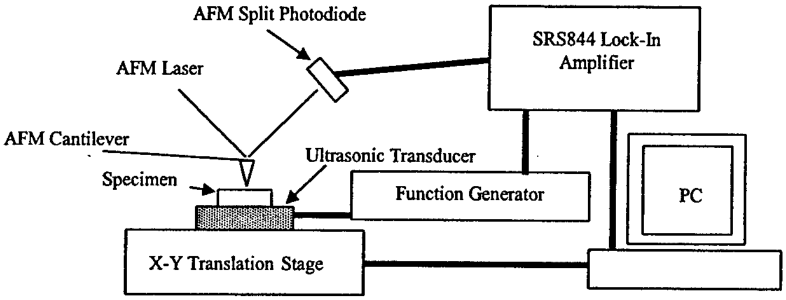

Figure 1. Schematic of the atomic force acoustic microscopy experiment. Both the topography and lock-in amplifier output are used for imaging.

In a typical experiment, the free and contact cantilever resonances are measured on both the reference and the sample of interest. The cantilever resonances are found by scanning an appropriate frequency range with the function generator and plotting the lock-in output. The contact resonances are functions of applied load on the AFM cantilever. The frequency shifts may be used to determine the mechanical properties of the unknown relative to the reference. First, the necessary spring stiffness of the contact k^* is determined from the natural frequency data and an appropriate vibration model. The value of k^* is then used to determine the contact modulus of the sample using the Hertzian contact relation $E_s^* = E_r^*\left(k_s^* / k_r^*\right)^{3/2}$, where the subscripts denote the sample and reference. The sample indentation modulus M_s is then determined from $\left(E_s^*\right)^{-1} = \left(M_{tip}\right)^{-1} + \left(M_s\right)^{-1}$, where M_{tip} is the indentation modulus of the tip. AFAM results for indentation modulus on samples of aluminum and niobium were compared with results using surface acoustic waves (SAW) and instrumented indentation (IIT) [1]. The results are summarized in Table 1. These results are typical of other measurements on different materials. The primary cause of the wide range in the AFAM results is thought to come from the choice of the reference material. For the results in Table 1, both glass and single crystal silicon were used as references. The appropriate use of reference samples for AFAM is the subject of ongoing research.

Table 1. Comparison of indentation modulus *M* (GPa) for aluminum and niobium using several different methods [1].

Material	Literature	SAW	IIT	AFAM
Al	76 – 81	78 ± 1	86 ± 4	54 – 81
Nb	116 – 133	120 ± 5	—	91 – 137

***Imaging*.** Once the resonances are measured, an AFAM image may be made. The transducer motion is fixed at a single frequency slightly higher or lower than the resonance for a given applied load. The feedback control loop of the AFM is set to constant force and the scan is made. The topography and stiffness images are obtained simultaneously. Example results for polysilicon are shown in Fig. 2. The topography images are in the lefthand column while the stiffness images (lock-in output) are shown in the righthand column. Results from two scans are shown. The stiffness images for these samples show the interesting contrast within regions that appear to be single grains in the topography image. Also of note are the single grains that appear to have different stiffness. Calibrated stiffness measurements may be made by comparing spectra measured from a known material, such as single crystal silicon, to spectra from the unknown.

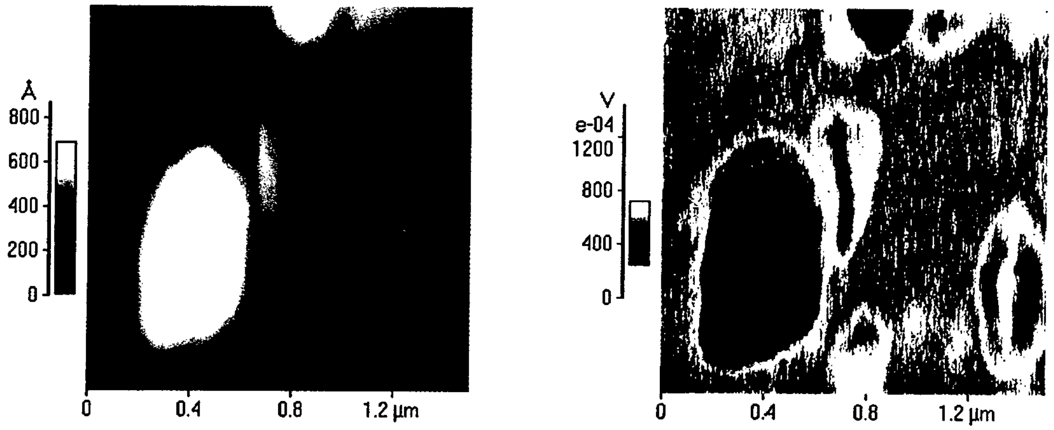

Topography, 0518T011.HDF

AUX4, 05180010.HDF

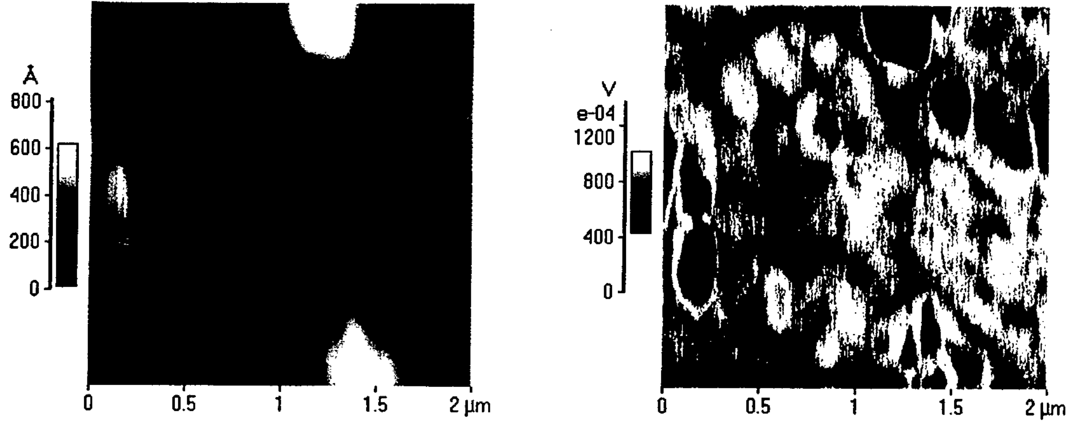

Topography, 0518T015.HDF

AUX4, 05180014.HDF

Figure 2. Example results of atomic force acoustic microscopy (AFAM) on a sample of polysilicon MEMS. The two lefthand images are topography, while the two righthand images are the AFAM images. Of particular note are the stiffness contrasts observed within single grains.

***Improved Modeling*.** Improved modeling of AFM cantilevers was undertaken as it became clear that the simple models based on cantilevers of uniform cross-section did not apply to many commercially available cantilevers. To date, AFAM experiments have been interpreted exclusively with an analytical model in which it is assumed that the cantilever cross-section is uniform over the length of the beam. The assumption is not strictly true, even for cantilevers that are uniform over the majority of their length. Thus, data interpretation using such analytical models is an approximation for real experimental conditions. Such approximations are very good in some cases. However, cantilevers such as dagger shaped, V-shaped, or triangular cantilevers are useful for measurements but are clearly not uniform.

To address the current deficiency in these simplified AFAM models, finite element models (FEM) have been developed for AFAM applications. Variations in geometry that extend over a small range of the cantilever, such as the triangular portion of dagger-shaped cantilevers, are easily modeled using FEM. Two types of cantilevers were investigated, one with rectangular plan view and one with a dagger-shaped plan view [1]. For both cantilevers, the length and width dimensions were measured using an optical microscope. The thickness was measured using scanning electron microscopy (SEM). The optical measurements were more accurate (relative to the degree of accuracy required) than the SEM measurements due to mounting and alignment issues. Moreover, the beam resonance frequencies are much more sensitive to thickness than to length or width. For these reasons, the cantilever thickness was the primary variable adjusted to match the experimental results. Other variations in the different cantilevers were also included in the models. For instance, the tip of the rectangular cantilever was not located exactly at its end, but some unknown distance. Therefore, the tip position was allowed to vary in the FEM. The location of the dagger cantilever's tip, on the other hand, was exactly at the end and was not a variable parameter in the model. Other parameters that were investigated in the FEM include tip mass, damping, and cantilever thickness variations. Example numerical results for both types of cantilevers are given in Table 2. The indentation modulus was calculated from the contact frequencies for both aluminum and niobium. The results are based on two reference materials. The FEM results in some cases are not necessarily an improvement over the simplified model. However, it should be noted that in many cases unphysical parameters are used in the simplified models, such as tip placement very far from the beam end. Further improvements to these modeling efforts are being examined.

Table 2. Comparison of results for indentation modulus *M* using analytical and finite element models of AFM beams [1].

Material	Cantilever	Reference	Model	M
Al	rectangular	glass	uniform	76 ± 3
			FEM	76 ± 10
Al	dagger	glass	uniform	64 ± 3
			FEM	54 ± 4
Nb	rectangular	glass	uniform	89 ± 7
		Si		140 ± 6
		glass	FEM	95 ± 14
		Si		128 ± 16
Nb	dagger	glass	uniform	87 ± 1
		Si		139 ± 5
		glass	FEM	92 ± 6
		Si		120 ± 14

Nonlinear Vibrations. The nonlinear forces that develop between the AFM tip and the specimen often result in nonlinear behavior in the vibrations. Experimental results have shown the type of softening nonlinearity expected. The fundamental problem of the nonlinear vibrations of a beam with cantilever-Hertzian contact boundary conditions was investigated [2]. The method of multiple scales was used to analyze this problem in which it was assumed that the beam remains in contact with the moving surface at all times. The contact between the AFM tip and the sample surface was modeled as Hertzian. One primary result from this analysis is the amplitude-frequency relation for the various flexural modes. The amplitude-frequency curves exhibit softening behavior as expected. The amount of softening depends on the linear contact stiffness relative to the beam stiffness (characterized by dimensionless parameter β) as well as the specific mode. An example result is shown in Fig. 3. The modal amplitude is plotted versus the detuning parameter for the first and second modes for two values of β. The sensitivity to the nonlinearity is similar to the linear sensitivity [3]. The sensitivity of the different modes is reflected in their nonlinear behavior — some modes exhibit larger shifts in natural frequency than others for the same type of contact stiffness. The associated nonlinear normal modes of this system were also derived. The modes include a nonlinear addition to the linear, harmonic component as well as a static offset term and second and third harmonic components.

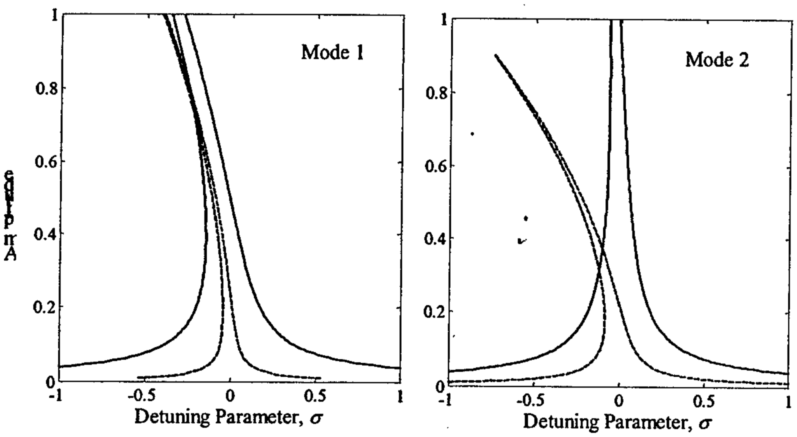

Figure 3. Nonlinear frequency shift of the first and second modes for two values of linear contact stiffness β = 50 (solid) and 500 (dashed). Each mode responds differently to the nonlinearity [2].

Modal Coupling. The coupling of flexural and torsional vibration modes of atomic force microscope cantilevers has also been investigated. This type of coupling occurs in cantilevers of certain geometries. Solutions were obtained using an analytical bending and torsional model as well as using the finite element method. The coupling considered arises from small geometric asymmetries in the cantilever, such as an offset tip or uneven distribution of cantilever mass. The asymmetries lead to coupling of the respective flexural and torsional governing equations. Specific conditions necessary for the coupling of the first torsional mode with various flexural modes were derived. For isotropic rectangular cantilevers with rectangular cross-section, the tendency for coupling is characterized by a dimensionless parameter $H = \frac{w}{12L}\sqrt{6(1+\nu)}$, where w is the width, L is the length, and ν is Poisson's ratio. Conditions for coupling are easily satisfied by commercially available AFM cantilevers. Example experimental results are shown in Fig. 4 [4]. The experiments were done with commercial rectangular AFM cantilever beams made of silicon. The cantilevers were set into vibration using a piezoelectric ultrasonic transducer coupled to the chip of a cantilever. The transducer was excited harmonically in the frequency range of 100 kHz to 3 MHz. The vibrations were monitored using an optical Michelson heterodyne-interferometer allowing the surface of the cantilever under examination to be scanned with a lateral resolution of several microns. The measured frequency spectrum was used to identify the various modes. The amplitude and phase of four free vibration modes of the beams are shown in Fig. 4. Theoretical predictions of the modal coupling are shown in Fig. 5 for $H = 0.025$. These results agree very well with the experimental results.

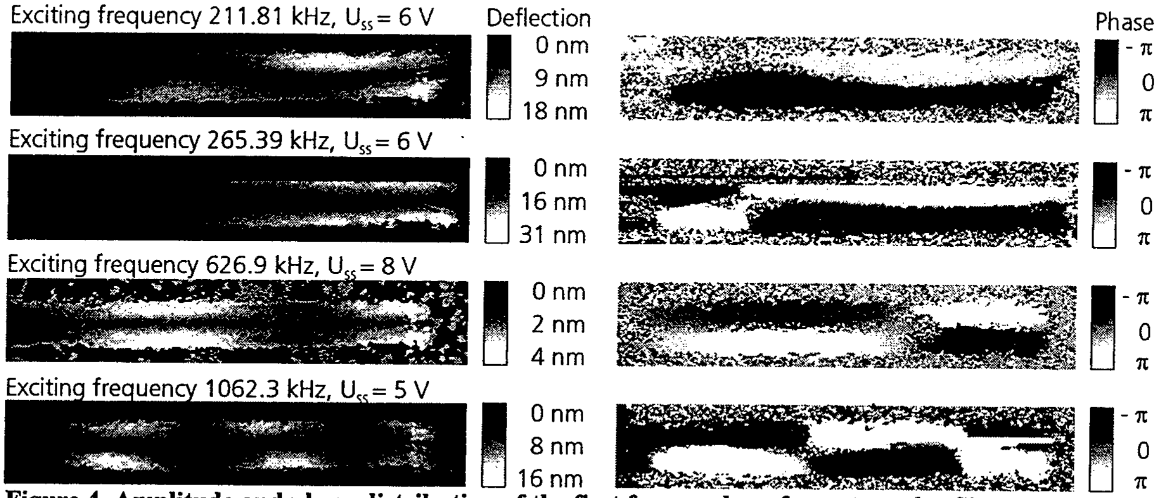

Figure 4. Amplitude and phase distribution of the first four modes of a rectangular Si-cantilever that are predominantly torsional. The scan size is about 550 x 100 µm² [4].

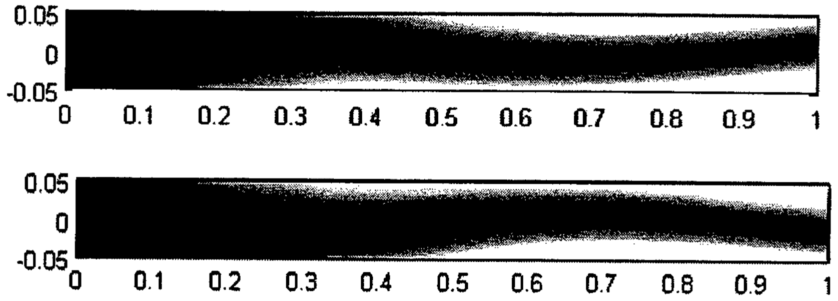

Figure 5. Predicted third and fourth mode shapes calculated from the flexural/torsional coupling model with $H = 0.025$. The interaction observed is a coupling between the first torsional and third flexural modes [4].

Interactions. Collaborative efforts have continued with Dr. D. C Hurley of the Materials Reliability Division of the National Institute for Standards and Technology (NIST) in Boulder, Colorado. This collaboration includes the sharing of test samples and AFM cantilevers, comparison of experimental data, and collaborative theoretical/experimental research. Collaborative research is also continuing with the group headed by Dr. W. Arnold at the Fraunhofer Institut für zerstörungsfreie Prüfverfarhen (IZFP) in Saarbrücken, Germany. The PI and students are collaborating with the IZFP on the development of finite element models, analytical vibration models, and experimental comparisons. Collaboration with the thin films group at UNL (S. Rohde) has also proven fruitful [5]. The AFAM research is continued through support of the National Science Foundation (ceramic nanofibers) and the Department of Energy (sintered materials).

References

[1] D. C. Hurley, J. S. Wiehn, J. A. Turner, and P. Rice, "Quantitative elastic-property information with acoustic AFM: measurements and modeling," *SPIE Conference on Nondestructive Evaluation and Reliability of Micro- and Nanomaterial Systems* **4703**, 65-73, (2002).

[2] J. A. Turner, "Nonlinear vibrations of an elastic beam with cantilever-Hertzian contact boundary conditions," *under review* (2002).

[3] J. A. Turner and J. S. Wiehn, "Sensitivity of flexural and torsional vibration modes of atomic force microscope cantilevers to surface stiffness variations," *Nanotechnology* **12,** 322-330 (2001).

[4] M. Reinstädtler, U. Rabe, V. Scherer, J. A. Turner, and W. Arnold, "Imaging of flexural and torsional resonance modes of atomic force microscopy cantilevers using optical interferometry," *Surface Science*, to appear (2003).

[5] S. M. Aouadi, F. Namavar, N. Finnegan, R. Haash, R. Nilchiani, J. A. Turner, and S. L. Rohde, "Characterization of CrBN films deposited by ion beam assisted deposition," *Journal of Applied Physics* **91**, 1040-1045 (2002).

Personnel

Personnel supported in part by this grant include: Joseph A. Turner (Associate Professor and Principal Investigator), and graduate students Baowei Wei (MS, August 2001), Joshua S. Wiehn (MS, December 2001), Roshanak Nilchiani (MS, May 2002), Kangzhi Shen (current PhD student).

Awards

Best NDE Paper Award for at the 2002 SPIE Symposium on NDE for Health Monitoring and Diagnostics (Second Place): "Quantitative Elastic-Property Information with Acoustic AFM: Measurements and Modeling," Donna C. Hurley, Joshua S. Wiehn, Joseph A. Turner, and Paul Rice.

Transitions

As an ongoing part of this research, the analysis and calculations used for AFAM have been developed into web-based calculation tools (http://em-jaturner.unl.edu/calcs.htm). For example, one of these tools calculates AFM cantilever frequency spectra and modal sensitivity as a function of the surface stiffness for both flexural and torsional vibrations (shown in Fig. 6). Current options include three cantilever plan views of rectangular, V-shaped, and triangular. The user chooses the cantilever shape and inputs material property and geometric data. The information is then passed to a MATLAB program that performs the calculations. The output is then posted in plot or table format in the browser frame. Additional tools focused on AFAM experiments are also now included.

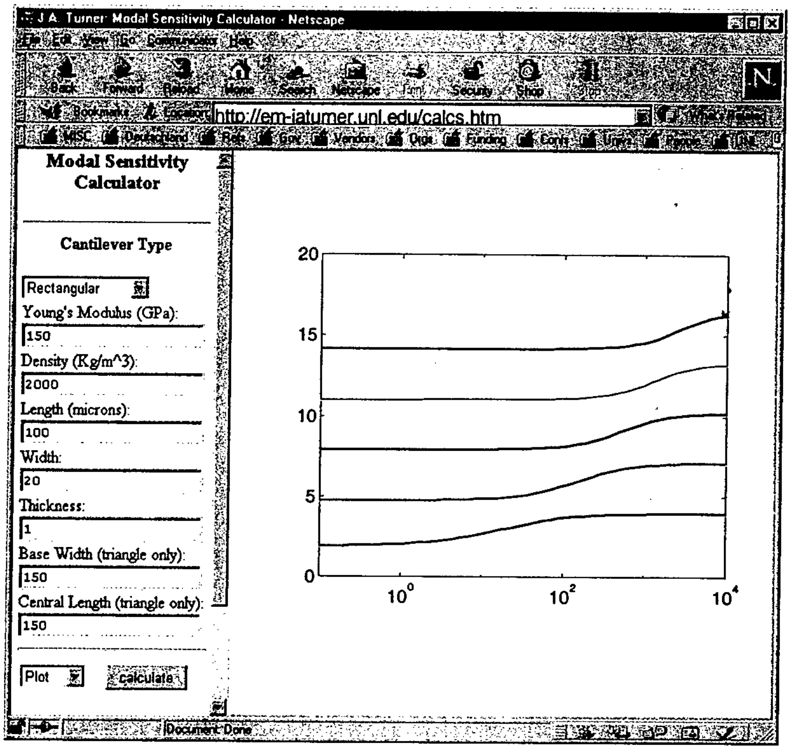

Modal Sensitivity Calculator

Cantilever Type

Rectangular

Young's Modulus (GPa): 150

Density (Kg/m^3): 2000

Length (microns): 100

Width: 20

Thickness: 1

Base Width (triangle only): 150

Central Length (triangle only): 150

Plot

Figure 6. Example output from one of the web-based AFM calculation tools. Several different cantilever geometries are included as are flexural and torsional modes.

PUBLICATIONS IN WHICH AFOSR SUPPORT IS ACKNOWLEDGED

Refereed Publications:

J. A. Turner, R. Nilchiani, J. S. Wiehn, "Atomic force acoustic microscopy for materials characterization of microelectromechanical systems," proceedings of the 7th ASME Topical Conference on NDE, **20**, 79-86 (2001).

J. A. Turner and J. S. Wiehn, "Sensitivity of flexural and torsional vibration modes of atomic force microscope cantilevers to surface stiffness variations," *Nanotechnology* **12,** 322-330 (2001).

D. C. Hurley, K. Shen, and J. A. Turner, "Quantitative atomic force acoustic microscopy methods to determine thin-film elastic properties," *under review* (2003).

S. M. Aouadi, F. Namavar, N. Finnegan, R. Haash, R. Nilchiani, J. A. Turner, and S. L. Rohde, "Characterization of CrBN films deposited by ion beam assisted deposition," *Journal of Applied Physics* **91**, 1040-1045 (2002).

M. Reinstädtler, U. Rabe, V. Scherer, J. A. Turner, and W. Arnold, "Imaging of flexural and torsional resonance modes of atomic force microscopy cantilevers using optical interferometry," *Surface Science*, to appear (2003).

J. A. Turner, "Nonlinear vibrations of an elastic beam with cantilever-Hertzian contact boundary conditions," *under review* (2002).

At least three additional journal publications are expected from Mr. K. Shen's PhD research.

Books and other one-time publications:

D. C. Hurley, J. S. Wiehn, J. A. Turner and P. Rice, "Quantitative elastic-property information with acoustic AFM: measurements and modeling," proceedings of the *SPIE Conference on Nondestructive Evaluation and Reliability of Micro- and Nanomaterial Systems*, **4703**, 65-73, (2002).

J. A. Turner, "Nonlinear vibrations in atomic force microscopy," proceedings of the *SPIE Conference on Nondestructive Evaluation and Reliability of Micro- and Nanomaterial Systems*, **4703**, 74-84 (2002).

K. Shen and J. A. Turner, "Finite element simulations of nonlinear vibrations of atomic force microscope cantilevers," *proceedings of the SPIE Conference on Nondestructive Evaluation and Reliability of Micro- and Nanomaterial Systems*, **4703**, 93-104 (2002).

J. S. Wiehn and J. A. Turner, "Sensitivity of atomic force microscope vibration modes to changes in surface stiffness," proceedings of the *SPIE Conference on Smart Structures* *and Materials 2001: Sensory Phenomena and Measurement Instrumentation for Smart Structures and Materials*, **4328**, 332-341 (2001).

J. A. Turner, "Atomic force microscopy for high-resolution measurements of Young's modulus," proceedings of the *SPIE Conference on Advanced Nondestructive Evaluation for Structural and Biological Health Monitoring*, **4335,** 352-360 (2001).

R. Nilchiani, "Atomic Force Acoustic Microscopy for Characterization of Microelectromechanical Systems," M.S. Thesis, University of Nebraska-Lincoln (May 2002).

J. S. Wiehn, "Modeling the Dynamics of Atomic Force Microscope Cantilevers," M.S. Thesis, University of Nebraska-Lincoln (December 2001).

B. Wei, "Vibrations of Atomic Force Microscope Cantilevers with a Contact Boundary Condition," M.S. Thesis, University of Nebraska-Lincoln (August 2001).

APPENDIX

Select Publications
Student Theses

158467

ELSEVIER
Available online at www.sciencedirect.com
SCIENCE @ DIRECT®
Surface Science xxx (2003) xxx–xxx
SURFACE SCIENCE
www.elsevier.com/locate/susc

Imaging of flexural and torsional resonance modes of atomic force microscopy cantilevers using optical interferometry

Michael Reinstaedtler [a,*], Ute Rabe [a], Volker Scherer [b], Joseph A. Turner [c], Walter Arnold [a]

[a] Fraunhofer Institute for Non-Destructive Testing, Bldg. 37, University, D-66123 Saarbrücken, Germany
[b] Federal-Mogul Burscheid GmbH, Bürgermeister-Schmidt-Str. 17, D-51399 Burscheid, Germany
[c] Department of Engineering Mechanics, University of Nebraska, Lincoln, NE 68588-0526, USA

Abstract

Commercial rectangular atomic force microscope cantilever beams made of silicon were set into vibration, using a piezoelectric ultrasonic transducer coupled to the chip of a cantilever. The transducer was excited with continuous rf in the frequency range of 100 kHz to 3 MHz. The vibrations were monitored using an optical Michelson heterodyne-interferometer allowing the surface of the cantilever under examination to be scanned with a lateral resolution of several μm. A number of free torsional and flexural vibration modes of the beams were imaged quantitatively. Comparison of the experimental resonance frequencies and the amplitude and phase distribution of the modes to theoretical models showed that asymmetries in the beam strongly influence the vibrational behavior of the beam. The consequences for quantitative local stiffness measurements are discussed.

© 2003 Published by Elsevier Science B.V.

Keywords: Atomic force microscopy; Acoustics; Cantilever vibrations; Torsional resonances; Non-linear vibration; Interferometerical imaging of vibration

1. Introduction

Since the invention of the atomic force microscope (AFM) [1] several different quasi-static and dynamic operating modes have been developed, for example friction force microscopy (FFM) [2] or atomic force acoustic microscopy [3]. During the past few years, many groups have been improving the quasi-static FFM technique [4,5] to a dynamic method, expanding the possibility to examine the origin of friction on a nanoscale [6–18] without the shortcomings of conventional FFM, which are time-consumptive measurements with high noise and unstable friction imaging.

One crucial component for all AFM-operating methods is the flexible force-sensing cantilever [19]. These micro-fabricated AFM cantilevers can be regarded as miniature elastic beams with characteristic bending and torsional vibration modes. By means of elasticity theory it is possible to calculate the resonance frequencies and the local vibration

---

[*] Corresponding author. Tel.: +49-681-93023935; fax: +49-681-93025903.

E-mail address: reinstaedtler@izfp.fhg.de (M. Reinstaedtler).

0039-6028/03/$ - see front matter © 2003 Published by Elsevier Science B.V.
doi:10.1016/S0039-6028(03)00183-3

amplitudes and phases of the modes. Depending on the geometry of the beam analytical or numerical methods [20,21] can be used. However, the exact cantilever geometry is often not known and can vary considerably within one set of commercial beams. Properties of the beams, such as vertical and lateral spring constants are of fundamental importance for quantitative measurements, in particular for local elasticity measurements [20]. By examining the vibration spectra of the cantilevers during our ultrasonic AFM measurements, we often noticed the appearance of additional resonances not expected theoretically. Here we show that the free vibrational modes of clamped-free silicon AFM cantilevers can be imaged quantitatively. This provides evidence about the origin of the additional modes and also allows a quality control of AFM sensors because the effective spring constant depends on the vibrational mode of the cantilever [22], which in turn is influenced by the geometry of the cantilever, the mass distribution along its length, and the position of the tip.

2. Theory

2.1. Flexural vibrations

Bending and torsional vibrations of uniform, homogenous beams with constant rectangular cross-section can be described by a fourth- and a second-order partial differential equation, respectively. The equation of motion for the bending modes can be found in textbooks [23]

$$EI\frac{\partial^4 y}{\partial x^4} + \rho A\frac{\partial^2 y}{\partial t^2} = 0 \qquad (1)$$

where E is the Young's modulus, $I = ab^3/12$ is the area moment of inertia of a beam with rectangular cross section, a is its width and b its thickness, ρ is the mass density and $A = ab$ is the cross sectional area. Here, x is the coordinate in the longitudinal direction of the cantilever, $y(x)$ is the excursion from the rest position of the length element at x. A general solution for Eq. (1) can be written as

$$y(x,t) = (a_1 e^{\gamma x} + a_2 e^{-\gamma x} + a_3 e^{i\gamma x} + a_4 e^{-i\gamma x})e^{i\omega t} \qquad (2)$$

Here, $\omega = 2\pi f$ is the angular frequency and $\gamma = 2\pi/\lambda$ the flexural wave number. Inserting Eq. (2) in Eq. (1) yields the dispersion relation

$$EI\gamma^4 - \rho A\omega^2 = 0 \qquad (3)$$

or

$$\omega = \gamma^2\sqrt{\frac{EI}{\rho A}} \qquad (4)$$

The constants a_i ($i = 1, 2, 3, 4$) can be determined by the boundary conditions. In free vibrations, the cantilever is clamped at $x = 0$, whereas the free end is at $x = L$. This yields the characteristic equation for the wave number γ_n

$$\cos\gamma_n L \cosh\gamma_n L + 1 = 0 \qquad (5)$$

Using Eq. (4) and the solutions $\gamma_n L$ of Eq. (5), one obtains the bending-mode eigenfrequencies

$$f_n = \frac{(\gamma_n L)^2}{2\pi L^2}\sqrt{\frac{b^2 E}{12\rho}} \qquad (6)$$

The amplitude distribution of the flexural cantilever vibration $y_n(x)$ of each mode is described by the following equation

$$y_n(x) = y_0\left[(\cos\gamma_n x - \cosh\gamma_n x) - \frac{\cos\gamma_n L + \cosh\gamma_n L}{\sin\gamma_n L + \sinh\gamma_n L}(\sin\gamma_n x + \sinh\gamma_n x)\right] \qquad (7)$$

where y_0 is the vibrational amplitude.

2.2. Torsional vibrations

The equation of motion for torsional modes is

$$c_T\frac{\partial^2\Theta}{\partial x^2} - \rho J\frac{\partial^2\Theta}{\partial t^2} = 0 \qquad (8)$$

where Θ is the angle of twist, $c_T = ab^3G/3$ is the torsional stiffness and $J = a^3b/12$ the polar area moment of inertia. A general solution for Eq. (7) can be written as

$$\Theta(x) = A\sin\eta x + B\cos\eta x \qquad (9)$$

where constants A and B are also given by the clamped-free boundary conditions for the cantilever oscillations, so the amplitude distribution is

$$\Theta(x) = A \sin \eta x \tag{10}$$

The torsional wave number η is obtained by the balance of the torsional moments [12,24]

$$c_{\mathrm{T}} \frac{\partial \Theta(x)}{\partial x}\bigg|_{x=L} = 0$$

The eigenfrequencies for torsional vibrations are obtained by solving Eq. (8)

$$f_n = \frac{2n-1}{2} \underbrace{\frac{1}{L}\frac{b}{a}\sqrt{\frac{G}{\rho}}}_{\Delta f} \tag{11}$$

Unlike the bending mode eigenfrequencies (Eq. (6)) the torsional modes are equally spaced by Δf, because Eq. (8) exhibits no dispersion.

3. Experiments

3.1. Cantilever

The examined cantilevers were manufactured from highly doped, single-crystal silicon with integrated single-crystal silicon tip. The tip was pointing into the ⟨100⟩ direction, whereas the cantilever pointed into the ⟨110⟩ direction. We used two low force constant types designed for contact mode (Fig. 1) and for lateral force microscopy, respectively, from the same manufacturer (Pointprobe©, Nanosensors, Wetzlar, Germany). For generating a high enough torsional vibration amplitude, we selected cantilevers with low bending and hence also low torsional stiffness. In order to determine the geometrical parameters, the width and length of the cantilevers were measured with an optical microscope. From the measured resonance frequency of the first ten bending modes the thickness of the cantilever was calculated using Eq. (6) avoiding time-consuming measurements using an electron-microscope.

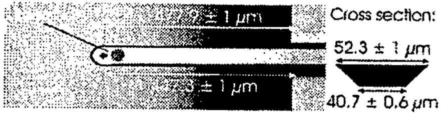

Fig. 1. Optical micrograph of the cantilever used for torsional mode measurement (type CONT); Calculated spring constant $k = 0.131$ N/m; nominal thickness: 2 ± 0.5 μm. The cantilever is supported by a single crystal silicon holder as can be seen on the right.

3.2. Atomic force microscope set-up

The experimental set-up to measure the free vibration spectra of the cantilever with the AFM is shown in Fig. 2. A commercial Scanning Probe Microscope (Dimension 3000, Digital Instruments, Santa Barbara, CA) with additional ultrasonic equipment was used to excite and measure flexural and torsional vibration resonances of the cantilever. A frequency generator (HP 33120 A) provides a sinusoidal signal, which is applied to a conventional ultrasonic shear wave transducer (Panametrics V151, 5 MHz center frequency) attached to the sample. As a sample, we used a piece of a silicon wafer. The ensuing sample surface vibration couples via the air column between the cantilever and the sample into the cantilever mounted over the sample with a distance of about 2–5 μm. The cantilever vibrations were measured with the internal optical detector of the instrument, provided its bandwidth was in the MHz

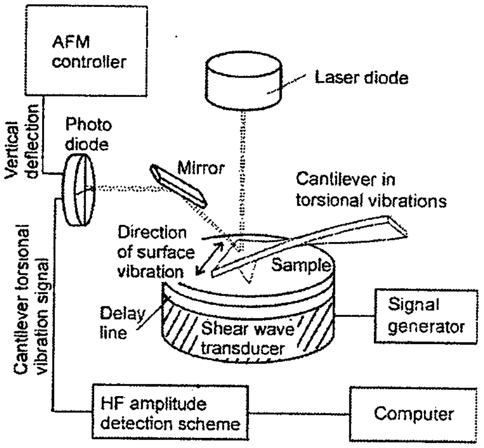

Fig. 2. Experimental set-up for torsional vibration measurements in an AFM.

regime, otherwise a fast external amplifying system was used. The HF amplitude detection scheme consists of a heterodyne down-converter which in addition receives a reference signal at the excitation frequency from the frequency generator. The heterodyne down-converter operates at frequencies from 75 kHz to 10 MHz and shifts the desired signal to a fixed 20 kHz intermediate frequency. It is evaluated by a lock-in amplifier. The set-up is controlled by a Labview program enabling one to change the frequency, to read the lock-in output, and to store the spectra.

Typical measured lateral vibration spectra of cantilever #1 (type CONT) are shown in Fig. 3. Besides torsional modes flexural modes also appeared in the lateral channel, however, never were torsional modes observed in the vertical channel. By calculating the first torsional eigenfrequency using Eq. (11), the 212 kHz peak in the lateral channel spectrum can be identified as belonging to a torsional resonance. However, a second peak appeared at 265.5 kHz without a corresponding peak in the vertical spectrum at the same frequency. In order to clarify the situation, we performed interferometric measurements of the displacements of the vibrating cantilevers in order to compare the experimentally determined vibration patterns to the expected patterns as calculated by Eqs. (7) and (11).

3.3. Interferometric measuring system

The interferometrical set-up is shown in Fig. 4. The chip of the cantilever was attached with a couplant to a shear ultrasonic transducer operated between 100 kHz and 3 MHz. It emitted into the chip transverse waves polarized perpendicular to the long axis of the cantilever beam and parallel to its width causing forced vibrations. The absolute amplitudes of the cantilever vibrations were measured with an optical Michelson heterodyne interferometer [25]. The He–Ne laser beam of the interferometer was focused onto the cantilever with a spot diameter of 2–5 μm. Using a motor-driven linear translation stage, the focal spot of the interferometer was scanned over the surface of the cantilever. A step size of 2 μm was chosen. To determine the resonance frequencies, a spectrum was taken at a location close to the free end of the cantilever. Then the modes were imaged by scanning the vibrating cantilever at its resonance frequencies and detecting the deflection of each position as a function of time. The amplitude and phase of each time signal were obtained by using Digital Fourier Transformation.

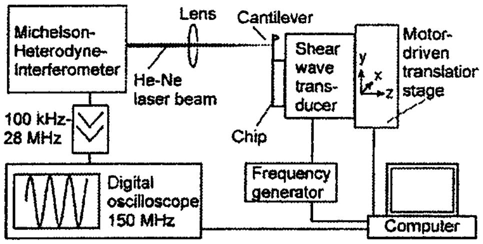

Fig. 4. Experimental set-up for imaging the resonance modes with an optical interferometer.

The measured amplitude and phase distribution of the third bending mode of a 225 μm long beam are shown in Fig. 5. Two nodes and three crests of the vibration are found according to theory. The phase of the signal is measured relative to the ex-

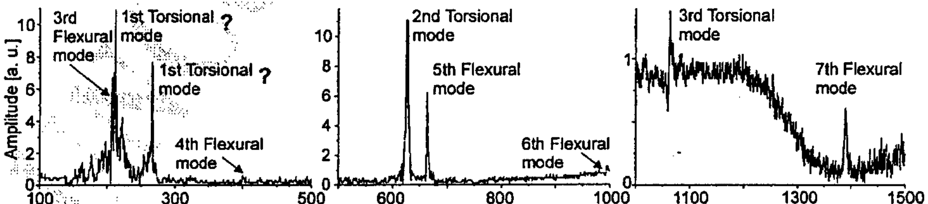

Fig. 3. AFM lateral channel spectra showing additional modes.

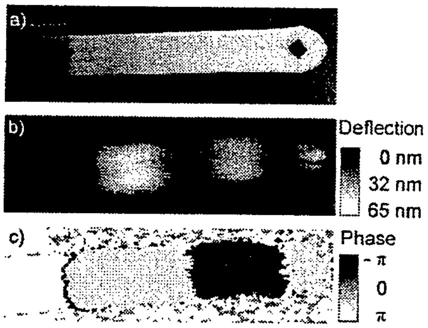

Fig. 5. (a) Optical micrograph of the cantilever measured; (b) amplitude and (c) phase distribution of the third bending mode of a rectangular cantilever. Scan size 300 × 100 μm^2.

citation signal. The phase difference between two neighboring crests is π.

The first three torsional modes of the 450 μm long rectangular silicon-cantilever used for the AFM measurement described above are shown in Fig. 6. The amplitude and phase distribution of the second and third torsional mode agree very well to the theoretical prediction. It is interesting to note that the first two modes with eigenfrequencies close to one another do not correspond to the modes expected according to Eq. (11), as shown in Fig. 7. Additionally, the position of the center line deviates from the middle of the cantilever for all modes shown in Fig. 6. Note that the amplitudes of the bending modes were much higher than the amplitudes of the torsional modes, though the transducer mainly excited lateral oscillations of the

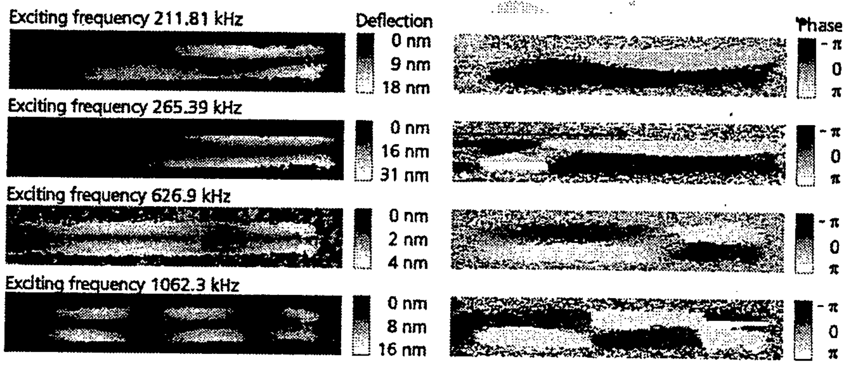

Fig. 6. Amplitude and phase distribution of the first three torsional modes of a rectangular Si-cantilever. The scan size is about 550 × 100 μm^2.

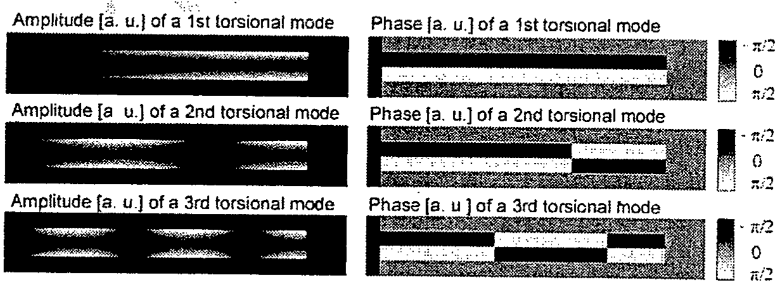

Fig. 7. Calculated amplitude and phase distribution of the first, second and third torsional mode.

cantilever base. This is caused by the lower bending stiffness of the cantilever compared to its torsional stiffness.

4. Mode coupling

We suggest that the origin of the asymmetrical shape of the modes is caused by geometrical asymmetries, mostly due to the tip positioned not exactly on the center line of the beam. These asymmetries in the vibration pattern entail a coupling of flexural and torsional vibrations via the tip when the tip is in force interaction with a sample surface. This holds in particular when additional static forces are applied in a measurement of elasticity [3]. Considering that the tip with the mass m_t is offset from the area center of the cross section by an amount d (see Fig. 8), the flexural and torsional modes are no longer independent. They couple via the forces acting on the tip and hence lead to an admixture of torsional motion in a flexural mode and vice versa. This coupling can be described by the Eqs. (1) and (8) taking account the following boundary conditions at the end with the tip ($x = L$)

$$EIy'''(x,t) = k_n y(x,t) - k_n \frac{d}{L}\theta(x,t) + m_t\left(\ddot{y}(x,t) - \frac{d}{L}\ddot{\theta}(x,t)\right) \qquad (12)$$

$$c_T\theta'(x,t) = -k_l h^2\theta(x,t) - k_n dLy(x,t) + m_t d(L\ddot{y}(x,t) - d\ddot{\theta}(x,t)) \qquad (13)$$

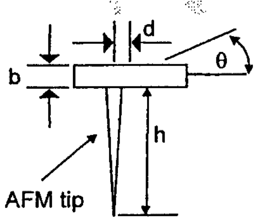

Fig. 8. Parameters entering in the description of mode coupling via the forces acting on an AFM tip of length h which is slightly offset by an amount d from the center-line of the beam.

k_l and k_n are the lateral and normal contact stiffness, respectively. Here, when the cantilever performs free oscillations, the boundary conditions reduce to

$$EIy'''(x,t) = m_t\left(\ddot{y}(x,t) - \frac{d}{L}\ddot{\theta}(x,t)\right) \qquad (14)$$

$$c_T\theta'(x,t) = m_t d(L\ddot{y}(x,t) - d\ddot{\theta}(x,t)) \qquad (15)$$

This still leads to a coupling of the modes because the mass of the tip is not centered. Seeking harmonic solutions $y(x,t) = y(x)e^{i\omega t}$ and $\theta(x,t) = \theta(x)e^{i\omega t}$ leads to the characteristic equations

$$EIy'''(x) = m_t\omega^2\left(\frac{d}{L}\theta(x) - y(x)\right) \qquad (16)$$

$$c_T\theta'(x) = m_t d\omega^2(d\theta(x) - Ly(x)) \qquad (17)$$

Inserting Eqs. (2) and (10) into Eqs. (16) and (17) leads to the relation $\eta = H\gamma^2$ between the flexural and torsional wave numbers γ and η where

$$H = \sqrt{EIJ/Ac_TL^2} \qquad (18)$$

It is this parameter H which determines the likelihood of modal coupling. The mode shape of the peak at 212 kHz is a combination of the flexural and torsional solution. The weighting of the combined solutions depends on the type of and degree of coupling as well as on the excitation method. Two modes have frequencies very close to each other. The frequencies of the third flexural mode and the first torsional mode lie within 5% of each other. Thus, during forced vibrations, they are often excited simultaneously. Fig. 9 shows a

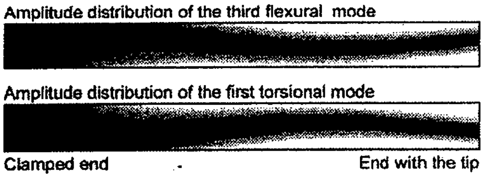

Fig. 9. Spatial plots of modes 3 and 4 calculated from the flexural/torsional coupling model with $H = 0.025$. When the frequencies are close together small perturbations cause these modes to couple.

plot of the combination of the first torsional and the third flexural mode.

A resonance was also observed at 265 kHz. The corresponding mode does not fit into an analysis based on mode coupling as explained above. Most likely, this mode originates from nonlinear coupling into flexural motion about an axis perpendicular to the plan view. Such a mode would have f_1 about $a/b = 22.5$ times the usual f_1 for flexure. This value matches with the observed frequency at 265 kHz. Calculating the elastic strain amplitudes prevailing in the beams for both modes, i.e. $\varepsilon_{\text{flex}} = (b/2)(\mathrm{d}^2y/\mathrm{d}x^2)$ and $\varepsilon_{\text{tors}} \approx \theta a/L$ (Eqs. (7) and (10)) and using the measurements for the amplitudes as shown in Figs. (5) and (6), one obtains values of the order $\varepsilon_{\text{flex}} \approx 10^{-5}$ and $\varepsilon_{\text{tors}} \approx 10^{-4}$. These rather large values make nonlinear mixing of modes based on higher-order elasticity possible [26].

5. Conclusion

In summary, we have shown that mode coupling due to geometrical and mass asymmetries account for a number of resonances besides the standard flexural and torsional modes. The coupled modes can be observed in many commercial cantilevers. They are sometimes called spurious modes, yet they can be explained using quite simple physical principles. The large strains values obtained in dynamic operations may lead to nonlinear mixing of modes.

Acknowledgements

This work was supported by the German Science Foundation through various grants. One of us (M.R.) is supported by a stipend via the Graduate College on "Advanced Materials for Efficient Energy Conversion". The support of the U.S. Air Force Office of Scientific Research (grant no. F49620-99-1-0254) for J.A.T. is gratefully acknowledged. We also thank U. Hartmann, Department of Experimental Physics, University of the Saarland, for discussions.

References

[1] G. Binnig, C.F. Quate, C. Gerber, Phys. Rev. Lett. 56 (1986) 930.
[2] C.M. Mate, G.M. McClelland, R. Erlandsson, S. Chiang, Phys. Rev. Lett. 59 (1987) 1942.
[3] U. Rabe, S. Amelio, M. Kopycinska, S. Hirsekorn, M. Kempf, M. Göken, W. Arnold, Surf. Interface Anal. 33 (2002) 65–70, and references contained therein.
[4] O. Marti, J. Colchero, J. Mlynek, Nanotechnology 1 (1990) 141–144.
[5] G. Meyer, N.M. Amer, Appl. Phys. Lett. 57 (1990) 2089–2092.
[6] P. Maivald, H.-J. Butt, S.A.C. Gould, C.B. Prater, B. Drake, J.A. Gurley, V.B. Elings, P.K. Hansma, Nanotechnology 2 (1991) 103–106.
[7] T. Göddenhenrich, S. Müller, C. Heiden, Rev. Sci. Instrum. 65 (1994) 2870–2873.
[8] K. Yamanaka, E. Tomita, Jpn. J. Appl. Phys. 34 (1995) 2879–2882.
[9] J. Colchero, M. Luna, A.M. Baró, Appl. Phys. Lett. 68 (1996) 2896–2898.
[10] R.W. Carpick, D.F. Ogletree, F. Salmeron, Appl. Phys. Lett. 70 (1997) 1548–1550.
[11] J. Kerssemakers, J.Th.M. De Hosson, Surf. Sci. 417 (1998) 281–291.
[12] K. Yamanaka, S. Nakano, Appl. Phys. A 66 (1998) 313–317.
[13] K. Yamanaka, A. Noguchi, T. Tsuji, T. Koike, T. Goto, Surf. Interface Anal. 27 (1999) 600–606.
[14] H.-U. Krotil, E. Weilandt, Th. Stifter, O. Marti, S. Hild, Surf. Interface Anal. 27 (1999) 341–347.
[15] H.-U. Krotil, Th. Stifter, O. Marti, Rev. Sci. Intrum. 71 (2000) 2765–2771.
[16] H.-U. Krotil, Th. Stifter, O. Marti, Rev. Sci. Intrum. 72 (2001) 150–156.
[17] P.-E. Mazeran, J.-L. Loubet, Tribol. Lett. 7 (1999) 199–212.
[18] A. Spychalski-Merle, K. Krischker, T. Göddenhenrich, C. Heiden, Appl. Phys. Lett. 77 (2000) 501–503.
[19] T.R. Albrecht, S. Akamine, T.E. Carver, C.F. Quate, J. Vac. Sci. Technol. A 8 (1990) 3386.
[20] U. Rabe, K. Janser, W. Arnold, Rev. Sci. Instrum. 67 (1996) 3281–3293.
[21] T. Drobek, R.W. Stark, M. Gräber, W.M. Heckl, New J. Phys. 1 (1999) 15.1.
[22] J.A. Turner, S. Hirsekorn, U. Rabe, W. Arnold, J. Appl. Phys. 82 (1997) 966–979.
[23] L. Landau, E.M. Lifschitz, Lehrbuch der theoretischen Physik, Auflage Bd. 7 (1991) 7.
[24] K. Yamanaka, S. Nakano, Appl. Phys. A 66 (1998) 313–317.
[25] B. Cretin, P.E. Mazeran, J.L. Loubet, Tribol. Lett. 3 (1995) 125.
[26] A.H. Nayfeh, Nonlinear Interactions, John Wiley and Sons, New York, 2000, p. 542.

NDE-Vol. 20, 7th ASME NDE Topical Conference
ASME 2001

Atomic Force Acoustic Microscopy for Materials Characterization of Microelectromechanical Systems

Joseph A. Turner, Roshanak Nilchiani, and Joshua S. Wiehn
Department of Engineering Mechanics, W317.4 Nebraska Hall
University of Nebraska-Lincoln Lincoln, Nebraska 68588-0526, USA

Abstract

Atomic force acoustic microscopy (AFAM) can be used to make quantitative images of surface stiffness with high resolution. The technique utilizes the dynamic response of the atomic force microscope (AFM) cantilever, specifically in terms of the higher-order cantilever modes. Motion of the specimen while in contact with the AFM tip induces vibrations in the cantilever. The dynamical properties of the cantilever change during scanning due to the variations of surface stiffness. Both stiff and compliant cantilevers may be used for stiffness imaging if the appropriate vibration mode is chosen. Experimental AFAM results on polysilicon for microelectromechanical systems (MEMS) are presented. The AFAM results provide stiffness information about the material microstructure that is not available from topography information alone. The technique provides in-situ stiffness information without damaging the MEMS.

Introduction

The atomic force microscope (AFM) was developed as an instrument for measuring surface topography while operating in a quasistatic mode [1]. The deflection of the microscope cantilever plotted as a function of surface location gives a high-resolution image of surface topography. More recent applications of the AFM have exploited the dynamic characteristics of the AFM. Many versions of dynamic atomic force microscopy have been proposed for imaging specimens and measuring material properties [2-5]. All of these methods rely on the relative motion between the atomic force microscope (AFM) tip and the specimen surface. The high frequency excitation of the specimen surface or AFM cantilever can provide a better signal-to-noise ratio for imaging while doing less damage to the specimen surface. These techniques utilize the dynamic response of the cantilever, specifically in terms of the vibrational modes. The dynamic response of an elastic cantilevered beam in contact with a surface, however, is not easily described. The tip-sample interaction forces are, in general, nonlinear and are the subject of intensive research themselves. When an elastic beam interacts with these surface forces, the many flexural and torsional modes must be included as part of the complete dynamics. These higher modes are often excited simultaneously in experiments.

In much of the current research, the amplitude of the surface motion is kept small. In this case, the motion may be studied by linearizing the nonlinear tip-sample interaction forces about an equilibrium point. The cantilever motion may then be modeled as a beam with a linear spring attached near the end. Measured natural frequencies of the cantilever with attached spring then define the spring stiffness. Appropriate tip-sample interaction models are then used to relate the spring stiffness to the Young's modulus of polysilicon. Atomic force acoustic microscopy (AFAM) is anticipated to have many uses for *in situ* measurements of polysilicon microelectromechanical systems (MEMS).

Atomic Force Acoustic Microscopy

The atomic force microscope cantilever, as shown schematically in Fig. 1, is modeled as an Euler-Bernoulli beam. The beam is assumed uniform and homogenous with constant cross-section. It is cantilevered at one end. At the end opposite of the cantilever a tip with small radius is attached. The sample is offset such that the beam has an initial static deformation $y(x)$. Motion about this initial equilibrium deformation is given by $w(x,t)$. The linearized boundary value problem for this system has a governing equation and boundary conditions given by [6,7]

$$EI\frac{\partial^4 w(x,t)}{\partial x^4}+\rho A\frac{\partial^2 w(x,t)}{\partial t^2}=0, \qquad (1)$$

$$w\left(x=0,t\right)=0, \qquad w'\left(x=0,t\right)=0, \tag{2}$$

$$w''\left(x=L,t\right) = 0, \tag{3}$$
$$EIw'''\left(x=L,t\right) = \kappa w\left(x=L,t\right). \tag{4}$$

In Eqs. (1)-(4), $w(x,t)$ defines the dynamic cantilever position relative to $y\left(x\right)$. The AFM cantilever is defined by the modulus E, the area moment of inertia I, the volume density ρ, and the cross-sectional area A. Here, EI and ρA are assumed uniform over the length of the cantilever. The boundary conditions given by Eqs. (2) correspond to conditions of zero displacement and zero slope at $x=0$. The boundary condition given by Eq. (3) corresponds to zero moment at $x=L$.

The force balance between the shear force of the beam and the force from the contact mechanics is given by Eq. (4). The contact force is, in general, nonlinear. Here, the motion is assumed small such that a linear contact force may be used. The contact force is proportional to the displacement of the end of the beam with the effective contact stiffness κ (linear spring constant) as the proportionality constant. Because a linear model is used to describe the tip-sample interaction force, the results are restricted to small tip displacements. Such a condition is easily satisfied experimentally. The actual value of κ is given in terms of the material properties of the tip and sample and depends on the interaction model used. Simple Hertzian theory [8-9], more complex Maugis mechanics [9], or other models [10-12] may all be linearized about some initial equilibrium position to determine this spring constant.

Eqs. (1)-(4) define completely the linearized flexural vibration problem. The natural frequencies of the cantilever vibrations are dependent on the linear spring constant κ. Solution of the corresponding eigenvalue problem leads to the characteristic equation that governs the allowable frequencies. The characteristic equation is given by [6]

$$\gamma^3\left(\cos\gamma\cosh\gamma+1\right) - \frac{\kappa}{EI/L^3}\left(\sinh\gamma\cos\gamma-\sin\gamma\cosh\gamma\right)=0. \tag{5}$$

Equation (5) is solved numerically for the values of γ. The dispersion relation

$$f=\gamma^2\frac{1}{2\pi}\sqrt{\frac{EI/L^3}{\rho AL}}, \tag{6}$$

is then used to determine the natural frequencies in terms of the wave numbers. The linear vibrations of the AFM may be used to study the material properties of specimens. Knowledge of the natural frequencies can be used to determine the effective spring constant κ. The tip-sample mechanics are then used to deduce the local Young's modulus. The most general contact mechanics model, due to Maugis [9] is discussed below. The Maugis model was first introduced to the AFM literature by Burnham and coworkers [13].

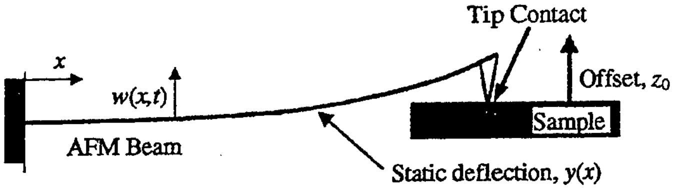

Figure 1: Schematic of the problem. The AFM probe is in contact with a specimen. Initial contact is made when the sample offset, z_0, is zero. The static sample offset causes a static beam deflection, $y(x)$. The dynamic motion, $w(x,t)$, is defined relative to $y(x)$. The contact forces between the tip and sample are may be discussed for different contact models.

Contact Mechanics

The mechanics of the AFM tip as it interacts with a specimen are complex and generally nonlinear. Here, the contact is assumed frictionless and the contact force is assumed to act normal to the tip. The geometry of the contact problem is shown in Fig. (2). The goal is to relate the applied force p to the penetration depth of the tip into the specimen δ. Important parameters for this problem are the radius of the contact area a, the work of adhesion at contact ω, and the stress in the cohesive zone σ_0.

The material properties and geometry of the specimen and AFM tip also are important. These parameters are shown in Fig. (3). The reduced tip-sample curvature,

$$\frac{1}{R}=\frac{1}{R_t}+\frac{1}{R_s}, \tag{7}$$

accounts for curvature of both tip (R_t) and specimen (R_s). Most often, the specimen is assumed flat such that $R=R_t$. The reduced elastic modulus K is defined by

$$\frac{1}{K}=\frac{3}{4}\left(\frac{1-\nu_t^2}{E_t}+\frac{1-\nu_s^2}{E_s}\right), \tag{8}$$

where E_t, ν_t, E_s, and ν_s are the Young's modulus and Poisson's ratio of the tip and sample, respectively. The general goal for materials characterization studies with AFAM is to extract and image Young's modulus of the specimen. Such a procedure involves measurement of K. The material properties of the tip are generally assumed to be known. In addition, a calibration procedure or scanning electron microscopy is necessary to determine the tip radius.

The most comprehensive tip mechanics model is that of Maugis [9,13,14]. The Maugis model captures many aspects of the contact mechanics observed in AFM studies through the use of fracture mechanics concepts. Most importantly, it can account for adhesion hysteresis. The Maugis model provides a continuous functional dependence from Hertzian (or DMT [11]) mechanics, without adhesion hysteresis, to the JKR [12] limit of maximum

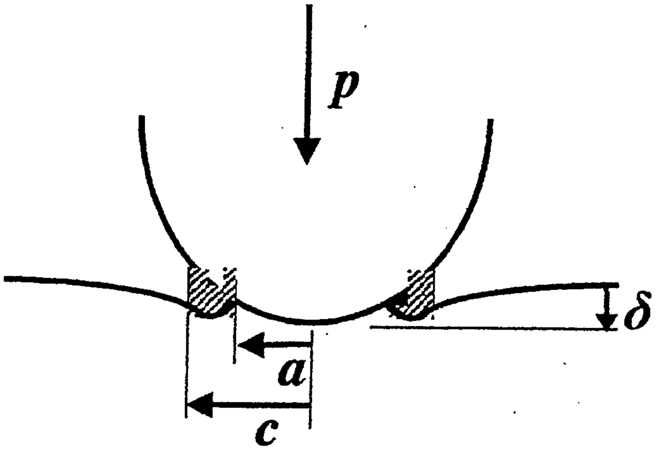

Figure 2: Schematic of the parameters of the contact mechanics. An applied load p results in a penetration to depth δ. The contact radius is given by a and the radius to the edge of the cohesive zone is denoted by c.

adhesion hysteresis. The dimensionless parameters used are defined as

$$A = a\left(\frac{K}{\pi\omega R^2}\right)^{1/3}, \quad P = p\left(\frac{1}{\pi\omega R}\right), \tag{9}$$

$$\Delta = \delta\left(\frac{K^2}{\pi^2\omega^2 R}\right)^{1/3}, \quad \lambda = 2\sigma_0\left(\frac{R}{\pi\omega K^2}\right)^{1/3}, \tag{10}$$

where A is the contact radius, P is the applied force, Δ is the penetration depth, and λ is the adhesion parameter.

In terms of these parameters, several different contact mechanics models may be described. Several of these models are illustrated by the force-penetration curves (P vs. Δ) shown in Fig. (4). Hertzian mechanics is given by

$$P_H = A^3, \qquad \Delta_H = A^2, \tag{11}$$

which may be written $P_H = \Delta_H^{3/2}$. In the Hertz model, adhesion is neglected such that there is no attractive force associated with loss of contact. The DMT model is a modified Hertzian model [11]. In this case, a constant attractive force is added to the Hertzian mechanics, $P_D = A^3 - 2$. However, the tip geometry is assumed not to change, $\Delta_D = A^2$. The DMT $P_D(\Delta)$ is noted in Fig. 4 for $\lambda = 0$. The Hertz and DMT models do not include adhesion hysteresis effects. Thus, they are most applicable to AFM research for low adhesion specimens, hard materials or small radii of curvature.

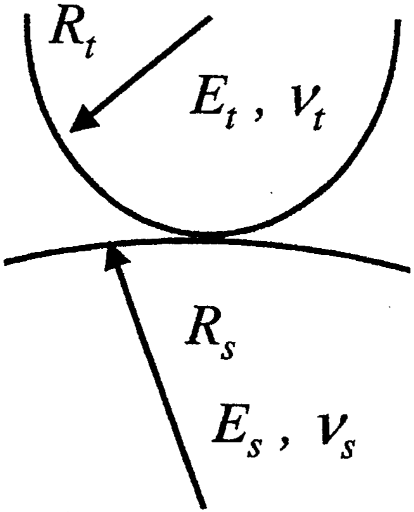

Figure 3: Geometry of the contact problem in terms of the tip parameters (subscript t) and specimen parameters (subscript s).

In the high adhesion limit, the JKR model is appropriate. It is given by [12]

$$P_J = A^3 - A\sqrt{6A}, \qquad \Delta_J = A^2 - \frac{2}{3}\sqrt{6A}. \tag{12}$$

This model is most applicable for high adhesion specimens, soft materials or large radii of curvature.

The model developed by Maugis is comprehensive in that it captures all types of tip-sample mechanics through the introduction of an adhesion parameter λ. Attractive (tensile) stresses are assumed to act between the tip and specimen in a cohesive zone that surrounds the contact area. These stresses are assumed constant (σ_0) within an annulus of width d. For the Maugis model, the force and deflection are

$$\begin{aligned} P_M &= A^3 - \lambda A^2 M_1, \\ \Delta_M &= A^2 - \frac{4}{3}A\lambda\sqrt{m^2-1}, \end{aligned} \tag{13}$$

where

$$M_1 = \sqrt{m^2-1} + m^2\tan^{-1}\sqrt{m^2-1}. \tag{14}$$

In Eqs. (13) and (14), $m = c/a$ is the ratio of the radius to the edge of the cohesive zone to the radius of the contact area. The width of the cohesive zone $d = c - a$. An additional equation is necessary for the Maugis mechanics. The Griffith equilibrium equation defines the relation between λ, m, and A. It is given by [9]

$$\frac{\lambda A^2}{2}M_2 + \frac{4\lambda^2 A}{3}M_3 = 1, \tag{15}$$

where

$$M_2 = \sqrt{m^2-1} + \left(m^2-2\right)\tan^{-1}\sqrt{m^2-1}, \quad (16)$$

$$M_3 = 1-m+\sqrt{m^2-1}\tan^{-1}\sqrt{m^2-1}. \quad (17)$$

A comparison of this contact model for several different values of λ is shown in Fig. 4. When Δ is positive, the sample is deflected away from the AFM tip. A negative value for Δ implies that the material is bulging out from the surface. The Maugis model includes attractive forces from adhesion such that the cantilever is deflected downward when contact is initiated. In this case, the tensile stresses in the cohesive annulus are greater than the compressive stresses in the contact area. The effect of adhesion hysteresis is also observed in Fig. 4. Several curves shown in Fig. 4 bend back on themselves. These curves have a section of positive slope when both P and Δ are negative. Points on this part of the curve are unstable equilibria. Thus, when moving continuously on these curves loss of contact occurs when the cantilever stiffness exceeds the contact stiffness. In addition, when contact is reinitiated, the tensile cohesive stresses would pull the AFM tip back into contact. This type of hysteretic behavior results for all values of λ that are larger than about 0.94. The Maugis model reduces to that of DMT mechanics when $\lambda = 0$. In the opposite high adhesion limit, when λ is large, the JKR limit [12] is approached.

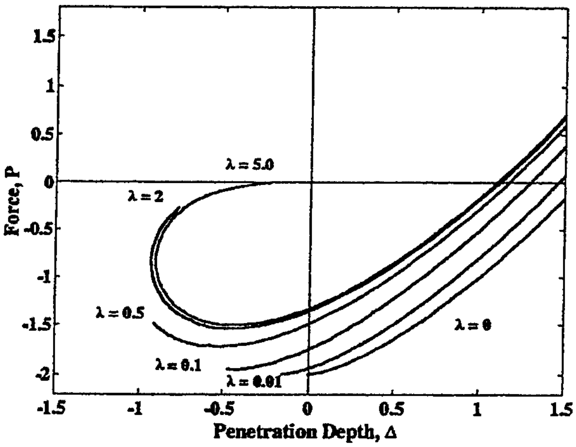

Figure 4: Normalized force-displacement relation for various values of λ using the Maugis contact mechanics model.

Surface Stiffness

As the AFM tip is placed in contact with the specimen, it initially settles at an equilibrium position somewhere on the $P(\Delta)$ curve. The AFM cantilever will have some initial deflection $y(x)$ determined by the force balance at the tip. The cantilever or sample is then vibrated at small amplitude. If the displacements of the AFM cantilever remain small, a linearization of the above contact models may be used to determine the appropriate spring stiffness necessary for the vibration problem. In this case, the linear spring constant (in nondimensional form) is defined as

$$\xi = \frac{dP}{d\Delta}. \quad (18)$$

In dimensional form, we have

$$\kappa = \frac{dp}{d\delta} = \left(\pi\omega R^2 K^2\right)^{1/3}\frac{dP}{d\Delta}. \quad (19)$$

For the Maugis model, the relation of the surface stiffness is found from Eqs. (13)-(15). The force and deflection are both given in terms of the contact area and parameter λ. In addition, the Griffith equilibrium equation shows that λ is also a function of A. Thus, we have

$$\frac{\partial P_M}{\partial A} = 3A^2 - M_1\left[2\lambda A + A^2\frac{\partial\lambda}{\partial A}\right], \quad (20)$$

$$\frac{\partial \Delta_M}{\partial A} = 2A - \frac{4}{3}\left[\lambda + A\frac{\partial\lambda}{\partial A}\right]\sqrt{m^2-1}. \quad (21)$$

The rate of change of λ with A is found from Eq. (15) to be

$$\frac{\partial\lambda}{\partial A} = -\frac{2\lambda}{A}\frac{3AM_2+4\lambda M_3}{3AM_2+16\lambda M_3}, \quad (22)$$

where M_2 and M_3 are defined in Eqs. (16) and (17). Thus, the contact stiffness from the Maugis model is

$$\xi_M = \frac{9}{2}A\frac{Q}{R}, \quad (23)$$

where

$$Q = 3A^2M_2 + 16A\lambda M_3 - 8\lambda^2 M_1 M_3, \quad (24)$$

and

$$R = 3M_2A\left(3A + 2\lambda\sqrt{(m^2-1)}\right) + 16M_3\lambda\left(3A - \lambda\sqrt{(m^2-1)}\right). \quad (25)$$

The general Maugis result for the stiffness reduces to the Hertz and DMT cases (both have the same ξ vs. P curves) for $\lambda \to 0$ and to the JKR result when λ is very large. Figure (5) is a plot of ξ as a function of applied load P for various values of λ.

Experiments

The experiment used here is similar to that described elsewhere [2]. A standard atomic force microscope (Thermomicroscopes, Autoprobe CP) is modified for AFAM capabilities. A schematic of the AFAM experiment is shown in Fig. (6). The specimen is placed on a broadband ultrasonic transducer (2.25

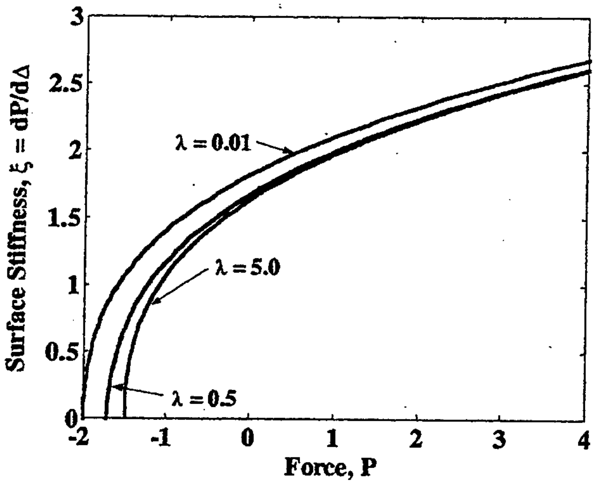

Figure 5: Normalized surface stiffness as a function of applied load P, for various values of λ using Maugis contact mechanics.

MHz center frequency). The transducer is mounted on the AFM stage and is excited by the function generator. The output from the AFM photodiode is mixed in the lock-in amplifier with the function generator output. The lock-in output and the photodiode output are both used by the AFM computer for imaging.

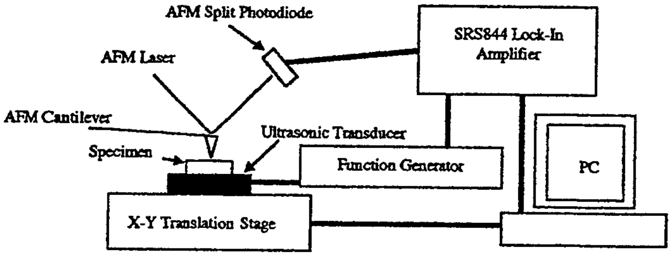

Figure 6: Schematic of the atomic force acoustic microscopy experiment. Both the topography and lock-in amplifier output are used for imaging.

Two sets of AFAM results are presented in Figs. (7)-(10). The specimens are polysilicon strips fabricated at the CRONOS MEMS foundry. The scan size of each figure is 2 μm x 2 μm.

Topography and AFAM results using mode 1 of a stiff cantilever (40 N/m) are shown in Figs. (7) and (8), respectively. The applied force was 1000 nN. The lightest color in the topography image is 85 nm higher than the darkest color. The topography image clearly shows a few of the grains of the polysilicon. The AFAM image, shown in Fig. (8), was made using an excitation frequency of 816 kHz. The contrast in this image is related to shifts in the cantilever resonance peak. The chosen excitation frequency was slightly higher than the resonance frequency. Thus, lighter colors implies less stiffness. The darkest colors are difficult to interpret. The peak may have shifted greatly higher or lower. The stiffness contrast (AFAM image) of the polysilicon is considerable. Within individual grains, contrast variations are observed. In particular, the grain indicated in Fig. (7) with the arrow is especially interesting. The AFAM image indicates that this grain has large variations in stiffness throughout. The grains are expected to be single crystal grains which grow perpendicular to the MEMS surface. The source of these stiffness variations is still under investigation.

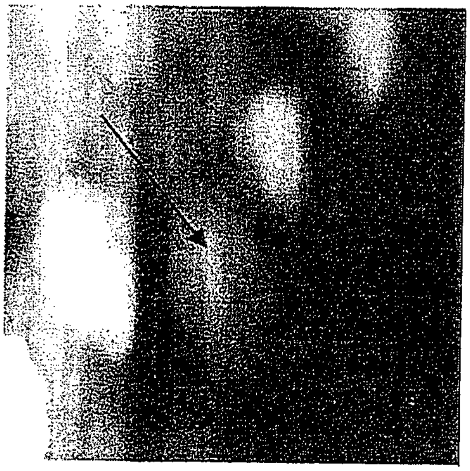

Figure 7: Topography image of polysilicon using a stiff cantilever (40 N/m). The scan size is 2 μm x 2 μm

Topography and AFAM results using a weaker cantilever (3 N/m) are shown in Figs. (9) and (10), respectively at a different location on the specimen. The topography image, Fig. (9), has a maximum height difference of 85 nm. The lightest color corresponds to the highest topography. The AFAM image is shown in Fig. (10). These images were made using the second vibration mode of a compliant cantilever with natural frequency in contact of 623 kHz. In this image, the lightest color corresponds to an amplitude of 1.2 mV. The applied force on the cantilever was 700 nN. Again the stiffness variations within the grains are clearly observed.

Effective Cantilever Length

AFM cantilevers are normally manufactured using etching processes. These techniques are not currently precise enough for the cantilever geometry to be known with high accuracy. For AFAM measurements the placement of the tip along the cantilever is a critical piece of information. SEM images show that

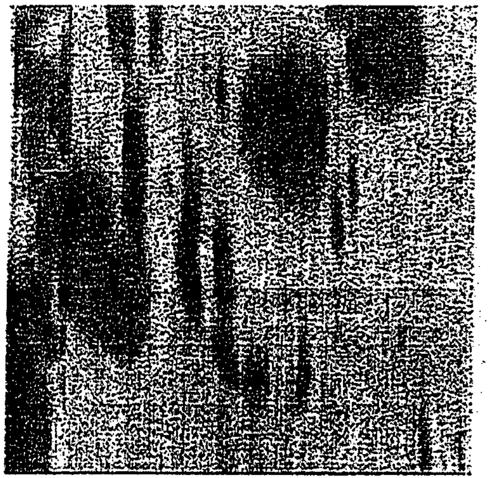

Figure 8: AFAM image using the first cantilever mode of a stiff cantilever. The first free natural frequency is 170 kHz. The scan size is 2 μm x 2 μm.

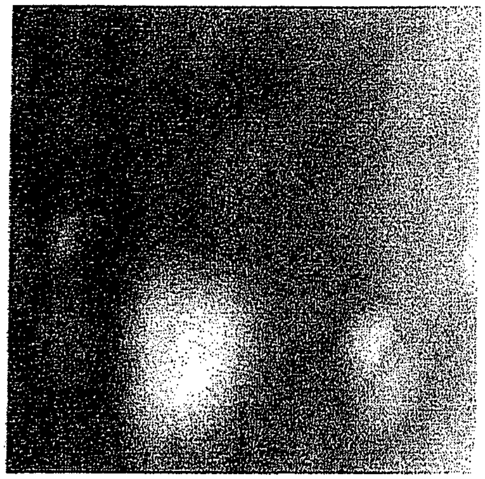

Figure 9: Topography image of polysilicon using a compliant cantilever (3 N/m). The scan size is 2 μm x 2 μm

the tip may be anywhere from 90-99% of the cantilever length from the fixed end. Attempts to characterize the effective length of the cantilever (i.e., the distance from the fixed end to the tip location) have met with some success [2]. Here an alternative method is proposed.

The shift in the natural frequencies of the beam are affected by the contact stiffness. This stiffness is a function of the applied load. If the Hertzian contact model is used we have

$$\kappa = \frac{3}{2}\sqrt[3]{K^2Rp}. \qquad (26)$$

For a certain applied load p_1 and values of R and K there is a unique corresponding stiffness κ_1. Now imagine that R and K are held constant while another load p_2 is applied with corresponding stiffness κ_2. If $p_2 = Bp_1$, where B is a constant factor, then $\kappa_2/\kappa_1 = B^{1/3}$. Thus, the shift in stiffness as a function of relative applied load is known. Also, the shifted frequencies corresponding to the different values of κ may be determined. For a set of applied forces, there is one effective length which provides the best fit to the data for a single value of L. To illustrate the method consider the following. A cantilever with first free frequency of 176 kHz is placed in contact with Si <100> with an applied load of 800 nN. The first natural frequency is measured to be 844 kHz as shown in Fig. (11). This frequency is 4.8 times larger than $(f_1)_{free}$. If the cantilever were pinned at the end, the maximum shift possible is 3.92 times greater than the free [15]. Thus, the effective length has shortened such that the frequency is higher. Next, another higher load is applied, such as 1600 nN. The contact stiffness should increase by a factor of $2^{1/3}$ with a known change in frequency. Other loads are also applied in a similar manner. Finally, the experimental results are compared with curves of natural frequencies for different values of the effective length. The curve for $L_{eff} = 0.969L$ was found to be the best fit to these data. This result is the unique solution for both the effective length and contact stiffness. It should be noted that this method requires no information about the tip radius R nor the material properties of the beam. The required measurements are *relative* to the free experimental measurements. Such a technique may be easily extended to non-uniform cross-sections. The effect of damping is expected to have an influence on this result, but was not considered. Comparison of this method for determining the effective length with other methods, such as SEM, are currently in progress. The technique is restricted to stiff cantilevers with high applied loads such that the Hertzian theory is valid.

Young's Modulus for Polysilicon

Estimates of Young's modulus for polysilicon are now made based on the results presented above. Both the first mode of the stiff cantilever (40 N/m) and the second mode of the more compliant cantilever (3 N/m) are used. For the stiff cantilever the effective length, $L_{eff} = 0.969L$ was used to determine the contact stiffness on the polysilicon MEMS material. Again the relative frequency shift is examined. If the applied load is the same on both the silicon and on the polysilicon, the ratio of the contact stiffnesses is

$$\frac{\kappa_{poly}}{\kappa_{\rm Si}} = \frac{\sqrt[3]{K_{poly}^2 R_{poly}}}{\sqrt[3]{K_{\rm Si}^2 R_{\rm Si}}}. \qquad (27)$$

Equation (27) is rearranged and solved for E_{poly} where use of

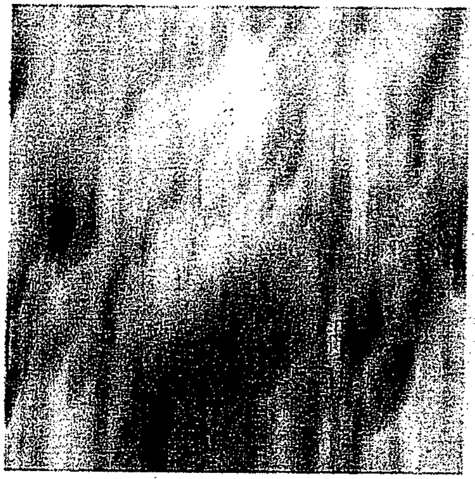

Figure 10: AFAM image using the second cantilever mode of a compliant cantilever (623 kHz). The first free natural frequency is 90 kHz. The scan size is 2 μm x 2 μm.

the reduced modulus, Eq. (8) has been used. The result is

$$E_{poly} = \frac{F\left(1-\nu_{poly}^2\right)}{[1-F]\,\frac{1-\nu_t^2}{E_t}+\frac{1-\nu_{\mathrm{Si}}^2}{E_{\mathrm{Si}}}}, \tag{28}$$

where the factor F is given by

$$F = \left(\frac{\kappa_{poly}}{\kappa_{\mathrm{Si}}}\right)^{3/2}\sqrt{\frac{R_{\mathrm{Si}}}{R_{poly}}}. \tag{29}$$

The reduced radius on silicon R_{Si} is assumed to be that of the tip radius R_t because the silicon specimens were very flat. The reduced radius for the polysilicon must reflect the topography seen in Figs. (7) and (9). In this case,

$$\sqrt{\frac{R_{\mathrm{Si}}}{R_{poly}}} = \sqrt{1+\frac{R_t}{R_s}}, \tag{30}$$

where R_s is the sample radius. The sample radius is estimated to be on the order of 50 nm. The tip radius, measured using calibration gratings, was $R_t = 120$ nm. Using $\nu_t = 0.181$, $E_t =$ 130.4 GPa, and $\nu_{poly} = 0.18$, gives the value for $E_{poly} \approx 104$ GPa. This value for E_{poly} is about 65% of that found from tensile tests of polysilicon [16]. The present results are encouraging, but still need improvement.

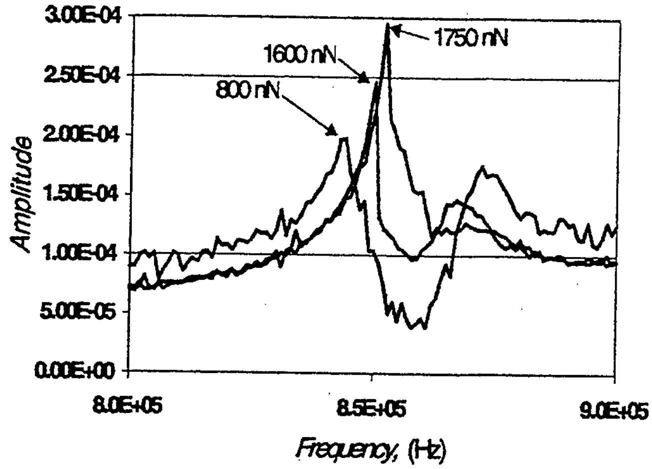

Figure 11: Experimental frequecy spectra for three different applied loads. The free natural frequency of the cantilever (40 N/m) was 176 kHz. The specimen was silicon <100>.

For the more compliant cantilever, the adhesion effects are much more important. Therefore, the method used for the stiff cantilever is not expected to apply. The tip radius was measured using calibrated gratings and determined to be $R_t = 160$ nm. The applied load was 700 nN. The measured second natural frequency of 623 kHz corresponds to a contact stiffness of $\kappa =$ 41.1 N/m. The measured pull-off force was 112 nN. From the definition of the dimensionless force, Eq. (13), this pull-off force implies that $P \approx 6.25$ for the applied load used. From Eq. (23), the range of values for $\xi = dP/d\Delta \approx 2.9 - 3.0$ for all values of λ. Rearranging Eq. (19) gives

$$K = \left[\frac{\kappa}{\left[(\pi\omega R)\,R\right]^{1/3}\frac{dP}{d\Delta}}\right]^{3/2}. \tag{31}$$

Substitution of the above values into Eq. (31) gives $K =$ 400 MPa. In terms of the specimen stiffness we have

$$E_s = \frac{1-\nu_s^2}{\frac{4}{3}\frac{1}{K}+\frac{1-\nu_t^2}{E_t}}. \tag{32}$$

Using $\nu_t = 0.181$, $E_t = 130.4$ GPa, and $\nu_s = 0.18$ gives $E_s = 290$ MPa. This value is unrealistically low for polysilicon. This result highlights the difficulties associated with making measurements of stiff materials with compliant cantilevers. Sources of error associated with these measurements include the tip radius, cantilever stiffness, and pull-off force. Errors associated with pull-off tests for measuring adhesion have been noted by others [14].

Conclusions

In this article, the use of atomic force acoustic microscopy (AFAM) has been discussed as applied to polysilicon microelectromechanical systems (MEMS). An estimate of Young's modulus of polysilicon has been made with this technique. The results presented here are, unfortunately, much lower than previous direct measurements. However, several improvements of the measurement technique may prove useful. The dependence on tip radius is substantial. The calibrated grating method for radius measurement has not yet been validated as an effective method to determine *R*. In addition, effects from surface forces may substantially alter the effective value for the contact load *P*. The value used in the above calculations corresponds to all forces sensed by the cantilever. All of these sources of error are being examined in order to improve the measurements. The use of AFAM for other materials has shown the potential of this technique for *in situ* measurements of MEMS.

Acknowledgments

This work was sponsored by the Air Force Office of Scientific Research under Grant No. F49620-99-1-0254. The views and conclusions contained herein are those of the authors and should not be interpreted as necessarily representing the official policies or endorsements, either expressed or implied, of the Air Force Office of Scientific Research or the U.S. Government. Support of the Center for Electro-Optics at the University of Nebraska-Lincoln is also gratefully acknowledged. The authors also thank Dr. William N. Sharpe, Jr. for providing the polysilicon material.

References

1. Binning, G., Quate, C. F., and Gerber, C., "Atomic Force Microscope," Phys. Rev. Lett., Vol. 56, 1986, pp. 930–933.

2. Rabe, U., Amelio, S., Kester, E., Scherer, V., Hirsekorn, S., and Arnold, W., "Quantitative Determination of Contact Stiffness Using Atomic Force Acoustic Microscopy," Ultrasonics, Vol. 38, 2000, pp. 430–437.

3. Dinelli, F., Biswas, S. K., Briggs, G. A. D., and Kolosov, O. V., "Measurements of Stiff-Material Compliance on the Nanoscale Using Ultrasonic Force Microscopy," Phys. Rev. B, Vol. 61, No. 20, 2000, pp. 13995–14006.

4. Yamanaka, K., Noguchi, A., Tsuji, T., Koike, T., and Goto, T., "Quantitative Material Characterization by Ultrasonic AFM," Surf. Interface Anal., Vol. 27, 1999, pp. 600–606.

5. Inagaki, K., Kolosov, O. V., Briggs, G. A. D., and Wright, O. B., "Waveguide Ultrasonic Force Microscopy at 60 MHz," Appl. Phys. Lett., Vol. 76, 2000, pp. 1836–1838.

6. Turner, J. A., Hirsekorn, S., Rabe, U., and Arnold, W., "High-Frequency Response of Atomic-Force Microscope Cantilevers," J. Appl. Phys., Vol. 82, 1997, pp. 966–979.

7. Rabe, U., Turner, J., and Arnold, W., "Analysis of the High-Frequency Response of Atomic Force Microscope Cantilevers," Appl. Phys. A, Mat. Science Proc., Vol. 66, 1998, pp. S277–S282.

8. Johnson, K. L., Contact Mechanics, Cambridge University Press, Cambridge, 1985.

9. Maugis, D., Contact, Adhesion and Rupture of Elastic Solids, Springer-Verlag, Berlin, 2000.

10. Hirsekorn, S., Rabe, U., and Arnold, W., "Theoretical Description of the Transfer of Vibrations from a Sample to the Cantilever of an Atomic Force Microscope," Nanotechnology, Vol. 8, 1997, pp. 57–66.

11. Derjaguin, B. V., Muller, V. M., and Toporov, Y. P., "Effect of Contact Deformations on the Adhesion of Particles," J. Coll. Interface Sci., Vol. 53, 1975, pp. 314–326.

12. Johnson, J. L., Kendall, K., and Roberts, A. D., "Surface Energy and the Contact of Elastic Solids," Proc. R. Soc. London A, Vol. 324, 1971, pp. 301–313.

13. Burnham, N. A., Behrend, O. P., Oulevey, F., Gremaud, G., Gallo, P.-J., Gourdon, D., Dupas, E., Kulik, A. J., Pollock, H. M., and Briggs, G. A. D., "How Does a Tip Tap?" Nanotechnology, Vol. 8, 1997, pp. 67–75.

14. Burnham, N. A. and Kulik, A. J., "Surface Forces and Adhesion," Handbook of Micro/Nanotechnology, ed. B. Bhushan, Vol. CRC Press, Boca Raton, 1999.

15. Rabe, U., Janser, K., and Arnold, W., "Vibrations of Free and Surface-Coupled Atomic Force Microscope Cantilevers: Theory and Experiment," Rev. Sci. Instrum., Vol. 67, No. 9, 1996, pp. 3281–3293.

16. Sharpe, W. N., K. T. Turner, J., and Edwards, R. L., "Tensile Testing of Polysilicon," Exp. Mech., Vol. 39, 1999, pp. 162–170.

Atomic force acoustic microscopy methods to determine thin-film elastic properties

D. C. Hurley*
Materials Reliability Division, National Institute of Standards & Technology, Boulder, CO USA 80305

K. Shen and J. A. Turner
Dept. of Engineering Mechanics, Univ. of Nebraska, Lincoln, NE USA 68588

(Dated: February 4, 2003)

Abstract

We discuss atomic force acoustic microscopy (AFAM) methods to determine quantitative values for the elastic properties of thin films. The AFAM approach measures the frequencies of an AFM cantilever's first two flexural resonances while in contact with a material. The indentation modulus M of an unknown or test material can be obtained by comparing the resonant spectrum of the test material to that of a reference material. We examined a niobium film (d=280±30 nm) with AFAM using two separate reference materials and two different cantilever geometries. Data were analyzed with two models: an analytical model based on conventional beam dynamics and a new finite-element model with variable cantilever cross-section and viscous damping. AFAM values of M varied significantly depending on the specific experimental configuration and analysis technique. By averaging values obtained with both reference materials, very good agreement (5–10 % difference) with values determined by other methods was achieved. These results provide insight into using AFAM methods to attain reliable, accurate measurements of elastic properties on the nanoscale.

(Partial contribution of NIST, an agency of the US government; not subject to copyright.)

---

*Electronic address: `hurley@boulder.nist.gov`

I. INTRODUCTION

Ever-decreasing length scales in many fields of science and technology present a serious challenge for materials characterization. New nondestructive measurement tools must be developed to accommodate submicrometer dimensions. Specifically, the ability to determine mechanical properties at the nanoscale is needed, especially for systems involving thin films. Knowledge of mechanical properties such as elastic modulus and interfacial quality (defects, strain, adhesion, etc.) is critical to the successful development of new film materials and structures.

To meet these needs, measurement tools that exploit the spatial resolution of atomic force microscopy (AFM) are being developed. Although standard AFM measures topography, other new techniques sense a sample's elastic properties. One promising approach is a hybrid acoustic/AFM technique called atomic force acoustic microscopy (AFAM) [1]. AFAM involves vibrating the cantilever at ultrasonic frequencies to excite its mechanical resonances. The resonant frequencies shift when the tip is brought into contact with a sample. By measuring the resonant frequencies under both free-space and surface-coupled conditions, information about the sample's elastic properties can be extracted. A major advantage of AFAM (and related methods such as ultrasonic force microscopy, UFM [2]) is that the small tip diameter (~10–100 nm) enables *in-situ* elastic-property information with nanoscale spatial resolution. Furthermore, AFM's scanning ability means that two-dimensional images of mechanical properties are possible.

Although the fundamental principles of AFAM have been established, many aspects of the measurement method are still being refined. We wish to understand which of these aspects most strongly affect AFAM's ability to make *quantitative* elastic-property measurements. In this paper, we discuss our AFAM measurement and analysis techniques to determine the quantitative elastic properties of thin films. We describe experiments on a thin-film sample using two AFM cantilevers with very different geometries. To understand the results more thoroughly, we compare two methods of AFAM data analysis. The analytical approach assumes a cantilever of uniform rectangular cross-section, while a new finite element model accounts for spatial variations in cantilever dimensions. The same data are interpreted with the two approaches to better understand measurement uncertainty and accuracy. We also compare the AFAM results to those obtained by other techniques such as instrumented indentation and surface acoustic waves. In this way, we hope to contribute to the current understanding of quantitative AFAM.

II. EXPERIMENTAL METHODS

A. AFAM Techniques

Our experimental apparatus, shown schematically in Fig. 1, is similar to that of Rabe *et al.* [1]. The sample under investigation is bonded to a longitudinal ultrasonic contact transducer that is subsequently affixed to the positioning stage of the AFM instrument. A function generator drives the transducer with a continuous sine wave. The frequency and amplitude of the sine wave (typically 0.1–2.5 MHz and 25–200 mV) are computer-controlled. The same sine wave signal is used for the reference signal of the lock-in amplifier. The output signal of the lock-in amplifier is the response of the AFM photodiode detector at the transducer excitation frequency and corresponds to the deflection of the cantilever at that frequency. In a standard experiment, the computer sweeps through a range of excitation frequencies and acquires a spectrum of the cantilever's deflection response versus frequency. Experimental values of the cantilever's first two flexural resonances are determined from this spectrum.

The entire measurement procedure is as follows. First, the free-space resonances are measured by sweeping the transducer frequency while the cantilever is close to, but not touching, the sample. As discussed below, knowledge of the free-space resonances is needed to characterize the properties of the specific cantilever in use.

The cantilever is then lowered and its tip is brought into contact with a reference or calibration sample. Resonant spectra are acquired for one or more values of the force F_N applied to the cantilever. F_N is related to the cantilever displacement δ by $F_N = k_c\delta$, where k_c is the spring constant of the cantilever. It is therefore equivalent to obtain spectra for different values of δ, which is simpler to determine experimentally. Typically, measurements

are made at three different values in the range $\delta \approx 15$–50 nm. Next, the cantilever is brought into contact with the test (unknown) material. The resonances are measured for the same values of F_N or δ. The final step in the experimental process is to repeat the measurements on the reference sample. Thus a "data set" usually consists of nine individual measurements of the spectrum: three on the unknown sample and six on the reference material. In these experiments, two reference samples were used and the sequence of measurements was as follows: reference #1, reference #2, test, reference #2, reference #1.

From the experimental resonant frequencies, values are calculated for the tip-sample contact stiffness, k^*, for both the test and reference materials. The calculation is based on a model for the cantilever dynamics. As described in Sect. II C, we have implemented both analytical and numerical approaches to the model. Finally, the values of k^* for the test and reference samples are compared in order to obtain the desired quantity, the elastic modulus of the test sample.

It can be seen that this measurement procedure relies on one or more reference samples with known elastic properties. Comparison of test and reference data eliminates the need for precise knowledge of parameters that are difficult to determine experimentally, for instance the tip radius [3]. The procedure yields two sets of results: one for the comparison between the test data and the first set of reference data, and one between the test data and the second set of reference data. The two sets of results are typically averaged to obtain a single value of the modulus. In this way, effects such as tip wear can be minimized.

B. Cantilever Types

Measurements were made with two different cantilevers with different geometries. Diagrams of the cross-section and plan view for both cantilevers are shown in Fig. 2. The dimensions of the cantilevers and their first two free-space flexural resonances are given in Table I. Dimensions were determined with an optical microscope, except for the thicknesses which were measured with a scanning electron microscope (SEM).

The plan view of the first cantilever is shown in Fig. 2(a). It was nearly rectangular and thus was referred to as the "rectangular" cantilever. The cantilever had a uniform, trapezoidal cross-section along its length except at the very end. The tip was located near, but not exactly at, the end of the cantilever. The position of the tip L_1 relative to the total length L of the cantilever can be characterized by the ratio L_1/L [1]. As discussed below, L_1/L is used as an adjustable parameter in the data analysis. By examining the cantilever in the SEM and the optical microscope, we estimated that L_1/L=0.95–0.97.

The second cantilever did not possess a rectangular geometry. Due to its shape, seen in Fig. 2(b), it was called the "dagger" cantilever. The figure indicates that the cantilever's cross-section was not uniform across its entire length. Although trapezoidal throughout, the cross-section varied in width along the pointed (triangular) region. Values for the widths w_1 and w_2 given in Table I correspond to the cantilever's rectangular region furthest from the tip. This type of cantilever is attractive for AFAM experiments, partly because the tip is located at exactly the end of the cantilever so that L_1/L=1.0. Moreover, the angle between the tip and the cantilever is not exactly 90°, as is typical for most cantilevers. Instead, the tip is tilted by approximately 12° so that when it is brought in contact with a sample, the tip is perpendicular to the sample surface. We have found this arrangement to work well in practice.

The two cantilevers varied not only in their geometry, but also in the relative values of the cantilever spring constant k_c. For our particular rectangular cantilever, a value of k_c=45.2 N/m was provided by the vendor. The precise value of k_c was not given for the dagger cantilever, but a range of possible values $k_c \approx$29–55 N/m was specified. The relative values of k_c for the two cantilevers can be estimated using the relation $k_c = Ewt^3/4L^3$ for a rectangular beam. Here, E is Young's modulus, w is the width, t is the thickness, and L is the length of the cantilever. Inserting the appropriate values in Table I into this equation, we find that the rectangular cantilever is about 2.5 times stiffer than the dagger cantilever. Because the equation applies to a rectangular beam, this is only an approximation. However, the ratio is likely to be even greater since the taper in the dagger cantilever makes it less stiff than a rectangular beam of the same length and thickness.

C. Sample Materials

To test the methods described above, we performed AFAM experiments on a thin film of niobium (Nb). The film was sputtered onto a (100) single-crystal silicon (Si) wafer approximately 0.5 mm thick. The specific film and substrate materials were chosen based on expected values of the elastic properties, ease of fabrication, and availability of literaure values for comparison. The film thickness d_{Nb} was measured by breaking the sample and examining it in cross-section in the SEM. A value d_{Nb}=280±30 nm was obtained by averaging a total of 26 measurements acquired at seven evenly spaced positions over a distance of 22 mm. The thickness uncertainty represents the standard deviation of the individual measurements.

Quantitative AFAM measurements require *in-situ* calibration with a reference sample. The elastic properties of the reference sample, namely its indentation modulus $M = E/(1-\nu^2)$ where E is Young's modulus and ν is Poisson's ratio, must be known. In previous research, a reference material with properties close to those expected in the test material has usually been selected. From literature values for bulk Nb, we estimate that M_{Nb}=116–133 GPa [4].

We could not identify an easily available reference material with M in this range. Instead, we used two calibration samples whose properties bracketed these values. The first was a (001) single-crystal Si wafer approximately 0.5 mm thick. We expect $M_{Si<100>}$=161 GPa from calculations of the effective anisotropic values for $E_{Si<100>}$ and $\nu_{Si<100>}$ from the second-order elastic moduli of silicon [5–7]. However, a value of M_{Si}=139 ± 10 GPa was obtained with instrumented indentation techiques (IIT) on the specific sample used. The IIT measurements also indicated that M was slightly depth-dependent, increasing to about 170 GPa at deeper penetration depths—closer to the expected value. It is possible that the sample possessed a thin surface layer of native oxide or polishing damage. Because the applied AFAM forces were smaller than those used in IIT, we used the surface value M_{Si}=139 GPa in the AFAM data analysis.

The other reference sample was a disk of borosilicate crown glass. Its properties were characterized using standard immersion, pulse-echo ultrasonic techniques [8]. Measurements of the longitudinal and shear wave velocities yielded a glass indentation modulus M_{gl}=85±3

GPa, identical to the nominal value quoted by vendors.

III. DATA ANALYSIS METHODS

A. Analytical Model

The standard approach for interpreting AFAM frequency data uses conventional beam dynamics to obtain an analytical relation between the contact stiffness and the resonant frequencies. This approach has been described in detail elsewhere [1, 3]; here, we only summarize the basic concepts. The cantilever is modeled as a beam with a perfectly uniform cross-section. One end of the cantilever is clamped. The other (tip) end is free to vibrate (free-space condition) or else coupled to the surface by a spring with stiffness k^* (sample-coupled condition). Closed-form, analytical expressions can be written to characterize the beam dynamics of the system. The equations relate the the frequencies of the free-space flexural resonances f_1^o and f_2^o to a parameter c_B that describes the cantilever properties [1]. c_B is combined with the sample-coupled resonant frequencies to form the argument of a characteristic equation for the sample-coupled vibrations. This transcendental equation is solved to determine the value of the contact stiffness k^* between the tip and the sample.

From the values of k^* and knowledge of the reference material's elastic properties, first the reduced Young's modulus E^* and then the indentation modulus M_{test} can be calculated [3]:

$$E^*_{test} = E^*_{ref}\left(\frac{k^*_{test}}{k^*_{ref}}\right)^n , \tag{1}$$

$$\frac{1}{E^*_{test}} = \frac{1}{M_{tip}} + \frac{1}{M_{test}}. \tag{2}$$

Here, the subscript *test* indicates the unknown sample and *ref* refers to the reference or calibration sample. We used a value M_{tip}=$M_{Si<001>}$=161 GPa for the <001> silicon tip. The value of n in Eq. (1) depends on the contact mechanics model used. For Hertzian contact, n=3/2; for a flat-punch (flat) contact, n=1. We cite the values of M calculated for both n=1 and n=3/2 to indicate the range of possible values. It should be noted that contact mechanics models that include effects from adhesion were not considered.

In theory, the frequency of only one flexural resonance is needed to determine k^* with this model. In practice, the frequencies of two or more modes are measured and k^* is calculated for each one. This practice is partially motivated by the fact that depending on the experimental configuration, one mode is usually more sensitive to changes in k^* [9]. The values for k^* obtained for different resonances, however, do not exactly agree if the assumed position of the AFM tip is the very end of the cantilever (that is, if L_1/L=1.0). Therefore, the characteristic equation for sample-coupled vibration has been modified to account for the possibility L_1/L<1.0 [1]. In this case, k^* is plotted as a function of L_1/L for each flexural mode. The value of k^* where the curves intersect is considered the solution for k^*. Thus L_1/L can be considered an adjustable parameter in the analytical method. Typically, L_1/L=0.91–0.99 depending on the specific cantilever geometry and other experimental variables. This procedure is usually carried out for each pair of resonant frequencies (f_1, f_2) separately.

Strictly speaking, the analytical model should not be applied to the dagger cantilever because its geometry does not meet the assumptions of the model. However, this model has been shown to be an effective means of analyzing AFAM experimental data and is in fact the only method widely available. Therefore we will include results obtained the analytical model for comparison to results with the numerical (finite-element) model described below.

B. Finite Element Model

To date, AFAM experiments have been interpreted exclusively with the above analytical method. This approach is somewhat limited in applicability, since it assumes that the cantilever's cross-section is exactly the same along its entire length. The assumption is not strictly true, even for cantilevers like our rectangular one. Thus data interpretation with the analytical model is based on an approximation to the actual experimental conditions. Previous work as well as our own results indicate that the approximation is a very good one in some cases. However, because the measured resonant frequencies for different flexural modes do not predict exactly the same value of c_B, it is clear that real cantilevers do not exactly fit the analytical model. Furthermore, cantilevers such as our dagger cantilever may be valuable for experimental use but do not satisfy the assumptions of the model.

To address these issues and to explore whether another approach might improve measurement accuracy, we have developed a numerical method for AFAM analysis. Many approaches may be used to create a model to describe the AFM cantilever vibrations. Although it is a likely candidate, an expansion in basis functions that span the length of the cantilever (*e.g.*, Rayleigh-Ritz) is not the most convenient for the cantilevers studied here. Variations in geometry that extend over a limited range of the cantilever, such as the triangular portion of the dagger probe, are more easily modeled using a solution derived by the finite element model (FEM). With the FEM, the geometric and mechanical properties of each element can be varied independently.

A finite element mesh was created for each cantilever type based on the dimensions in Fig. 2. Each cantilever was discretized into Timoshenko beam elements that included the rotational inertia of the element. The number of elements was chosen for good convergence of the first five flexural modes when compared with exact solutions for cantilevers with uniform cross-sections. For the rectangular cantilever 107 beam elements were used, while the mesh for the dagger cantilever contained 247 elements. The numerical results given here were calculated assuming that all of the elements possessed the same material properties.

The dimensions of the cantilever mesh were initially assigned the measured values in Table I. For the rectangular cantilever, the width, length, and thickness were then adjusted to match the free-space response of the model beam to the experimental results. We were able to match the experimental frequencies by making only small adjustments within the uncertainty of the dimensional measurements. A linear thickness gradient of 5.0 % along the length of the cantilever was then introduced to precisely match the *ratio* of the first two resonant frequencies to the equivalent experimental ratio. The frequency ratio is nearly unaffected by uniform changes in width or thickness and thus is an indicator of the variation in thickness along the cantilever. Examination in the SEM indicated that this amount of thickness variation was physically possible. The same approach was used for the dagger cantilever, except that the length of the dagger point or triangle was also adjusted. In this case, a thickness gradient of only 3.5 % was needed.

The values used in the FEM calculations are given in Table I. Also shown are the

values of the first two flexural free resonances calculated from the FEM dimensions. The agreement in both dimensions and frequency with the actual (measured) values is very good for both cantilevers. However, it should be noted that our combination of modeling parameters is not a unique solution. It is possible to obtain similar results for the cantilever free frequencies using other combinations of E_{Si} and t. The values in Table I represent one of these combinations that is close to the measured values.

Once the optimum mesh dimensions were determined, the contact vibration response could be calculated. The contact model contained a spring of stiffness k^* located at one node of the mesh. The parameter L_1/L decribed the location of the node with the spring. L_1/L was allowed to vary between 0.9 and 1.0 for the rectangular cantilever. The FEM calculation then involved predicting values of f_1 and f_2 for each combination of k^* and L_1/L. The output values were those values of k^* (and L_1/L) that gave the best agreement between the predicted and experimental frequencies. "Best agreement" meant that the values minimized the sum of the error between experimental and numerical values for both f_1 and f_2. Specifically, we sought to minimize an error function, χ, where

$$\chi = 10\frac{|f_1 - f_1^T|}{f_1} + \frac{|f_2 - f_2^T|}{f_2}. \tag{3}$$

The superscript T indicates the numerical value and the unsuperscripted value corresponds to the measured value. The maximum error allowed was 0.3 %. A 10:1 error weighting was used to compensate for the different sensitivities of f_1 and f_2 to changes in surface stiffness [9]. For the relevant range of values of k^*, the 10:1 ratio causes the magnitude of the errors associated with both f_1 and f_2 to be of roughly equal importantce. Thus, for some cases, the match for either frequency may not have appeared optimized, but the condition on the minimum error was met. It should also be noted that the search space was limited to local minima. The possibility of finding a global minimum of χ was not explored.

Our first numerical approach for the dagger cantilever duplicated that used for the rectangular, that is, only L_1/L and k^* were varied. The results clearly showed that the experimental data could not be matched with only these parameters. Because experimental data indicated a greater effect of damping for the dagger cantilever, a viscous damper was added to the numerical model. Viscous damping was included in the form of a dashpot with damping constant c in parallel with the spring corresponding to k^*. For the minimization procedure, L_1/L and k^* were first varied to minimize the error. Then, an appropriate value of c was added to further reduce the error. The process was repeated until the required error level was achieved. For this cantilever, the range over which L_1/L was allowed to vary was limited to 0.97–1.0.

The predicted response of the dagger cantilever was quite sensitive to the value of c used in the calculation. To obtain good agreement with the experimental results, the values of c varied by more than a factor of 100 for some of the data sets. The reasons for the variation in c are not clear. Experimentally, we have observed that the damping can be a function of the applied load. We have also found that the importance of damping was dependent on the cantilever stiffness. Data from the rectangular cantilever, which was stiffer, were analyzed using the model that included damping. We found that these results were relatively insensitive to the value of c. For the less stiff dagger cantilever, we could not match the numerical and experimental results unless damping was included. The relevant levels of cantilever stiffness that necessitate the use of damping have not yet been determined. However, the influence of contact damping level on AFM vibrations has been discussed previously [10]. Appropriate models of the tip damping are currently under development.

The procedures described above were performed for each separate AFAM measurement. Each calculation for the optimum contact parameters required less than five minutes on a desktop computer (processing speed 1 GHz). The first calculation for each material/cantilever combination was the most time consuming. Subsequent searches using the first results as an initial guess required less time. Once the values for k^* were determined, the analysis procedure was the same as for the analytical method: the ratio k^*_{test}/k^*_{ref} was calculated and M_{test} evaluated from Eqs. (1) and (2).

IV. RESULTS AND DISCUSSION

Table II summarizes our AFAM results for the Nb film sample. Shown are values for the indentation modulus M_{Nb} determined using different combinations of cantilever geometry, reference material, and analysis approach. Values of M_{Nb} are shown for both n=1 and n=3/2

in Eq. (1). Each entry in Table II represents the average of four data sets; as described in Sect. II A, each data set typically yielded six values of M_{Nb}. The uncertainties quoted in Table II represent the standard deviation of these multiple measurements. The accuracy of the value used for M_{ref} is potentially an additional source of measurement uncertainty. If the true value of M_{ref} differs from the value used, a systematic measurement error exists. The value assumed for M_{tip} can also systematically change the measurement results. However, this effect is quite small. We found that changes in M_{tip} of 20–25 GPa changed the calculated values of M_{Nb} by less than 1 GPa.

Table II contains additional entries labeled "average." These indicate the values of M_{Nb} obtained by calculating an average E^* from *all* measurements with *both* reference materials and then computing M with Eq. (2). Due to the relationship between E^* and M, this value differs slightly from the average of the two final values of M_{Nb} obtained with the separate reference materials. The uncertainty for the averages was calculated from an uncertainty in reduced modulus δE^*_{avg} determined by $\delta E^*_{avg} = \sqrt{(\delta E^*_{gl})^2 + (\delta E^*_{Si})^2}$, where δE^*_{gl} and δE^*_{Si} are the standard deviations in the measurements from each separate reference material.

For comparison with the AFAM results, Table III contains values for M_{Nb} obtained by other methods. The first column in Table III indicates a range of values for polycrystalline bulk Nb obtained from the literature [4]. The second and third columns contain values for M_{Nb} measured on the same Nb film sample with surface acoustic wave spectroscopy (SAWS) [11] and instrumented indentation techniques (IIT) [12]. The values indicated are the average of multiple measurements on the same sample. In the analysis of the SAWS data, the film density ρ was assumed to be that of bulk Nb (ρ=8570 kg/m^3). Both ρ and M could not be determined simultaneously from the SAWS data. If the actual film density was lower, as can be the case for thin films, M_{Nb} would be lower than that shown. To obtain the IIT value of M_{Nb}=97 GPa from our SAWS data, the film density would have to be ~5 % less than the bulk value.

Inspection of Tables II and III provides insight into the accuracy and effectiveness of our methods. For the rectangular cantilever, the analysis approach had virtually no effect on the resulting value of M_{Nb}. Discrepancies in the value of M_{Nb} between the two models are much smaller than the measurement uncertainty for both reference materials. Thus the results from the two models can be considered identical within the uncertainty. For the dagger cantilever, results with the glass reference sample are identical for both analysis approaches. Using the Si reference sample, however, results with the analytical approach are 8–10 % higher than those obtained by FEM analysis of the same data. Although the discrepancies between the two models were larger than the measurement uncertainty, the error bars still overlap and thus the differences are not considered significant. Thus we conclude that our finite element models for both cantilevers successfully captured the key features of the physical systems.

Tables II and III indicate that better agreement between the AFAM and IIT results is achieved by averaging AFAM results from two reference materials. For the rectangular cantilever, M_{Nb} determined by the Si reference sample is 20–30 % higher than M_{Nb}(IIT), while M_{Nb} determined by the glass reference sample alone is lower by $\sim$10 %. When the two data sets are combined, M_{Nb}(AFAM)=105–106 GPa is obtained. This is in very good agreement with the IIT value (higher by $\sim$5 % and within measurement uncertainty). For the dagger cantilever, M_{Nb} for the average of the two reference materials from the analytical model is slightly higher than the corresponding FEM results. However, the values from the two models are the same within measurement uncertainty. The results are also identical within the error bars to the corresponding values with the rectangular cantilever. In fact, the average values of M_{Nb} for the dagger cantilever agree more closely with the IIT values. The consistency between AFAM results from different cantilever geometries and analysis approaches, as well as the good agreement with results from other methods, strongly suggests that our AFAM methods are valid.

We believe these AFAM experiments to be the first in which two different reference materials were used for quantitative measurements. Our results suggest that with the current analysis approach, the choice of reference material is critical to measurement accuracy. It appears that if M_{ref} differs substantially from M_{test}, the experimentally determined M_{test} may be incorrect. Such behavior might occur if the contact between the nonideal AFM tip and the nonideal surface differs for different sample materials. The contact mechanics model

used for our data analysis does not include such variability. Until this can be verified and a more detailed contact mechanics model developed, however, our results indicate that reasonable values of M_{test} can be obtained using two reference materials. Multiple reference samples may be needed if no single suitable reference material is available, as was the case here. More importantly, an estimate of M_{test} may not be available, as can occur in the development of new film materials. In this case, AFAM measurements with multiple references could serve to iteratively determine the value of M_{test}. As the AFAM technique is refined and its precision is increased, we hope to examine this behavior more thoroughly and determine how measurement accuracy can be improved.

A question that arises in this context is how similar M_{test} and M_{ref} should be to obtain accurate results. To address this question, we compare these experiments with previous ones we have performed [13]. With AFAM we measured an aluminum (Al) film about 1 μm thick. In this case, only the glass sample was used as a reference (M_{gl}=85±3 GPa). AFAM data obtained with the rectangular cantilever and analyzed with the analytical model yielded M_{Al}(AFAM)=80±3 GPa (n=3/2). The SAWS value for the same sample was M_{Al}(SAWS)=78±1 GPa. Thus, AFAM results with a single reference appeared accurate when M_{test} differed from M_{ref} by 5–10 %. Assuming that the true value of M_{Nb} is approximately 100 GPa, then for the current experiments M_{Si} was about 40 % higher and M_{gl} was 15–20 % lower than M_{Nb}. Further experiments are needed to more fully quantify this behavior.

As mentioned above, both analysis methods used a variable L_1/L describing the tip position as an adjustable parameter. The value of L_1/L was determined for each separate (f_1, f_2) data pair. For the rectangular cantilever, the range of values obtained with the analytical approach was L_1/L=0.913–0.926 while L_1/L=0.916–0.930 for the FEM approach. For the dagger cantilever, L_1/L=0.57–0.58. This is quite different from the value L_1/L=1 observed in the SEM and illustrates our interest in developing an alternative analysis approach. With the finite element model, L_1/L=0.975–0.985 for the dagger cantilever. Further analysis or more sophisticated modeling is needed to clarify the slight but consistent differences in L_1/L between the observed and model values.

V. SUMMARY AND CONCLUSIONS

We have described AFAM methods to determine the quantitative elastic properties of thin films. Experiments were performed on a metallic thin-film sample using two cantilevers with different geometries. The cantilever resonant frequencies for the lowest two flexural modes were measured both in free space and while the tip was in contact with the sample. Comparison of results to those from reference samples with known elastic properties enabled the sample indentation modulus M to be determined. Data were analyzed with two methods. The first was an analytical model for beam dynamics that assumed a perfectly uniform cantilever cross-section. The second method involved a new finite element model specifically developed to accommodate variations in thickness and width along the length of the cantilever.

With these measurement and analysis methods, we determined AFAM values for M in a niobium film 280 nm thick. Measurements were made on the same film with two other techniques: surface acoustic wave spectroscopy and instrumented indentation. The agreement between these values and those determined with AFAM were only fair (10–25 % different) if a single reference material was used. Much better agreement ($\sim$5 % different) was achieved by combining measurements from the two different reference samples.

For a cantilever geometry that deviated only slightly from a perfect rectangular beam, the two analysis methods yielded values for M that were the same within measurement uncertainty. Thus the analytical model—a much simpler approach—appears adequate for this type of geometry. For cantilevers with a nonuniform cross-section, it was necessary to include the effects of viscoelastic damping in the FEM analysis. FEM values for M_{Nb} with this cantilever were the same within measurement uncertainty to those with the rectangular cantilever. Although not strictly applicable to this cantilever geometry, the rectangular model produced very similar values for M_{Nb}. However, its values of the tip parameter L_1/L were unphysical. Therefore we believe that the FEM approach should be applied to cantilevers with distinctly nonrectangular geometry.

These results demonstrate the validity of our AFAM methods for quantitative measurements of the elastic properties of thin films and surfaces. Future work will include extending the measurement techniques to additional samples with a wider range of M in order to investigate the limits of applicability in more detail. We also plan to examine the issues that affect precision and repeatability more thoroughly. Furthermore, results from additional cantilever geometries will be examined with FEM calculations to explore the utility of the approach.

Acknowledgments

This work was sponsored in part (JAT and KS) by the Air Force Office of Scientific Research (grant # F49620-99-1-0254) and the National Science Foundation (grant # DMI-0210850). We thank N. M. Jennett (NPL, UK) for providing the indentation results and analysis, P. D. Dresselhaus (NIST) for fabricating the Nb sample, and P. S. Rice (NIST) for assistance with AFAM measurements. We are grateful to W. Arnold, U. Rabe, S. Hirsekorn, and M. Kopycinska (IZFP, Germany) for many valuable technical discussions.

REFERENCES

[1] U. Rabe, S. Amelio, E. Kester, V. Scherer, S. Hirsekorn, and W. Arnold, Ultrasonics **38**, 430 (2000).

[2] K. Yamanaka, A. Noguchi, T. Tsuji, T. Koike, and T. Goto, Surf. Interface Anal. **27**, 600 (1999).

[3] U. Rabe, S. Amelio, M. Kopycinska, S. Hirsekorn, M. Kempf, M. Göken, and W. Arnold, Surf. Interface Anal. **33**, 65 (2002).

[4] G. Simmons and H. Wang, *Single Crystal Elastic Constants and Calculated Aggregated Properties: A Handbook* (MIT Press, Cambridge, 1971).

[5] G. Grimvall, *Thermophysical Properties of Materials* (Elsevier, New York, 1999).

[6] H. J. McSkimin and P. A. Andreatch, J. Appl. Phys. **35**, 2161 (1964).

[7] J. J. Vlassak and W. D. Nix, Phil. Mag. A **67**, 1045 (1993).

[8] E. P. Papadakis, in *Physical Acoustics, vol. 12*, edited by W. P. Mason and R. N. Thurston (Academic Press, San Diego, 1976), p. 277.

[9] J. A. Turner and J. S. Wiehn, Nanotechnology **12**, 322 (2001).

[10] J. A. Turner, S. Hirsekorn, U. Rabe, and W. Arnold, J. Appl. Phys. **82**, 966 (1997).

[11] D. C. Hurley, V. K. Tewary, and A. J. Richards, Meas. Sci. Technol. **12**, 1486 (2001).

[12] W. C. Oliver and G. M. Pharr, J. Mater. Res. **7**, 1564 (1992).

[13] D. C. Hurley, J. S. Wiehn, J. A. Turner, and P. S. Rice, in *SPIE Symposium Proceedings Vol. 4703*, edited by N. Meyendorf, G. Y. Baaklini, and B. Michel (2002), p. 65.

FIGURE CAPTIONS

Fig. 1. Schematic of experimental AFAM apparatus.

Fig. 2. Geometry of AFM cantilevers used for AFAM experiments. The top two drawings correspond to the plan view of (a) the rectangular cantilever and (b) the dagger cantilever. The cross-sectional diagram in (c) applies to both cantilevers. The drawings in (a) and (b) are approximately to scale.

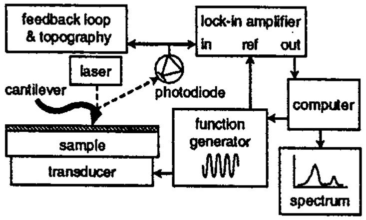
feedback loop & topography
lock-in amplifier
in
ref
out
laser
cantilever
photodiode
computer
function generator
sample
transducer
spectrum

FIG. 1:

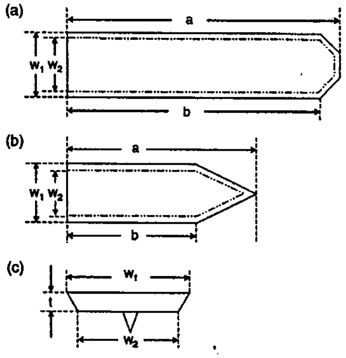
(a)
a
b
w_1
w_2
(b)
a
b
w_1
w_2
(c)
w_1
t
w_2

FIG. 2:

TABLE I: Properties of cantilevers used in AFAM experiments. Entries include the dimensions defined in Fig. 2 and the frequencies of the two lowest free-space flexural resonances, f_1° and f_2°. The columns labeled "actual" indicate the actual measured values. Columns labeled "FEM" contain the values used in, or obtained by, the finite element model.

property	*cantilever type*			
	rectangular		dagger	
	actual	FEM	actual	FEM
a (μm)	232±2	232.0	156±1	156.9
b (μm)	223±2	223.0	101±1	100.8
w_1 (μm)	52±1	52.0	49±1	48.0
w_2 (μm)	42±1	42.0	39±2	38.7
t (μm)	8.1±0.2	7.72	4.1±0.2	3.85
f_1° (kHz)	180.8±0.2	180.0	257.9±0.2	257.9
f_2° (kHz)	1157.8±0.2	1156.0	1427.7±0.2	1427.7

TABLE II: AFAM values for the indentation modulus M_{Nb} of Nb film. The type of cantilever, reference material and analysis model used to determine M_{Nb} are indicated. Values for M_{Nb} were determined from Eqs. (1) and (2) using n=1 or n=3/2 as indicated.

cantilever	reference	model	$M(n=1)$ (GPa)	$M(n=3/2)$ (GPa)
rectangular	glass	analytical	88±9	90±14
		FEM	89±11	92±17
	Si	analytical	127±7	122±10
		FEM	126±8	120±12
	average	analytical	106±14	105±22
		FEM	106±12	105±18
dagger	glass	analytical	86±2	87±3
		FEM	86±3	87±4
	Si	analytical	127±5	121±9
		FEM	118±4	110±5
	average	analytical	105±5	103±7
		FEM	101±5	98±6

TABLE III: Values for the indentation modulus M of Nb (in GPa). A range of values for bulk Nb obtained from the literature is shown. Also included are results obtained by surface acoustic wave spectroscopy (SAWS) and instrumented indentation techniques (IIT) on the same sample measured by AFAM. The minimum and maximum AFAM values from Table II are given.

lit. (bulk)	SAWS	IIT	AFAM
116–133	121±7	97±10	86–127

Nonlinear Vibrations of a Beam with Cantilever-Hertzian Contact Boundary Conditions

Joseph A. Turner[1]

Dept. of Engineering Mechanics, W317.4 Nebraska Hall

University of Nebraska-Lincoln, Lincoln, NE 68588-0526

July 22, 2002

Abstract

The nonlinear vibrations of a linear beam with cantilever-Hertzian contact boundary conditions are investigated. The method of multiple scales is used to analyze this problem in which it is assumed that the beam remains in contact with the moving surface at all times. One primary result from this analysis is the amplitude-frequency relation for the various flexural modes. The amplitude-frequency curves exhibit softening behavior as expected. The amount of softening is shown to depend on the linear contact stiffness as well as the specific mode. In addition, the associated nonlinear normal modes of this system are derived. The modes include a nonlinear modification to the linear, harmonic component as well as a static offset term and second and third harmonic components.

Keywords: nonlinear vibration, Hertz contact, elastic beam

---

[1] Contact information: jaturner@unl.edu; http://em-jaturner.unl.edu; phone 402-472-8856; fax 402-472-8292

I. Introduction

The dynamics of moving surfaces that are in contact with each other is important in a number of scientific and engineering applications. The vibrations of such contacts have been examined previously by a number of authors [1,2,3]. The focus in these studies was primarily on a single-degree-of-freedom (SDOF) system in Hertzian contact with a moving surface. Although Bryant [2] was interested in the vibrations of a beam in Hertzian contact, for modeling actuator dynamics, the beam was ultimately simplified to a SDOF system as well. The flexural vibrations of beams with nonlinearities has been examined in a variety of other forms using many different methods. Nonlinear vibrations of linearly elastic beams with nonlinear boundary conditions have been studied far less using techniques including the harmonic balance method [4], the method of Shaw and Pierre [5], and the method of multiple scales [6]. Nonlinear normal modes have been observed in many other contexts as well [7].

More recently, the problem of a cantilevered beam in Hertzian contact with a moving surface has been applied to atomic force microscope (AFM) applications [8,9]. Dynamic AFM methods rely on the relative motion between the AFM tip and the specimen surface. These techniques are used to extract quantitative information about the surface stiffness with high resolution [9]. These techniques utilize the dynamic response of the AFM beam, specifically in terms of the flexural cantilever modes. A stiff cantilever with high contact force is typically used to confine the tip-surface forces to the Hertzian contact regime. In these studies, the amplitude of the surface motion is kept small such that the motion may be analyzed by linearizing the nonlinear tip-surface interaction forces. Such linearization has proven very effective for a variety of materials. As the surface amplitude increases, the motion eventually becomes nonlinear. If the motion is very large, the nonlinear motion is chaotic [10]. Before chaotic motion occurs however, there is a range of nonlinear motion that is stable. It is anticipated that a perturbation approach may be applicable to describe this motion. It is in this regime that the effects of this softening nonlinearity have been observed experimentally in terms of the shifts of resonant frequencies as a function of amplitude [8]. The method of harmonic balance was recently used to examine a similar contact AFM vibration problem [11].

In this article, the nonlinear vibrations of an elastic beam with cantilever-Hertzian contact boundary conditions are examined. It is assumed throughout that the beam remains in contact with the vibrating surface at all times. In addition, the vibrational amplitude in the beam is assumed to remain small such that the beam remains in the linear regime. Experimental evidence suggests that the beam loses contact before nonlinear effects in the beam are important [8]. In the next section, the appropriate boundary value problem is described. The method of multiple scales is then used to analyze this problem. The primary results from this analysis include the amplitude-frequency relation for the various flexural modes as well as the nonlinear normal modes. Finally, example results are presented. It is shown that the nonlinear behavior, in terms of the nonlinear frequency shift and the change in mode shape, are sensitive to the particular mode and to the linear contact stiffness. The dependence on the nonlinear parameters of the problem is clearly defined. The theoretical results have the same qualitative features as experimental AFM results.

II. Problem Description

A uniform, homogenous beam of constant, cross-section is cantilevered at one end as depicted in Fig. 1. At the end opposite of the cantilever ($x = L$), a massless tip with small radius is attached. The tip is in contact with a surface as shown. The boundary value problem for this system has a governing equation given by

$$EIq''''(x,t) + \rho A\ddot{q}(x,t) = 0, \tag{1}$$

with boundary conditions

$$q(x,t) = 0 \quad \text{at} \quad x = 0, \tag{2}$$

$$q'(x,t) = 0 \quad \text{at} \quad x = 0, \tag{3}$$

$$q''(x,t) = 0 \quad \text{at} \quad x = L, \tag{4}$$

$$EIq'''(x,t) - 3\tfrac{EI}{L^3}y(L) + K_0\left[z_0 - y(L) - q(x,t)\right]^{3/2} = 0 \quad \text{at} \quad x = L. \tag{5}$$

In Eqs. (1)-(5), $q(x,t)$ defines the cantilever position relative to its initial static deflection $y(x)$. Also, the primes indicate spatial derivatives, while the overdots indicate time derivatives. The beam is defined by the modulus E, the area moment of the cantilever I, the volume density ρ, and the cross-sectional area A. Here, EI and ρA are assumed uniform over the length of the beam. The boundary conditions given by Eqs. (2)-(4) correspond to conditions of zero displacement and zero slope at $x = 0$, and zero moment at $x = L$. The boundary condition given by Eq. (5) is the force balance between the shear force in the beam and the interaction force associated with the tip and the surface. Here, this interaction force is assumed the Hertz contact condition of a sphere in contact with a plane [12,13]. The Hertz coefficient, $K_0 = \frac{4}{3}E^* \sqrt{R}$, is defined in terms of the reduced elastic modulus, E^*, and the tip radius, R. The reduced modulus is defined by the material properties (elastic modulus, E, and Poisson's ratio, ν) of the surface and tip. It is defined by

$$\frac{1}{E^*} = \frac{1-\nu_t^2}{E_t} + \frac{1-\nu_s^2}{E_s}, \tag{6}$$

where the subscripts t and s denote the tip and surface, respectively.

The function $y(x)$ in Eq. (5) defines the static deflection of the cantilever due to the surface offset. A static offset results from changes in the relative position between the beam and the surface. The end deflection, $y(L)$, will be slightly less than the surface offset, z_0. The difference between the two is the result of deformation. The end deflection is defined by consideration of the static problem. The initial deflection of the cantilever is written in terms of the end deflection as

$$y(x) = \frac{1}{2} y(L) \left(\frac{x}{L}\right)^2 \left(3 - \frac{x}{L}\right). \tag{7}$$

The end deflection is governed by

$$-3\frac{EI}{L^3} y(L) + K_0 (z_0 - y(L))^{3/2} = 0, \tag{8}$$

which defines $y(L)$ in terms of the surface offset, z_0. Without loss of generality, it is assumed that z_0 is zero when the tip first comes in contact with the surface. This assumption also implies that the cantilever is horizontal when it first makes contact with the surface. In Eqs. (5) and (8), the quantity $\Delta = z_0 - y(L)$ may be identified as the static Hertz deformation. Note that no attractive forces are assumed present.

The nonlinear analysis which follows requires a more amenable form for the nonlinear contact.

The contact boundary condition, Eq. (5), is first rewritten as

$$EIw'''(x,t) - 3\tfrac{EI}{L^3}(z_0/\Delta - 1) + K_0\Delta^{1/2}\left[1 - w(x,t)\right]^{3/2} = 0 \quad \text{at} \quad x = L, \tag{9}$$

where $w = q/\Delta$ defines the beam deflection relative to the static Hertz deformation. Note that the beam remains in contact with the surface as long as $w(L,t) \leq 1$. Finally, the term in Eq. (9) with the 3/2 exponent is expanded in a Taylor series expansion about the equilibrium position, $w(L,t) = 0$. The result is

$$EIw''' = \kappa w - \kappa_1 w^2 - \kappa_2 w^3, \tag{10}$$

where the linear and nonlinear spring constants are given by

$$\kappa = \frac{3}{2}K_0\Delta^{1/2}, \qquad \kappa_1 = \frac{3}{8}K_0\Delta^{1/2}, \qquad \kappa_2 = \frac{1}{16}K_0\Delta^{1/2}. \tag{11}$$

The error in this expansion is less than 1% over the range in which the contact is not lost. A similar type of expansion has been successfully used to model Hertzian contact vibrations in single-degree of freedom systems [2,3].

III. Method of Multiple Scales

The nonlinear vibration problem described in Section II is now solved using the method of multiple scales. The problem is first recast in dimensionless form. The governing equation is thus given by

$$\ddot{w} + w'''' = 0, \tag{12}$$

with boundary conditions

$$w = w' = 0 \quad \text{at} \quad x = 0, \qquad w'' = 0 \quad \text{at} \quad x = 1, \tag{13}$$

$$w''' - \beta w - \varepsilon^2 c\dot{w} + \varepsilon\beta_1 w^2 + \varepsilon^2\beta_2 w^3 = \varepsilon^2 F\cos\Omega t \quad \text{at} \quad x = 1. \tag{14}$$

where ε is a dimensionless parameter introduced to order the different scales of the problem. A viscous damping term (as observed experimentally) and a forcing term (typical of dynamic AFM experiments) have been added to the final boundary condition. A uniformly valid approximation requires the damping, forcing, and the cubic nonlinearity to occur at the same level of perturbation, in this case at ε^2 [14]. In Eqs. (12)-(14), the position along the beam is measured in units of L and time is measured in units of $\sqrt{(\rho AL)/(EI/L^3)}$. The dimensionless linear and nonlinear spring constants are defined by

$$\beta = \frac{3}{2}\frac{K_0\Delta^{1/2}}{EI/L^3}, \qquad \beta_1 = \frac{\beta}{4}, \qquad \beta_2 = \frac{\beta}{24}. \tag{15}$$

Thus, β defines the stiffness of the contact relative to the stiffness of the beam. The contact stiffnesses are determined by Δ which is related to the static offset through Eq. (8).

The method of multiple scales is applied to this nonlinear boundary value problem [6]. We look for solutions of the form

$$w(x;T_0,T_1,T_2) = w_0(x;T_0,T_1,T_2) + \varepsilon w_1(x;T_0,T_1,T_2) + \dots \tag{16}$$

where T_0, T_1, and T_2 are the different time scales of the problem, $T_n = \varepsilon^n t$. The expansion is substituted into Eqs. (12)-(14) and like orders of ε are collected. This procedure defines the ε^0

problem as

$$w_0'''' + D_0^2 w_0 = 0, \tag{17}$$

$$w_0 = w_0' = 0 \quad \text{at} \quad x = 0, \qquad w_0'' = 0 \quad \text{at} \quad x = 1, \tag{18}$$

$$w_0''' = \beta w_0 \quad \text{at} \quad x = 1. \tag{19}$$

The ε^1 problem is given by

$$w_1'''' + D_0^2 w_1 = -2D_0D_1 w_0, \tag{20}$$

$$w_1 = w_1' = 0 \quad \text{at} \quad x = 0, \qquad w_1'' = 0 \quad \text{at} \quad x = 1, \tag{21}$$

$$w_1''' = \beta w_1 - \beta_1 w_0^2 \quad \text{at} \quad x = 1, \tag{22}$$

and for ε^2

$$w_2'''' + D_0^2 w_2 = -2D_0D_1 w_1 - \left(D_1^2 + 2D_0D_2\right) w_0, \tag{23}$$

$$w_2 = w_2' = 0 \quad \text{at} \quad x = 0, \qquad w_2'' = 0 \quad \text{at} \quad x = 1, \tag{24}$$

$$w_2''' = \beta w_2 + cD_0 w_0 - \beta_1 w_0 w_1 - \beta_2 w_0^3 - F\cos\Omega t \quad \text{at} \quad x = 1. \tag{25}$$

Each of these problems is now solved.

A. Order ε^0 Problem

The ε^0 problem has solution

$$w_0(x;T_0,T_1) = A_m(T_1,T_2)\, e^{i\omega_m T_0} W(x) + cc, \tag{26}$$

for the mth mode where cc denotes the complex conjugate of the previous expression. The modal subscripts on A_m and ω_m are implicit throughout the remainder of the article. The linear mode shape $W(x)$ is given by

$$W(x) = W_0 (\sin\gamma x - \sinh\gamma x - H_0 (\cos\gamma x - \cosh\gamma x)), \qquad (27)$$

where

$$W_0 = \frac{\cos\gamma + \cosh\gamma}{2(\sin\gamma\cosh\gamma - \sinh\gamma\cos\gamma)}, \qquad H_0 = \frac{\sin\gamma + \sinh\gamma}{\cos\gamma + \cosh\gamma}. \qquad (28)$$

The normalization factor W_0 is included to ensure that the displacement of the cantilever end $W(1)$ does not lose contact, such that $W(1) = 1$.

The values of the dimensionless wave numbers γ are determined from the characteristic equation of the linear problem

$$\gamma^3 (\cosh\gamma\cos\gamma + 1) - \beta(\sinh\gamma\cos\gamma - \sin\gamma\cosh\gamma) = 0. \qquad (29)$$

The wave numbers are related to the natural frequencies through the dispersion relation $\omega^2 = \gamma^4$.

B. Order ε^1 Problem

The solution for w_0 is necessary for the order ε^1 problem. The problem for w_1 is given by

$$w_1'''' + D_0^2 w_1 = -2i\omega D_1 A e^{i\omega T_0} W(x) + cc, \qquad (30)$$

$$w_1 = w_1' = 0 \quad \text{at} \quad x = 0, \qquad w_1'' = 0 \quad \text{at} \quad x = 1, \qquad (31)$$

and the contact boundary condition is given by

$$w_1''' = \beta w_1 - \beta_1 \left[A^2 e^{2i\omega_m T_0} + 2A\bar{A} + \bar{A}^2 e^{-2i\omega_m T_0}\right] \quad \text{at} \quad x = 1. \qquad (32)$$

First we seek solutions of the form

$$w_1(x; T_0, T_1, T_2) = g_1(x; T_1, T_2)\, e^{i\omega T_0}. \qquad (33)$$

The problem for g_1 is then

$$g_1'''' - \omega^2 g_1 = -2i\omega D_1 A W(x), \qquad (34)$$

with boundary conditions

$$g_1 = g_1' = 0 \quad \text{at} \quad x = 0, \qquad g_1'' = 0 \quad \text{at} \quad x = 1, \qquad (35)$$

$$g_1'' = \beta g_1 \quad \text{at} \quad x = 1. \qquad (36)$$

Because the homogeneous equations for g_1 have a nontrivial solution, the nonhomogeneous equations for g_1 have a solution only if a solvability condition is satisfied. By virtue of the characteristic equation defining γ, Eq. (29), the solvability condition implies that $D_1 A = 0$, or $A = A(T_2)$.

The two other parts of the w_1 solution are also found. One solution is of the form

$$w_1 = g_2(x)\, e^{2i\omega T_0}. \qquad (37)$$

Substitution gives

$$g_2'''' - 4\omega^2 g_2 = 0, \qquad (38)$$

$$g_2 = g_2' = 0 \quad \text{at} \quad x = 0, \qquad g_2'' = 0 \quad \text{at} \quad x = 1. \qquad (39)$$

The final BC is given by

$$g_2'''(1) - \beta g_2(1) = -\beta_1 A^2. \qquad (40)$$

The solution is thus

$$g_2(x) = \frac{\beta_1 A^2}{2} G(\chi_2, x), \qquad (41)$$

where $\chi_2 = \sqrt{2\omega}$ and the function $G(\chi, x)$ is defined as

$$G(\chi, x) = -\frac{(\cos\chi + \cosh\chi)(\sinh\chi x - \sin\chi x) + (\cos\chi x - \cosh\chi x)(\sin\chi + \sinh\chi)}{\chi^3(1 + \cos\chi\cosh\chi) - \beta(\sinh\chi\cos\chi - \sin\chi\cosh\chi)}. \quad (42)$$

The final part of the w_1 solution is related to the static shift due to the nonlinearity. Such a response is expected in systems with quadratic nonlinearities [6]. We look for solutions of the form

$$w_1 = g_0(x). \quad (43)$$

Substitution into the boundary conditions gives

$$g_0(x) = -\frac{\beta_1 A\bar{A}}{2(3+\beta)} x^2 (x-3). \quad (44)$$

The complete solution for w_1 is thus

$$w_1 = -\frac{\beta_1 A\bar{A}}{2(3+\beta)} x^2 (x-3) + \frac{\beta_1 A^2}{2} G(\chi_2, x) e^{2i\omega T_0} + \text{cc}, \quad (45)$$

where A is found from the ε^2 problem. As expected, the w_1 solution is proportional to β_1 and quadratic in amplitude.

C. Order ε^2 Problem

The solutions obtained for w_0 and w_1 are necessary for the order ε^2 problem. The ε^2 problem is written in terms of these solutions

$$w_2'''' + D_0^2 w_2 = -2i\omega A' e^{i\omega T_0} W(x), \quad (46)$$

where $A' = D_2 A$. The appropriate boundary conditions are

$$w_2 = w_2' = 0 \quad \text{at} \quad x = 0, \qquad w_2'' = 0 \quad \text{at} \quad x = 1, \quad (47)$$

$$w_2''' = \beta w_2 + ci\omega A e^{i\omega T_0} + \left(\beta_1^2 G(\chi_2, 1) - \frac{2\beta_1^2}{3+\beta} - 3\beta_2\right) A\bar{A}^2 e^{i\omega T_0}$$
$$+ \left(\beta_1^2 G(\chi_2, 1) - \beta_2\right) A^3 e^{3i\omega T_0} + \text{cc.}$$

Next, we seek solutions of the form

$$w_2(x; T_0, T_2) = h_1(x; T_2) e^{i\omega T_0}. \quad (48)$$

Substitution gives

$$h_1'''' - \omega^2 h_1 = -2i\omega A' W(x), \quad (49)$$

with boundary conditions

$$h_1 = h_1' = 0 \quad \text{at} \quad x = 0, \qquad h_1'' = 0 \quad \text{at} \quad x = 1, \quad (50)$$

$$h_1''' - \beta h_1 = ci\omega A + \left(\beta_1^2 G(\chi_2, 1) - \tfrac{2\beta_1^2}{3+\beta} - 3\beta_2\right) A\bar{A}^2, \quad \text{at} \quad x = 1. \quad (51)$$

The homogeneous equations for h_1 have a nontrivial solution. Thus, the nonhomogeneous equations for h_1 require a solvability condition. This condition is

$$P(\gamma)\, i\omega A' = ci\omega A + \beta_1^2 \bar{A} A^2 \left(G(\chi_2, 1) - \frac{2}{3+\beta}\right) - 3\beta_2 \bar{A} A^2, \quad (52)$$

where

$$P(\gamma) = \frac{3\gamma^2(\cos\gamma + \cosh\gamma)(1 + \cos\gamma\cosh\gamma) - \gamma^3 \sin\gamma\sinh\gamma(\sin\gamma + \sinh\gamma)}{\gamma^3(\cos\gamma + \cosh\gamma)^2}$$
$$+ \beta\frac{\sin\gamma\sinh\gamma(\cos\gamma + \cosh\gamma) + (1 + \cos\gamma\cosh\gamma)(\cosh\gamma - \cos\gamma)}{\gamma^3(\cos\gamma + \cosh\gamma)^2}.$$

The dependence of Eq. (52) on the particular mode is implicit in the factors of $P(\gamma)$ and $G(\chi_2, 1)$.

The solution for the harmonic component of w_2 is then

$$h_1(x) = \left[ci\omega A + \beta_1^2 \bar{A} A^2 \left(G(\chi_2, 1) - \frac{2}{3+\beta}\right) - 3\beta_2 \bar{A} A^2\right] H(x), \quad (53)$$

where

$$H(x) = \frac{1}{2\gamma^3 P(\gamma)}\left[(\cos\gamma x - \cosh\gamma x)\left(\frac{2(1+\cos\gamma\cosh\gamma)}{(\cos\gamma+\cosh\gamma)^2} - x\right)\right.$$
$$\left. - x\frac{\sin\gamma+\sinh\gamma}{\cos\gamma+\cosh\gamma}(\sin\gamma x + \sinh\gamma x)\right].$$

The final part of the solution for w_2 is found in a similar manner to that for g_2 in the order ε^1 problem. We look for solutions like

$$w_2 = h_3(x)\, e^{3i\omega T_0}. \tag{54}$$

The solution is thus

$$h_3(x) = -\frac{A^3}{2}\left(\beta_1^2 G(\chi_2, 1) - \beta_2\right) G(\chi_3, x), \tag{55}$$

with $G(\chi, x)$ defined in Eq. (42) and $\chi_3 = \sqrt{3\omega}$.

The complete nonlinear mode that tends to the linear mode when β_1 and β_2 tend to zero is then

$$\begin{aligned} w(x; T_0, T_2) = {} & (W(x) + i\alpha\omega H(x))\, A e^{i\omega_m T_0} \\ & + \left(\beta_1^2 G(\chi_2, 1) - \frac{2\beta_1^2}{3+\beta} - 3\beta_2\right)\bar{A}A^2 H(x)\, e^{i\omega T_0} - \frac{\beta_1 A\bar{A}}{2(3+\beta)}x^2(x-3) \\ & + \frac{\beta_1 A^2}{2}G(\chi_2, x)\, e^{2i\omega T_0} - \left(\frac{A^3}{2}\left(\beta_1^2 G(\chi_2, 1) - \beta_2\right) G(\chi_3, x)\right) e^{3i\omega T_0} + \text{cc}, \end{aligned}$$

where A is defined by Eq. (52).

To solve Eq. (52) we look for solutions of the form $A = \frac{1}{2}pe^{iq}$ where p and q are real functions of T_2. Substitution into Eq. (52) gives

$$P(\gamma)(i\omega p' - \omega p q') = ci\omega p + \frac{1}{4}\beta_1^2 p^3\left(G(\chi_2, 1) - \frac{2}{3+\beta}\right) - \frac{3}{4}\beta_2 p^3 - 2Fe^{i\sigma T_2 - iq}. \tag{56}$$

Next we define $\psi = \sigma T_2 - q$ such that $q' = \psi' - \sigma$. Separating Eq. (56) into real and imaginary

parts gives

$$P(\gamma)(-\omega p\psi' + \omega p\sigma) = \frac{\beta_1^2 p^3}{4}\left(G(\chi_2, 1) - \frac{2}{3+\beta}\right) - \frac{3}{4}\beta_2 p^3 - 2F\cos\psi, \tag{57}$$

$$P(\gamma)\,\omega p' = \alpha\omega p - 2F\sin\psi. \tag{58}$$

Steady-state motion occurs when $\psi' = p' = 0$. Thus,

$$2F\cos\psi = \frac{\beta_1^2 p^3}{4}\left(G(\chi_2, 1) - \frac{2}{3+\beta}\right) - \frac{3}{4}\beta_2 p^3 - P(\gamma)\,\omega p\sigma, \tag{59}$$

$$2F\sin\psi = \alpha\omega p. \tag{60}$$

Eqs. (59) and (60) are squared and added. The result is solved for σ giving

$$\sigma = \frac{\left[\beta_1^2\left(G(\chi_2, 1) - \frac{2}{3+\beta}\right) - 3\beta_2\right]}{4P(\gamma)\,\omega}p^2 \pm \frac{1}{P(\gamma)\,\omega}\sqrt{\frac{4F^2}{p^2} - \omega^2 c^2}. \tag{61}$$

The detuning parameter σ is related to p in Eq. (61). The phase shift ψ is then found from

$$\psi = \tan^{-1}\left(\frac{4\alpha\omega}{\beta_1^2 p^2\left(G(\chi_2, 1) - \frac{2}{3+\beta}\right) - 3\beta_2 p^2 - 4P(\gamma)\,\omega\sigma}\right), \tag{62}$$

such that $A = \frac{1}{2}pe^{i\sigma T_2 - i\psi}$. The maximum value for p is

$$p_{\max} = \frac{2F}{\alpha\omega}, \tag{63}$$

which occurs when

$$\sigma = \left(\frac{F}{\alpha\omega}\right)^2 \frac{\beta_1^2\left(G(\chi_2, 1) - \frac{2}{3+\beta}\right) - 3\beta_2}{P(\gamma)\,\omega} \tag{64}$$

In terms of the parameters p and q, the nonlinear normal mode reduces to (damping has been dropped from the mode as discussed by Nayfeh [6])

$$\begin{aligned} w\left(x;T_0,T_2\right) = &\left(W\left(x\right)p + \left(\beta_1^2 G\left(\chi_2,1\right) - \frac{2\beta_1^2}{3+\beta} - 3\beta_2\right) H\left(x\right)\frac{1}{4}p^3\right)\cos\left(\omega T_0 + q\right) \\ &- \frac{\beta_1 x^2\left(x-3\right)}{4\left(3+\beta\right)}p^2 + \frac{\beta_1}{4}G\left(\chi_2,x\right)p^2\cos\left(2\omega T_0 + 2q\right) \\ &- \left(\beta_1^2 G\left(\chi_2,1\right) - \beta_2\right)G\left(\chi_3,x\right)\frac{1}{8}p^3\cos\left(3\omega T_0 + 3q\right). \end{aligned} \tag{65}$$

The nonlinear amplitude-frequency relation, Eq. (61), and the nonlinear normal mode, Eq. (65), are the main results of this derivation. The dependence on the different modes is included in the amplitude-frequency relation by the functions P and G.

The various components of the nonlinear normal mode include a harmonic component and static offset as well as second and third harmonic components. The static shift due to the nonlinearity is proportional to $\beta_1/\left(3+\beta\right)$ and quadratic in amplitude. The spatial dependence of the second and third harmonics are proportional to $G\left(\chi,x\right)$, for $\chi = \chi_2$ or $\chi = \chi_3$, respectively. The second harmonic is quadratic in amplitude and proportional to β_1. The third harmonic is cubic in amplitude and dependent on β_1, β_2, and $G\left(\chi_2,1\right)$. In the next section, example results are presented using Eqs. (61), (65), and (42).

IV. Example Results

The nonlinear amplitude-frequency behavior for several modes using Eq. (61) is first presented. It should be noted that the dependence of σ on the forcing amplitude F is inverse to the dependence of σ on damping c. Plots for fixed c and increasing F are presented in Figs. (2) and (3). Similar behavior is observed for fixed F and decreasing c. Figure (2) is a plot of amplitude versus σ for

modes 1 and 2 for $\beta = 300$ and $c = 0.12$ for several values of F. The values of σ for both modes are of the same order over the range of amplitude shown, as large as -0.5. The response of mode 1 to the higher amplitudes ($F = 3,4,6$) leads to a response that is larger than 1. In terms of the quantities defined here, these values would lead to a loss of contact. Mode 2, however, does not have a response larger than 1 for any of the values of forcing used. Similar results for modes 3 and 4 for $\beta = 1800$ and $c = 0.08$ are shown in Fig. (3).

Another important effect in the results is shown in Figs. (4) and (5). In this case, a fixed value of F and c are used with results for two different values of linear stiffness β shown. In Fig. (4), amplitude-frequency plots are shown for the first and seconds modes for $\beta = 50$ and $\beta = 500$ ($F = 1$; $c = 0.025$). The frequency shift for the first mode is larger than the second for $\beta = 50$. However, for $\beta = 500$, the second frequency is observed to shift more than the first. In Fig. (5), a comparison between the first and fourth modes is shown for $\beta = 500$ and $\beta = 2300$ ($F = 1$; $c = 0.025$). The fourth mode is observed to shift much more when $\beta = 2300$ in comparison with the first mode. The behavior of the first mode is very similar for both of these values of β. It was observed that the modal amplitudes and ranges of σ for each mode could be significantly different depending on β. The linear stiffness is primarily dependent on the static surface offset, defined in Eq. (5) by z_0. This type of modal sensitivity has also been noted for the case of an elastic beam coupled to a moving surface by a linear spring [15]. Because the nonlinearity is localized to a single position of the beam, the mode shape greatly effects the influence of the nonlinearity.

Plots of the harmonic component of the mode shapes are shown in Figs. (6) and (7). In both of these figures, the linear (Eq. (27)) and nonlinear (the term in Eq. (65) that multiplies $\cos(\omega t)$) components are shown as solid and dashed lines, respectively. In Fig. (6), the amplitude of the first mode is shown for $\beta = 100$. The linear and nonlinear components are almost identical for the portion of the beam closest to the cantilevered end. The difference between the linear and nonlinear in this case is at the end ($x = 1$) of the beam. The softening effect is clearly shown. For large amplitudes, such that the cubic dependency on amplitude is important, the spring is effectively less stiff. Thus, the beam at $x = 1$ has a larger amplitude relative to the linear amplitude. The second mode is shown in Fig. (7) for $\beta = 1900$. A similar behavior is observed for this mode as well. The deviation from linearity is largest at the end with the contact. The deviation of the nonlinear mode shapes from the linear mode shapes follows the trend observed for the detuning parameter. For a given value of β, a mode may have a small or large nonlinear response. The modal sensitivity to a contact nonlinearity is dependent on the linear mode shape.

Finally, plots relevant to the second and third harmonic components of the nonlinear responses are shown in Figs. (8)-(10). In Fig. (8), $G(\chi_2, x)$ for the first mode is plotted for values of linear stiffness $\beta = 10$, 100, 500, and 1000. Although only a few results may be presented here, the general trends observed are summarized. As β increases, the overall amplitude of G decreases and the position of the node moves toward the cantilevered end of the beam. The trends for $G(\chi_2, x)$ for the second and third modes, as shown in Figs. (9) and (10), respectively, are similar to the plot for the first mode in that the amplitude decreases for increasing β. The positions of the nodes of G for these modes are also observed to move toward the cantilevered end of the beam as β

increases. In addition, it may be observed that an additional node is introduced in these shapes when β is above a certain value. For example, the first mode results, Fig. (8), have a node between $x/L = 0.6 - 0.7$ for the higher three values of β, but not for $\beta = 10$. For the third mode, Fig. (10), the additional node is only apparent for the highest value of β shown. Thus, each mode has some threshold value of β for which the function G has an increase in number of nodes.

V. Discussion

The nonlinear vibrations of a beam with cantilever-Hertzian contact boundary conditions have been investigated using the method of multiple scales. The nonlinear amplitude-frequency relation was derived and was shown to depend on the mode number and linear contact stiffness. The linear contact stiffness is primarily dependent on the static offset of the surface. Example results show the expected softening behavior in terms of the forcing amplitude and damping. These results may also be used to predict which modes may be most suitable for nonlinear experiments. In particular, it was observed that the first mode lost contact ($p > 1$) in many cases before a significant change in frequency was achieved. The derivation of the nonlinear normal modes was also presented. The nonlinear modes included terms of a modification to the harmonic linear mode, a static offset, and second and third harmonic components.

The nonlinear analysis showed the amplitude-frequency shift that has been observed experimentally in the weakly nonlinear regime for atomic force microscope experiments [8]. These nonlinear effects provide important information about the contact mechanics. The nonlinear behavior of the beam vibrations have been analyzed here using a Hertzian contact model for the tip-surface interaction. The results showed that the influence of the nonlinearity on each mode is a function of the surface stiffness relative to the stiffness of the cantilever. The modal sensitivity is also seen to influence the nonlinear behavior. Each mode has a different amplitude near the end of the beam such that the role of the nonlinearity changes. Results from other contact models will provide necessary insight into the expected effects from other factors important for AFM imaging.

VI. Acknowledgment

This work was sponsored by the Air Force Office of Scientific Research under Grant No. F49620-99-1-0254. The views and conclusions contained herein are those of the authors and should not be interpreted as necessarily representing the official policies or endorsements, either expressed or implied, of the Air Force Office of Scientific Research or the U.S. Government. Support of the Center for Electro-Optics at the University of Nebraska-Lincoln is also gratefully acknowledged.

VII. References

[1]P. R. Nayak, "Contact Vibrations," Journal of Sound and Vibration **22**, 297–322 (1972).

[2]M. D. Bryant, "Non-Linear Forced Oscillation of a Beam Coupled to an Actuator Via Hertzian Contact," Journal of Sound and VIbration **99**, 403–414 (1985).

[3]D. P. Hess and A. Soom, "Normal Vibrations and Friction Under Harmonic Loads: Part I - Hertzian Contacts," ASME Journal of Tribology **113**, 80–86 (1991).

[4]W. Szemplinska-Stupnicka, *The Behavior of Nonlinear Vibrating Systems* (Kluwer, Dordrecht, 1990).

[5]S. W. Shaw and C. Pierre, "Normal Modes of Vibration for Nonlinear Continuous Systems," J. Sound Vib. **169**, 319–347 (1994).

[6]A. H. Nayfeh, *Nonlinear Interactions* (Wiley and Sons, New York, 2000).

[7]A. F. Vakakis, *Normal Modes and Localization in Nonlinear Systems* (Wiley, New York, 1996).

[8]U. Rabe, E. Kester, and W. Arnold, "Probing Linear and Non-Linear Tip-Sample Interaction Forces by Atomic Force Acoustic Microscopy," Surface and Interface Analysis **27**, 386–391 (1999).

[9]U. Rabe, S. Amelio, E. Kester, V. Scherer, S. Hirsekorn, and W. Arnold, "Quantitative Determination of Contact Stiffness Using Atomic Force Acoustic Microscopy," Ultrasonics **38**, 430–437 (2000).

[10]N. A. Burnham, A. J. Kulik, G. Gremaud, and G. A. D. Briggs, "Nanosubharmonics: The Dynamics of Small Nonlinear Contacts," Phys. Rev. Lett. **74**, 5092–5095 (1995).

[11]M. Muraoka and W. Arnold, "A Method of Evaluating Local Elasticity and Adhesion Energy from the Nonlinear Response of AFM Cantilever Vibrations," JSME INT J A-SOLID M **44**, 396–405 (2001).

[12]K. L. Johnson, *Contact Mechanics* (Cambridge University Press, Cambridge, 1985).

[13]D. Maugis, *Contact, Adhesion and Rupture of Elastic Solids* (Springer-Verlag, Berlin, 2000).

[14]A. H. Nayfeh and D. T. Mook, *Nonlinear Oscillations* (Wiley and Sons, New York, 1979).

[15]J. A. Turner and J. S. Wiehn, "Sensitivity of Flexural and Torsional Modes of Atomic Force Microscope Cantilevers to Surface Stiffness Variations," Nanotechnology **12**, 322–330 (2001).

VIII. Figures Captions

Figure 1. Schematic of the problem. The linearly elastic beam is in contact with a surface. Initial contact is made when the surface offset, z_0, is zero. This static offset causes a static beam deflection, $y(x)$. The dynamic motion, $w(x,t)$, is defined relative to $y(x)$. The contact forces between the tip and sample are assumed Hertzian with no attractive forces.

Figure 2. Example results for the primary nonlinear response for $\beta = 300$ and four values of F ($= 1, 2, 3, 4$) with $c = 0.12$.The first and second modes are shown.

Figure 3.Example results for the primary nonlinear response for $\beta = 500$ and four values of F ($= 1, 2, 3, 4$) with $c = 0.08$.The first and second modes are shown.

Figure 4. Nonlinear frequency shift of the first and second modes for two values of linear stiffness β (solid: $\beta = 50$; dashed: $\beta = 500$) with $c = 0.025$.

Figure. 5. Nonlinear frequency shift of the first and fourth modes for two values of linear stiffness β (solid: $\beta = 500$; dashed: $\beta = 2300$) with $c = 0.025$. These plots illustrate the modal sensitivity to the contact as has been examined previously for linear AFM vibrations [15].

Figure 6. Comparison between the first linear and the nonlinear normal mode (harmonic component) for $\beta = 100$ (solid: linear; dashed: nonlinear). Note the softening effect of the nonlinearity.

Figure 7. Comparison between the second linear and the nonlinear normal mode (harmonic component) for $\beta = 1900$ (solid: linear; dashed: nonlinear).

Figure 8. Plot of $G(\chi_2, x)$ for mode 1 as a function of beam length [$\beta = 10$ (dot-dash);

$\beta = 100$ (dashed); $\beta = 500$ (solid); $\beta = 1000$ (dotted)]. The second harmonic component of the displacement is proportional to G.

Figure 9. Plot of $G(\chi_2, x)$ for mode 2 as a function of beam length (line styles are as in Fig. 8). The second harmonic component of the displacement is proportional to G.

Figure 10. Plot of $G(\chi_2, x)$ for mode 3 as a function of beam length (line styles are as in Fig. 8). The second harmonic component of the displacement is proportional to G.

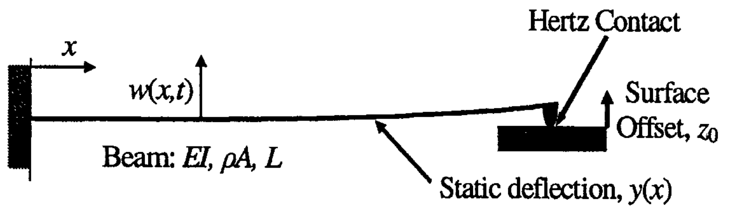

Figure 1.Schematic of the problem. The linearly elastic beam is in contact with a surface. Initial contact is made when the surface offset, z_0, is zero. This static offset causes a static beam deflection, $y(x)$. The dynamic motion, $w(x,t)$, is defined relative to $y(x)$. The contact forces between the tip and sample are assumed Hertzian with no attractive forces.

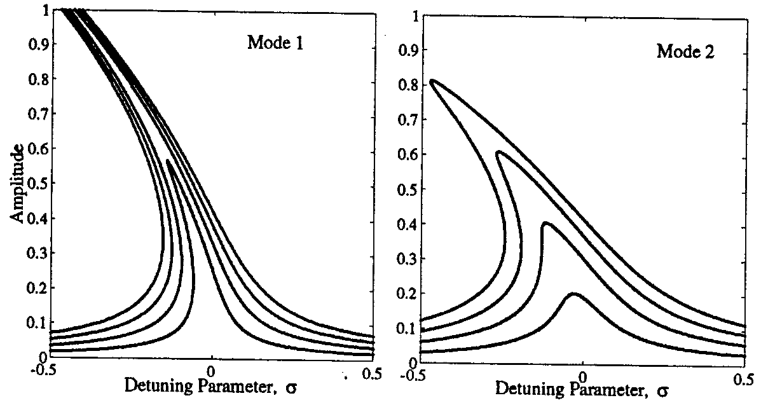

Figure 2.Example results for the primary nonlinear response for $\beta = 300$ and four values of F $(= 1, 2, 3, 4)$ with $c = 0.12$.The first and second modes are shown.

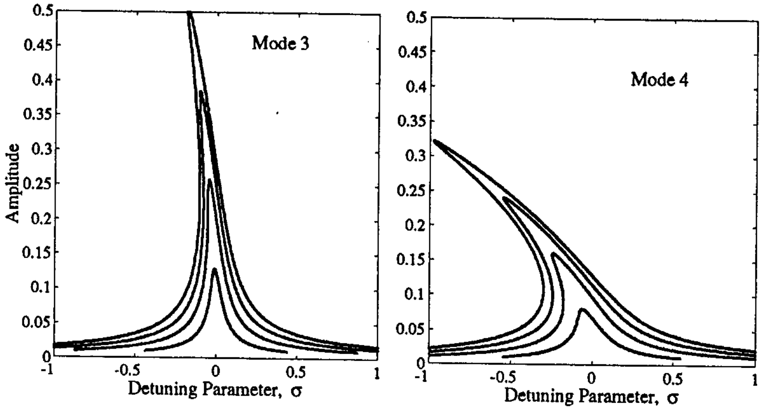

Figure 3.Example results for the primary nonlinear response for $\beta = 1800$ and four values of F $(= 1, 2, 3, 4)$ with $c = 0.08$.The third and fourth modes are shown.

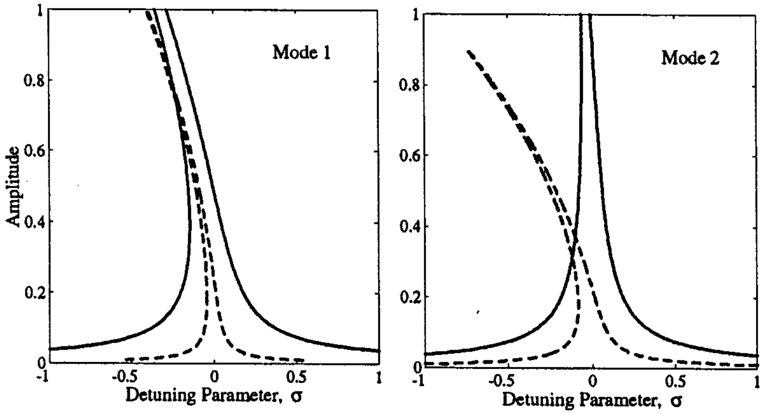

Figure 4.Nonlinear frequency shift of the first and second modes for two values of linear stiffness β (solid: $\beta = 50$; dashed: $\beta = 500$) with $c = 0.025$.

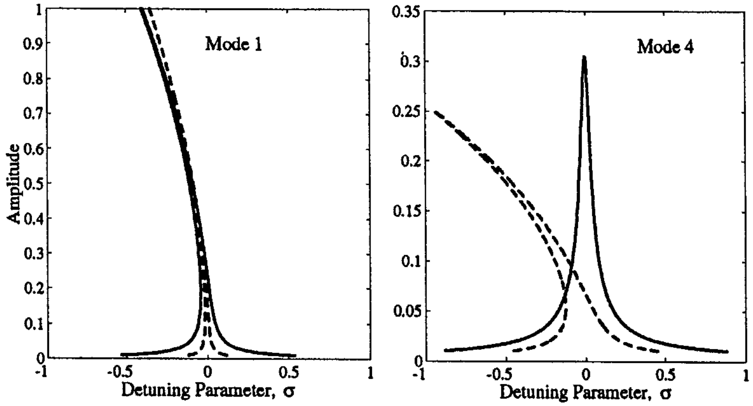

Figure 5.Nonlinear frequency shift of the first and fourth modes for two values of linear stiffness β (solid: $\beta = 500$; dashed: $\beta = 2300$) with $c = 0.025$. These plots illustrate the modal sensitivity to the contact as has been examined previously for linear AFM vibrations [15].

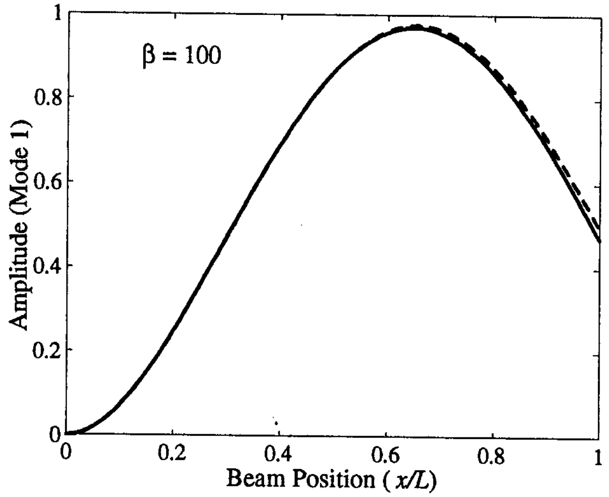

Figure 6.Comparison between the first linear and the nonlinear normal mode (harmonic component) for $\beta = 100$ (solid: linear; dashed: nonlinear). Note the softening effect of the nonlinearity.

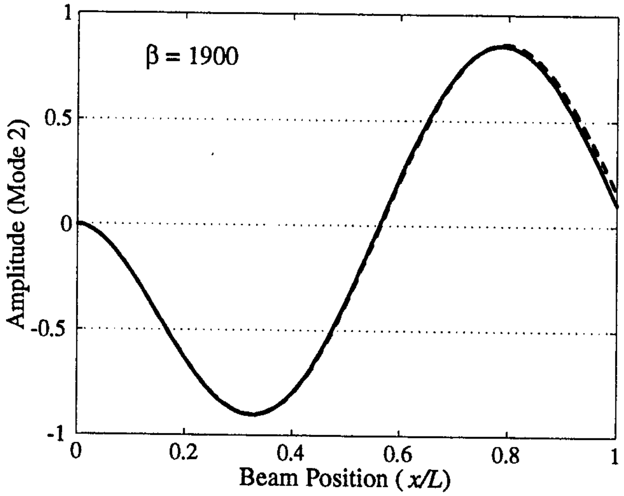

Figure 7.Comparison between the second linear and the nonlinear normal mode (harmonic component) for $\beta = 1900$ (solid: linear; dashed: nonlinear).

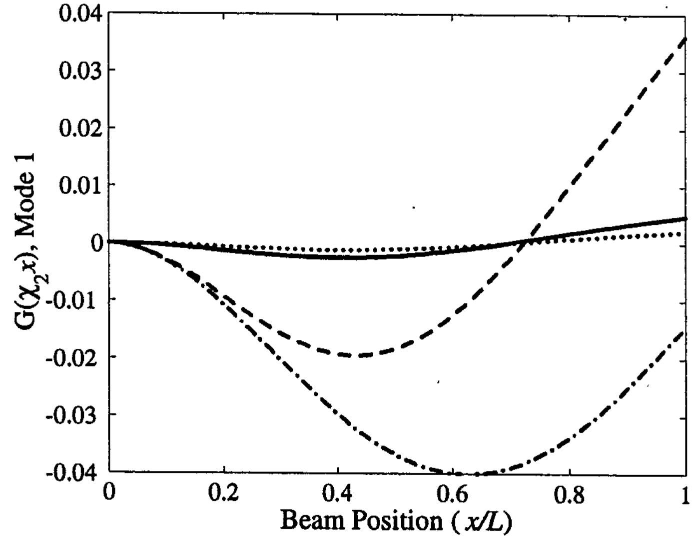

Figure 8.Plot of $G(\chi_2, x)$ for mode 1 as a function of beam length [$\beta = 10$ (dot-dash); $\beta = 100$ (dashed); $\beta = 500$ (solid); $\beta = 1000$ (dotted)]. The second harmonic component of the displacement is proportional to G.

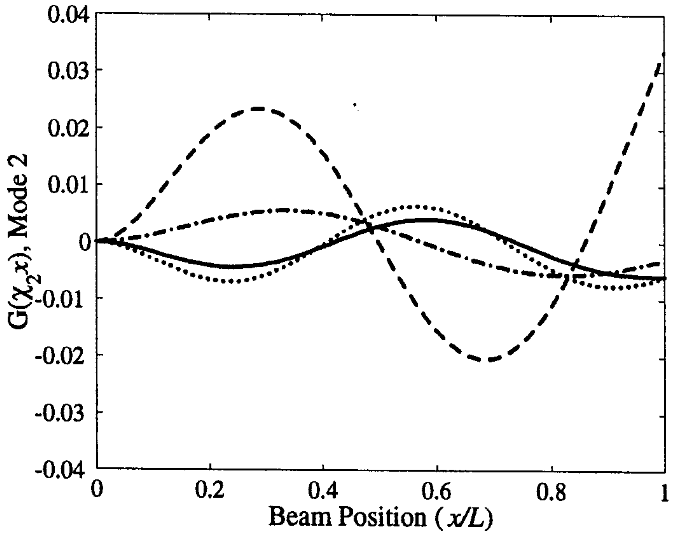

Figure 9.Plot of $G(\chi_2, x)$ for mode 2 as a function of beam length (line styles are as in Fig. 8). The second harmonic component of the displacement is proportional to G.

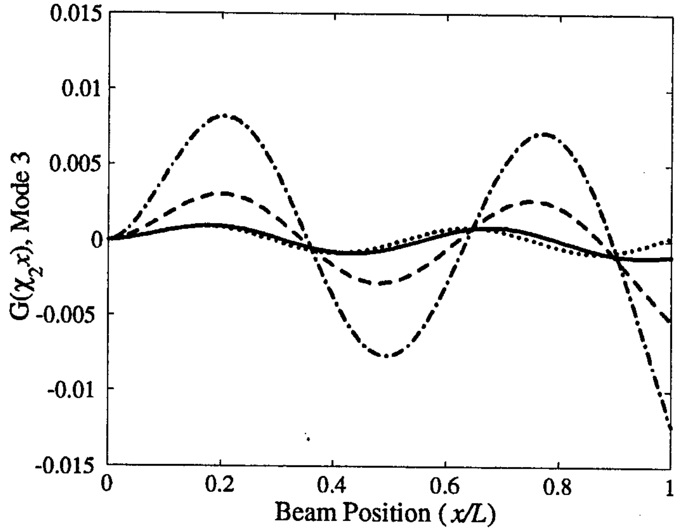

Figure 10.Plot of $G(\chi_2, x)$ for mode 3 as a function of beam length (line styles are as in Fig. 8). The second harmonic component of the displacement is proportional to G.

VIBRATIONS OF ATOMIC FORCE MICROSCOPE CANTILEVERS WITH A CONTACT BOUNDARY CONDITION

By

Baowei Wei

A THESIS

Presented to the Faculty of
The Graduate College at the University of Nebraska
In Partial Fulfillment of the Requirements
For the Degree of Master of Science

Major: Engineering Mechanics
Under the Supervision of Professor Joseph A. Turner

Lincoln, Nebraska
August 2001

VIBRATIONS OF ATOMIC FORCE MICROSCOPE CANTILEVER WITH A CONTACT BOUNDARY CONDITION

Baowei Wei, M.S.

University of Nebraska, 2001

Advisor: Joseph A. Turner

The quantitative measurement of material properties with nanometer resolution has increasingly become important for fundamental research as well as for industry applications. In many industries that use thin films or microelectromechanical systems (MEMS), it is important to acquire material property information with high resolution, even down to the nanoscale. Recently, techniques have been developed to make such measurements using the atomic force microscope (AFM). These include the scanning tunneling micrscopy based method, force modulation microscopy, ultrasonic atomic force microscopy (UAFM), and other high-frequency vibration modes. The AFM has surpassed its traditional applications in topography measurement and found various applications in the field of nondestructive evaluation. Research into the dynamic behavior of AFM cantilever in contact with a sample surface may be used to extract material properties of the sample. In this thesis, the vibrations of the AFM cantilever with a contact boundary condition are studied.

During a typical measurement, the AFM cantilever vibrates while its tip contacts with a sample surface. Various material parameters are involved in the contact. The interaction forces between the AFM tip and the sample surface are complex and essentially nonlinear. Contact mechanics theories such as Hertzian theory or Maugis theory are used in this thesis to model the contact forces. The AFM cantilever is assumed to be a homogeneous elastic beam with a massless tip.

In the first part of this thesis, the undamped nonlinear free vibrations are studied. Also the effects of interaction damping are explored. Forced vibration with damping is studied in the second part. Nonlinear approximation methods including the method of harmonic balance and the method of multiple scales are used for the analyses. The influence of specimen material properties on the response of AFM cantilever is examined. The results clearly show the dependence of the nonlinear behavior on the material properties of the specimen and the contact parameters. Also, it is shown that when the AFM cantilever is excited at a frequency very near certain natural frequencies, the nonlinearity of the contact forces shifts the frequency-response curve away from the linear results.

Acknowledgements

First, I would like to thank my advisor Dr. Joseph A. Turner for his advice and support in this research. I would also thank the thesis committee members Dr. Ruqiang Feng, Dr. Florin Bobaru and Dr. Jiashi Yang for their input and evaluation.

In addition, I would like to thank all the people who were involved in this research. Mr. Josh Wiehn has offered many creative ideas and suggestions.

Also, secretaries Ms. Betty Stukenholtz and Ms. Kathie Hiatt at the Engineering Mechanics Department have provided help in equipment and supplies.

Special thanks are due to my dear wife Yuhong, whose love and dedication has made our life in Lincoln always happy and refreshing. Also, I would like to express my very true appreciation to our parents and brothers, sisters and their families in China, whose encouragement and support has made my research possible and successful.

This research was sponsored by the Air Force Office of Scientific Research under Grant No. F49620-99-1-0254. The views and conclusions contained herein should not be interpreted as necessarily representing the official policies or endorsements, either expressed or implied, of the Air Force Office of Scientific Research or the U.S. Government. Support of the Center for Electro-Optics at the University of Nebraska-Lincoln is also gratefully acknowledged.

CONTENTS

1. Introduction

2. Atomic Force Microscopy (AFM)

3. Governing Equations and Linear Approximation

4. Nonlinear Response

5. Interaction Damping Effects

6. Forced Vibration with Damping

7. Conclusions

1. Introduction

1.1 Background

The atomic force microscope (AFM) [1] was originally developed to provide high-resolution surface topography information. In these measurements, the deflection of the microscope cantilever as a function of the surface locations is used to generate high precision mapping of the surface. The results in air [1] demonstrate a lateral resolution of 30 Å and a vertical resolution less than 1 Å.

Recent developments in AFM have moved beyond the original quasi-static implementation into a fully dynamic regime in which the AFM cantilever is driven to vibrate with its tip in contact with the sample surface. Dynamic implementations of the atomic force microscope turn this device into a powerful tool for material characterization. Ultrasonic methods like atomic force acoustic microscopy (AFAM) [5], scanning micro-deformation microscopy (SMM), and ultrasonic force microscopy (UFM) [9] enable high-resolution measurement of the local modulus of material surfaces.

The interaction force between the cantilever tip and sample surface is complex and highly nonlinear. The resulting dynamical system is complicated due to the nonlinearity of the contact forces involved. Many factors are involved in this interaction. There are different models to describe this very complicated contact interaction, like the Hertzian contact theory, JKRS theory, DMT theory and Maugis theory, etc. In previous work, the cantilever is treated using the point-mass model [5] and the contact force linearized. Numerical calculations have also been applied to study the nonlinear effects in the dynamical analysis [5][6].

In this thesis, the main objective is to find an analytical basis for quantitative measurements of surface stiffness by means of analyzing the dynamic response of the AFM cantilever with its tip in contact with a sample surface during vibration. The technique utilizes the dynamic response of the AFM cantilever, specifically in terms of the higher-order cantilever modes. It has been shown that the nonlinearity of the contact interaction acts to shift the natural frequencies of the cantilever. The nonlinear effects act to soften some modes. It was also shown that the higher frequency modes are very important when an accurate view of the dynamics is needed [4].

1.2 Objective

In this research, nonlinear analytical methods such as the method of harmonic balance and the method of multiple scales [2], are applied to study the vibrations of the atomic force microscope (AFM) [1] when its cantilever tip contacts with the sample surface. This analysis of the dynamical behavior of the AFM can provide insight into the relationship between the sample surface properties such as Young's modulus and the vibration modes of the AFM cantilever. The main purpose of this study is to establish a theoretical model to apply to the frequency shift in AFM vibrations as a measurement for the sample surface material properties.

1.3 Research Methods

In this thesis, the AFM is modeled as a homogeneous elastic beam. The beam is cantilevered at one end and a small radius tip is attached at the other end. The tip is assumed to be massless. During vibration, this tip is always in contact with the sample surface. The contact force between the tip and sample surface is very complicated and essentially nonlinear. There are several contact mechanics theories used to model the relationship between the contact depth and the contact forces. If sufficient force is applied to the cantilever, the contact force can be described by the Hertzian model. With the presence of this nonlinear contact force, significant nonlinear features can be observed in the vibration, some of which are directly linked to the material properties of the surface. By studying the dynamic response of the AFM cantilever, it is possible to establish a quantitative measurement of surface material properties.

Hertzian model is a simplified model; it does not take into consideration adhesion hysteresis and attractive surface forces. In this model, the contact force is purely repulsive. A more sophisticated model, the Maugis model, is comprehensive in that it encompasses a wide variety of contact materials and includes surface forces. Both Hertzian theory and Maugis theory are examined in this thesis with regard to the nonlinear vibrations.

Due to the nonlinearity of the contact forces, this vibration problem becomes very complicated and an exact analytical solution is not possible. The vibration of a continuous system with a nonlinear boundary condition has been studied using different approximate methods [22][23][24][25]. In this thesis, nonlinear approximation methods like the method of multiple scales and the method of harmonic balance [2] are used.

These analyses show the anticipated frequency shift of the natural frequencies as a function of contact force and excitation amplitude. The dependence on the nonlinear parameters of the problem is clearly defined. This reveals the possibility of measuring sample surface material properties by exploiting the dynamic behavior of the AFM.

2. Atomic Force Microscope

2.1 Atomic Force Microscope (AFM)

The atomic force microscope was originally designed by G. Binning and C .F. Quate in 1986 [1]. The atomic force microscope is a combination of the principles of the scanning tunneling microscope (STM) and the stylus profilometer [10]. An STM is capable of measuring forces as small as 10^{-18} N [1]. AFM is proposed as a method to investigate the surface topography on an atomic scale. In the experiments, images are generated by measurements of the forces of a sharp tip when it is near or it contacts the surface of the sample. This measurement has very high resolution: results by G. Binnig and C. F. Quate demonstrated a lateral resolution of 30 Å and a vertical resolution of less than 1 Å.

Besides its usage in surface topography measurements, which are generally dubbed as static methods, new capabilities of AFM have been developed. To measure surface properties such as adhesive energy or sample stiffness with the same high local resolution as the topography, dynamic methods such as force modulation microscopy [10], scanning local acceleration microscopy [11], pulsed force microscopy [12], tapping mode or atomic force acoustic microscopy (AFAM) [7] have been developed. Atomic force acoustic microscopy is a near-field technique, which combines the ability of ultrasonics to image elastic properties with the high lateral resolution of scanning probe microscopes [7]. In AFAM, the increased dynamic stiffness of the cantilever vibration modes can be exploited for quantitative measurements and imaging. Experimental setups of different combinations of AFM and ultrasonics have been proposed [9][14][15].

The most significant difference of the dynamic methods versus the static or quasi-static methods is that the microscope cantilever is vibrating when it scans across the sample surface with the sensor tip very close to or in contact with the sample surface. The vibration modes of the cantilever can change significantly when different materials are present on the sample surface [7]. This change in the vibration modes of the cantilever is attributed to the surface material properties and can be exploited as a means of evaluating them quantitatively.

A critical component of an AFM is the cantilever, which is typically micro-fabricated from low-stress silicon nitride or single crystal silicon. The cantilever can be treated as a miniature elastic beam with its characteristic vibration modes and frequencies. It is highly resilient with a wide range of force constants, from 0.5 to 0.01 N/m. Consider the products of Park Scientific Instruments for example. There are two sets of products, Microlevers™ and Ultralevers™ as in Figures (2.1) and (2.2). The tips of Microlevers can be of two shapes: standard or sharpened pyramidal.

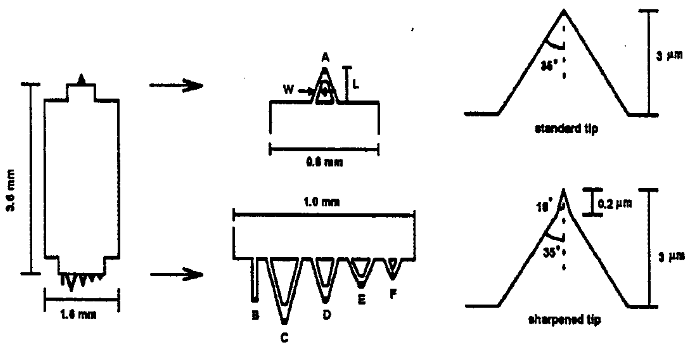

Figure 2.1. Microlever chips with six cantilevers [27, pp. 4-31].

The typical radius of curvature is 500 Å for standard tips and 200 Å for sharpened tips. Also, there are two different shapes of cantilever: rectangular and V-shaped. Table 2.1 lists detailed information about these cantilevers.

Table 2.1. Parameters of the Microlevers™ [27].

Type	Length (µm)	Width (µm)	Thickness (µm)	Force constant (N/m)	First resonance frequency (kHz)
A	180	18	0.6	0.05	22
B	200	20	0.6	0.02	15
C	320	22	0.6	0.01	7
D	220	22	0.6	0.03	15
E	140	18	0.6	0.10	38
F	85	18	0.6	0.50	120

Figure 2.2 shows the Ultralevers™. They are gold-coated, all silicon cantilevers with integrated high aspect ratio conical tips. The typical radius of curvature for Ultralever tips is 100 Å, a more than fourfold improvement over the radius of standard Microlever tips. This reduced radius can greatly improve the resolution. The tip aspect ratio, the ratio of tip length to width, fundamentally limits the ability of an AFM to measure steep sidewall features and deep trenches that can be characteristic of patterned semiconductor devices and reticles. The typical aspect ratio of Ultralevers is about 3:1, whereas that of pyramidal tips is on the order of 1:1.

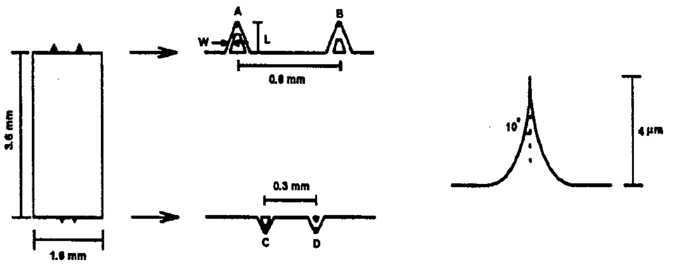

Figure 2.2. Ultralever chips with four cantilevers [28, pp. 4-32].

Table 2.2 shows the detailed information about Ultralevers.

Table 2.2. Parameters of the Ultralevers™ [28].

Type	Length (μm)	Width (μm)	Thickness (μm)	Force constant (N/m)	First resonance frequency (kHz)
A	180	25	1.0/2.0	0.26/2.1	40/80
B	180	38	1.0/2.0	0.40/3.2	45/90
C	85	18	1.0/2.0	1.6/13	140/280
D	85	28	1.0/2.0	2.1/17	160/320

The AFM has a wide range of applications in material property characterization. On and near the surface, topography, adhesion, visco-elasticity, hardness, friction, and other properties can be revealed with nanometer resolution. The AFM can work in different modes in a wide variety of applications. In these applications, the AFM cantilever is either static or vibrating for different measurements.

The primary concern in this thesis is the dynamic behavior of the AFM. That is, the AFM cantilever is vibrating while scanning over the sample surface. Generally speaking, there are three AFM modes that use a vibrating cantilever: Contact AFM, non-contact AFM (NC-AFM) and intermittent-contact AFM (IC-AFM). In these modes, the sensor tip contacts with the sample (contact AFM), or the cantilever tip either does not come into contact with the sample surface (NC-AFM), or it comes into contact only at the lowest point in its vibration cycle (IC-AFM).

For non-contact AFM (NC-AFM) imaging, the cantilever tip is held about 50 to 100 Å above the sample surface during a scan. The cantilever is excited to vibrate at a constant frequency with amplitude of tens of angstroms. As the sensor tip scans across the surface, the cantilever vibration amplitude changes in response to the force gradients that vary with respect to the tip-to-sample spacing. An image of the sample surface topography is generated from these amplitude changes. Non-contact mode is useful in

imaging the samples of low moduli, such as soft polymers, biological materials etc, that are very susceptible to tip damage.

Intermittent-contact AFM (IC-AFM) is very similar to NC-AFM, except that in IC-AFM the vibrating cantilever tip is brought closer to the sample so that the sensor tip contacts with the sample at its lowest point in vibration cycle. For some types of sample this mode is preferable to full contact AFM because it does not induce the lateral forces such as friction or drag that might damage the tip or sample. NC-AFM works better than IC-AFM on soft samples and when the maximum lateral resolution is required on samples with low-profile topography.

For contact AFM, the sensor tip is always, or in majority of the vibration cycle, is in contact with the sample surface. Therefore, the interaction forces between sample surface and sensor tip are higher than the non-contact modes.

In this thesis, concentration is on the contact or intermittent-contact modes of AFM, in which case the AFM tip contacts the sample surface somewhere in its vibration cycle. A typical experimental setup is presented in the Figure (2.3).

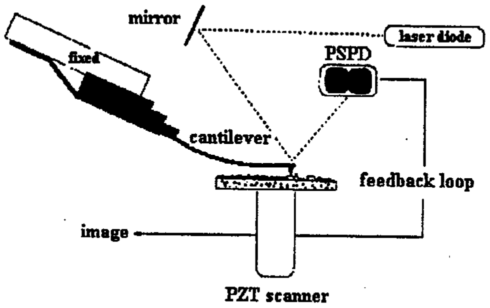

Figure 2.3. AFM scanning [26, pp. 2-32].

In Figure (2.3), the AFM cantilever is pushed to make its tip in contact with the sample surface and the cantilever is driven at a constant frequency. The sensor tip reflects a laser beam onto a position sensitive photodetector (PSPD). This technique is known as the "beam bounce" detection. The position of the laser spot on the PSPD shifts when the cantilever moves. This shift in position gives a measure of how much the cantilever has been deflected.

The dynamic techniques involve driving the AFM cantilever to vibrate at a certain frequency and measuring the cantilever resonance frequencies. The experimental setup will be different.

2.2 Applications of AFM in Material Properties Evaluation

The AFM has found various applications in the field of surface material properties evaluation. Here, two examples are presented.

U. Rabe, et al. [6] has shown one application of the atomic force acoustic microscopy to measure the Young's modulus of the films of Fe_3O_4 and of other spinel films. This film of nanocrystalline ferrites with spinel or hexagonal structure is used in magneto-optic and magnetic recording systems. The modulus of these films is an important parameter that must be known for applications. The contact resonances of an AFM cantilever are used to measure the Young's modulus of these films. This quantitative measurement yields very high lateral resolution.

K. Yamanaka and S. Nakano [16] have also done quantitative elasticity evaluation by contact resonance and reported their results on several materials. In their experiments, they investigated Si(001) crystal, soda lime glass, and a carbon-fiber-reinforced plastic (CFRP). In conclusion, they stated that the continuum model proved to be essential for

the precise measurement of local elasticity by resonance in the contact mode AFM.

2.3 Contact Forces

The interaction forces between the AFM cantilever tip and the sample surface are very complex. The distance between the AFM tip and the sample surface determines the interaction forces between them. When the cantilever vibrates, the tip-sample separation distance varies, the interaction forces changes accordingly. There are different types of forces acting between the atoms on the tip and atoms on the sample surface. These forces are closely related to the tip-to-sample distance as illustrated in the Figure (2.4).

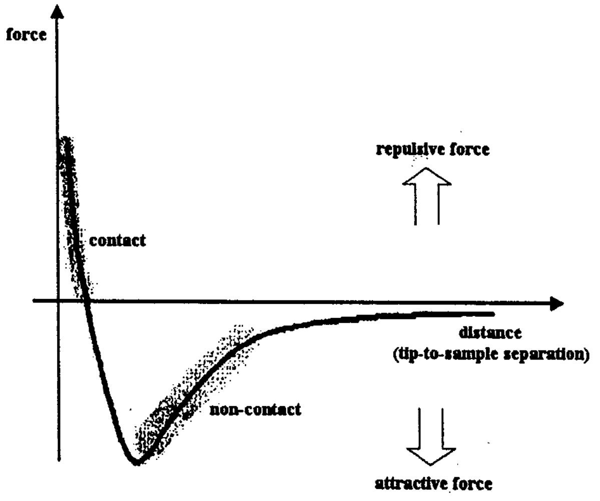

Figure 2.4. Typical interaction force vs. distance curve [26, pp. 4-28].

Clearly, it can be seen that there are two distance regimes labels as "contact" regime and "non-contact" regime. In the "contact" regime, the distance between tip and sample surface is less than a few angstroms, whereas in the "non-contact" regime the distance ranges from tens of angstroms to hundreds of angstroms. In the "contact" regime, the inter-atomic forces are exclusively repulsive, while in the "non-contact" regime they are attractive, largely a result of long range van der Waals interactions. The total force between the tip and sample surface is typically very low. For the non-contact modes, generally the force is about 10^{-12} N. Thus, it is more difficult to measure these forces than in contact regime, where the force can be several orders of magnitude higher. In this thesis, the study is concentrated on the "contact" regime where the tip and sample surface actually come into contact. During contact, the interaction forces between them are purely repulsive.

The contact forces between the sensor tip and the sample surface are essentially nonlinear. Some experiments have shown the effects of this nonlinearity [7]. In Figure (2.5), when the amplitude is increased, the resonance peaks become more and more asymmetric, the maximum shifts to lower frequencies and a jump in amplitude develops. This bending of the resonances to the left-hand side corresponds to the behavior of a softening nonlinearity [1]. The "backbone" curve, which connects all the peaks in this figure, indicates the relationship between the frequency shift and vibration amplitude. Different contact parameters will generate different backbone curves. Also, due to the nonlinear contact forces, the resonances show hysteresis [7].

There are several theoretical models used to described the normal contact of elastic bodies. To name a few, there are the Hertzian model, DMT (Derjaguin, Muller, Toporov) model, BCP (Burnham, Colton, Pollock) model, JKRS (Johnson, Kendall, Roberts,

Sperling) model and the Maugis model [29].

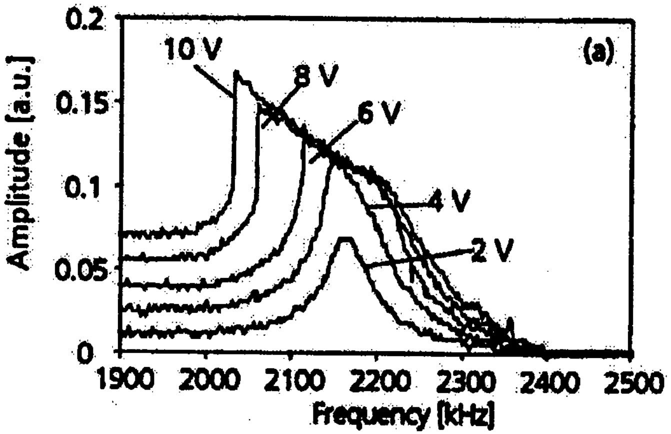

Figure 2.5. Experimental measurements of the first mode by U.Rabe, et al. [7].

To describe these models, some notation is introduced here. The reduced elastic modulus for the tip-sample system, E^* is defined by

$$\frac{1}{E^*}=\left(\frac{1-\nu_{tip}^2}{E_{tip}}\right)+\left(\frac{1-\nu_{sample}^2}{E_{sample}}\right), \qquad (2.3.1)$$

where E_{tip} is the Young's modulus of the tip, E_{sample} is the Young's modulus of the sample, ν_{tip} is the Poisson's ratio of the tip and ν_{sample} is the Poisson's ratio of the sample.

Other necessary parameters include: ξ_0, the inter-atomic equilibrium distance at the tip-sample interface; a, the radius of the contact area; ϖ, the work of adhesion at contact; P, the load; and δ, the penetration depth of the tip into the sample.

R, the reduced tip-sample curvature, is related to the curvatures of both the tip and the sample. It is given by

$$\frac{1}{R}=\frac{1}{R_{tip}}+\frac{1}{R_{sample}}. \tag{2.3.2}$$

In Hertzian theory, it is assumed there are no surface forces and no adhesion effects. This theory dates back to 1888. The relationship between the load P and the other system parameters are given by $P=\frac{4}{3}\frac{E^{*}a^{3}}{R}$. The relationship between the contact radius a and the indentation depth δ is $\delta=\frac{a^{2}}{R}$. Hence, the relation between P and δ is

$$P=\frac{4}{3}E^{*}\sqrt{R}\delta^{3/2}=K_{0}\delta^{3/2},\ \text{where}\ K_{0}=\frac{4}{3}E^{*}\sqrt{R}. \tag{2.3.3}$$

K_0 is defined as the Hertzian coefficient.

The DMT (Derjiaguin, Muller, Toporov) theory is essentially the Hertzian model with an additional static attractive force due to surface forces. This model dates back to 1975 [29]. The equations take the following form:

$$P=\frac{4}{3}E^{*}\sqrt{R}\delta^{3/2}-2\pi R\varpi. \tag{2.3.4}$$

There is no hysteresis between loading and unloading.

The BCP (Burnham, Colton, Pollock) theory is a semi-empirical approach formulated in 1991 [29]. In BMP theory,

$$P=\frac{4}{3}\frac{E^{*}a^{3}}{R}-\sqrt{2\pi E^{*}a^{3}\varpi}-\pi R\varpi, \tag{2.3.5}$$

$$\delta=\frac{a^{2}}{R}-\left(\frac{9\pi^{2}R\varpi^{2}}{16E^{*2}}\right)^{1/3}. \tag{2.3.6}$$

The second term in equation (2.3.5) accounts for the attractive forces that act to deform the tip-sample geometry causing non-rigid materials to bulge out towards each other during tip-sample approach.

In the JKRS (Johnson, Kendall, Roberts, Sperling) theory, it is assumed that there is no force between the two surfaces when they are not in contact. Upon contact, short-ranged attractive forces show up within the contact area and the tip-sample geometry is not constrained to remain Hertzian. This set of assumptions applies well to the highly adhesive systems that have large radii of curvature and low stiffness. There is adhesion hysteresis between loading and unloading. During unloading, a connective neck is formed between the tip and sample and contact is ruptured at negative loads. In this case,

$$P=\frac{4}{3}\frac{E^{*}a^{3}}{R}-\sqrt{8\pi\varpi E^{*}a^{3}}, \tag{2.3.7}$$

$$\delta=\frac{a^{2}}{R}-\sqrt{\frac{2\pi\varpi a}{E^{*}}}. \tag{2.3.8}$$

While all the above three contact mechanics theories work in some cases, they have their limitations. The Maugis theory, formulated by Maugis in 1992 [29], is a more complex and more accurate description of the sphere-flat contact mechanics. In this model, no assumption is made about the particular material property limits. Thus it can be applied to a wide range of systems, from the large compliant spheres with strong adhesion, to small diamond/diamond systems with extremely low adhesion.

The parameter λ is used to characterize the spectrum of materials possibilities. It is defined as

$$\lambda=\frac{2.06}{\xi_{0}}\left(\frac{9R\varpi^{2}}{16\pi E^{*2}}\right)^{1/3}. \tag{2.3.9}$$

Large λ is for the more compliant, adhesive combinations and vice verse for small λ. In the limit of infinite λ, Maugis equations will approach those of the JKRS theory. For the limit of λ equal to zero, the system reduces to the DMT model. A new parameter m is introduced in Maugis model. This parameter defines the ratio of the width of the annular region to the radius of the contact area. The equations of the Maugis model are

$$P = \frac{4}{3}\frac{E^* a^3}{R} - \lambda a^2 \left(\frac{16\pi\varpi E^{*2}}{9R}\right)^{1/3} \left[\sqrt{m^2-1} + m^2 \arctan\sqrt{m^2-1}\right], \qquad (2.3.10)$$

$$\delta = \frac{a^2}{R} - \frac{4\lambda a}{3}\left(\frac{3\pi\varpi}{4E^* R}\right)^{1/3} \sqrt{m^2-1}, \qquad (2.3.11)$$

$$1 = \frac{\lambda a^2}{2}\left(\frac{4E^*}{3\pi R^2 \varpi}\right)^{2/3}\left[\sqrt{m^2-1} + (m^2-2)\arctan\sqrt{m^2-1}\right] + \frac{4\lambda^2 a}{3}\left(\frac{4E^*}{3\pi R^2\varpi}\right)^{1/3}\left[1 - m + \sqrt{m^2-1}\arctan\sqrt{m^2-1}\right] \qquad (2.3.12)$$

Figure (2.7) illustrates the the Hertzian, DMT, BCP and JKRS models. In the figure, the normalized force $\tilde{P}$ is plotted as a function of normalized penetration depth $\tilde{\Delta}$. The normalization factors are given as

$$\text{radius } \tilde{A} = \frac{a}{\left(\frac{3\pi R^2\varpi}{4E^*}\right)^{1/3}}, \qquad (2.3.13)$$

$$\text{load } \tilde{P} = \frac{P}{\pi R\varpi}, \qquad (2.3.14)$$

$$\text{depth } \tilde{\Delta} = \frac{\delta}{\left(\frac{9\pi^2 R\varpi^2}{16E^{*2}}\right)^{1/3}}. \qquad (2.3.15)$$

It can be seen from Figure (2.7) that Hertz, DMT, BCP are not hysteretic, whereas JKRS is.

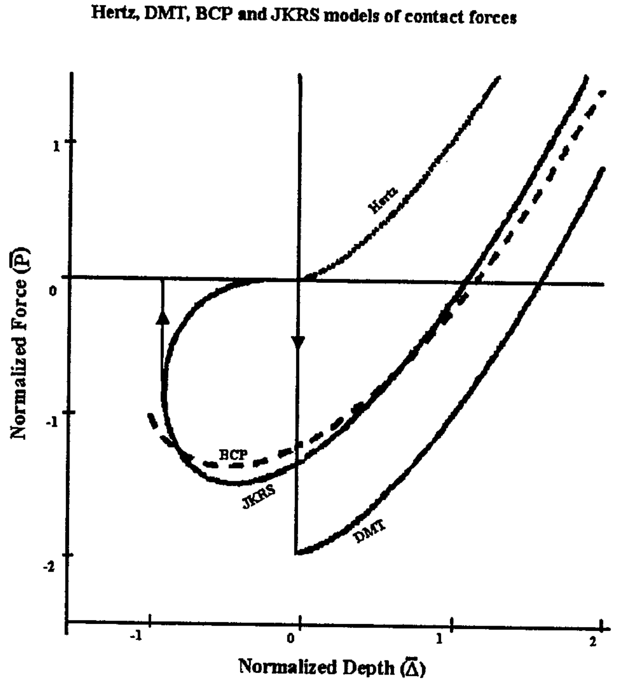

Figure 2.7. The Hertz, DMT, BCP and JKRS models of contact forces [28].

Figure (2.8) shows the Maugis theory. In the figure, it shows that low λ values approach DMT, and high λ values approach JKRS. Adhesion hysteresis appears for $\lambda >$ 0.94. At $\lambda = 0$, Maugis theory will be the same as DMT.

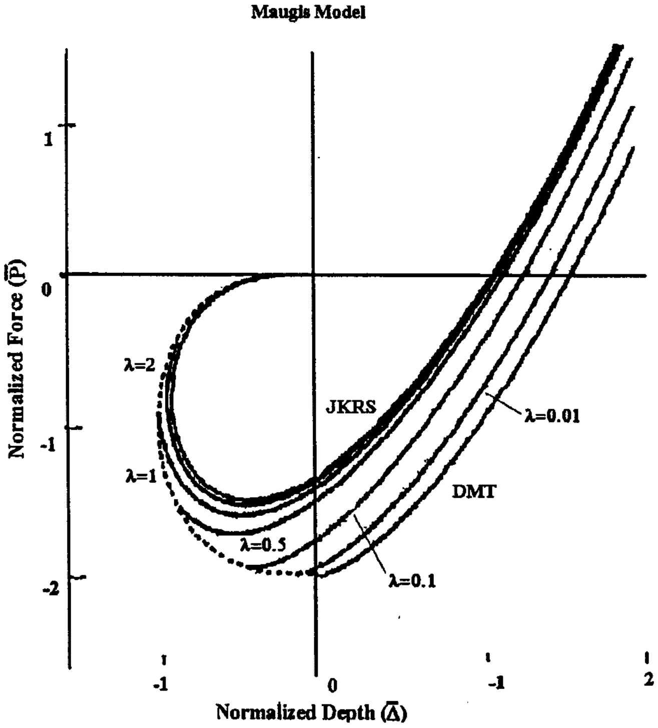

Figure 2.8. Maugis contact mechanics theory [28].

In summary, the differences between these models are listed in Table 2.3. Among these contact mechanics theories, the Hertzian theory is the simplest with the assumption that there are no surface forces. In experiments, if the cantilever is pushed hard into

sample, the surface forces will become negligible. Under such circumstances the Hertzian theory is an appropriate approach. As the first step in this thesis, Hertzian theory is applied in describing the contact interaction between the AFM tip and the sample surface.

Table 2.3. Comparison of the contact theories [28].

Theory	Assumption	Limitations
Hertz	No surface forces.	Not appropriate for low loads if surface forces present
DMT	Long-ranged surface forces act only outside contact area. Geometry constrained to be Hertzian.	May underestimate contact area due to restricted geometry. Applies to low λ systems only.
BCP	Long-ranged surface forces act only outside contact area. Hertzian functional relationship between penetration depth and contact radius is retained.	May underestimate pull-off force due to Hertzian function for geometry. Applies to moderate λ systems.
JKRS	Short-ranged surface forces act only inside contact area. Contact geometry is allowed to deform.	May underestimate loading due to surface forces. Applies to high λ systems only.
Maugis	Periphery of tip-sample interface modeled as a crack that fails at its theoretical strength.	Solution analytical, but parametric equations. Applies to all values of λ.

3. Governing Equations and Linear Approximation

3.1 Theoretical Approach

For simplification, the AFM cantilever is modeled as a homogeneous elastic beam. This beam is fixed at one end and a small radius tip is attached at the other end. The mass of this tip is assumed negligible. It is also assumed that the tip resides at the very end of the beam. During vibration, this tip is always in contact with the sample surface. Figure (3.1) illustrates the idealized model of the AFM vibration system.

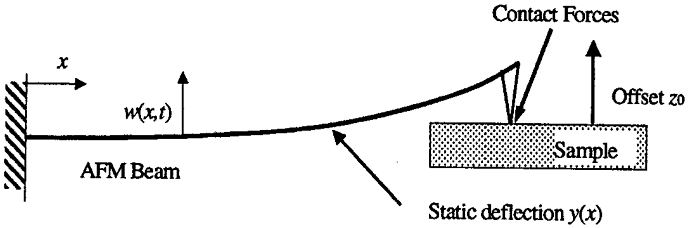

Fig 3.1. Schematic of the problem. The AFM probe is in contact with a specimen. Initial contact is made when the sample offset z_0 is zero. The static sample offset causes a static beam deflection $y(x)$. The dynamic motion of the beam $w(x,t)$ is defined relative to $y(x)$. The contact forces between the tip and the sample surface are nonlinear. They will be described by Hertzian or Maugis model.

The interaction force from the contact between the cantilever tip and sample surface is very complex and highly nonlinear. As has been discussed in the previous chapter, there are several models to describe the contact. In this thesis, Hertzian theory and Maugis theory are used. A rough estimation can be made using the theory of Hertzian contact when the tip penetrates into the sample surface. In experiments, the force applied by the cantilever can be adjusted to be negligible compared with the adhesion force. This Hertzian description is valid only when the surface forces are negligible. When this condition is not true, the Maugis model is applied.

Apart from the flexural vibrations, longitudinal vibrations and Lamb modes are also possible. For common AFM cantilevers, however, the resonance frequencies of these modes are much higher than the resonance frequencies of the flexural vibrations in the z direction. Additionally, most position detectors, such as beam deflection sensors are not sensitive to movements in the x-z plane. The lowest torsional vibration frequencies are about ten times higher than the flexural frequencies for typical AFM cantilevers. In this thesis the torsional vibrations are not considered.

Since the contact force is highly nonlinear, different nonlinear approximation methods are applied to study the cantilever vibration. These methods include the harmonic balance method [2][23] and the method of multiple scales [21][24]. The governing equations and boundary conditions of this problem will be discussed in detail in the next chapter.

3.2 Governing Equations

In the theoretical model, the AFM cantilever is treated as a homogeneous elastic beam. Figure (3.2) shows a beam in bending vibration under the distributed transverse force $f(x,t)$. In addition, it is assumed that the beam is subjected to the axial force $P(x)$. The boundary-value problem of this beam can be derived by means of the extended Hamilton's principle, which can be written in the form

$$\int_{t_1}^{t_2} (\delta T(t) - \delta V(t) + \delta W_{nc}(t))dt = 0, \qquad \delta w(x,t) = 0,\ t = t_1, t_2,$$

where $T(t)$ is the kinetic energy, $V(t)$ the potential energy and $W_{nc}(t)$ the virtual work due to non-conservative forces.

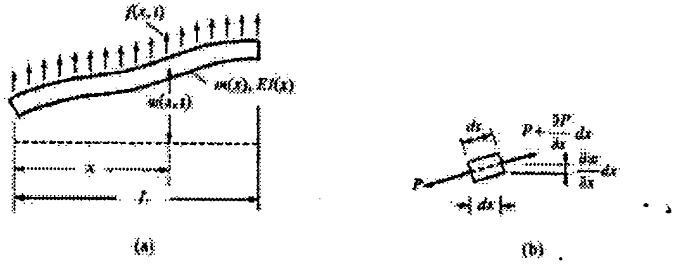

Figure 3.2. (a) Beam in bending vibration (b) Axial forces acting on a beam differential element [8].

It is assumed that the kinetic energy is due entirely to translation. Hence, denoting the transverse displacement by $w(x,t)$, the kinetic energy is of the form

$$T(t)=\frac{1}{2}\int_0^L m(x)\left[\frac{\partial w(x,t)}{\partial t}\right]^2 dx,$$

where $m(x)$ is the mass per unit length of beam. The potential energy contains two parts: one from the bending and one from the axial force. It is written

$$V(t)=\frac{1}{2}\int_0^L \left\{ EI(x)\left[\frac{\partial^2 w(x,t)}{\partial x^2}\right]^2 + P(x)\left[\frac{\partial w(x,t)}{\partial x}\right]^2 \right\} dx,$$

where $EI(x)$ is the bending stiffness, or flexural rigidity, in which E is the Young's modulus of elasticity and $I(x)$ is the area moment of inertia about an axis normal to the plane of x and w. The potential energy due to the gravitational forces is neglected because $w(x)$ may be defined as the displacement from the equilibrium position.

By Hamilton's principle, it is assumed that variations and differentiations are interchangeable. The virtual work due to non-conservative forces is

$$\delta W_{nc}=\int_0^L f(x,t)\delta w(x,t)dx.$$

The variation in the kinetic energy is

$$\delta T=\int_0^L m\frac{\partial w}{\partial t}\delta\frac{\partial w}{\partial t}dx=\int_0^L m\frac{\partial w}{\partial t}\frac{\partial}{\partial t}\delta w dx.$$

Thus,

$$\int_{t_1}^{t_2}\delta T dt=\int_{t_1}^{t_2}\int_0^L m\frac{\partial w}{\partial t}\frac{\partial}{\partial t}\delta w dx dt=\int_0^L\int_{t_1}^{t_2} m\frac{\partial w}{\partial t}\frac{\partial}{\partial t}\delta w dt dx=$$

$$=\int_0^L m\frac{\partial w}{\partial t}\delta w\,|_{t_1}^{t_2}\,dx-\int_0^L\int_{t_1}^{t_2} m\frac{\partial^2 w}{\partial t^2}\delta w dt dx=-\int_{t_1}^{t_2}\int_0^L m\frac{\partial^2 w}{\partial t^2}\delta w dt dx.$$

The variation in the potential energy is

$$\delta V=\int_0^L (EI\frac{\partial^2 w}{\partial x^2}\delta\frac{\partial^2 w}{\partial x^2}+P\frac{\partial w}{\partial x}\delta\frac{\partial w}{\partial x})dx=\int_0^L (EI\frac{\partial^2 w}{\partial x^2}\frac{\partial^2}{\partial x^2}\delta w+P\frac{\partial w}{\partial x}\frac{\partial}{\partial x}\delta w)dx$$

$$=EI\frac{\partial^2 w}{\partial x^2}\frac{\partial}{\partial x}\delta w\,|_0^L-\frac{\partial}{\partial x}(EI\frac{\partial^2 w}{\partial x^2})\delta w\,|_0^L+P\frac{\partial w}{\partial x}\delta w\,|_0^L$$

$$+\int_0^L\left[\frac{\partial^2}{\partial x^2}(EI\frac{\partial^2 w}{\partial x^2})-\frac{\partial}{\partial x}(P\frac{\partial w}{\partial x})\right]\delta w dx.$$

Hence, by extended Hamilton's principle,

$$-\int_{t_1}^{t_2}\left\{\left[-\frac{\partial}{\partial x}(EI\frac{\partial^2 w}{\partial x^2})+P\frac{\partial w}{\partial x}\right]\delta w\,|_0^L+EI\frac{\partial^2 w}{\partial x^2}\delta\frac{\partial w}{\partial x}\,|_0^L\right.$$

$$\left.+\int_0^L\left[m\frac{\partial^2 w}{\partial t^2}+\frac{\partial^2}{\partial x^2}(EI\frac{\partial^2 w}{\partial x^2})-\frac{\partial}{\partial x}(P\frac{\partial w}{\partial x})-f\right]\delta w dx\right\}dt=0.$$

The virtual displacements δw are arbitrary over the domain $0 < x < L$. It is assumed that either δw or its coefficients are zero at $x = 0$ and $x = L$, or either $\delta(\partial w/\partial x)$ or its coefficients are zero at $x = 0$ and $x = L$. Consequently the equation of motion is

$$m\frac{\partial^2 w}{\partial t^2}+\frac{\partial^2}{\partial x^2}(EI\frac{\partial^2 w}{\partial x^2})-\frac{\partial}{\partial x}(P\frac{\partial w}{\partial x})-f=0, \qquad \text{for } 0<x<L.$$

The boundary conditions are given by

$$-\frac{\partial}{\partial x}(EI\frac{\partial^2 w}{\partial x^2})+P\frac{\partial w}{\partial x}=0 \text{ or } w=0, \qquad \text{at } x=0,L,$$

and

$$EI\frac{\partial^2 w}{\partial x^2}=0 \text{ or } \frac{\partial w}{\partial x}=0, \qquad \text{at } x=0,L.$$

The model of a beam in bending vibration considered here is called an Euler-Bernoulli beam.

In the specific case for the AFM cantilever, the beam is assumed to be homogeneous and uniform. It is also assumed there is no external load and there are no axial forces. Thus, if $f(x) = 0$, $P(x) = 0$, $m(x) = \rho A$ (A is the area of cross-section and ρ is the volume density), and $EI(x)$ is constant, the equation of motion is then written

$$EI\frac{\partial^4 w(x,t)}{\partial x^4}+\rho A\frac{\partial^2 w(x,t)}{\partial t^2}=0. \tag{3.2.1}$$

with the boundary conditions

$$\begin{aligned} &w(0,t)=0,\\ &w'(0,t)=0,\\ &w''(L,t)=0,\\ &EIw'''(L,t)-f_c(w,\dot{w})=0. \end{aligned} \tag{3.2.2}$$

The last boundary condition takes into account the contact force f_c at the tip of the AFM cantilever. Referring to Figure (3.2), the boundary conditions given above correspond to conditions of zero displacement and zero slope at $x = 0$, and zero moment at $x = L$. The last boundary condition is the force balance between the beam and the interaction force associated with the contact of the tip and the sample surface.

Here, it is assumed that this interaction force is the Hertzian contact condition of a sphere in contact with a plane [3]. In a later section, Maugis theory is applied to describe the contact. As was introduced in section 2.4, the Hertzian coefficient K_0 is defined in equation (2.3.3) in terms of the reduced elastic modulus $E*$ and the contact radius R.

Function $y(x)$ defines the static deflection of the cantilever due to the sample surface offset. The static position of the end of the cantilever $y(L)$ must satisfy the final boundary condition of (3.2.2). A static offset may result from changes in topography or from an applied force. The end deflection $y(L)$ will be slightly less than the sample surface offset z_0. This difference between the two is the result of deformation. The end deflection is defined by consideration of the static problem [4]. The initial deflection of the cantilever can be written in terms of the end deflection as

$$y(x)=\frac{1}{2}y(L)\left(\frac{x}{L}\right)^2\left(3-\frac{x}{L}\right)$$

The end deflection is governed by

$$-3\frac{EI}{L^3}y(L)+K_0(z_0-y(L))^{\frac{3}{2}}=0. \tag{3.2.3}$$

which defines $y(L)$ in terms of the sample surface offset z_0. Without loss of generality, it is assumed that z_0 is zero when the tip first comes into contact with the sample surface. This assumption also implies that the cantilever is horizontal when it first makes contact. The quantity $\Delta = z_0 - y(L)$ is identified as the static Hertz deformation. Note that no attractive forces are assumed present.

From the above equations and boundary conditions, it can be seen that the vibration modes of the AFM cantilever are directly related to the material properties of the sample surface. The goal for characterizing the sample properties is to assess the Hertz coefficient K_0. If K_0 can be measured, a calibration can be used to extract E from K_0. Such a calibration procedure is performed by applying a variety of forces to the cantilever using a specimen with know properties such as silicon.

3.3 General Solution

With the governing equation (3.2.1), a harmonic solution is assumed,

$$w(x,t) = W(x)e^{j\omega t}.$$

Substituting this solution into (3.2.1), gives

$$EIW''''(x)e^{j\omega t} - \rho A\omega^2 W(x)e^{j\omega t} = 0,$$

or, $W''''(x) - \dfrac{\rho A\omega^2}{EI}W(x) = 0.$

The general solution of this ordinary differential equation is

$$W(x) = A\sin kx + B\cos kx + C\sinh kx + D\cosh kx, \qquad (3.3.1)$$

where $k^4 = \dfrac{\rho A}{EI}\omega^2$.

By applying the first three boundary conditions, equation (3.3.1) becomes

$$W(x) = D[\sin kx - \sinh kx - D_0(\cos kx - \cosh kx)] \qquad (3.3.2)$$

where $D_0 = \dfrac{\sin kL + \sinh kL}{\cos kL + \cosh kL}$, with D an arbitrary constant.

If there is no contact at the free end, i.e., the vibration is free, the boundary condition at the free end is $W'''(L) = 0$. This boundary condition leads to the characteristic equation

$$1 + \cos kL \cosh kL = 0. \qquad (3.3.3)$$

Equation (3.3.3) is the characteristic equation corresponding to the free vibration of the cantilever beam. The allowable wave numbers (kL) of this free vibration system can be solved numerically from this equation. The first five roots (kL) of equation (3.3.3) are

$$kL = 1.87510, 4.69409, 7.85476, 10.99554, 14.13717.$$

The first natural frequency ω_0 of the free cantilever is

$$\omega_0 = \sqrt{\frac{EI}{\rho A}}k_0^2 = \frac{3.516}{L^2}\sqrt{\frac{EI}{\rho A}}.$$

3.4 Contact Boundary Condition

The boundary condition (3.2.2) involves the tip and sample contact force. The contact force is nonlinear. This nonlinear term makes analytical solution impossible. As a first approximation, this boundary condition is linearized. Based on the assumption that the displacement of the tip remains very small relative to its equilibrium position, the boundary condition can be expanded with respect to its equilibrium position.

In this section, the contact force is described by the Hertzian model as

$$f(w) = \begin{cases} K_0(\Delta - w(L,t))^{3/2} & \text{if } \Delta - w(L,t) \ge 0 \\ 0 & \text{if } \Delta - w(L,t) < 0 \end{cases} \qquad (3.4.1)$$

where $\Delta = z_0 - y(L)$.

Expanding (3.4.1) in a Taylor's series and keeping the terms up to the cubic order, it becomes

$$EIw'''(L,t) - \kappa w(L,t) + \kappa_1 w^2(L,t) + \kappa_2 w^3(L,t) = 0,$$
$$\kappa = \frac{3}{2}K_0\Delta^{\frac{1}{2}},\ \ \kappa_1 = \frac{3}{8}K_0\Delta^{-\frac{1}{2}},\ \ \kappa_2 = \frac{1}{16}K_0\Delta^{-\frac{3}{2}}. \qquad (3.4.2)$$

The linear spring constant κ is defined as above. It can be seen that as the specimen offset z_0 increases, the effective spring constants will increase in a known manner. As a first approximation, in the expanded boundary condition (3.4.2) only the linear term κ is kept. That is, the last boundary condition is written as

$$EIw'''(L,t) = \kappa w(L,t). \qquad (3.4.3)$$

This equation defines the linearized boundary condition.

The Taylor's series expansion of (3.4.1) is based on the assumption that the displacement of the tip $w(L,t)$ remains very close to its equilibrium position. In (3.4.2), it is expected that $\kappa_2 w^3(L,t) < \kappa_1 w^2(L,t) < \kappa w(L,t)$. Otherwise, the expansion will not be convergent. From this restriction, it is easily seen that

$$w(L,t) < \Delta. \tag{3.4.4}$$

From the definition of the Hertz contact force in (3.4.1), $f = 0$ when $w(L,t) > \Delta$. Thus, (3.4.4) is always true for Hertz contact. Also, since the contact boundary condition is $EIw'''(L,t) = f(w)$, it implies that $w'''(L,t) \geq 0$.

Thus, from (3.4.2), it is easily seen that

$$EIw'''(L,t) + \kappa_1 w^2(L,t) = \kappa w(L,t) - \kappa_2 w^3(L,t) = \frac{3}{2}K_0\sqrt{\Delta}w(L,t)(1-\frac{w^2(L,t)}{24\Delta^2}) \tag{3.4.5}$$

Since $w'''(L,t) \geq 0$, and $w(L,t) < \Delta$, from (3.4.5), it shows that $w(L,t) \geq 0$. Therefore, for the Taylor's series expansion of the contact boundary condition to be valid, the condition on the end deflection must satisfy

$$0 \leq w(L,t) \leq \Delta. \tag{3.4.6}$$

3.5 Numerical Results

From the linearized boundary condition (3.4.3) and the general solution (3.3.2), the following characteristic equation is reached:

$$\gamma^3(\cos\gamma\cosh\gamma+1) - \frac{\kappa}{EI/L^3}(\sinh\gamma\cos\gamma - \sin\gamma\cosh\gamma) = 0, \tag{3.5.1}$$

where $\gamma = kL$ is the normalized wave number. From this equation the allowable wave numbers can be found. U. Rabe, K. Janser and W. Arnold have done extensive work on this linearized problem [5].

For a homogeneous AFM cantilever of constant rectangular cross section, the spring constant k_c of it is defined as $k_c = \frac{Eb^3a}{4L^3}$, where a is the width, b is the thickness and L is the length of the beam. Equation (3.5.1) can be rewritten as

$$\sinh\gamma\cos\gamma - \sin\gamma\cosh\gamma = \frac{\gamma^3}{3}\frac{k_c}{\kappa}(1+\cos\gamma\cosh\gamma). \tag{3.5.2}$$

Characteristic equation (3.5.2) can be solved for the allowable wave numbers with respect to different ratios of (k_c/κ). Some examples of solutions of γ as a function of the ratio (k_c/κ) are given in Table (3.1). When $\kappa = 0$, i.e., the effective contact stiffness is infinitely small, equation (3.5.2) reduces to (3.3.3). It can be seen from Table 4.1 that the resonance frequencies of every mode of the clamped-spring-coupled cantilever are between the resonance frequency of the clamped-free cantilever mode and the resonance frequency of the clamped-pinned cantilever mode.

Table 3.1. Wave numbers of equation (3.5.2).

N	free end ($\kappa = 0$)	$k_c/\kappa=10$	$k_c/\kappa=1$	$k_c/\kappa=0.1$	$k_c/\kappa=0.01$	$k_c/\kappa=$ 0.001	Pinned end $\kappa=\infty$
0	1.87510	1.91891	2.21350	3.16765	3.82981	3.91704	3.92662
1	4.69409	4.69699	4.72342	5.00112	6.40415	7.00766	7.06858
2	7.85476	7.85538	7.86097	7.91896	8.58742	10.0122	10.2102
3	10.9955	10.9958	10.9978	11.0185	11.2559	12.8511	13.3518
4	14.1372	14.1373	14.1382	14.1479	14.2523	15.4765	16.4934
5	17.2788	17.2788	17.2793	17.2846	17.3396	18.0795	19.6355
6	20.4205	20.4204	20.4207	20.4239	20.4567	20.8774	22.7765
7	23.5619	23.5620	23.5622	23.5642	23.5853	23.8390	25.9181

To further demonstrate this relation, Figure (3.3) is presented which illustrates the relationship between the first five resonance frequencies and the ratio (κ/k_c). As can be observed from this figure, the resonance frequencies acquired from the characteristic equation (3.5.2) show a consistent trend of increasing with ratio (κ/k_c). When κ/k_c

increases from 0 to infinity, the resonance frequency of every mode shifts from the free case to the pinned case.

The relationship between the effective stiffness κ and the resonance frequency of the AFM cantilever is clearly defined. Therefore, if the resonance frequency is known, κ can easily be determined. From κ, the material property of the sample surface can be deduced from the contact theories.

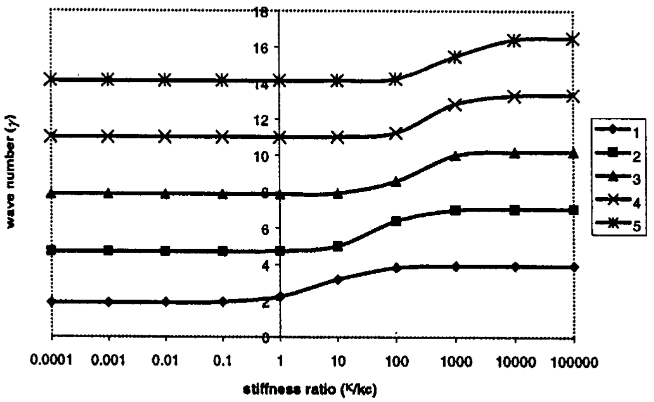

Figure 3.3. Relation between wave number (γ) and stiffness (κ) from Equation (3.5.2).

As discussed earlier, there are several theories depicting the contact interaction between the AFM tip and the sample surface. According to the Hertzian model,

$$\kappa = -\frac{\partial F}{\partial z}\Big|_{z=z_0} = \sqrt[3]{6E^{*2}RF_N} ,$$

in which E^* is the reduced Young's modulus which is determined by the Young's modulus and Poisson's ratio of both the AFM tip and the sample surface. F_N is the normal force acting on the tip. From Equations (?), Young's modulus of the sample surface E_s

can be calculated if Young's modulus of the tip (E_t), Poisson's ratio of the tip v_t and the Poisson's ratio of the sample surface v_s are known. In most cases, E_t and v_t are assumed to be known. K. Yamanaka and S. Nakano [16] also proposed a method to determine the Poisson's ratio of the sample using the torsional vibration excited by a transducer attached to the base of cantilever [18].

When Young's modulus is calculated from the contact resonance frequencies, care must be taken to use small excitation amplitudes and high static cantilever forces in order to allow linear approximation of the forces. With the lowest excitation amplitude, a symmetric resonance peak is obtained, showing that the linear approximation is valid. When the amplitude is increased, the resonance peaks become more and more asymmetric, the maximal shift to lower frequencies and a jump in amplitude develops. This bending of the resonances to the left-hand side corresponds to the behavior of a softening non-linearity [19].

This linearized procedure is used to calibrate the AFAM system [6]. The cantilever is placed in contact with some specimen of known properties, then different forces are applied to the AFM cantilever and the first three frequencies are measured. In this case, the parameter known with least certainty is the tip radius. Therefore, the resulting frequency-force curves are used to extract an effective tip radius. However, the observations by Rabe, et al. [1] show that the calibration itself does not give consistent values of the tip radius. They observed that the results from the higher frequencies corresponded to smaller values of tip radius. When a correction for the tip location is used, the results from the different frequencies converge.

Yamanaka and Nakano [16] have studied this problem with the similar linearized contact boundary condition. However, they used the Johnson-Kendall-Roberts model

[17] which gives the reduced modulus by

$$E^* = (\frac{2}{3})^{3/2} \frac{\left[1+\sqrt{F_d/(F+F_d)}\right]^{3/2}}{\sqrt{R\left[F+2F_d+2(F_dF+F_d^2)^{1/2}\right]}} K^{3/2} .$$

where R is the radius of curvature of the tip, F is the applied normal force and $F_d = \frac{3}{2}\gamma\pi R$ is the adhesion force with γ the surface energy [17]. They also have used Maugis theory [19].

Thus, with the known Young's modulus and Poisson's ratio of the AFM cantilever, the Young's modulus of the sample can be determined if Poisson's ratio of the sample is known.

4. Nonlinear Response

4.1 Nonlinear Boundary Condition

In the previous chapter the numerical results from a linearized boundary condition have been discussed. In this chapter the focus is on the influence of the nonlinear terms to this system. Here, it is assumed that the vibration amplitude is large enough that the nonlinear effects are created, but not to the extent of chaotic motion.

In nonlinear systems, the frequency response will be a function of amplitude [1]. Such an effect has been observed experimentally for the AFM [7]. At high amplitude excitation, chaotic behavior of the AFM vibrations has been observed, in which the tip moves erratically into and out of contact with the specimen.

The square and cubic terms are kept in the expansion of the Hertzian contact boundary condition,

$$EIw'''(L,t) - \kappa w(L,t) + \kappa_1 w^2(L,t) + \kappa_2 w^3(L,t) = 0,$$
$$\kappa = \frac{3}{2}K_0\Delta^{\frac{1}{2}},\ \ \kappa_1 = \frac{3}{8}K_0\Delta^{-\frac{1}{2}},\ \ \kappa_2 = \frac{1}{16}K_0\Delta^{-\frac{3}{2}}. \qquad (4.1.1)$$

The dimensionless form of this equation is

$$\tilde{w}'''(L,t) - \beta\tilde{w}(L,t) + \beta_1\tilde{w}^2(L,t) + \beta_2\tilde{w}^3(L,t) = 0, \qquad (4.1.2)$$

where $\tilde{w} = \frac{w}{L}$ is the normalized displacement. The dimensionless linear and nonlinear spring constants are given by

$$\beta = \frac{\kappa}{EI/L^3},\ \ \beta_1 = \frac{\kappa_1 L}{EI/L^3},\ \ \beta_2 = \frac{\kappa_2 L^2}{EI/L^3}. \qquad (4.1.3)$$

Note that these spring constants are not independent. They are all defined by the material properties of the tip and specimen together with the initial offset. The nonlinear constants may be written in terms of β as

$$\beta_1 = \frac{1}{4}\frac{\beta}{\tilde{\Delta}}, \quad \beta_2 = \frac{1}{24}\frac{\beta}{\tilde{\Delta}^2} \quad \text{, where } \tilde{\Delta} = \frac{\Delta}{L}.$$

The method of harmonic balance is applied to solve this nonlinear vibration system.

4.2 Maugis boundary condition

In the previous section, the contact boundary condition was described using the Hertzian theory. Because of the limitation of this Hertzian theory as discussed in Chapter 2, the more accurate and more complicated Maugis theory is used to model the tip-sample contact. Taking the normalized load, radius and depth as defined in (2.3.13)-(2.3.15), the normalized equations for Maugis theory are

$$\tilde{P} = \tilde{A}^3 - \lambda\tilde{A}^2\left[\sqrt{m^2-1} + m^2 \arctan\sqrt{m^2-1}\right], \tag{4.2.1}$$

$$\tilde{\Delta} = \tilde{A}^2 - \frac{4\lambda}{3}\tilde{A}\sqrt{m^2-1}, \tag{4.2.2}$$

$$\begin{aligned} 1 = \frac{\lambda}{2}\tilde{A}^2\left[\sqrt{m^2-1} + (m^2-2)\arctan\sqrt{m^2-1}\right] \\ + \frac{4\lambda^2}{3}\tilde{A}\left[1 - m + \sqrt{m^2-1}\arctan\sqrt{m^2-1}\right]. \end{aligned} \tag{4.2.3}$$

In the boundary condition, the contact force is

$$\tilde{F} = \tilde{P}(\tilde{\Delta} - \tilde{w}(L,t)).$$

Based on the assumption that the displacement of the cantilever at its tip end $w(L,t)$ is within close range of the indentation depth Δ, the contact force can be expanded in a Taylor's series

$$\begin{aligned} \tilde{F} = \tilde{P}(\tilde{\Delta} - \tilde{w}(L,t)) = \tilde{P}(\tilde{\Delta}) - \tilde{P}'(\tilde{\Delta})\tilde{w}(L,t) + \frac{1}{2}\tilde{P}''(\tilde{\Delta})\tilde{w}^2(L,t) \\ - \frac{1}{6}\tilde{P}'''(\tilde{\Delta})\tilde{w}^3(L,t) + O(\tilde{w}^4(L,t)). \end{aligned} \tag{4.2.4}$$

Letting

$$M_1 = \sqrt{m^2-1} + m^2 \arctan\sqrt{m^2-1}, \tag{4.2.5}$$

$$M_2 = \sqrt{m^2-1} + (m^2-2)\arctan\sqrt{m^2-1}, \tag{4.2.6}$$

$$M_3 = 1 - m + \sqrt{m^2-1}\arctan\sqrt{m^2-1}. \tag{4.2.7}$$

Equations (4.2.1) – (4.2.3) may be written as

$$\tilde{P} = \tilde{A}^3 - \lambda\tilde{A}^2 M_1, \tag{4.2.8}$$

$$\tilde{\Delta} = \tilde{A}^2 - \frac{4\lambda}{3}\tilde{A}\sqrt{m^2-1}, \tag{4.2.9}$$

$$1 = \frac{\lambda}{2}\tilde{A}^2 M_2 + \frac{4\lambda^2}{3}\tilde{A}M_3. \tag{4.2.10}$$

From equation (4.2.8), the first derivative of $\tilde{P}$ is

$$\tilde{P}'(\tilde{\Delta}) = \frac{d\tilde{P}/d\tilde{A}}{d\tilde{\Delta}/d\tilde{A}} = \frac{3\tilde{A}^2 - M_1(\frac{d\lambda}{d\tilde{A}}\tilde{A}^2 + 2\lambda\tilde{A})}{2\tilde{A} - \frac{4}{3}\sqrt{m^2-1}(\frac{d\lambda}{d\tilde{A}} + \lambda)}. \tag{4.2.11}$$

From equation (4.2.9),

$$\frac{d\tilde{\Delta}}{d\tilde{A}} = 2\tilde{A} - \frac{4}{3}\sqrt{m^2-1}(\frac{d\lambda}{d\tilde{A}}\tilde{A} + \lambda), \tag{4.2.12}$$

and from equation (4.2.10),

$$\frac{d\lambda}{d\tilde{A}} = -\frac{\lambda(6\tilde{A}M_2 + 8\lambda M_3)}{\tilde{A}(3\tilde{A}M_2 + 16\lambda M_3)}. \tag{4.2.13}$$

Substituting equations (4.2.11) and (4.2.12) into equation (4.2.13) gives

$$\tilde{P}'(\tilde{\Delta})=\frac{\tilde{A}^2(3\tilde{A}-2\lambda M_1)(3\tilde{A}M_2+16\lambda M_3)+\tilde{A}^2M_1\lambda(6\tilde{A}M_2+8\lambda M_3)}{\tilde{A}(2\tilde{A}-\frac{4}{3}\lambda\sqrt{m^2-1})(3\tilde{A}M_2+16\lambda M_3)+\frac{4}{3}\lambda^2\sqrt{m^2-1}(6\tilde{A}M_2+8\lambda M_3)}. \quad (4.2.14)$$

Similarly, the higher derivatives are obtained from equation (4.2.14) by

$$\tilde{P}''(\tilde{\Delta})=\frac{d\tilde{P}'(\tilde{\Delta})}{d\tilde{\Delta}}=(\frac{d^2\tilde{P}}{d\tilde{A}^2}-\tilde{P}'(\tilde{\Delta})\frac{d^2\tilde{\Delta}}{d\tilde{A}^2})(\frac{d\tilde{\Delta}}{d\tilde{A}})^2, \quad (4.2.15)$$

and

$$\begin{aligned}\tilde{P}'''(\tilde{\Delta})=\frac{d\tilde{P}''(\tilde{\Delta})}{d\tilde{\Delta}}&=(\frac{d^3\tilde{P}}{d\tilde{A}^3}\frac{d\tilde{A}}{d\tilde{\Delta}}-\tilde{P}''(\tilde{\Delta})\frac{d^2\tilde{\Delta}}{d\tilde{A}^2}-\tilde{P}'(\tilde{\Delta})\frac{d^3\tilde{\Delta}}{d\tilde{A}^3}\frac{d\tilde{A}}{d\tilde{\Delta}})(\frac{d\tilde{\Delta}}{d\tilde{A}})^2\\&+2(\frac{d^2\tilde{P}}{d\tilde{A}^2}-\tilde{P}'(\tilde{\Delta})\frac{d^2\tilde{\Delta}}{d\tilde{A}^2})\frac{d^2\tilde{\Delta}}{d\tilde{A}^2}.\end{aligned} \quad (4.2.16)$$

From equation (4.2.8),

$$\frac{d^2\tilde{P}}{d\tilde{A}^2}=6\tilde{A}-M_1(\frac{d^2\lambda}{d\tilde{A}^2}\tilde{A}^2+4\tilde{A}\frac{d\lambda}{d\tilde{A}}+2\lambda) \quad (4.2.17)$$

$$\frac{d^3\tilde{P}}{d\tilde{A}^3}=6-M_1(\frac{d^3\lambda}{d\tilde{A}^3}\tilde{A}^2+6\tilde{A}\frac{d^2\lambda}{d\tilde{A}^2}+6\frac{d\lambda}{d\tilde{A}}) \quad (4.2.18)$$

From equation (4.2.9),

$$\frac{d^2\tilde{\Delta}}{d\tilde{A}^2}=2-\frac{4}{3}\sqrt{m^2-1}(2\frac{d\lambda}{d\tilde{A}}+\tilde{A}\frac{d^2\lambda}{d\tilde{A}^2}), \quad (4.2.19)$$

$$\frac{d^3\tilde{\Delta}}{d\tilde{A}^3}=-\frac{4}{3}\sqrt{m^2-1}(3\frac{d^2\lambda}{d\tilde{A}^2}+\tilde{A}\frac{d^3\lambda}{d\tilde{A}^3}). \quad (4.2.20)$$

From equation (4.2.10),

$$\frac{d^2\lambda}{d\tilde{A}^2}=-\frac{\lambda M_2+2\tilde{A}M_2\frac{d\lambda}{d\tilde{A}}+\frac{16}{3}\lambda M_3\frac{d\lambda}{d\tilde{A}}+\frac{8}{3}\tilde{A}M_3(\frac{d\lambda}{d\tilde{A}})^2}{\frac{1}{2}\tilde{A}^2M_2+\frac{8}{3}\tilde{A}\lambda M_3}, \quad (4.2.21)$$

and

$$\frac{d^3\lambda}{d\tilde{A}^3}=-\frac{3\frac{d\lambda}{d\tilde{A}}M_2+3\tilde{A}M_2\frac{d^2\lambda}{d\tilde{A}^2}+8M_3((\frac{d\lambda}{d\tilde{A}})^2+\lambda\frac{d^2\lambda}{d\tilde{A}^2})+8AM_3\frac{d\lambda}{d\tilde{A}}\frac{d^2\lambda}{d\tilde{A}^2}}{\frac{1}{2}\tilde{A}^2M_2+\frac{8}{3}\tilde{A}\lambda M_3}. \quad (4.2.22)$$

Substituting equations (4.2.17), (4.2.18), (4.2.19), (4.2.20), (4.2.21) and (4.2.22) into equations (4.2.15) and (4.2.16), the second and third derivatives can be expressed in terms of A and λ.

The definition of the normalized load, in the Maugis contact theory in (2.3.13) – (2.3.15), the load is $P=\pi R\varpi\tilde{P}$. From the boundary conditions (4.1.2) and (4.2.4), it is obvious that

$$\beta=\frac{\tilde{P}'(\tilde{\Delta})}{\pi R\varpi EI/L^3}, \quad \beta_1=\frac{\tilde{P}''(\tilde{\Delta})}{2\pi R\varpi EI/L^3}, \quad \beta_2=-\frac{\tilde{P}'''(\tilde{\Delta})}{6\pi R\varpi EI/L^3}. \quad (4.2.23)$$

The factor λ in Maugis model is used to characterize the work of adhesion between two materials in contact. In the limit of infinite λ, the Maugis model will approach that of the JKRS theory. When λ goes to zero, the equations reduce to the DMT model.

At $\lambda=0$, from (4.2.1) and (4.2.2), $\tilde{P}=\tilde{A}^3, \Delta=\tilde{A}^2$, thus, $\tilde{P}(\tilde{\Delta})=\tilde{\Delta}^{3/2}$. The derivatives are reduced to

$$\tilde{P}'(\tilde{\Delta})=\frac{3}{2}\tilde{\Delta}^{\frac{1}{2}}, \quad \tilde{P}''(\tilde{\Delta})=\frac{3}{4}\tilde{\Delta}^{-\frac{1}{2}}, \quad \tilde{P}'''(\tilde{\Delta})=-\frac{3}{8}\tilde{\Delta}^{-\frac{3}{2}}. \quad (4.2.24)$$

Substitution of (4.2.24) into boundary condition (4.2.4) gives the contact force

$$\tilde{F}=\tilde{P}(\tilde{\Delta})-\frac{3}{2}\tilde{\Delta}^{\frac{1}{2}}\tilde{w}(L,t)+\frac{3}{8}\tilde{\Delta}^{-\frac{1}{2}}\tilde{w}^2(L,t)+\frac{1}{16}\tilde{\Delta}^{-\frac{3}{2}}\tilde{w}^3(L,t)+O(\tilde{w}^4(L,t)).$$

Clearly, it is identical to the Hertz contact boundary condition. This simplification shows that, at $\lambda=0$, Maugis theory becomes Hertzian. Maugis theory is comprehensive in that it encompasses a continuous variation of the adhesion parameter λ. In the limit of m going to $1 + \varepsilon$, the Maugis theory will approach the JKRS theory. Note that

$$\lim_{m\to 1+\varepsilon} \arctan\sqrt{m^2-1} = \sqrt{2\varepsilon}(1-\frac{5}{12}\varepsilon).$$

From equations (4.2.5) to (4.2.7), the appropriate limits for M_1, M_2 and M_3 are

$$\lim_{m\to 1+\varepsilon} M_1 = 2\sqrt{2}\varepsilon^{\frac{1}{2}} + \frac{19}{12}\sqrt{2}\varepsilon^{\frac{3}{2}}, \tag{4.2.25}$$

$$\lim_{m\to 1+\varepsilon} M_2 = \frac{29}{12}\sqrt{2}\varepsilon^{\frac{3}{2}}, \tag{4.2.26}$$

$$\lim_{m\to 1+\varepsilon} M_3 = \varepsilon. \tag{4.2.27}$$

Thus, from equation (4.2.10),

$$\lim_{m\to 1+\varepsilon} \lambda = \frac{\sqrt{3}}{2\sqrt{\varepsilon}}\tilde{A}^{-\frac{1}{2}}. \tag{4.2.28}$$

Hence,

$$\lim_{m\to 1+\varepsilon} \frac{d\lambda}{d\tilde{A}} = -\frac{\sqrt{3}}{4\sqrt{\varepsilon}}\tilde{A}^{-\frac{3}{2}}. \tag{4.2.29}$$

Thus,

$$\lim_{m\to 1+\varepsilon} \tilde{\Delta} = \tilde{A}^2 - \frac{2}{3}\sqrt{6}\tilde{A}^{\frac{1}{2}}, \tag{4.2.30}$$

and

$$\lim_{m\to 1+\varepsilon} \tilde{P} = \tilde{A}^3 - \sqrt{6}\tilde{A}^{\frac{3}{2}}. \tag{4.2.31}$$

Equations (4.2.30) and (4.2.31) are exactly the normalized form of JKRS equations (2.3.7) and (2.3.8). From these, the derivatives can be derived. The first derivative is

$$\lim_{m\to 1+\varepsilon} \tilde{P}'(\tilde{\Delta}) = \lim_{m\to 1+\varepsilon} \frac{d\tilde{P}/d\tilde{A}}{d\tilde{\Delta}/d\tilde{A}} = \lim_{m\to 1+\varepsilon} \frac{3\tilde{A}^2 - \tilde{A}M_1(2\lambda + \tilde{A}\frac{d\lambda}{d\tilde{A}})}{2\tilde{A} - \frac{4}{3}\sqrt{m^2-1}(\lambda - \tilde{A}\frac{d\lambda}{d\tilde{A}})} = \frac{3\tilde{A}^2 - \frac{3}{2}\sqrt{6}\tilde{A}^{\frac{1}{2}}}{2\tilde{A} - \frac{\sqrt{6}}{3}\tilde{A}^{-\frac{1}{2}}}$$

All other derivatives can be deduced henceforth.

4.3 Characteristic Equation and Numerical Results

The contact forces in the boundary conditions are nonlinear. This fact brings tremendous difficulty for solving this problem. When a closed-form solution is impossible, nonlinear perturbation analysis methods may be applied. Here the method of harmonic balance is used.

In the harmonic balance method, the solution is assumed to be a combination of different frequencies while these frequencies are amplitude dependent. Consider an equation having the form $\ddot{u} + f(u) = 0$. In general, f is a nonlinear function. The harmonic balance method expresses the periodic solution of the equation in the form $u(t) = \sum_{m=0}^{M} a_m \cos(m\omega t + m\beta_0)$, m is integer. By substituting this formal solution into the governing equation and equating the coefficients of each of the lowest $M + 1$ harmonics to zero, there will be a system of $M + 1$ algebraic equations relating ω and the a_m. Usually these equations are solved for a_0, a_2, a_3, …, a_m and ω in terms of a_1. Terms of higher orders are dropped in the process.

The accuracy of the resulting periodic solution depends on the value of a_1 and the number of harmonics in the assumed solution. Following this process, the characteristic equation of this nonlinear system will be found, from which the allowable wave numbers can be calculated. As stated by Nayfeh, to obtain a consistent solution, one needs either to know a great deal about the solution a priori or to carry enough terms in the solution and check the order of the coefficients of all the neglected harmonics. Otherwise one might get an inaccurate approximation [2].

There is no limitation as to how many terms can be used in the linear combination of harmonics. However, the more terms that are used, the more complicated the analysis. Most of the time it is not necessary to carry all the higher order terms [2]. Generally, a three-term expansion is sufficient [25]. To obtain an accurate approximation, it is necessary to check the order of the coefficients of all the neglected harmonics. Caution must be taken to make sure all the terms dropped in the development are really high order terms.

First, the time and spatial dependencies are assumed to be separable. Then the time dependence is expanded in a linear combination of harmonics as

$$\tilde{w}(x,t)=\tilde{W}(x)\sum_{n=0}^{N}a_n\cos(n\omega t), \tag{4.3.1}$$

where $\tilde{W}(x)=\dfrac{W(x)}{L}$. The mode shape $W(x)$ is the general solution in (3.3.2),

$$W(x)=D[\sin kx-\sinh kx-D_0(\cos kx-\cosh kx)], \tag{4.3.2}$$

where $D_0=\dfrac{\sin kL+\sinh kL}{\cos kL+\cosh kL}$. The arbitrary amplitude D is determined by setting the amplitude of the beam at $x = L$ to unity, i.e., $W(L) = 1$. Thus,

$$D=\frac{1}{\sin kL-\sinh kL-D_0(\cos kL-\cosh kL)}\ . \tag{4.3.3}$$

Substituting D_0 into (4.3.3), D can be simplified to

$$D=\frac{\cos kL+\cosh kL}{2(\sin kL\cosh kL-\cos kL\sinh kL)}.$$

With three harmonic terms, the proposed solution (4.3.1) is given by

$$\tilde{w}(x,t)=\tilde{W}(x)(a_0+a_1\cos(\omega t)+a_2\cos(2\omega t))\,. \tag{4.3.4}$$

Substituting this into the boundary condition (4.1.2) gives

$$\begin{aligned}&\tilde{W}'''(L)(a_0+a_1\cos(\omega t)+a_2\cos(2\omega t))-\beta\tilde{W}(L)(a_0+a_1\cos(\omega t)+a_2\cos(2\omega t))\\&\quad+\beta_1\tilde{W}^2(L)(a_0+a_1\cos(\omega t)+a_2\cos(2\omega t))^2\\&\quad+\beta_2\tilde{W}^3(L)(a_0+a_1\cos(\omega t)+a_2\cos(2\omega t))^3=0.\end{aligned}$$

Dropping all the higher order terms (higher than $O(a_1^{\,3})$) gives

$$\begin{aligned}&\tilde{W}'''(L)(a_0+a_1\cos(\omega t)+a_2\cos(2\omega t))-\beta\tilde{W}(L)(a_0+a_1\cos(\omega t)+a_2\cos(2\omega t))\\&\quad+\beta_1\tilde{W}^2(L)(a_1^2\cos^2(\omega t)+2a_0a_1\cos(\omega t)+2a_1a_2\cos(\omega t)\cos(2\omega t))\\&\quad+\beta_2\tilde{W}^3(L)(a_1^3\cos^3(\omega t))=0.\end{aligned} \tag{4.3.5}$$

Using the trigonometric identities

$$\cos^2(\omega t)=\frac{1}{2}(1+\cos(2\omega t)),\quad \cos^3(\omega t)=\frac{1}{4}\cos(3\omega t)+\frac{3}{4}\cos(\omega t),$$

$$\cos(\omega t)\cos(2\omega t)=\frac{1}{2}(\cos(\omega t)+\cos(3\omega t)),$$

equation (4.3.5) is reduced to

$$\begin{aligned}&(\tilde{W}'''(L)-\beta\tilde{W}(L))a_0+\frac{1}{2}\beta_1a_1^2\\&\quad+(((\tilde{W}'''(L)-\beta\tilde{W}(L))a_1)+\beta_1(2a_0a_1+a_1a_2)+\frac{3}{4}\beta_2a_1^3)\cos(\omega t)\\&\quad+((\tilde{W}'''(L)-\beta\tilde{W}(L))a_2+\frac{1}{2}\beta_1a_1^2)\cos(2\omega t)=0.\end{aligned} \tag{4.3.6}$$

Finally, equating all the coefficients of the different harmonic terms in (4.3.6) to zero yields the following three equations

$$(\tilde{W}'''(L)-\beta\tilde{W}(L))a_0+\beta_1\tilde{W}^2(L)(\frac{1}{2}a_1^2)=0, \tag{4.3.7}$$

$$(\tilde{W}'''(L)-\beta\tilde{W}(L))+\beta_1\tilde{W}^2(L)(2a_0+a_2)+\beta_2\tilde{W}^3(L)(\frac{3}{4}a_1^2)=0, \tag{4.3.8}$$

$$(\tilde{W}'''(L)-\beta\tilde{W}(L))a_2+\beta_1\tilde{W}^2(L)(\frac{1}{2}a_1^2)=0. \tag{4.3.9}$$

Equations (4.3.7) and (4.3.9) may be solved for a_0 and a_2 as function of a_1. The expressions are

$$a_0=a_2=-\frac{1}{2}\frac{\beta_1\tilde{W}^2(L)}{\tilde{W}'''(L)-\beta\tilde{W}(L)}a_1^2. \tag{4.3.10}$$

Equation (4.3.8) is the characteristic equation of the nonlinear natural frequencies as a function of amplitude a_1. Substituting a_0 and a_2 as in (4.3.10) into this equation will result in the first order nonlinear correction to the characteristic equation. The result is

$$(\tilde{W}'''(L)-\beta\tilde{W}(L))+\beta_1\tilde{W}^2(L)\left(-\frac{3}{2}\frac{\beta_1\tilde{W}^2(L)}{\tilde{W}'''(L)-\beta\tilde{W}(L)}a_1^2\right)+\beta_2\tilde{W}^3(L)(\frac{3}{4}a_1^2)=0,$$

or,

$$\begin{aligned}(\tilde{W}'''(L)-\beta\tilde{W}(L))^2&=(\frac{3}{2}\beta_1^2\tilde{W}^4(L)-\frac{3}{4}(\tilde{W}'''(L)-\beta\tilde{W}(L))\beta_2\tilde{W}^3(L))a_1^2\\&=\frac{3}{2}\beta_1^2\tilde{W}^4(L)a_1^2\left(1-\frac{1}{2}\frac{\beta_2}{\beta_1^2}\left(\frac{\tilde{W}'''(L)}{\tilde{W}(L)}-\beta\right)\right).\end{aligned} \tag{4.3.11}$$

For the Hertzian contact force, recall that the nonlinear spring constants β_1 and β_2 are related to β as in (4.1.4), equation (4.3.11) is written in terms of β and Δ as

$$(\tilde{W}'''(L)-\beta\tilde{W}(L))^2=\frac{3}{32}\frac{\beta^2}{\tilde{\Delta}^2}\tilde{W}^4(L)a_1^2\left(1-\frac{1}{3\beta}\left(\frac{\tilde{W}'''(L)}{\tilde{W}(L)}-\beta\right)\right) \tag{4.3.12}$$

Further, equation (4.3.12) can be written as

$$\left(\frac{\tilde{W}'''(L)}{\beta\tilde{W}(L)}-1\right)^2=\frac{1}{32}\tilde{W}^2(L)\left(\frac{a_1}{\tilde{\Delta}}\right)^2\left(4-\frac{\tilde{W}'''(L)}{\beta\tilde{W}(L)}\right) \tag{4.3.13}$$

It can be seen in equation (4.2.13) that, if $4-\frac{\tilde{W}'''(L)}{\beta\tilde{W}(L)}<0,$ there will be no real roots of this equation. A closer examination of the boundary condition reveals that this situation cannot arise. From the boundary condition (4.1.2), it follows that

$$\begin{aligned}\tilde{w}'''(L,t)&=\beta\tilde{w}(L,t)-\beta_1\tilde{w}^2(L,t)-\beta_2\tilde{w}^3(L,t)\\&=\beta\tilde{w}(L,t)-\frac{1}{4}\frac{\beta}{\tilde{\Delta}}\tilde{w}^2(L,t)-\frac{1}{24}\frac{\beta}{\tilde{\Delta}^2}\tilde{w}^3(L,t)\\&=\beta\tilde{w}(L,t)(1-\frac{1}{4}\frac{\tilde{w}(L,t)}{\tilde{\Delta}}-\frac{1}{24}\frac{\tilde{w}^2(L,t)}{\tilde{\Delta}^2}).\end{aligned}$$

Thus,

$$\frac{\tilde{w}'''(L,t)}{\beta\tilde{w}(L,t)}=1-\frac{1}{4}\frac{\tilde{w}(L,t)}{\tilde{\Delta}}-\frac{1}{24}\left(\frac{\tilde{w}(L,t)}{\tilde{\Delta}}\right)^2. \tag{4.3.14}$$

Since $0\le w(L,t)\le\Delta$, equation (4.3.14) shows that $\frac{\tilde{w}'''(L,t)}{\beta\tilde{w}(L,t)}\le 1$. Hence,

$$\frac{\tilde{W}'''(L)}{\beta\tilde{W}(L)}=\frac{\tilde{w}'''(L,t)}{\beta\tilde{w}(L,t)}\le 1. \tag{4.3.15}$$

Equation (4.3.13) is quadratic. For every value of a_1, equation (4.3.13) will give a pair of real roots (denoted by $\gamma_{\rm nlin}$) within the vicinity of the corresponding linear roots (denoted by $\gamma_{\rm lin}$) given by the linearized characteristic equation

$$\tilde{W}'''(L)=\beta\tilde{W}(L). \tag{4.3.16}$$

The linear result comes from a special case of (4.3.13) at $a_1=0$.

Equation (4.3.13) can be written in the form

$$\left(\frac{\tilde{W}'''(L)}{\beta\tilde{W}(L)}-1\right)\pm\tilde{W}(L)\frac{a_1}{\tilde{\Delta}}\sqrt{\frac{1}{32}\left(4-\frac{\tilde{W}'''(L)}{\beta\tilde{W}(L)}\right)}=0. \tag{4.3.17}$$

It is found that in (4.3.17), the equation with a plus sign always gives the lower roots. Thus, all the ensuing numerical results are based on the equation

$$\left(\frac{\tilde{W}'''(L)}{\beta\tilde{W}(L)}-1\right)+\tilde{W}(L)\frac{a_1}{\Delta}\sqrt{\frac{1}{32}\left(4-\frac{\tilde{W}'''(L)}{\beta\tilde{W}(L)}\right)}=0. \tag{4.3.18}$$

An example is shown in Figure (4.1). For $\beta = 125$, $a_1 = 0.01\Delta$, the two roots of equation (4.3.13) lie on both sides of the linear roots γ_{lin}, i.e., one is higher and the other is lower than γ_{lin}.

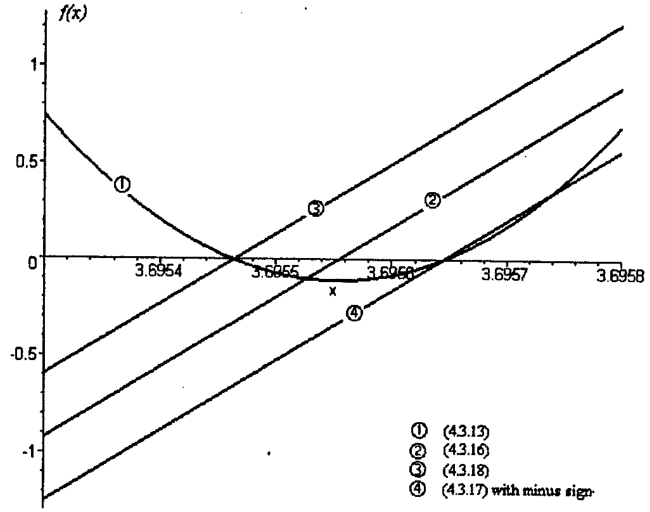

Figure 4.1. The first two roots of characteristic equation (4.3.13) and the first root of the linear characteristic equation (4.3.16). It is shown here that the pair of roots of (4.3.13) lie on both sides of the root of (4.3.16).

Since the form of the force-displacement curve is concave, the beam vibrations are expected to act according to nonlinear softening. Thus, from the physical perspective, the

---

one root that is lower than γ_{lin} is physically appropriate.

Equations (4.3.11), (4.3.12), (4.3.13), (4.3.16), (4.3.17) and (4.3.18) are equations of wave number $\gamma = kL$. To show this explicitly, write $\varphi(\gamma) = \tilde{W}'''(L)$. Since $\tilde{W}(L) = 1$, then (4.3.18) can be written as

$$\left(\frac{\varphi(\gamma)}{\beta}-1\right)+\left(\frac{a_1}{\Delta}\right)\sqrt{\frac{1}{32}\left(4-\frac{\varphi(\gamma)}{\beta}\right)}=0. \tag{4.3.19}$$

where $\varphi(\gamma)$ is defined by

$$\varphi(\gamma) = -\gamma^3\frac{1+\cos\gamma\cosh\gamma}{\sin\gamma\cosh\gamma-\cos\gamma\sinh\gamma}.$$

Thus, if written explicitly in terms of γ, (4.3.19) becomes

$$\left(-\frac{\gamma^3(1+\cos\gamma\cosh\gamma)}{\beta(\sin\gamma\cosh\gamma-\cos\gamma\sinh\gamma)}-1\right)+\left(\frac{a_1}{\Delta}\right)\sqrt{\frac{1}{32}\left(4+\frac{\gamma^3(1+\cos\gamma\cosh\gamma)}{\beta(\sin\gamma\cosh\gamma-\cos\gamma\sinh\gamma)}\right)}=0.$$

In the characteristic equations (4.3.19), the left side is the characteristic equation for the linear case, which defines the dimensionless wave number γ in terms of the linear spring constant β. On the right side there is the excitation amplitude a_1. The wave numbers γ solved in these equations are a function of the excitation amplitude a_1.

When a_1 is zero, (4.3.18) reduces to the linear characteristic equation (4.3.16). With the increase of a_1, nonlinearity exerts influence on the resonance frequency of the vibration system. The maximum a_1 allowed is determined by the observation that the Taylor's series expansion of the contact boundary condition holds true only if $w(L,t) < \Delta$ as shown in (3.4.4). Thus a_1 must satisfy $a_1 < \Delta$.

The vibration amplitude a_1 and the resonance frequencies of the beam are closely related. The characteristic equation is solved numerically and the amplitude-frequency relationship is revealed.

4.4 Numerical Results

Equation (4.3.19) is solved numerically. In the computations, the roots of these equations are found for different amplitude a_1. In the following calculations, the system parameters applied are:

For the AFM cantilever, (all units are SI), Young's modulus $E_t = 1.69\text{x}10^{11}\text{N/m}^2$, length $L = 233$ μm, width $W = 51$μm, thickness $t = 15$ μm, mass density $\rho = 2330\text{kg/m}^3$, contact radius $R = 50\text{x}10^{-9}$m, Poisson's ratio $\nu_t = 0.3$, static deflection at the tip end $y(L) = L/100 = 2.33$μm.

It is also assumed that Poisson's ratio of the sample surface ν_s is the same as that of the sensor tip ν_t. Young's modulus of the sample surface E_s is related to the Young's modulus of the cantilever E_t, as $E_s = \eta E_t\,(\eta > 0)$. The effective Young's modulus of the contact is defined by (2.3.1), such that

$$E^* = \frac{\eta E_t}{(\eta+1)(1-\nu_t^2)}. \tag{4.4.1}$$

The Hertzian coefficient K_0 as defined in (2.3.3) is then

$$K_0 = \frac{4}{3}E^*\sqrt{R} = \frac{4\eta E_t\sqrt{R}}{3(\eta+1)(1-\nu_t^2)}. \tag{4.4.2}$$

Static Hertz deformation, defined as $\Delta = z_0 - y(L)$, is determined from (3.2.3)

$$\Delta = \left(\frac{3E_tI}{K_0L^3}y(L)\right)^{2/3} = \left(\frac{9I(\eta+1)(1-\nu_t^2)}{4\eta\sqrt{R}L^3}y(L)\right)^{2/3}. \tag{4.4.3}$$

The normalized effective spring constant β, as defined in (4.1.3), is

$$\beta = \frac{\kappa}{E_tI/L^3} = \frac{\frac{3}{2}K_0\Delta^{\frac{1}{2}}}{E_tI/L^3} = L^2\left(\frac{3\sqrt{2Ry(L)}\eta}{I(\eta+1)(1-\nu_t^2)}\right)^{2/3}. \tag{4.4.4}$$

On the condition that L, R, $y(L)$ and ν_t remain constant, β will be decided by η, which is the ratio of the Young's moduli of the AFM cantilever and the sample surface. Next, define

$$\beta_c = L^2\left(\frac{3\sqrt{2Ry(L)}}{I(1-\nu_t^2)}\right)^{2/3}. \tag{4.4.5}$$

This β_c will be constant for a given set of cantilever and contact parameters. Then β can be written in terms of the moduli ratio η as

$$\beta = \beta_c\left(\frac{\eta}{\eta+1}\right)^{2/3}. \tag{4.4.6}$$

For example, at $\eta = 1$, i.e., the Young's moduli of the sample surface and the cantilever are the same, then

$E^* = 9.286\text{x}10^{10}\,\text{N/m}^2$, $K_0 = 2.7685\text{x}10^7$ N/m, $\Delta = 1.3278\text{x}10^{-9}$m, $\beta = 7896.27$.

The other two effective spring constants β_1 and β_2 can also be calculated.

The first five roots $(\gamma_n)_0$ of equation (4.3.19) when $a_1 = 0$, i.e., the linearized case, are 3.9230, 7.0459, 10.1396, 13.1836, 16.1449. These are the wave numbers of the linear system. When a_1 is larger than zero, nonlinearity is present and the wave numbers solved from equation (4.3.19) will change accordingly. In the calculation, a_1 is increased from 0, the linearized case, to 90% of Δ, and the first five roots of (4.3.19) are found.

Define δ_n as the ratio of frequency shift of the nth mode, which is the ratio of nth root of the nonlinear characteristic equation (4.3.19), denoted as $(\gamma_{nl})_n$, over the nth root of the linear characteristic equation (4.3.16), denoted as $(\gamma_l)_n$. Write it as $\delta_n = \dfrac{(\gamma_{nl})_n}{(\gamma_l)_n}$.

In Figures (?), the x-axis is δ_n. The y-axis is the normalized amplitude $z = \dfrac{a_1}{\tilde{\Delta}}$, which varies from 0 to near 1, or from linear to high nonlinearity. Results are shown for different values of β. The numbers ①, ②, ③, ④ and ⑤ represent the frequency shift curves of the first five modes respectively. With the variation of β, it is expected that different frequency shift patterns will be shown.

In Figures (?), it is obvious that the first five resonance frequencies all show a trend of lowering when the vibration amplitude a_1 increases. What is more interesting is that the amounts of frequency shift of the modes are different, and these amounts are directly determined by β. For example, when $\beta = 2$, the first mode shifts the most; when $\beta = 100$, it is the second mode that shifts most. Also noticeable is the magnitude of the shifts: when $\beta = 2$, the maximal shift of the first mode is about 0.975; when $\beta = 100$, the maximal shift of the first mode is about 0.975, and the maximal shift of the second mode is approximately 0.965. The trend is, the higher the β, the less the maximal shift.

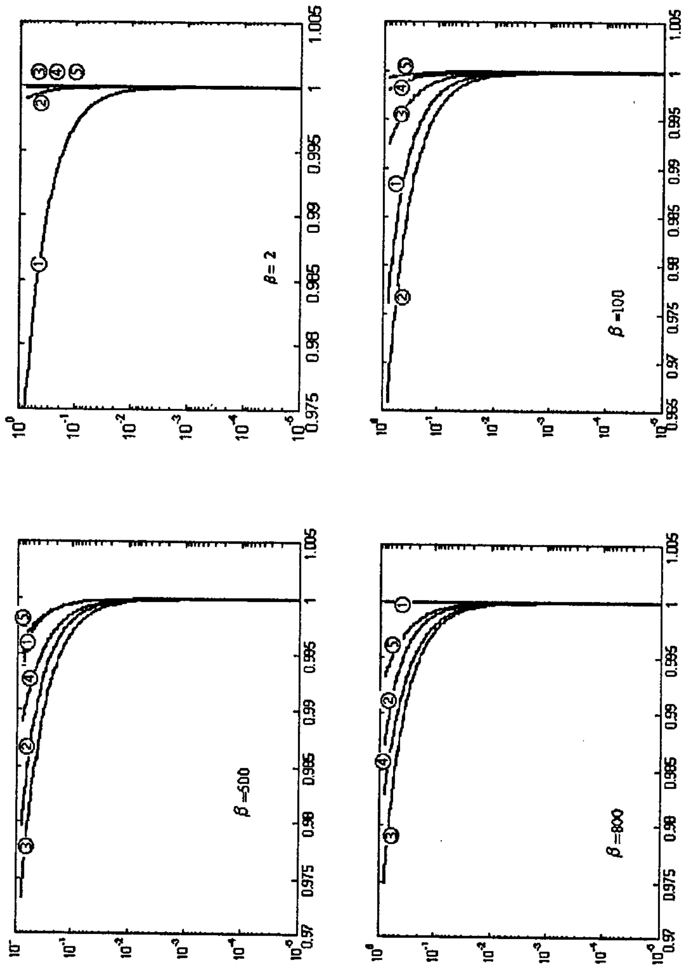

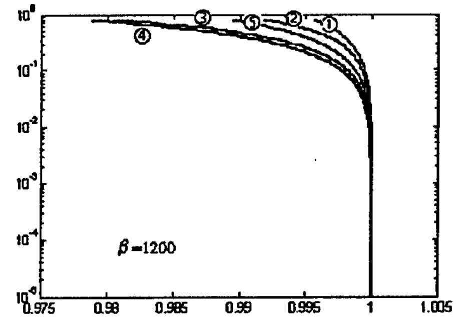
β=1200
①
②
③
④
⑤
10^0
10^{-1}
10^{-2}
10^{-3}
10^{-4}
10^{-5}
0.975
0.98
0.985
0.99
0.995
1
1.005

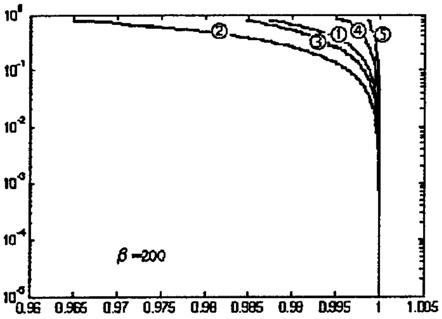
β=200
①
②
③
④
⑤
10^0
10^{-1}
10^{-2}
10^{-3}
10^{-4}
10^{-5}
0.96
0.965
0.97
0.975
0.98
0.985
0.99
0.995
1
1.005

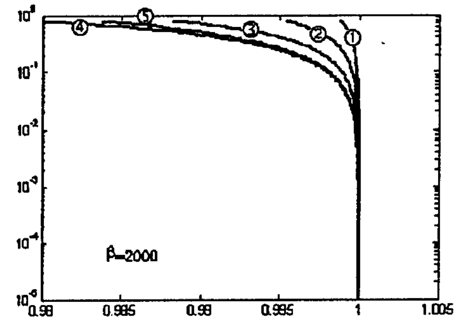
β=2000
①
②
③
④
⑤
10^0
10^{-1}
10^{-2}
10^{-3}
10^{-4}
10^{-5}
0.98
0.985
0.99
0.995
1
1.005

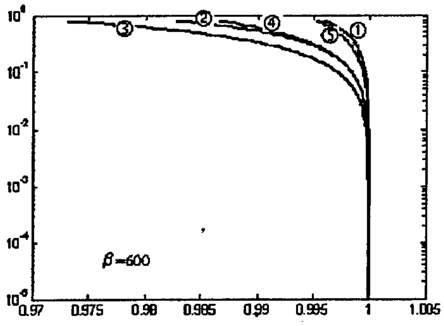
β=600
①
②
③
④
⑤
10^0
10^{-1}
10^{-2}
10^{-3}
10^{-4}
10^{-5}
0.97
0.975
0.98
0.985
0.99
0.995
1
1.005

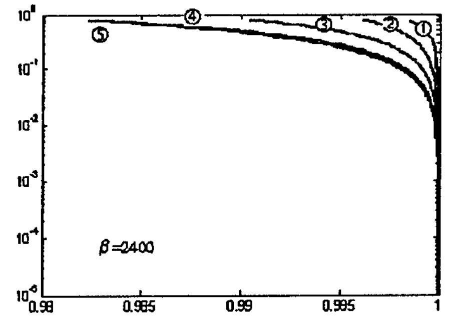
β=2400
①
②
③
④
⑤
10^0
10^{-1}
10^{-2}
10^{-3}
10^{-4}
10^{-5}
0.98
0.985
0.99
0.995
1

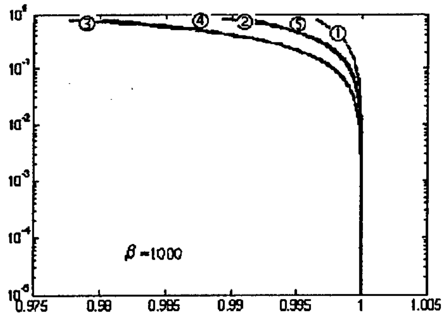
β=1000
①
②
③
④
⑤
10^0
10^{-1}
10^{-2}
10^{-3}
10^{-4}
10^{-5}
0.975
0.98
0.985
0.99
0.995
1
1.005

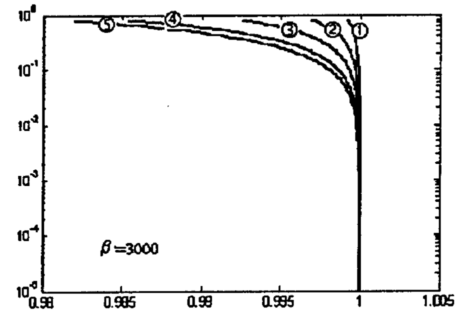
β=3000
①
②
③
④
⑤
10^0
10^{-1}
10^{-2}
10^{-3}
10^{-4}
10^{-5}
0.98
0.985
0.99
0.995
1
1.005

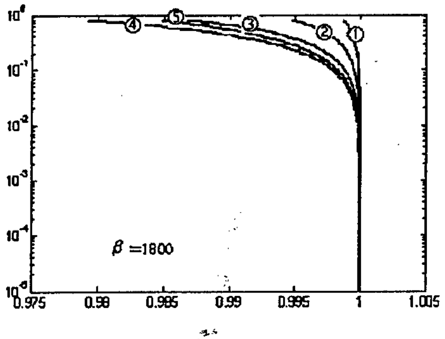
β=1800
①
②
③
④
⑤
10^0
10^{-1}
10^{-2}
10^{-3}
10^{-4}
10^{-5}
0.975
0.98
0.985
0.99
0.995
1
1.005

4.5 Modal Sensitivity

In the previous section, it has been shown that the resonance frequency shift is determined by the contact spring constant β if all other conditions remain the same. It is interesting to see how changes in β will influence the resonance frequency shift in the AFM. That is to say, which mode will change the most for a small variation in β. This relationship is the so-called modal sensitivity [30]. In the following, the flexural modal sensitivity of the nonlinear system is derived.

Define the modal sensitivity as ψ and define $z = \frac{a_1}{\Delta}$ as the normalized amplitude. Hence $\gamma = kL$ is the normalized wave number and it is treated as a function of amplitude z, such that $\gamma = \gamma(z)$. $\tilde{W}'''(L)$ is a function of γ, designated as $\varphi(\gamma)$, such that

$$\varphi(\gamma) = -\gamma^3 \frac{1+\cos\gamma\cosh\gamma}{\sin\gamma\cosh\gamma - \cos\gamma\sinh\gamma}. \tag{4.5.1}$$

Its derivative is

$$\varphi'(\gamma) = \gamma^3 - \gamma^2 \frac{1+\cos\gamma\cosh\gamma}{\sin\gamma\cosh\gamma - \cos\gamma\sinh\gamma}\left(3 - 2\gamma\frac{\sin\gamma\sinh\gamma}{\sin\gamma\cosh\gamma - \cos\gamma\sinh\gamma}\right) \tag{4.5.2}$$

The mode shape is normalized such that it may be written $\tilde{W}(L) = 1$. Therefore, the characteristic equation (4.3.19) becomes

$$\left(\frac{\varphi(\gamma)}{\beta} - 1\right) + \frac{z}{\sqrt{32}}\sqrt{4 - \frac{\varphi(\gamma)}{\beta}} = 0. \tag{4.5.3}$$

On the condition that β remains the same, equation (4.5.3) shows that the amplitude z plays a decisive role in the frequency shift. If $\psi_z = \frac{d\gamma}{dz}$ is defined as an indicator of the sensitivity of frequency shift to changes of amplitude, then, from (4.5.3), it gives

$$\psi_z = \frac{d\gamma}{dz} = \frac{-2\beta(4\beta - \varphi(\gamma))}{\varphi'(\gamma)[8\sqrt{2\beta(4\beta - \varphi(\gamma))} - z\beta]}. \tag{4.5.4}$$

When β is constant, equation (4.5.4) defines the relationship between z and γ that is illustrated in the previous section.

For the characteristic equation (4.5.3) of the nonlinear boundary condition system, if the amplitude z is fixed, the allowable wave number solved from this equation also possesses the same property as described in section (3.5) for the linear system. Figure (4.2) illustrates the dependency of γ on β at a fixed amplitude z ($z = 0.1$). The first five wave numbers are plotted. Figure (4.2) illustrates the wave number dependence on β when z is fixed at 0.1. Apparently this figure is very similar to Figure (3.3), which corresponds to the linear system. Both of them show γ increases along with β.

The modal sensitivity to changes in surface stiffness β is defined as $\psi_s = \frac{d\gamma}{d\beta}$. From equation (4.5.3),

$$\dot{\psi}_s = \frac{d\gamma}{d\beta} = \frac{8\sqrt{2\beta(4\beta - \varphi(\gamma))} - z(8\beta - \varphi(\gamma))}{\varphi'(\gamma)[8\sqrt{2\beta(4\beta - \varphi(\gamma))} - z\beta]} \tag{4.5.5}$$

When $z = 0$, equation (4.5.5) becomes $\psi_s = \frac{1}{\varphi'(\gamma)}$ which corresponds to the modal sensitivity of the linear system. Figure (4.3) is a plot of the relation of ψ_s and β, for $z =$ 0.1.

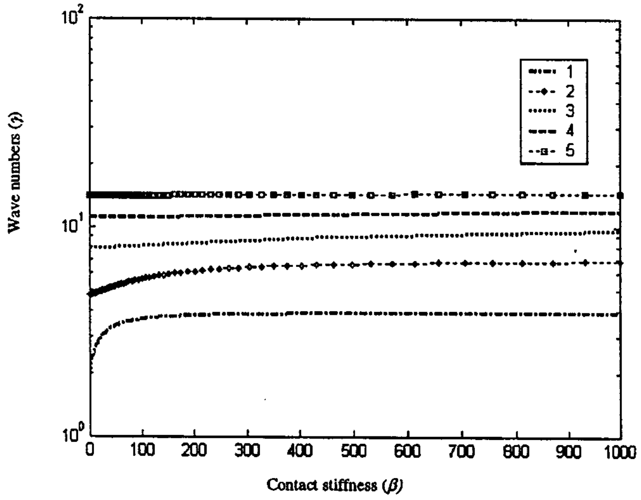

Figure 4.2. Changes of wave number γ for β ranging from 0 to 1000.

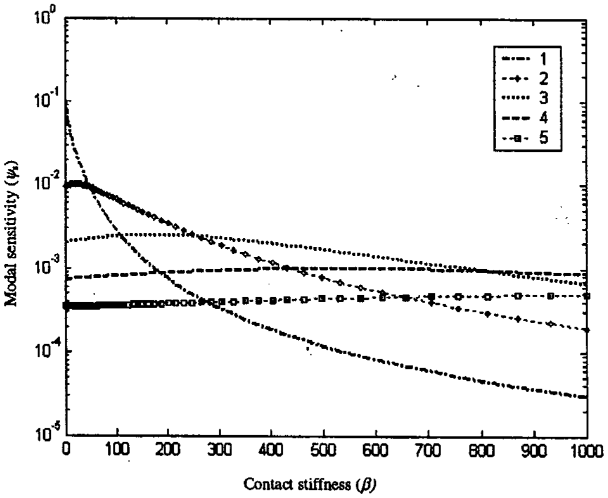

Figure 4.3. Sensitivity (ψ_k) to changes for β ranging from 0 to 1000.

Also, changes in z will not make significant differences to the change in the sensitivity on β, as is shown in Figure (4.4). In this figure, solid lines represent the modal sensitivity of the nonlinear system at $z = 0.1$, the dotted line with diamond markers represents the modal sensitivity of the linear system where $z = 0$.

It can be seen that z has a different influence on modal sensitivity of the different modes. When $z = 0.1$, the modal sensitivity of the first mode becomes less, whereas the modal sensitivities of the other modes become higher. However, there is no significant difference between these two sets of curves. The observations from Figure (4.4) can be safely applied to other nonlinear systems with z less than 0.1.

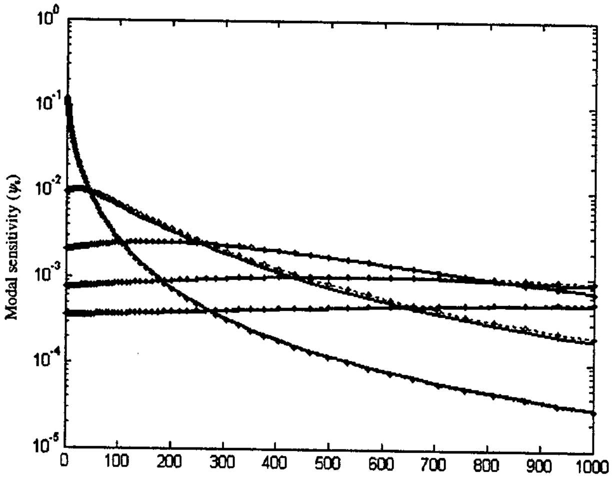

Figure 4.4. Influence of amplitude z on modal sensitivity.

Along with β changing from 0 to 1000, the sensitivity level of different modes changes respectively. When β is very small, the sequence is $\psi_1 > \psi_2 > \psi_3 > \psi_4 > \psi_5$. Then, ψ_1 sharply decreases as β increases. ψ_3, ψ_4 and ψ_5 are slowly increasing too. At one point around $\beta = 50$, ψ_1 equals to ψ_2. This result means, at this specific β, denoted as β_{12}, and at $z = 0.1$, the magnitudes of frequency shift of the first and second modes become equal. It is also interesting to notice that this β_{12} is the only β at which the curves of the first and second modes intersect.

The other intersection points β_{13}, β_{14}, β_{15}, β_{23}, β_{24}, β_{25}, β_{34}, β_{35}, β_{45} can also be found. (Note: In Figure (4.3), because of the limited range of β, β_{35}, β_{45} are not shown. They can be found in Figure (4.6), which encompasses a wider range of β.)

Figure (4.5) shows the same relation as Figure (4.2) except with a wider range of β from 0 to 10^4. It illustrates that when β becomes extremely large, the change in γ becomes smaller and smaller. After β is larger than 2000, no significant change in γ can be seen.

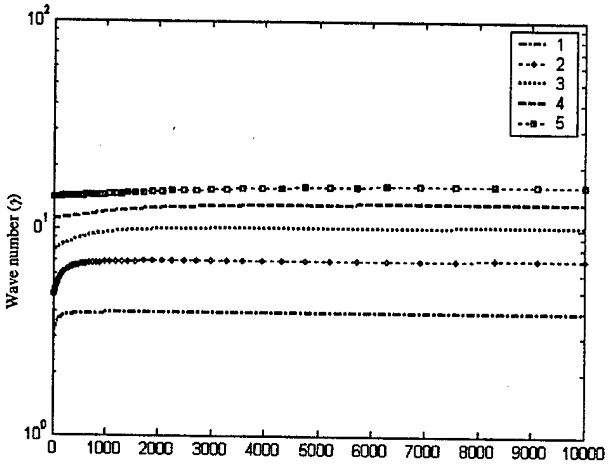

Figure 4.5. Changes of wave number γ with β ranging from 0 to 10000.

Figure (4.6) shows the sensitivity for a wider range of β up to 10^4. The intersection points β_{35}, β_{45} are visible in this figure. The sequence of all the ten intersection points, in ascending order, is β_{12}, β_{13}, β_{14}, β_{23}, β_{15}, β_{24}, β_{25}, β_{34}, β_{35}, β_{45}. After the intersection point β_{45}, the sequence of sensitivity level for the first five modes is completely reversed and remains so for larger values of β. Results for β greater than 10000 have also been obtained and they indicate a sensitivity pattern consistent with Figure (4.6).

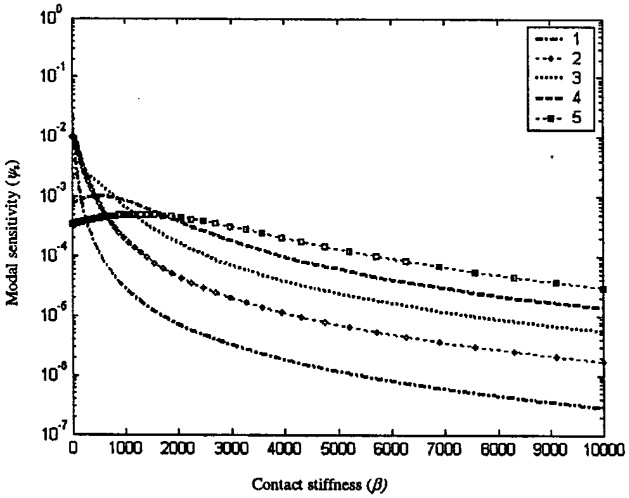

Figure 4.6. Sensitivity (ψ_s) to changes in spring stiffness (β) ranging from 0 to 10000.

For relatively small β, less than 500, the sensitivity levels of all the five modes are substantially higher, all above 10^{-4} level. After that, with only exception of mode 5, the sensitivity drops quickly below that level. In particular, the modal sensitivity of mode 1 decreases sharply to below 10^{-5} after β greater than 1000. In experiments, usually the first mode is measured. For small βs, the first mode has the highest level of sensitivity. Thus, a small change in β can be reflected in the measurement. The low level of sensitivity implies a very small frequency shift for large β, which in turn will pose enormous difficulties in experiments for accurate measurements of the frequency shift.

The resonance frequency shift of the nonlinear system is dependent both on the vibration amplitude and the effective spring stiffness of the sample surface. At different levels of β, the magnitudes of the shifts of different modes vary. It has also been shown that the modal sensitivity of the nonlinear system is essentially identical to that of the linear system.

5 Interaction Damping Effects

There is damping in the interaction of sensor tip and sample surface. This damping is primarily caused by adhesion effects and is the main source of damping in this vibration system [4]. In this Chapter, the influence of the interaction damping on the linear and nonlinear vibrations is studied.

5.1 Characteristic Equation

With this interaction damping, the contact boundary condition (4.1.1) is changed to

$$EIw'''(L,t) = \kappa w(L,t) - \kappa_1 w^2(L,t) - \kappa_2 w^3(L,t) + \sigma_{\text{int}} \dot{w}(L,t). \qquad (5.1.1)$$

where σ_{int} is the interaction damping coefficient. The normalized form of (5.1.1) is

$$\tilde{w}'''(L,t) = \beta \tilde{w}(L,t) - \beta_1 \tilde{w}^2(L,t) - \beta_2 \tilde{w}^3(L,t) + p\dot{\tilde{w}}(L,t), \qquad (5.1.2)$$

where $p = \dfrac{\sigma_{\text{int}} L}{\sqrt{EI\rho A}}$.

The normalized amplitude is defined as $z = \dfrac{a_1}{\tilde{\Delta}}$. The characteristic equation with respect to this boundary condition is

$$\varphi(\gamma) - \beta - jp\gamma^2 - \frac{\beta}{32} z^2 \left[\frac{2\beta}{\varphi(\gamma) - \beta} + \frac{\beta}{\varphi(\gamma) - \beta - jp\gamma^2} - 1 \right] = 0, \qquad (5.1.3)$$

in which $\varphi(\gamma) = -\gamma^3 \dfrac{1 + \cos\gamma \cosh\gamma}{\sin\gamma \cosh\gamma - \cos\gamma \sinh\gamma}$.

First, consider the linear system

$$\tilde{w}'''(L,t) = \beta \tilde{w}(L,t) + p\dot{\tilde{w}}(L,t). \qquad (5.1.4)$$

The characteristic equation becomes

$$\varphi(\gamma) - \beta - jp\gamma^2 = 0. \qquad (5.1.5)$$

From the characteristic equations (5.1.3) and (5.1.5) of the nonlinear and linear systems, allowable wave numbers γ can be determined. Generally, the wave numbers are complex. The meaning of these complex wave numbers can be understood by expanding the definition of the modes.

The displacement is expanded as a superposition of modes in the following form

$$w(x,t) = e^{j\omega t} \sum_{n=1}^{\infty} \left[B_{1n} e^{jk_n x} + B_{2n} e^{-jk_n x} + B_{3n} e^{k_n x} + B_{4n} e^{-k_n x} \right], \qquad (5.1.6)$$

where the B_ns are determined from the boundary condition [4]. In (5.1.6), each mode is composed of two harmonic components and two evanescent components. The first two terms are harmonic left and right traveling waves; the other two terms are left and right evanescent waves that decay exponentially in space. When k_n is complex, it can be written as $k_n = \alpha + j\beta$. Then, for the harmonic traveling waves, $e^{jk_n x} = e^{-\beta x} e^{j\alpha x}$ and $e^{-jk_n x} = e^{\beta x} e^{-j\alpha x}$, they are augmented by a spatial decay related to β. For the evanescent waves, $e^{k_n x} = e^{\alpha x} e^{j\beta x}$ and $e^{-k_n x} = e^{-\alpha x} e^{-j\beta x}$, they acquire a harmonic component related to α. Consequently, the real part of the complex wave number corresponds to the stiffness of the harmonic modes and thus the wave speed and frequency; the imaginary part governs the damping of the mode.

5.2 Linear System

The characteristic equation of the linear system is now examined in detail. In equation (5.1.5), besides the surface stiffness β, there is also interaction damping p. Equation (5.1.5) is solved for the wave numbers (both the real and imaginary parts) as a function of p for certain values of β.

In the Figures (5.1) and (5.2), β is 100, and p is varied from 1 to 100. For most AFM measurements, p is less than 100. It can be seen that the first and second mode curves intersects at p near 7, and the second mode curve decreases below the first curve. This implies that when p is large enough, the second resonance frequency will decrease until it is less than the first resonance frequency. At the same time, the real parts of the third, fourth and fifth modes all show similar trends in a reduction in frequency with increasing p. The real part of the first mode increases slowly as p increases.

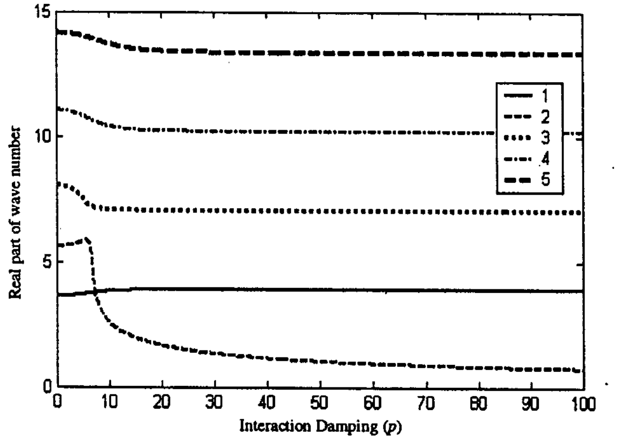

Figure 5.1. Real part of the first five modes (β = 100).

Figure (5.2) presents the variation of the imaginary part with respect to p. Concurrently with the decrease of the real part of the second mode, its imaginary part increases quickly. The imaginary parts of the other modes are well below that of the second mode. This result implies that the damping of the second mode is much higher

than the other modes, especially at p near 7, where the damping of the second mode reaches maximum.

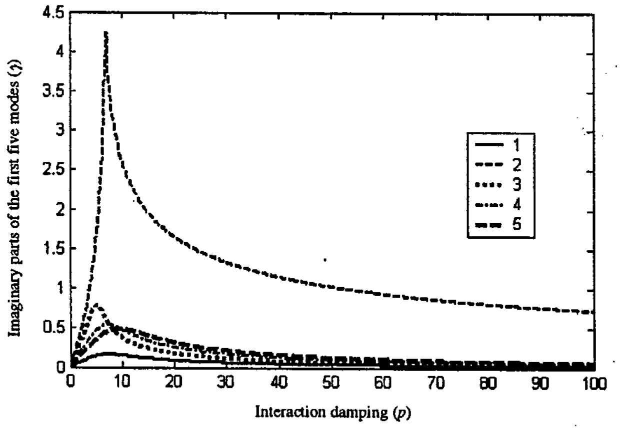

Figure 5.2. Imaginary parts of the first five modes at β = 100.

The real and imaginary parts of the second mode are plotted together in Figure (5.3). This result shows that the real part of the mode decays sharply at p near 7, while the imaginary part increases quickly until the two parts merge into one another. This reveals a very interesting property of the interaction damping: at a certain level of damping, in this case near 7, the real parts of the first and second modes become very close to each other while their dampings are wide apart. This result indicates that these two modes have very different sensitivity to interaction damping. When one mode is over-damped, the other modes are not. If the damping is sufficiently large, all the modes will be over-damped.

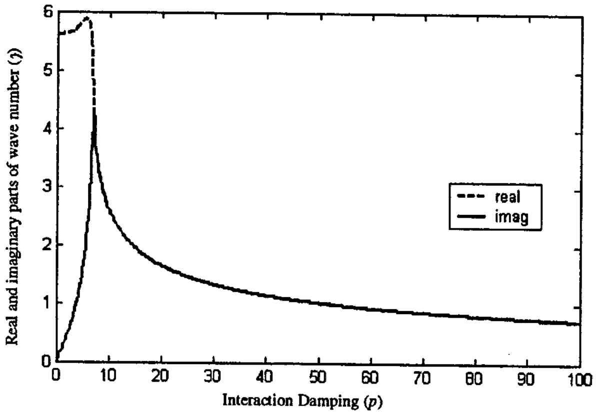

Figure 5.3. Merger of the real and imaginary part of the second mode.

If p is kept constant and β is slightly changed, as shown in Figures (5.4) and (5.5), the real part of the second mode becomes higher. This result is consistent with the results in Figure (4.2). Also, at higher β, the imaginary part starts lower and becomes higher after the maximal value. If only small p is concerned, then the increase in β will exert different influences on the real and imaginary parts of the second mode. Similar phenomena can be observed for other stiffness values. Figures (5.6) – (5.8) show the real parts of the first five modes when β is 200, 500 and 1400.

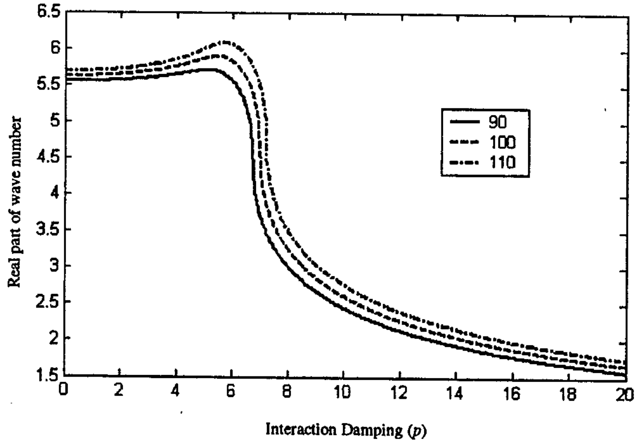

Figure 5.4. Changes of the real part of the second mode with respect to p and small variation in β.

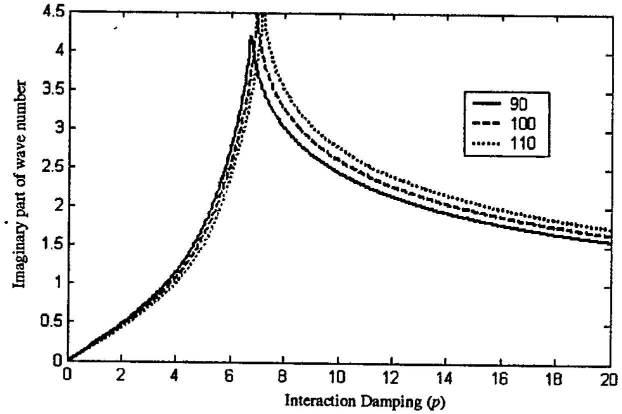

Figure 5.5. Changes of the imaginary part of the second mode with respect to p and small variation in β.

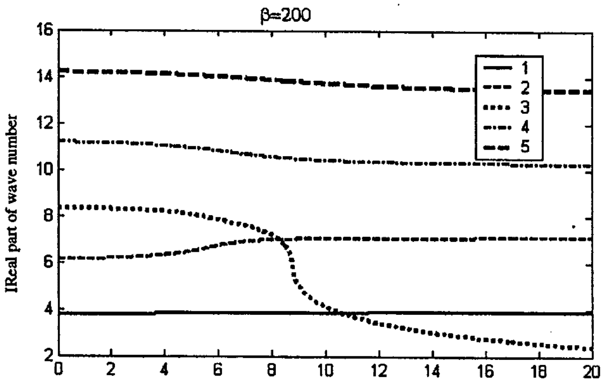

Figure 5.6. Decrease of the third mode at $\beta = 200$.

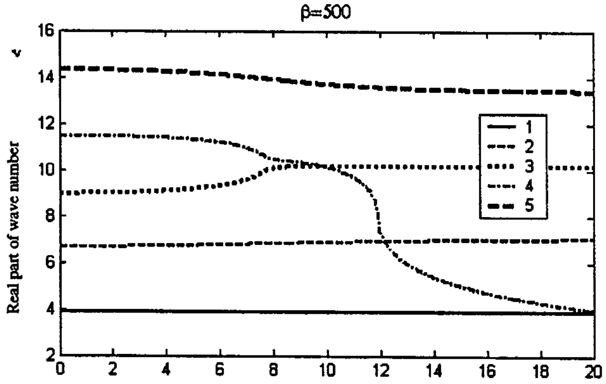

Figure 5.7. Decrease of the fourth mode at $\beta = 500$.

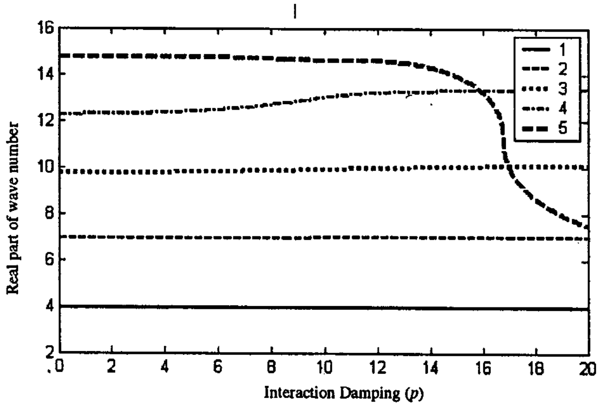

Figure 5.8. Decrease of the fifth mode at $\beta = 1400$.

In Figure (5.6), the third mode decays below the second mode at p approximately 8.2. Similar observations on the fourth and fifth modes are seen in Figures (5.7) and (5.8). The decay of the first mode is also present at β less than 10. It is not presented here because it is not significant in the sequencing of the resonance frequencies.

It is very interesting to see that with the presence of interaction damping, one mode is over-damped and will decrease depending on the contact stiffness. When one mode decreases, for instance, the third mode at $\beta = 200$, it becomes less than the second mode, or even less than the first mode. Consequently, the first or second modes observed in experiments may differ from the estimation without interaction damping included.

The interaction damping acts on the modes differently. As seen in Figure (5.7), modes 4 and 5 decrease while modes 1, 2 and 3 increase. Meanwhile, the points where the two modes intersect are different: in Figure (5.1), it is about 7.3; in Figure (5.6), it is about 8;

in Figure (5.7), it is about 10; in Figure (5.8), it is about 16. A tentative conclusion here is that the intersection point moves right for higher modes.

5.3 Nonlinear Effects

Now, consider the nonlinear response with respect to amplitude. When the vibration amplitude a_1 is increased, a certain pattern of resonance frequency shift is observed. With the presence of interaction damping, the patterns are different. Figure (5.9) shows the influence of p on the shift of the first resonance frequency.

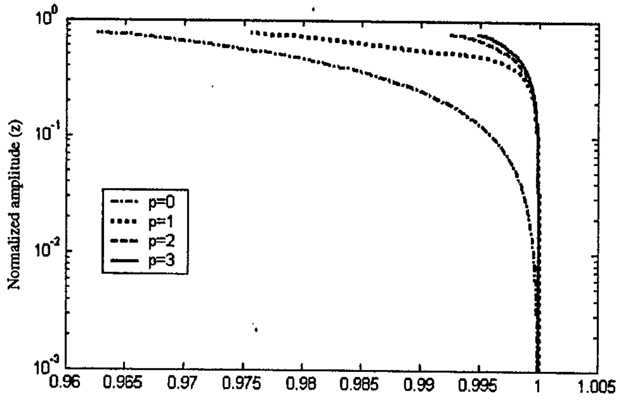

Ratio of the real parts of nonlinear wave numbers over their linear counterparts.

Figure 5.9. Frequency shift of the first resonance frequency of the nonlinear system for different p.

It is already known from the study of modal sensitivity that a certain mode is more sensitive than others at specific β. That is, the resonance frequency of that mode shifts more than those of others when amplitude increases. In Figure (5.9), the influence of interaction damping is significant. At $\beta = 50$, from the results of modal sensitivity, it is

known that the first mode will shift the most. The frequency shift becomes less and less with increased damping. Unclear Recall the figures in the previous section, because of damping, the first root (γ) of the linear systems becomes larger than that of linear system with no damping. The higher the p, the larger the γ. However, when the shift ratio is shown in the figure, it is in the opposite way: the higher the p, the lower the ratio.

When $\beta = 100$, the second mode is the most sensitive. In Figure (5.10), the first and second modes are plotted for different p. The plot indicates a pattern change: when there is no damping ($p = 0$), the second mode shifts more than the first. But when there is damping ($p = 1$ or $p = 2$), it becomes that the first mode shifts more than the second. Also, the magnitudes of these shifts become less with higher damping.

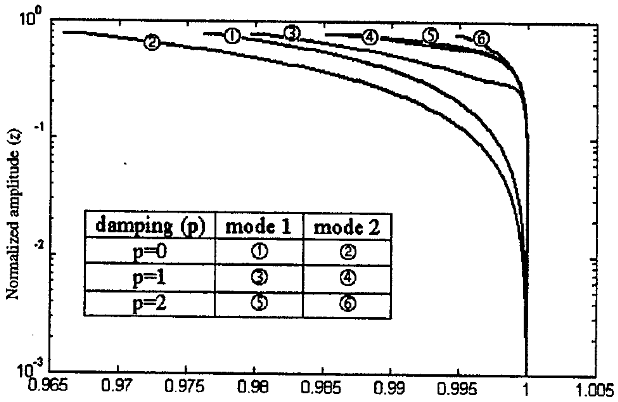

Ratio of the real parts of nonlinear wave numbers over their linear counterparts.

Figure 5.10. Real parts of the first and second modes under different damping (β = 100).

This change in the pattern is significant in that it differs from the results of the modal sensitivity of the system with no interaction damping. In real AFM systems, the interaction damping may be large enough to make the frequency shift pattern totally different from the estimation based on no damping.

From the above discussion, it is obvious that the interaction damping has significant influence on the modal sensitivity. At certain combination of p and β, some mode will decay. This may answer the question why some modes are difficult to observe in experiments. Also, the frequency shift pattern that is used in determination of β may be changed by this damping. If the damping is not properly included in the analysis, errors will be introduced into the results.

6. Forced Vibration with Damping

6.1 Governing Equation

In non-ideal environments, there are damping forces in the beam vibration. Damping forces are non-conservative, so that the transient vibration will dissipate eventually. The damping of vibrating atomic force microscope cantilevers is caused mainly by two different effects: system damping is the damping caused by internal losses in the beam as well as losses to any surrounding fluid in which the beam vibrates. There is also damping caused by the interaction forces which act through the contact between the cantilever tip and the sample surface. The latter is thought to be caused primarily by adhesion hysteresis effects. This case has been studied previously [4][5]. In this chapter, the system damping caused by internal losses is studied.

It is assumed the damping forces are proportional to the velocity and opposite in the direction to velocity,

$$f_d = -C\dot{w}(x,t), \tag{6.1.1}$$

where C is in general a linear homogeneous differential operator which may include different orders of differential terms. For the kind of viscous damping studied in this research, it is assumed that the damping operator C be a constant: $C = c$.

Also, the vibration system is assumed to be driven by external forcing $q(x,t)$. The equation of motion for this damped externally driven system is

$$EI\frac{\partial^4 w(x,t)}{\partial x^4} + c\frac{\partial w(x,t)}{\partial t} + \rho A\frac{\partial^2 w(x,t)}{\partial t^2} = q(x,t), \tag{6.1.2}$$

with boundary conditions

$$\begin{aligned} &w(0,t) = 0, \quad w'(0,t) = 0, \\ &w''(L,t) = 0, \quad EIw'''(L,t) = f(w(L,t)). \end{aligned} \tag{6.1.3}$$

The last boundary condition involves the contact interaction at the tip end. It can be expanded by Taylor's series when the displacement is small relative to the initial position. For Hertzian contact, the expanded form of (6.1.3) is

$$EIw'''(L,t)-\kappa w(L,t)+\kappa_1 w^2(L,t)+\kappa_2 w^3(L,t)=0,$$

$$\kappa=\frac{3}{2}K_0\Delta^{\frac{1}{2}},\quad \kappa_1=\frac{3}{8}K_0\Delta^{-\frac{1}{2}},\quad \kappa_2=\frac{1}{16}K_0\Delta^{-\frac{3}{2}}.$$

Generally speaking, in the vibration system of AFM beams, the damping is relatively small. In many experiments the AFM beams vibrate in air, so the damping due to friction is negligible. Hence it is assumed that c is $O(\varepsilon)$. Further, the external driving force is assumed to be harmonic, that is, $q(x,t) = Q(x)e^{j\Omega t}$, in which Ω is the driving frequency.

Letting $c=\varepsilon\tilde{c}$, the governing equation and boundary conditions are written as

$$\begin{aligned}
&\frac{\partial^4 w(x,t)}{\partial x^4}+\varepsilon\frac{\tilde{c}}{EI}\frac{\partial w(x,t)}{\partial t}+\frac{\rho A}{EI}\frac{\partial^2 w(x,t)}{\partial t^2}=\frac{Q(x)}{EI}e^{j\Omega t},\\
&w(0,t)=0,\\
&w'(0,t)=0,\\
&w''(L,t)=0,\\
&w'''(L,t)=\frac{\kappa}{EI}w(L,t)-\frac{\kappa_1}{EI}w^2(L,t)-\frac{\kappa_2}{EI}w^3(L,t).
\end{aligned}\tag{6.1.4}$$

6.2 Primary response with linear boundary condition

First the problem with the linearized boundary condition as (3.4.2) is studied. Closed-form solutions of the above boundary-value problem for damped systems are not possible due to the difficulties in solving the eigenvalue problem. An approximate method, the method of multiple scales [2] is used. By this method, new independent variables are introduced according to $T_n=\varepsilon^n t,\quad n=0,1,2,\ldots$, each of which represents a

different time scale. Thus, the derivatives with respect to t can be rewritten in terms of the partial derivatives with respect to T_n such as

$$\frac{d}{dt}=\frac{dT_0}{dt}\frac{\partial}{\partial T_0}+\frac{dT_1}{dt}\frac{\partial}{\partial T_1}+\ldots=D_0+\varepsilon D_1+\varepsilon^2 D_2+\ldots,$$

$$\frac{d^2}{dt^2}=D_0^2+2\varepsilon D_0 D_1+\varepsilon^2(D_1^2+2D_0D_2)+\ldots.$$

It should be noted that the number of independent time scales needed depends on the order to which the expansion is carried out. If the expansion is carried out to $O(\varepsilon^2)$, then T_0 and T_1 are needed. If the expansion is carried out to $O(\varepsilon^3)$, then T_0, T_1 and T_2 are needed. In this part, the $O(\varepsilon)$ solution is concerned. Hence, the solution is assumed of the form

$$w(x,t;\varepsilon)=w_0(x,T_0,T_1)+\varepsilon w_1(x,T_0,T_1)+O(\varepsilon^2).\tag{6.2.1}$$

This form of solution will be substituted into the governing equation and the coefficients of different ε orders will be combined to yield a group of equations from which w_0 and w_1 may be solved.

For the primary response $\Omega=\omega$, a detuning parameter σ is introduced, which quantitatively describes the nearness of Ω to ω. This parameter helps to identify the terms in the governing equation that lead to secular behavior. Accordingly, Ω is written as $\Omega=\omega+\varepsilon\sigma$ where $\sigma=O(1)$. The linear undamped theory will predict unbounded oscillations when $\sigma=0$ irrespective of how small the excitation is. In the actual system, the damping and the nonlinearity limit these large oscillations. Thus, to obtain a uniformly valid approximate solution of this problem, it is necessary to order the excitation so that it will appear when the damping and the nonlinearity appear. To do this, the driving force is set as $Q(x)=\varepsilon\tilde{Q}(x)$. This scheme for ordering the terms is consistent with the notion of primary resonance. It is anticipated that in a lightly damped system a small amplitude excitation produces a relatively large-amplitude response.

The expansion (6.2.1) is substituted into equation (6.1.4). The governing equation becomes

$$\begin{aligned}&(w_0+\varepsilon w_1+O(\varepsilon^2))'''' + \varepsilon\frac{\tilde{c}}{EI}(D_0+\varepsilon D_1+\varepsilon^2 D_2)(w_0+\varepsilon w_1+O(\varepsilon^2))\\ &+\frac{\rho A}{EI}(D_0^2+\varepsilon 2D_1D_0+\varepsilon^2(D_1^2+2D_0D_2))(w_0+\varepsilon w_1+O(\varepsilon^2))=\varepsilon\frac{\tilde{Q}(x)}{EI}e^{j\Omega T_0}.\end{aligned} \tag{6.2.2}$$

Thus, for the order ε^0 system, combining all the coefficients of the ε^0 terms, the equation of motion is

$$w_0'''' + \frac{\rho A}{EI}D_0^2 w_0 = 0. \tag{6.2.3}$$

The boundary conditions are

$$\begin{aligned}&w_0(0,t)=0, \qquad w_0'(0,t)=0,\\ &w_0''(L,t)=0, \qquad w_0'''(L,t)=\frac{\kappa}{EI}w_0(L,t).\end{aligned} \tag{6.2.4}$$

The solution of equation (6.2.3) and boundary conditions (6.2.4) is assumed of the form $w_0(x,T_0,T_1) = \phi_0(x)A_0(T_1)e^{j\omega T_0}$, for which $\phi_0(x)$ can be solved as

$$\begin{aligned}&\phi_0(x) = D[\sin kx - \sinh kx - C_0(\cos kx - \cosh kx)],\\ &C_0 = \frac{\sin kL + \sinh kL}{\cos kL + \cosh kL}, \quad k^4 = \frac{\rho A}{EI}\omega^2.\end{aligned} \tag{6.2.5}$$

In (6.2.5), D is an arbitrary constant. It is determined by setting $\phi_0(L)=1$. Thus,

$$D = \frac{\cos kL + \cosh kL}{2(\sin kL\cosh kL - \cos kL\sinh kL)}.$$

Similarly, by combining all the coefficients of the ε^1 order terms, the ε^1 order equation and boundary conditions are

$$\begin{aligned}&w_1'''' + \frac{\rho A}{EI}D_0^2 w_1 = -\frac{\tilde{c}}{EI}D_0 w_0 - \frac{\rho A}{EI}2D_0D_1w_0 + \frac{\tilde{Q}(x)}{EI}e^{j\Omega T_0},\\ &w_1(0,t)=0, \qquad w_1'(0,t)=0,\\ &w_1''(L,t)=0, \qquad w_1'''(L,t)=\frac{\kappa}{EI}w_1(L,t).\end{aligned} \tag{6.2.6}$$

Letting $w_1(x,T_0,T_1) = \phi_1(x)A_1(T_1)e^{j\omega T_0}$, equations (6.2.6) become

$$\begin{aligned}&\phi_1''''(x)A_1(T_1) - k^4\phi_1(x)A_1(T_1) = -j\omega\frac{\tilde{c}}{EI}A_0(T_1)\phi_0(x) - 2j\omega\frac{\rho A}{EI}A_0'(T_1) + \frac{\tilde{Q}(x)}{EI}e^{j\sigma T_1},\\ &\phi_1(0)=0, \quad \phi_1'(0)=0,\\ &\phi_1''(L)=0, \quad \phi_1'''(L)=\frac{\kappa}{EI}\phi_1(L).\end{aligned} \tag{6.2.7}$$

Since

$$\begin{aligned}\int_0^L \phi_1''''(x)\phi_0(x)dx &= \int_0^L \phi_0(x)d\phi_1'''(x) = \phi_0(x)\phi_1'''(x)\Big|_0^L - \int_0^L \phi_1'''(x)\phi_0(x)dx,\\ &= \phi_0(L)\phi_1'''(L) - \int_0^L \phi_0(x)d\phi_1''(x),\\ &= \phi_0(L)\phi_1'''(L) - \phi_1(L)\phi_0'''(L) + \int_0^L \phi_0''''(x)\phi_1(x)dx,\\ &= \phi_0(L)\phi_1'''(L) - \phi_1(L)\phi_0'''(L) + k^4\int_0^L \phi_0(x)\phi_1(x)dx.\end{aligned}$$

Thus,

$$\int_0^L \phi_0(x)[\phi_1''''(x) - k^4\phi_1(x)]dx = \phi_0(L)\phi_1'''(L) - \phi_1(L)\phi_0'''(L). \tag{6.2.8}$$

Multiplying both sides of (6.2.7) by $\phi_0(x)$ and integrating from 0 to L, gives

$$\begin{aligned}&\int_0^L\left[-j\omega\frac{\tilde{c}}{EI}A_0(T_1)\phi_0^2(x) - 2j\omega\frac{\rho A}{EI}A_0'(T_1)\phi_0^2(x) + \frac{\tilde{Q}(x)}{EI}e^{j\sigma T_1}\phi_0(x)\right]dx =\\ &\qquad \phi_0(L)\phi_1'''(L) - \phi_1(L)\phi_0'''(L) = \phi_0(L)\frac{\kappa}{EI}\phi_1(L) - \phi_1(L)\frac{\kappa}{EI}\phi_0(L) = 0.\end{aligned} \tag{6.2.9}$$

Thus,

$$-j\omega(\tilde{c}A_0(T_1) + 2(\rho A)A_0'(T_1))\int_0^L \phi_0^2(x)dx + e^{j\sigma T_1}\int_0^L \tilde{Q}(x)\phi_0(x)dx = 0. \tag{6.2.10}$$

Next, let

$$A_0(T_1) = \frac{1}{2}\alpha(T_1)e^{j\beta(T_1)}, \text{ and}$$

$$b_1 = \int_0^L \phi_0^2(x)dx,\ b_2 = \int_0^L \tilde{Q}(x)\phi_0(x)dx.$$

Then, (6.2.10) becomes

$$-j\omega(\frac{1}{2}\tilde{c}\alpha + \rho A(\alpha' + j\alpha\beta'))b_1 + b_2 e^{j(\sigma T_1 - \beta)} = 0. \tag{6.2.11}$$

The real part of (6.2.11) is

$$\omega\rho A\alpha\beta' b_1 + b_2\cos(\sigma T_1 - \beta) = 0. \tag{6.2.12}$$

The imaginary part of (6.2.11) is

$$-\frac{1}{2}\omega\tilde{c}\alpha b_1 - \rho A\omega\alpha' b_1 + b_2\sin(\sigma T_1 - \beta) = 0. \tag{6.2.13}$$

Defining $\gamma = \sigma T_1 - \beta$, (6.2.12) and (6.2.13) become

$$\begin{cases} \rho A\alpha(\gamma' - \sigma) = \dfrac{b_2}{b_1\omega}\cos\gamma, \\ \dfrac{\tilde{c}}{2}\alpha + \rho A\gamma' = \dfrac{b_2}{b_1\omega}\sin\gamma. \end{cases} \tag{6.2.14}$$

Steady-state motion occurs when $\alpha' = \gamma' = 0$, which corresponds to the singular points of (6.2.14). That is, they correspond to the solutions of

$$\begin{cases} -\rho A\alpha\sigma = \dfrac{b_2}{b_1\omega}\cos\gamma, \\ \dfrac{\tilde{c}}{2}\alpha = \dfrac{b_2}{b_1\omega}\sin\gamma. \end{cases} \tag{6.2.15}$$

Squaring and adding the equations in (6.2.15) gives

$$\left(\frac{b_2}{b_1\omega}\right)^2 = \left[(\rho A\sigma)^2 + \left(\frac{\tilde{c}}{2}\right)^2\right]\alpha^2. \tag{6.2.16}$$

From (6.2.15), γ and α are expressed as

$$\gamma = -\tan(\frac{\tilde{c}}{2\rho A\sigma}),\quad \alpha = \frac{2b_2}{\tilde{c}b_1\omega}\sin\gamma. \tag{6.2.17}$$

Equation (6.2.16) is an implicit equation for the amplitude of the response α as a function of the detuning parameter σ (i.e., the frequency of the excitation) and the amplitude of the driving force $Q(x)$ which is implicitly represented by b_2. Equation (6.2.16) is called the frequency-response equation.

Recall that $w_0(x, T_0, T_1) = \phi_0(x)A_0(T_1)e^{j\omega T_0}$. Substituting α and β back into $A_0(T_1)$, the first approximation is obtained as

$$w(x,t) = \phi_0(x)\alpha\cos(\omega t - \beta) + O(\varepsilon) \tag{6.2.18}$$

in which α and β are defined in (6.2.14).

Since $\Omega = \omega + \varepsilon\sigma$, the first approximation to the steady-state solution is given by

$$w(x,t) = \phi_0(x)\alpha\cos(\omega t + \varepsilon\sigma t - \gamma) + O(\varepsilon) = \phi_0(x)\alpha\cos(\Omega t - \gamma) + O(\varepsilon). \tag{6.2.19}$$

where α and γ are constants as defined in (6.2.17). Hence, the steady-state response is exactly tuned to the frequency of the excitation. However, the phase of the response is shifted from that of the excitation by $-\gamma$.

The plot of α as functions of σ while other parameters are fixed is called a frequency-response curve. Each point on this curve corresponds to a singular point in a different state plane. There is one state plane for each combination of parameters.

Equation (6.2.16) is rewritten as

$$\sigma^2 = \frac{1}{(\rho A)^2}\left(\left(\frac{b_2}{b_1\omega\alpha}\right)^2 - \frac{\tilde{c}^2}{4}\right)$$

Hence, $\left(\frac{b_2}{b_1\omega}\right)^2\frac{1}{\alpha^2}-\frac{\tilde{c}^2}{4}\geq 0$. The maximum amplitude is then $\alpha_p=\frac{2b_2}{b_1\omega\tilde{c}}$. Figure (6.1) shows the response curve (6.2.16). Since this is a linear system, the curve is symmetric. At $\sigma = 0$, the response amplitude reaches the maximum.

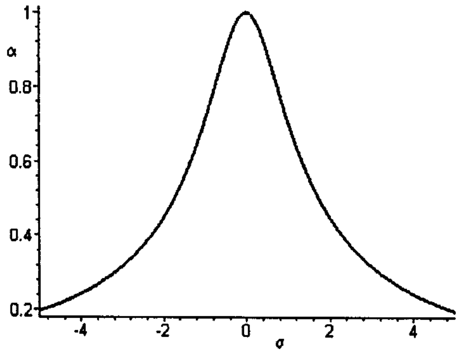

Figure 6.1. Frequency-Response curve of (6.2.16).

(This figure is only for illustrative purpose, and no exact scaling is applied.)

6.3 Nonresonant hard excitation for linearized system

In the previous section the excitation at frequency Ω very near ω_0 was discussed. When Ω is away from ω_0, the effect of the excitation will be small unless its amplitude is hard; that is, unless $Q(x)$ is $O(1)$ instead of $O(\varepsilon)$. Therefore, from (6.1.4), the governing equation gives the order ε^0 equations,

$$w_0'''' + \frac{\rho A}{EI}D_0^2 w_0 = \frac{Q(x)}{EI}e^{j\Omega T_0}, \qquad (6.3.1)$$

with the same boundary conditions as (6.2.4).

The general solution of (6.3.1) is

$$w_0(x,T_0,T_1) = \phi_0(x)A_0(T_1)e^{j\omega T_0} + \psi_0(x)e^{j\Omega T_0} + cc,$$

$$\psi_0(x) = \frac{1}{2EIK^3}\Big(-\int \cos Kx Q(x)dx \sin Kx + \int \sin Kx Q(x)dx \cos Kx + \int \sinh Kx Q(x)dx \cosh Kx + \int \cosh Kx Q(x)dx \sinh Kx\Big), \qquad (6.3.2)$$

$$K^4 = \frac{\rho A}{EI}\Omega^2,$$

in which $\phi_0(x)$ is the same as defined in (6.2.5), and cc is the complex conjugate of the preceding terms.

The order ε^1 equation and boundary conditions are:

$$\begin{aligned} & w_1'''' + \frac{\rho A}{EI}D_0^2 w_1 = -\frac{\tilde{c}}{EI}D_0 w_0 - \frac{\rho A}{EI}2D_0 D_1 w_0, \\ & w_1(0,t) = 0, \qquad w_1'(0,t) = 0, \\ & w_1''(L,t) = 0, \qquad w_1'''(L,t) = \frac{\kappa}{EI}w_1(L,t). \end{aligned} \qquad (6.3.3)$$

The solution of w_1 is written in the form $w_1(x,T_0,T_1) = \phi_1(x)A_1(T_1)e^{j\omega T_0} + \psi_1(x)e^{j\Omega T_0}$. Thus, from (6.3.1) and (6.3.3), there are equations of the coefficients of ωT_0 and ΩT_0 harmonic terms,

$$\begin{aligned} & \phi_0''''(x) - k^4\phi_0(x) = 0, \\ & \psi_0''''(x) - K^4\psi_0(x) = \frac{Q(x)}{EI} \\ & \phi_0(0) = \psi_0(0) = 0,\ \phi_0'(0) = \psi_0'(0) = 0, \\ & \phi_0''(L) = \psi_0''(L) = 0,\ \phi_0'''(L) = \frac{\kappa}{EI}\phi_0(L),\ \psi_0'''(L) = \frac{\kappa}{EI}\psi_0(L), \\ & k^4 = \frac{\rho A}{EI}\omega^2,\ K^4 = \frac{\rho A}{EI}\Omega^2, \end{aligned} \qquad (6.3.4)$$

and

$$\begin{aligned}
&\phi_1''''(x)A_1(T_1) - k^4\phi_1(x)A_1(T_1) = -\frac{\tilde{c}}{EI}j\omega\phi_0(x)A_0(T_1) - \frac{2\rho A}{EI}j\omega\phi_0(x)A_0'(T_1),\\
&\psi_1''''(x) - \mathrm{K}^4\psi_1(x) = -\frac{\tilde{c}}{EI}j\Omega\psi_0(x),\\
&\phi_1(0) = \psi_1(0) = 0,\ \phi_1'(0) = \psi_1'(0) = 0,\\
&\phi_1''(L) = \psi_1''(L) = 0,\ \phi_1'''(L) = \frac{\kappa}{EI}\phi_1(L),\ \psi_1'''(L) = \frac{\kappa}{EI}\psi_1(L).
\end{aligned} \qquad (6.3.5)$$

Since $\int_0^L \phi_0(x)[\phi_1''''(x) - k^4\phi_1(x)]dx = \phi_0(L)\phi_1'''(L) - \phi_1(L)\phi_0'''(L)$, therefore

$$\int_0^L [-\frac{\tilde{c}}{EI}j\omega\phi_0^2(x)A_0(T_1) - \frac{2\rho A}{EI}j\omega\phi_0^2(x)A_0'(T_1)]dx = 0.$$

Hence,

$$\tilde{c}A_0(T_1) + 2\rho AA_0'(T_1) = 0.$$

Thus,

$$A_0(T_1) = e^{-\frac{\tilde{c}}{2\rho A}T_1}. \qquad (6.3.6)$$

Also, $\psi_1(x)$ can be solved as

$$\begin{aligned}
\psi_1(x) = -\frac{j\tilde{c}\Omega}{2EI\mathrm{K}^3}(&-\int \cos\mathrm{K}x\psi_0(x)dx\sin\mathrm{K}x + \int \sin\mathrm{K}x\psi_0(x)dx\cos\mathrm{K}x\\
&+\int \sinh\mathrm{K}x\psi_0(x)dx\cosh\mathrm{K}x + \int \cosh\mathrm{K}x\psi_0(x)dx\sinh\mathrm{K}x)).
\end{aligned} \qquad (6.3.7)$$

In the case of a hard excitation, the response has both ωT_0 and ΩT_0 harmonic terms. Equation (6.3.6) shows that the amplitude of harmonic term decreases exponentially. Coefficients of the harmonic terms give the solution as

$$w(x,t) = (\psi_0(x) + \varepsilon\psi_1(x))\cos\Omega t + O(\varepsilon^2).$$

6.4 Eigenfunction method

The eigenfunctions of the undamped system can be used to decouple the modal equations in this forced damped vibration system. For the undamped vibration system with linearized boundary condition,

$$\begin{aligned}
&\frac{\partial^4 w(x,t)}{\partial x^4} + \frac{\rho A}{EI}\frac{\partial^2 w(x,t)}{\partial x^2} = 0,\\
&w(0,t) = 0, \quad w'(0,t) = 0,\\
&w''(L,t) = 0, \quad w'''(L,t) = \frac{\kappa}{EI}w(L,t).
\end{aligned} \qquad (6.4.1)$$

The eigenfunctions that satisfy the equation of motion and boundary conditions in (6.4.1) are

$$\begin{aligned}
&W_r(x) = D(\sin k_r x - \sinh k_r x - \frac{\sin k_r L + \sinh k_r L}{\cos k_r L + \cosh k_r L}(\cos k_r x - \cosh k_r x)),\\
&k_r^4 = \frac{\rho A}{EI}\omega_r^2.
\end{aligned} \qquad (6.4.2)$$

The characteristic equation is

$$\gamma^3(\cos\gamma\cosh\gamma + 1) - \frac{\kappa}{EI/L^3}(\sinh\gamma\cos\gamma - \sin\gamma\cosh\gamma) = 0,$$

where $\gamma = kL$ is the normalized wave number. The solution of the boundary-value problem (6.1.4) is assumed to be of the form

$$w(x,t) = \sum_{r=0}^{\infty} W_r(x)\eta_r(t) \quad r = 0,1,2... \qquad (6.4.3)$$

where $W_r(x)$ are the eigenfunctions as in (6.4.2). Due to the orthogonality of those eigenfunctions, the following modal equations are obtained

$$\ddot{\eta}_r(t) + \frac{\varepsilon\tilde{c}}{\rho A}\dot{\eta}_r(t) + \omega_r^2\eta_r(t) = N_r(t), \quad r = 0,1,2,.... \qquad (6.4.4)$$

where

$$N_r(t) = \frac{\varepsilon}{\rho A}\int_0^L W_r(x)\tilde{Q}(x)dx e^{j\Omega t}. \tag{6.4.5}$$

Let

$$\phi_r = \int_0^L W_r(x)\tilde{Q}(x)dx, \text{ then } N_r(t) = \varepsilon\frac{\phi_r}{\rho A}e^{j\Omega T_0}. \tag{6.4.6}$$

Therefore, (6.4.4) becomes

$$\ddot{\eta}_r(t) + \varepsilon\frac{\tilde{c}}{\rho A}\dot{\eta}_r(t) + \omega_r^2\eta_r(t) = \varepsilon\frac{\phi_r}{\rho A}e^{j\Omega T_0}. \tag{6.4.7}$$

In the following analysis, the method of multiple scales is used to solve the above modal equations. With the method of multiple scales, the solutions to the modal equations (6.4.7) can be represented as an expansion in different time scales in the form

$$\eta_r(t;\varepsilon) = \eta_{r0}(T_0,T_1,T_2) + \varepsilon\eta_{r1}(T_0,T_1,T_2) + \varepsilon^2\eta_{r2}(T_0,T_1,T_2) + O(\varepsilon^3). \tag{6.4.8}$$

Next, this expansion is substituted into the modal equations in (6.4.7), and all the terms of same ε order on both sides are combined. The coefficients of order ε^0 terms give the equations

$$D_0^2\eta_{r0} + \omega_r^2\eta_{r0} = 0. \tag{6.4.9}$$

Assuming a harmonic solution, $\eta_{r0}(t)$ can be solved from (6.4.9) as

$$\eta_{r0}(t) = A_r(T_1,T_2)e^{j\omega_r T_0} + \bar{A}_r(T_1,T_2)e^{-j\omega_r T_0}, \quad r = 0,1,2..... \tag{6.4.10}$$

Note that $\eta_{r0}(t)$'s are simple harmonic functions with varying amplitude that is dependent on T_1 and T_2. Combining the coefficients of the order ε terms gives the following equation

$$D_0^2\eta_{r1} + \omega_r^2\eta_{r1} = \frac{\phi_r}{\rho A}e^{j\Omega T_0} - 2D_0D_1\eta_{r0} - \frac{\tilde{c}}{\rho A}D_0\eta_{r0}. \tag{6.4.11}$$

From equation (6.4.10), η_{r0} is substituted into equations (6.4.11) to yield

$$D_0^2\eta_{r1} + \omega_r^2\eta_{r1} = \frac{\phi_r}{\rho A}e^{j\Omega T_0} - 2j\omega_r\frac{\partial A_r}{\partial T_1}e^{j\omega_r T_0} - \frac{\tilde{c}}{\rho A}j\omega_r A_r e^{j\omega_r T_0}. \tag{6.4.12}$$

In equation (6.4.12), the right hand side has harmonic terms of Ω and ω_r. The left hand side has the harmonic term of ω_r. Thus, for this equation, any particular solution to it with respect to the harmonic term ω_r will have a secular term containing the factor $T_0 exp(j\omega_r T_0)$ which grows with T_0. This result is physically unreasonable, so these ω_r terms on the right side must be removed. To eliminate these secular terms, the function A_r must satisfy

$$-2j\omega_r\frac{\partial A_r}{\partial T_1} - j\omega_r\frac{\tilde{c}}{\rho A}A_r = 0.$$

Thus,

$$A_r(T_1,T_2) = e^{-\frac{\tilde{c}}{2\rho A}T_1}f_r(T_2), \tag{6.4.13}$$

where $f_r(T_2)$ is an arbitrary functions of T_2 to be determined later.

At this point, it is very clear that the amplitude A_r takes exponential terms that decay with T_1 at a speed dictated by the damping constant. This solution is expected for a damped system. Hence, equations in (6.4.11) can be simplified as

$$D_0^2\eta_{r1} + \omega_r^2\eta_{r1} = \frac{\phi_r}{\rho A}e^{j\Omega T_0}. \tag{6.4.14}$$

Equation (6.4.14) can be solved as

$$\eta_{r1} = \frac{\phi_r}{\rho A(\omega_r^2 - \Omega^2)}e^{j\Omega T_0}. \tag{6.4.15}$$

The coefficients of the $O(\varepsilon^2)$ terms are governed by

$$D_0^2\eta_{r2} + \omega_r^2\eta_{r2} = -2D_0D_1\eta_{r1} - (D_1^2 + 2D_0D_2)\eta_{r0} - \frac{\tilde{c}}{\rho A}(D_0\eta_{r1} + D_1\eta_{r0}). \tag{6.4.16}$$

Equations (6.4.11) and (6.4.15) are then substituted into (6.4.16). On the right side, there are terms containing ω_r harmonic terms. These terms are secular terms that need be eliminated. To do so, it must have

$$(D_1^2+2D_0D_2)\eta_{r0}+\frac{\tilde{c}}{\rho A}D_1\eta_{r0}=0.$$

Thus, $\frac{\tilde{c}^2}{4\rho^2A^2}f_r(T_2)-2j\omega_r f_r(T_2)=0$. From this result, $f_r(T_2)$ can be solved as

$f_r(T_2)=e^{-j\frac{\tilde{c}^2}{8\omega_r(\rho A)^2}T_2}$. Thus, $A_r(T_1,T_2)=e^{-\frac{\tilde{c}}{2}T_1}e^{-j\frac{\tilde{c}^2}{8\omega_r(\rho A)^2}T_2}$.

Equation (6.4.16) then becomes

$$D_0^2\eta_{r2}+\omega_r^2\eta_{r2}=-\tilde{c}D_0\eta_{r1}=-\frac{\tilde{c}\phi_r}{(\rho A)^2(\omega_r^2-\Omega^2)}j\Omega e^{j\Omega T_0}. \tag{6.4.18}$$

A solution of this equation is

$$\eta_{r2}=-j\frac{\tilde{c}\phi_r\Omega}{(\rho A)^2(\omega_r^2-\Omega^2)^2}e^{j\Omega T_0}. \tag{6.4.19}$$

Recall from (6.4.9), then the solution of η_r can be put in the form

$$\begin{aligned}\eta_r(t)&=\eta_{r0}+\varepsilon\eta_{r1}+\varepsilon^2\eta_{r2}+O(\varepsilon^3),\\&=e^{-\frac{\tilde{c}}{2\rho A}T_1}e^{-j\frac{\tilde{c}^2}{8\omega_r(\rho A)^2}T_2}e^{j\omega_r T_0}+\varepsilon\frac{\phi_r}{(\rho A)(\omega_r^2-\Omega^2)}e^{j\Omega T_0}\\&\quad-\varepsilon^2\frac{\tilde{c}\phi_r}{(\rho A)^2(\omega_r^2-\Omega^2)^2}j\Omega e^{j\Omega T_0}+O(\varepsilon^3).\end{aligned} \tag{6.4.20}$$

Letting $F_r=\varepsilon\frac{\phi_r}{\rho A}$, (6.4.20) can be written without ε as

$$\eta_r(t)=e^{-\frac{c}{2}t}e^{-j\frac{c^2}{8\omega_r}t}e^{j\omega_r t}+\frac{F_r}{\omega_r^2-\Omega^2}e^{j\Omega t}-\frac{cF_r}{(\omega_r^2-\Omega^2)^2}j\Omega e^{j\Omega t}+O(\varepsilon^3).$$

The real part of $\eta_r(t)$ is

$$\eta_r(t)=e^{-\frac{c}{2}t}\cos(\omega_r t-\frac{c^2}{8\omega_r}t)+\frac{F_r}{\omega_r^2-\Omega^2}\cos(\Omega t)-\frac{cF_r\Omega}{(\omega_r^2-\Omega^2)^2}\sin(\Omega T_0)+O(\varepsilon^3). \tag{6.4.21}$$

It can be rewritten as

$$\eta_r(t)=e^{-\frac{c}{2}t}\cos(\omega_r t-\frac{c^2}{8\omega_r}t)+R_r\cos(\Omega t-\varphi_r)+O(\varepsilon^3), \tag{6.4.22}$$

where $R_r=\frac{F_r\sqrt{(\omega_r^2-\Omega^2)^2+c^2\Omega^2}}{(\omega_r^2-\Omega^2)^2}$, $\varphi_r=\tan^{-1}(-\frac{c\Omega}{\omega_r^2-\Omega^2})$. In (6.4.22), for sufficiently large t, the $\omega_r t$ harmonic term will eventually become negligible. Since the steady-state response is the primary concern, the Ωt harmonic term will dominate. Thus,

$$\eta_r(t)=R_r\cos(\Omega t-\varphi_r)+O(\varepsilon^3) \tag{6.4.23}$$

As a particular case, in the undamped system where $c=0$,

$$\eta_r(t)=\frac{F_r}{\omega_r^2-\Omega^2}\cos(\Omega t) \tag{6.4.24}$$

Note that F_r is $O(\varepsilon)$, so the amplitude of Ωt harmonic terms are $O(\varepsilon)$.

6.4.1 Primary Resonance ($\Omega = \omega_0$)

When the excitation frequency Ω is very near the primary natural frequency ω_0, the system is at primary resonance. Ω is written in the form

$$\Omega=\omega_0+\varepsilon\sigma. \tag{6.4.25}$$

where the detuning parameter σ is $O(1)$. Note that this ω_0 is the natural frequency of the undamped and linear system (6.4.1). In experiments, the natural frequencies of the linear system are easier to measure.

For an undamped linear system, if the frequency of the driving force is very close to the primary natural frequency (ω_0) of the system, the oscillation of the system will become unbounded regardless of the amplitude of the excitation. In a continuum system like the beam, it is possible that the system be driven at frequencies very close to the natural frequencies.

The driving force is

$$N_0(t) = \varepsilon\frac{\phi_0}{\rho A}e^{j\Omega T_0} = \varepsilon\frac{\phi_0}{\rho A}e^{j(\omega_0 T_0+\sigma T_1)}.$$

Assume the solution of modal equation of the first mode as

$$\eta_0(t;\varepsilon) = \eta_{00}(T_0,T_1,T_2)+\varepsilon\eta_{01}(T_0,T_1,T_2)+\varepsilon^2\eta_{02}(T_0,T_1,T_2)+O(\varepsilon^3).$$

Then, following the procedures of the method of multiple scales, for the ε^0 terms:

$$D_0^2\eta_{00}+\tilde{\omega}_0^2\eta_{00} = 0. \tag{6.4.26}$$

In (6.4.26), $\tilde{\omega}_0$ stands for the natural frequency of the nonlinear system that is to be determined by the contact boundary condition. With damping and the nonlinear spring constants present, it is expected that $\tilde{\omega}_0$ is different from ω_0. Define this difference as $\tilde{\omega}_0 = \omega_0+\varepsilon\delta$, where δ is $O(1)$. The parameter δ quantitatively measures the difference of $\tilde{\omega}_0$ from ω_0. From the discussion in the previous chapters, it is reasonable to assume δ as a function of the vibration amplitude α.

The solution of (6.4.26) is

$$\eta_{00}(T_0,T_1,T_2) = A_0(T_1,T_2)e^{j\tilde{\omega}_0 T_0}+\bar{A}_0(T_1,T_2)e^{-j\tilde{\omega}_0 T_0}. \tag{6.4.27}$$

If only the ε^1 order approximation is considered, A_0 is treated as a function of T_1 only, then the coefficients of the ε^1 terms are

$$\begin{aligned} D_0^2\eta_{01}+\tilde{\omega}_0^2\eta_{01} &= \frac{\phi_r}{\rho A}e^{j\Omega T_0}-2D_0D_1\eta_{00}-\frac{\tilde{c}}{\rho A}D_0\eta_{00} \\ &-2j\tilde{\omega}_0A_0'(T_1)e^{j\tilde{\omega}_0 T_0}+\frac{\phi_0}{\rho A}e^{j(\omega_0 T_0+\sigma T_1)}-j\frac{\tilde{c}}{\rho A}\tilde{\omega}_0A_0(T_1)e^{j\tilde{\omega}_0 T_0}+cc, \end{aligned} \tag{6.4.28}$$

where *cc* is the complex conjugate of the preceding terms.

To eliminate the secular terms,

$$-2j\tilde{\omega}_0A_0'(T_1)+\frac{\phi_0}{\rho A}e^{j\sigma T_1}-j\frac{\tilde{c}}{\rho A}\tilde{\omega}_0A_0(T_1) = 0. \tag{6.4.29}$$

Then, let $A_0(T_1) = \frac{1}{2}\alpha e^{j\theta}$ where α and θ are real functions of T_1. Substituting $A_0(T_1)$ into (6.4.29) gives

$$-2j\tilde{\omega}_0(\frac{1}{2}\alpha'e^{j\theta}+\frac{1}{2}\alpha j\theta'e^{j\theta})-\frac{\tilde{c}}{\rho A}j\tilde{\omega}_0(\frac{1}{2}\alpha e^{j\theta})+\frac{\phi_0}{\rho A}e^{j(\sigma-\delta)T_1} = 0.$$

If the ε^1 order terms are dropped and the dependence of δ on α is noted,

$$\begin{aligned} &-j\omega_0\alpha'+\omega_0\alpha\theta'+\frac{\phi_0}{\rho A}\cos((\sigma-\delta(\alpha))T_1)-\theta) \\ &\qquad -\frac{1}{2}j\omega_0\frac{\tilde{c}}{\rho A}\alpha+j\frac{\phi_0}{\rho A}\sin((\sigma-\delta(\alpha))T_1-\theta)) = 0. \end{aligned} \tag{6.4.30}$$

Let $\gamma=(\sigma-\delta(\alpha))T_1-\theta$, then $\theta' = (\sigma-\delta(\alpha))-\delta'(\alpha)\alpha'T_1-\gamma'$. Then the real part of (6.4.30) yields

$$\omega_0\alpha(\sigma-\delta(\alpha)-\delta'(\alpha)\alpha'T_1-\gamma') = -\frac{\phi_0}{\rho A}\cos\gamma. \tag{6.4.31}$$

The imaginary part of (6.4.30) is

$$\omega_0(\alpha'+\frac{1}{2}\frac{\tilde{c}}{\rho A}\alpha) = \frac{\phi_0}{\rho A}\sin\gamma. \tag{6.4.32}$$

To determine the character of solutions, first the singular points are located and then the motion in neighborhoods of the singular points is examined. Because the amplitude and phase are not changing at a singular point, the response of the system is said to be in steady-state motion. The nature of the trajectories in the neighborhoods of singular points shows whether a small perturbation in the steady state motion decays or grows; that is, they illustrate the stability of the steady-state motion.

Steady-state motions occur when $\alpha' = \gamma' = 0$, which corresponds to the singular points. From (6.4.31) and (6.4.32), they correspond to the solutions of equations

$$\frac{\tilde{c}}{2\rho A}\alpha = \frac{\phi_0}{\rho A\omega_0}\sin\gamma, \quad -\alpha(\sigma-\delta(\alpha)) = \frac{\phi_0}{\rho A\omega_0}\cos\gamma. \tag{6.4.33}$$

Combining the squares of the above two equations gives

$$\left(\frac{\tilde{c}^2}{(2\rho A)^2}+(\sigma-\delta(\alpha))^2\right)\alpha^2 = \frac{\phi_0^2}{(\rho A)^2\omega_0^2}\ . \tag{6.4.34}$$

Equation (6.4.34) shows the relationship between the amplitude α of the first mode and the detuning parameter σ. For the linear system, $\delta = 0$. In this case, if the damping coefficient c and forcing remain constant, this relation is the same as illustrated in Figure (6.1).

From the steady-state equations (6.4.33), γ, α and θ are expressed as

$$\begin{gathered}\gamma = -\tan^{-1}\left(\frac{\tilde{c}}{2\rho A(\sigma-\delta(\alpha))}\right) = -\tan^{-1}\left(\frac{\tilde{c}\,\omega_0\alpha}{\sqrt{4\phi_0^2-\tilde{c}^2\omega_0^2\alpha^2}}\right)\\ \alpha = \frac{2\phi_0}{\tilde{c}\,\omega_0}\sin\gamma, \quad \theta = (\sigma-\delta(\alpha))T_1-\gamma.\end{gathered} \tag{6.4.35}$$

Hence, the first order approximation of η_0 is

$$\eta_0 = A_0(T_1)e^{j\omega_0 T_0} + O(\varepsilon^2) = \frac{1}{2}\alpha e^{j\beta}e^{j\omega_0 T_0} + O(\varepsilon^2) = \frac{\phi_0 \sin\gamma}{\tilde{c}\,\omega_0}e^{j(\Omega t-\gamma)} + O(\varepsilon^2).$$

The real part is

$$\eta_0(t) = \frac{2\phi_0\sin\gamma}{\tilde{c}\,\omega_0}\cos(\Omega t-\gamma) + O(\varepsilon^2). \tag{6.4.36}$$

For the other modes, from (6.4.23), the real part is

$$\eta_r(t) = R_r\cos(\Omega t-\varphi_r) + O(\varepsilon^2),\ r = 1,2,3... \tag{6.4.37}$$

From (6.4.37), it can be seen that $\eta_r(t)$ is composed of two harmonic terms, ω_r and ω_0. The amplitude of ω_0 harmonic term is of order $O(\varepsilon)$.

Next, consider the normalized contact boundary condition (4.1.2),

$$\tilde{w}''''(L,t) - \beta\tilde{w}(L,t) + \beta_1\tilde{w}^2(L,t) + \beta_2\tilde{w}^3(L,t) = 0\,.$$

Using a modal expansion

$$\tilde{w}(L,t) = \sum_{r=0}^{\infty}\tilde{W}_r(L)\eta_r(t) = \sum_{r=0}^{\infty}\tilde{W}_r(L)(\eta_{r0}+\varepsilon\eta_{r1}+\varepsilon^2\eta_{r2}+O(\varepsilon^3)) \tag{6.4.38}$$

From (6.4.36) and (6.4.37), and because Ω is very close to ω_0 as in (6.4.25), the amplitudes of the Ωt harmonic terms are

$$\alpha = \frac{2\phi_0\sin\gamma}{\tilde{c}\,\omega_0}, \tag{6.4.39}$$

and.

$$a_r = R_r = \frac{\varepsilon\phi_r\sqrt{(\omega_r^2-\omega_0^2)^2+c^2\omega_0^2}}{(\omega_r^2-\omega_0^2)^2}, \quad r = 1,2,3... \tag{6.4.40}$$

Then, (6.4.38) becomes

$$\tilde{w}(L,t) = \sum_{r=0}^{\infty}\tilde{W}_r(L)\eta_r(t) = \tilde{W}_0(L)\alpha\cos(\Omega t-\gamma) + \sum_{r=1}^{\infty}\tilde{W}_r(L)a_r\cos(\Omega t-\theta_r)\,, \tag{6.4.41}$$

Note that a_r is $O(\varepsilon)$, such that first order approximation is

$$\tilde{w}(L,t) = \tilde{W}_0(L)\alpha\cos(\Omega t - \gamma) + O(\varepsilon). \qquad (6.4.42)$$

Using (6.4.42), a similar characteristic equation like (4.3.18) is found by the method of harmonic balance in section (4.3). Thus,

$$\left(\frac{\tilde{W}_0''''(L)}{\beta\tilde{W}_0(L)} - 1\right) + \tilde{W}_0(L)\frac{\alpha}{\tilde{\Delta}}\sqrt{\frac{1}{32}\left(4 - \frac{\tilde{W}_0''''(L)}{\beta\tilde{W}_0(L)}\right)} = 0. \qquad (6.4.43)$$

Figure (6.1) shows the relation between excitation amplitude σ and the vibration amplitude α for the linear system. For the nonlinear system, δ is a nontrivial function of α. There are two approaches to solve equation (6.4.34): solve for α based on given σ, or, solve for σ based on given α. Because of the implicit relation of $\delta(\alpha)$ as defined in (6.4.43), the first approach is much more difficult than the second one. Further, it is highly probable that for each σ there are multiple roots for α. Here, the second approach is used. In this case, (6.4.43) is rewritten as

$$\sigma = \pm\frac{1}{\rho A}\sqrt{\frac{\phi_0^2}{\omega_0^2\alpha^2} - \frac{1}{4}\tilde{c}^2} + \delta(\alpha). \qquad (6.4.44)$$

Note that from (6.4.44), it is implied that

$$\frac{\phi_0^2}{\omega_0^2\alpha^2} - \frac{1}{4}\tilde{c}^2 \geq 0 .$$

Thus, $\alpha \leq \frac{2\phi_0}{\omega_0\tilde{c}}$, such that the maximum amplitude $\alpha_p = \frac{2\phi_0}{\omega_0\tilde{c}}$ of this system is defined. The higher the damping, the lower the maximum amplitude.

In the AFM beam vibration system, the damping coefficient c is assumed to be a known constant. If the forcing is a constant force applied at the tip end, i.e.,

$q(x,t) = Q(x)\delta(x - L)e^{i\Omega t}$, then $F_0 = \varepsilon\phi_0 = \frac{1}{\rho A}\int_0^L W_0(x)Q\delta(x-L)dx = \frac{Q}{\rho A}W_0(L)$.

Figures (6.2) to (6.5) show the results obtained from the first approach. The same system parameters of the AFM cantilever as in section 4.4 are used in the computation. In all the figures, damping $\tilde{c}$ is at 0.01. Two curves are shown in the figures, one for the linear system and the other for the nonlinear system. The symmetric curve is of the linear system and the asymmetric curve is of the nonlinear system.

Comparison of these two response curves shows that the effect of the nonlinearity is to bend the amplitude curve. Since $\delta(\alpha) < 0$, The nonlinearity has softening characteristics. In this case, the response curve bends to the left, which implies that the maximum amplitude is reached at a frequency lower than the natural frequency of the linear system.

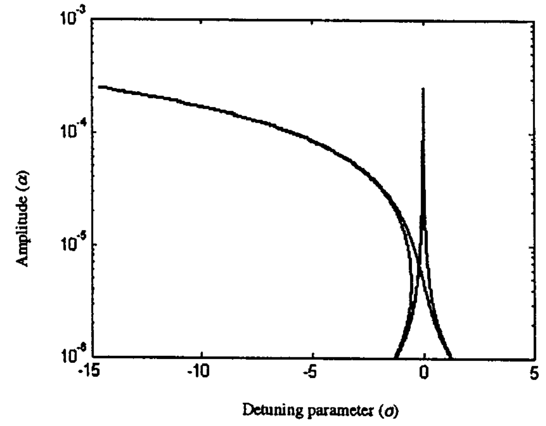

Figure 6.2. Response curve at β = 50, $\tilde{c}$ = 0.01.

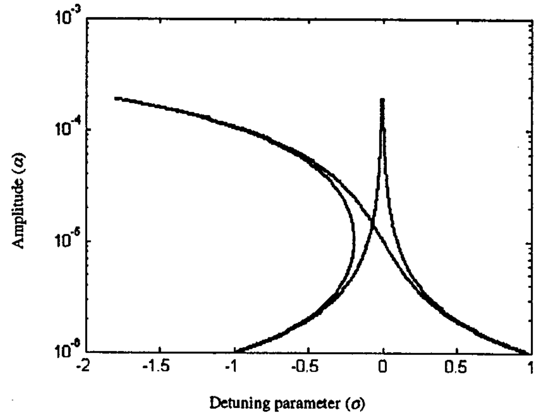

Figure 6.3. Response curve at β =500, $\tilde{c}$ = 0.01.

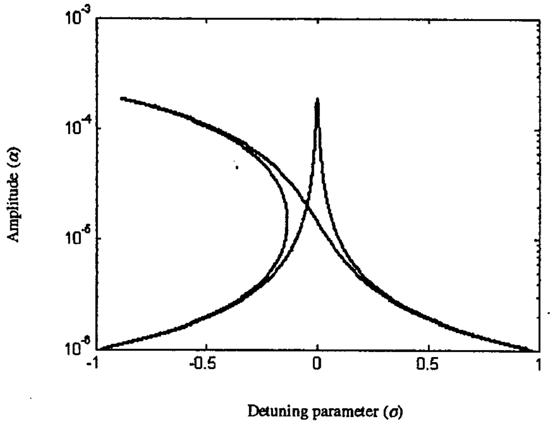

Figure 6.4. Response curve at β = 1000, $\tilde{c}$ = 0.01.

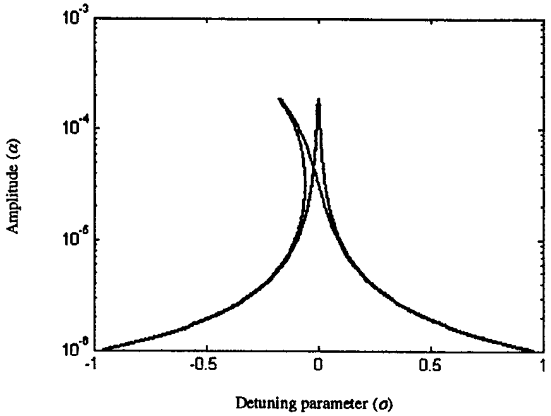

Figure 6.5. Response curve at β = 5000, $\tilde{c}$ =0.01.

Different values of β are used in the figures. The parameter β is 50, 500, 1000, 5000 in Figures (6.2), (6.3), (6.4) and (6.5), respectively. In these figures, the x-axis is σ and y-axis is α. Equation (6.4.43) generates different δ on different values of β, so the shapes of the nonlinear response curves differ from each other.

In the nonlinear response curves, multi-valued regions are formed. The multivaluedness of the response curves due to the nonlinearity has significance from the physical point of view because it leads to jump phenomenon. To explain this result, suppose an experiment is performed in which the amplitude of the excitation is held fixed, the frequency of the excitation σ is varied very slowly up and down through the linear natural frequency and the amplitude of the harmonic response is observed. The experiment starts at a frequency corresponding to point 1 on the curve in Figure (6.6).

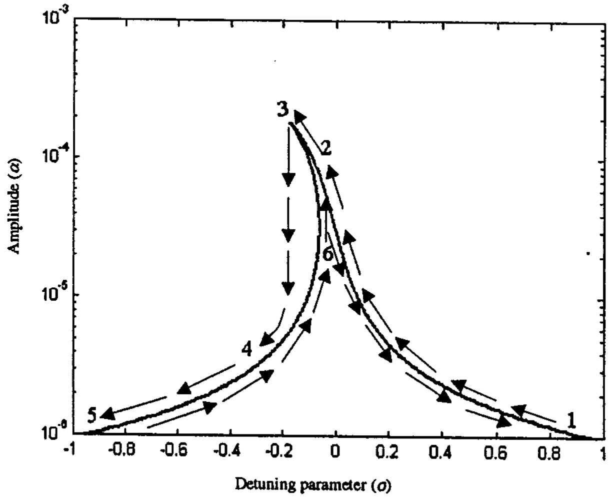

Figure 6.6. Jump phenomenon for primary response.

As the frequency is reduced, σ decreases and α increases through point 2 until point 3, the peak is reached. As σ is decreased further, a jump from point 3 to point 4 takes place with a sharply decrease in α. After point 4, α decreases along with σ.

If the experiment is started at point 5 and σ is increased, α increases slowly until point 6 is reached. After that, when σ is increased, a jump from point 6 to point 2 takes place with a sharp increase in α. Then α decreases when σ is further increased.

The maximum amplitude corresponding to point 3 is attainable only when approached from a higher excitation frequency. The portion of curve between point 3 and point 6 is unstable and hence cannot be produced experimentally [1]. The maximum amplitude is inversely proportional to damping. Figure (6.7) shows the influence of

damping on the response curve.

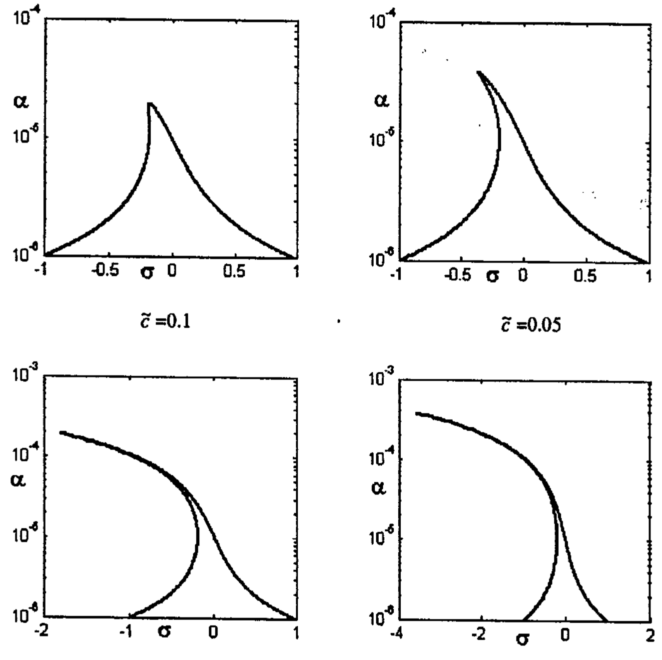

$\tilde{c}$ =0.1

$\tilde{c}$ =0.05

$\tilde{c}$ =0.01

$\tilde{c}$ =0.005

Figure 6.7. Response curve with different damping (β = 500).

The above results can easily be extended to cases when Ω is close to other natural frequencies like ω_1, ω_2, ω_3 etc. They are summarized as:

When Ω is very close to a natural frequency ω_n(n = 0,1,2,3....), then the amplitudes of mode n and other modes are

$$\alpha_n = \frac{2\phi_n}{\tilde{c}\,\omega_n}\sin\gamma_n, \quad \gamma_n = -\tan^{-1}\left(\frac{\tilde{c}}{2\rho A(\sigma-\delta_n(\alpha))}\right). \tag{6.4.46}$$

$$a_r = R_r = \frac{\varepsilon\phi_r\sqrt{(\omega_r^2-\omega_n^2)^2+c^2\omega_n^2}}{(\omega_r^2-\omega_n^2)^2}, \quad r=0,1,2,3\ldots,r\neq n \tag{6.4.47}$$

The characteristic equation for mode n is then

$$\left(\frac{\tilde{W}_n'''(L)}{\beta\tilde{W}_n(L)}-1\right)+\tilde{W}_n(L)\frac{a_n}{\tilde{\Delta}}\sqrt{\frac{1}{32}\left(4-\frac{\tilde{W}_n'''(L)}{\beta\tilde{W}_n(L)}\right)}=0. \tag{6.4.48}$$

The frequency-response relation is

$$\sigma = \pm\frac{1}{\rho A}\sqrt{\frac{\phi_0^2}{\omega_n^2\alpha^2}-\frac{1}{4}\tilde{c}^2}+\delta_n(\alpha). \tag{6.4.49}$$

In the Figures (6.8) - (6.11), the response curves of the second, third, fourth and fifth modes are plotted for $\beta = 50$ and $\tilde{c} = 0.01$.

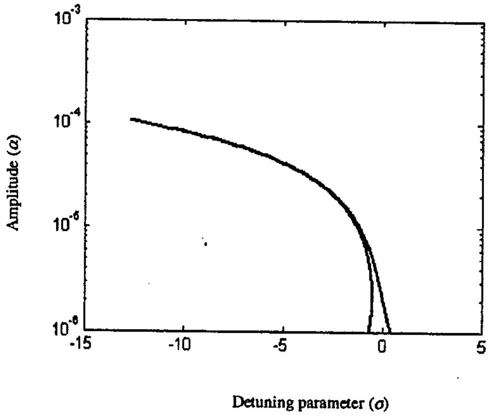

Figure 6.8. Response curve of the second mode for $\beta = 50$, $\tilde{c} = 0.01$.

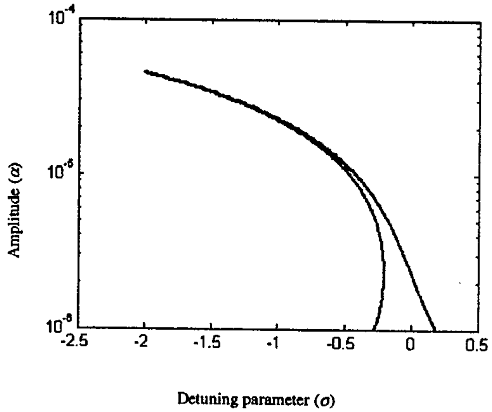

Figure 6.9. Response curve of the third mode for $\beta = 50$, $\tilde{c} = 0.01$.

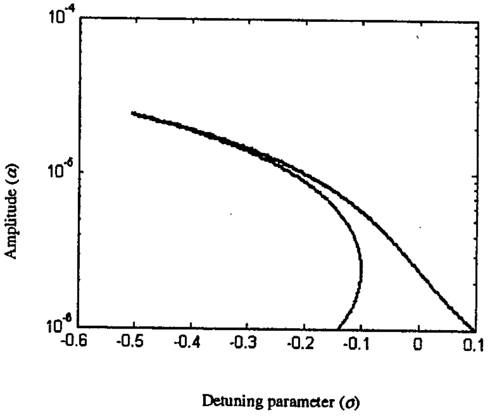

Figure 6.10. Response curve of the fourth mode for β=50, $\tilde{c} = 0.01$.

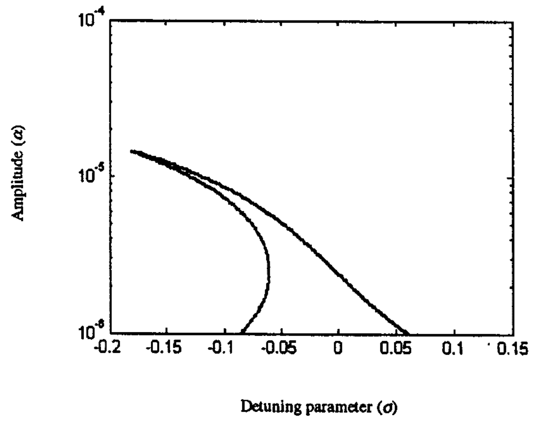

Figure 6.11. Response curve of the fifth mode for $\beta = 50$, $\tilde{c} = 0.01$.

Due to the differences in modal sensitivity, the response curves of these higher modes show different degrees of bending. At $\beta = 50$, the first mode is the most sensitive. In the response curve, its maximum is the highest among all modes.

6.4.2 Superharmonic Resonances

Superharmonic resonances occur when the driving frequency Ω is a fraction of the primary natural frequency ω_0. In this case, as for the nonresonant hard excitations, the effect of the excitation will be small unless its amplitude is hard. That is, unless $Q(x)$ is $O(1)$ instead of $O(\varepsilon)$. Thus, the order ε^1 equations are

$$D_0^2\eta_{r0} + \tilde{\omega}_r^2\eta_{r0} = N_r e^{j\Omega T_0}. \tag{6.4.50}$$

The general solution of (6.4.50) can be written as

$$\eta_{r0} = A_r(T_1)e^{j\omega_r T_0} + \Lambda_r e^{j\Omega T_0}, \quad \Lambda_r = \frac{N_r}{\omega_r^2 - \Omega^2}. \tag{6.4.51}$$

With the solution as (6.4.51), combined with the method of harmonic balance, the contact boundary condition will yield a relation of the wave number and driving frequency. By the method of harmonic balance, the solution is written as

$$w(x,t) = W(x)(A_0 + A_1\cos(\omega t) + A_2\cos(2\omega t) + \Lambda\cos\Omega t). \tag{6.4.52}$$

It is assumed that Λ is $O(A_1)$, and A_0, A_2 are both $O(A_1^2)$.

6.4.2.1 $\Omega = \omega_0/2$

In this case, $2\Omega = \omega_0 + \varepsilon\sigma$. Substituting (6.4.52) into boundary condition and dropping the higher order terms gives

$$\begin{aligned} A_0 &= -\frac{\beta_1\tilde{W}^2(L)(A_1^2+\Lambda^2)}{2(\tilde{W}'''(L)-\beta\tilde{W}(L))}, \\ A_2 &= -\frac{\beta_1\tilde{W}^2(L)A_1^2}{2(\tilde{W}'''(L)-\beta\tilde{W}(L))}. \end{aligned} \tag{6.4.53}$$

The characteristic equation is

$$[\tilde{W}'''(L)-\beta\tilde{W}(L)]A_1 + \beta_1\tilde{W}^2(L)[A_1(2A_0+A_2)+\frac{1}{2}\Lambda^2 e^{j\sigma T_1}] + \beta_2\tilde{W}^3(L)\frac{3}{4}A_1^3 = 0.$$

Hence,

$$\begin{aligned} &2[\tilde{W}'''(L)-\beta\tilde{W}(L)]^2 A_1 + \beta_1\tilde{W}^2(L)[\frac{1}{2}\Lambda^2 e^{j\sigma T_1} - A_1\beta_1\tilde{W}^2(L)(3A_1^2+\Lambda^2)] \\ &\qquad + \frac{3}{2}\beta_2\tilde{W}^3(L)A_1^3(\tilde{W}'''(L)-\beta\tilde{W}(L)) = 0. \end{aligned} \tag{6.4.54}$$

Equation (6.4.54) can be written in the form

$$\begin{aligned} [\tilde{W}'''(L)-\beta\tilde{W}(L)]^2 &= \frac{3}{32}\beta^2\tilde{W}^4(L)(\frac{A_1}{\tilde{\Delta}})^2\left(1-\frac{1}{3\beta}\left(\frac{\tilde{W}'''(L)}{\tilde{W}(L)}-\beta\right)\right) \\ &\qquad -\frac{\beta\tilde{W}^2(L)\Lambda^2}{16\tilde{\Delta}}\left(\frac{e^{j\sigma T_1}}{A_1}-\frac{\beta\tilde{W}^2(L)}{2\tilde{\Delta}}\right) \end{aligned} \tag{6.4.55}$$

For simplicity, designate the three parts in (6.4.55) as $qlin(\gamma)$, $qfree(\gamma)$, and $qforced(\gamma)$ respectively, then $qlin(\gamma) = qfree(\gamma) + qforced(\gamma)$.

Note that the first parts of equation (6.4.55) are same as that of (4.3.12), but the last part accounts for the driving forces. From equation (6.4.55) it is possible to solve the wave numbers of this nonlinear vibration system.

Let the first root of equation (4.3.12) be γ_0 and the first root of equation (6.4.55) be $\tilde{\gamma}_0$. Due to the forcing factor, these two roots ought to be different. Denote this difference as $\tilde{\gamma}_0 = \gamma_0 + \xi$, in which ξ is very small. Then

$qlin(\gamma_0) = qfree(\gamma_0)$,

$qlin(\tilde{\gamma}_0) = qfree(\tilde{\gamma}_0) + qforced(\tilde{\gamma}_0)$.

By expansion, $qlin(\tilde{\gamma}_0) = qlin(\gamma_0) + \xi qlin'(\gamma_0) + O(\xi^2)$, and

$qfree(\tilde{\gamma}_0) = qfree(\gamma_0) + \xi qfree'(\gamma_0) + O(\xi^2)$, and

$qforced(\tilde{\gamma}_0) = qforced(\gamma_0) + \xi qforced'(\gamma_0) + O(\xi^2)$.

Since $qforced'(\gamma_0) = 0$,

$$\xi qlin'(\gamma_0) = \xi qfree'(\gamma_0) + qforced(\gamma_0) + O(\xi^2). \qquad (6.4.56)$$

Thus, ξ is approximately

$$\xi = \frac{qforced(\gamma_0)}{qlin'(\gamma_0) - qfree'(\gamma_0)} \qquad (6.4.57)$$

Let $\tilde{W}(L) = 1$ and $\tilde{W}'''(L) = \varphi(\gamma)$, then $qlin(\gamma) = (\varphi(\gamma) - \beta)^2$,

$$qfree(\gamma) = \frac{1}{32}\beta(\frac{A_1}{\tilde{\Delta}})^2(4\beta - \varphi(\gamma)),$$

$$qforced(\gamma) = -\frac{\beta\Lambda^2}{16\tilde{\Delta}}\left(\frac{e^{j\sigma T_1}}{A_1} - \frac{\beta}{2\tilde{\Delta}}\right).$$

Accordingly,

$qlin'(\gamma) = 2(\varphi(\gamma) - \beta)\varphi'(\gamma)$,

$qfree'(\gamma) = -\frac{\beta}{32}(\frac{A_1}{\tilde{\Delta}})^2\varphi'(\gamma)$,

Equation (6.4.57) can be written in the form

$$\xi = -\frac{\frac{\beta\Lambda^2}{16\tilde{\Delta}}\left(\frac{e^{j\sigma T_1}}{A_1} - \frac{\beta}{2\tilde{\Delta}}\right)}{2(\varphi(\gamma_0) - \beta)\varphi'(\gamma_0) + \frac{\beta}{32}(\frac{A_1}{\tilde{\Delta}})^2\varphi'(\gamma_0)} = \frac{\beta\Lambda^2(\beta A_1 - 2\tilde{\Delta}e^{j\sigma T_1})}{\varphi'(\gamma_0)A_1[64\tilde{\Delta}^2(\varphi(\gamma_0) - \beta) + \beta A_1^2]} \qquad (6.4.58)$$

At $\sigma = 0$, i.e., $2\Omega = \omega_0$, the variation in wave number is given by

$$\xi = \frac{\beta\Lambda^2(\beta A_1 - 2\tilde{\Delta})}{\varphi'(\gamma_0)A_1[64\tilde{\Delta}^2(\varphi(\gamma_0) - \beta) + \beta A_1^2]}. \qquad (6.4.59)$$

6.4.2.2 $\Omega = \omega_0/3$

In this case, write $3\Omega = \omega_0 + \varepsilon\sigma$. Substituting (6.4.52) into boundary condition and dropping all the higher order terms gives

$$A_0 = -\frac{\beta_1\tilde{W}^2(L)(A_1^2 + \Lambda^2)}{2(\tilde{W}'''(L) - \beta\tilde{W}(L))},$$
$$A_2 = -\frac{\beta_1\tilde{W}^2(L)A_1^2}{2(\tilde{W}'''(L) - \beta\tilde{W}(L))} \qquad (6.4.60)$$

The characteristic equation is

$$[\tilde{W}'''(L) - \beta\tilde{W}(L)]A_1 + \beta_1\tilde{W}^2(L)[A_1(2A_0 + A_2)] + \beta_2\tilde{W}^3(L)[\frac{3}{4}A_1^3 + \frac{\Lambda^3}{4}e^{j\sigma T_1}] = 0. \qquad (6.4.61)$$

Substituting (6.4.60) into (6.4.61) gives

$$2[\tilde{W}''''(L)-\beta\tilde{W}(L)]^2A_1-3\beta_1^2\tilde{W}^4(L)A_1^3 \\ +\frac{3}{2}\beta_2\tilde{W}^3(L)(A_1^3+\Lambda^3e^{j\sigma T_1})(\tilde{W}''''(L)-\beta\tilde{W}(L))=0. \tag{6.4.62}$$

Thus,

$$[\varphi(\gamma_0)-\beta]^2=\frac{\beta}{32}(\frac{A_1}{\tilde{\Delta}})^2(\varphi(\gamma_0)-4\beta)-\frac{\beta}{32}(\frac{\Lambda^3}{\tilde{\Delta}^2A_1})e^{j\sigma T_1}(\varphi(\gamma_0)-\beta) \tag{6.4.63}$$

and

$$\xi=\frac{-\beta\Lambda^3e^{j\sigma T_1}(\varphi(\gamma_0)-\beta)}{\varphi'(\gamma_0)[64(\varphi(\gamma_0)-\beta)\Delta^2A_1-\beta(A_1^3-\Lambda^3e^{j\sigma T_1})]}. \tag{6.4.64}$$

At $\sigma = 0$, i.e., $3\Omega = \omega_0$, the variation in wave number is given by

$$\xi=\frac{-\beta\Lambda^3(\varphi(\gamma_0)-\beta)}{\varphi'(\gamma_0)[64(\varphi(\gamma_0)-\beta)\Delta^2A_1-\beta(A_1^3-\Lambda^3)]}. \tag{6.4.65}$$

6.4.3 Subharmonic Resonances

Two cases of subharmonic resonances are studied. The driving frequencies are $2\omega_0$ and $3\omega_0$ respectively. Following similar procedures as in previous section, analytical results for these cases can be attained.

6.4.4 Combination Resonances ($\Omega = \omega_0 + \omega_1$)

In this case, write $\Omega = \omega_0 + \omega_1 + \varepsilon\sigma$. Now write

$$w_1(x,t)=W_1(x)(A_0+A_1\cos(\omega_0t)+A_2\cos(2\omega_0t)+\Lambda_1\cos(\Omega t)),$$

$$w_2(x,t)=W_2(x)(A_0^*+A_1^*\cos(\omega_0t)+A_2^*\cos(2\omega_0t)+\Lambda_2\cos(\Omega t)).$$

Then, by the characteristic equation,

$$A_0=-\frac{\beta_1\tilde{W}_1^2(L)(A_1^2+\Lambda_1^2)}{2(\tilde{W}_1''''(L)-\beta\tilde{W}_1(L))},\quad A_0^*=-\frac{\beta_1\tilde{W}_2^2(L)(A_1^{*2}+\Lambda_2^2)}{2(\tilde{W}_2''''(L)-\beta\tilde{W}_2(L))}, \\ A_2=-\frac{\beta_1\tilde{W}_1^2(L)A_1^2}{2(\tilde{W}_1''''(L)-\beta\tilde{W}_1(L))},\quad A_2^*=-\frac{\beta_1\tilde{W}_2^2(L)A_1^{*2}}{2(\tilde{W}_2''''(L)-\beta\tilde{W}_2(L))}, \tag{6.4.66}$$

The two characteristic equations are

$$(\tilde{W}_1''''(L)-\beta\tilde{W}_1(L))+\beta_1\tilde{W}_1^2(2A_0+A_2) \\ +\left(\frac{A_1^*}{A_1}\right)\beta_1\tilde{W}_2^2(L)\Lambda_2e^{j\sigma T_1}+\beta_2\tilde{W}_1^3(L)\frac{3}{4}(A_1^2+2\Lambda_1^2)=0, \tag{6.4.67}$$

and

$$(\tilde{W}_2''''(L)-\beta\tilde{W}_2(L))+\beta_1\tilde{W}_2^2(2A_0^*+A_2^*) \\ +\left(\frac{A_1}{A_1^*}\right)\beta_1\tilde{W}_1^2(L)\Lambda_1e^{j\sigma T_1}+\beta_2\tilde{W}_2^3(L)\frac{3}{4}(A_1^{*2}+2\Lambda_2^2)=0. \tag{6.4.68}$$

In the above two equations, the amplitudes are coupled.

7 Conclusions

7.1 Material Properties Measurement

The interaction forces between the AFM sensor tip and the sample surface are highly nonlinear. This nonlinearity brings in some interesting phenomena in the AFM vibrations. Our interest lies in the intricate relationship between the vibration behavior of the AFM cantilever and the sample material properties, like Young's modulus, and surface properties such as adhesion. The AFM has the capability of nanometer resolution measurement of these properties. Also, the contact resonance frequencies can be used to determine the Young's modulus of surfaces and the tip-sample interaction damping.

The tip-sample interaction forces are nonlinear and are the subject of intensive research. There are different theories to describe the contact forces; some of them are briefly discussed in chapter 2. In this thesis, mainly two contact mechanics theories, the Hertzian theory and the Maugis theory, were used. The numerical results based on the Hertzian contact theory are presented.

Some nonlinear approximation methods were used for analytical solutions. The method of harmonic balance and the method of multiple scales are applied throughout the research. Results for the linearized problem as well as the nonlinear problem are presented. One obvious observation is that, at the presence of the nonlinear contact boundary condition, the resonance frequency is related to the vibration amplitude and the frequency shift is clearly visible. This frequency shift is further shown to be dependent on the elastic material property (Young's modulus) of the sample surface. Both the free vibration and the forced vibration with damping are studied.

Previous works [4][5][6][7] are mainly concerned about the first resonance frequency and generally use a simplified point-mass model for the AFM cantilever. These results show limited success in material characterization. In this thesis, beam theory is used in analyzing the vibrations of AFM cantilever. The higher vibration modes are studied and the frequency shifts of these modes as a function of vibration amplitude is clearly presented. Also, the effect of interaction damping is explored. It is shown that interaction damping must be considered because it can significantly change the modal sensitivity.

In the case of forced vibration, primary response as well subharmonic and superharmonic responses is studied. It is shown that due to nonlinearity in contact boundary condition, the response curves shift from the linear system. Jump phenomena are also observed.

7.2 Discussions on the Limitations of this Research

Based on the contact mechanics theories, such as the Hertzian contact theory and the Maugis contact theory as discussed in this thesis, some material properties of the sample surface can be quantitatively determined by measuring the resonance frequency of the AFM cantilever.

However, it is possible that the macroscopic models used in this thesis, which treat the AFM cantilever as a homogeneous elastic beam and consider no plastic deformation and material transfer between the tip and the sample surface, may not accurately describe the contact at nanometer scale. Also, the contact interaction between the AFM tip and the sample surface is very complicated. The contact mechanics theories applied in this thesis are just approximate. Further work needs to be done to study the different contact mechanics theories especially the Maugis contact theory.

Another cause for loss of precision is that in the theoretical model the sensor tip is assumed to be massless and fixed at the end of the AFM cantilever beam. The total mass of the tip is very small and generally negligible. However, in real AFM, the sensor tip is some distance away from the beam end. Usually this distance is about 3-10% of the full length. Some examples are shown in Table 7.1.

Table 7.1. Distance of the sensor tip from the cantilever end [27]
Data of the rectangular cantilevers made of monocrystalline silicon.

	Cantilever			
	1	2	3	4
Distance δ (μm)	25	29	18	7
Full Length (μm)	475	262	248	142
Ratio (%)	5.26	11	7.26	4.9

In Ref [6], the distance between the sensor tip and the cantilever end is not neglected and the characteristic equation for the AFM cantilever with linearized boundary condition is given as

$$\begin{aligned}&\frac{\kappa}{k_c}[-(\cosh k_nL_1\sin k_nL_1-\sinh k_nL_1\cos k_nL_1)(1+\cos k_nL'\cosh k_nL')\\&\quad+(\cosh k_nL'\sin k_nL'-\sinh k_nL'\cos k_nL')(1-\cos k_nL_1\cosh k_nL_1)]\\&\qquad=\frac{2}{3}(k_nL_1)^3(1+\cos k_nL\cosh k_nL),\end{aligned}$$

where L_1 is the length between the tip and the cantilever base, L' is the length from the tip to the end of the cantilever, L is the full length: $L=L_1+L'$.

When the distance L_1 is relatively small, like cantilevers 1 and 4 in Table 7.2 at about 5% of the total length, the effect may not be significant. But for those cantilevers with a higher distance-to-full-length ratio, the distance can no longer be neglected and the theoretical model must be adjusted.

Another important factor is the geometry of the AFM cantilever. It is shown that the frequency shift of the resonances caused by the tip-sample contact elasticity is highly

dependent on the geometry of the AFM cantilever [7]. Because of this fact, cantilevers with a simple and well-defined geometry are preferred. In this thesis, numerical results are attained on the AFM cantilever with uniform rectangular cross section. However, the AFM cantilevers of other shapes such as the V-shape or triangular etc are used extensively. The theoretical model in this thesis is valid for these cantilever shapes too.

In the discussion of the forced vibration with damping, the damping coefficient c is treated as a constant. However, this is most likely not the case experimentally. Generally speaking, c is related to the vibration frequency.

In this thesis, the AFM cantilever is assumed to be a homogeneous elastic beam. No plastic deformation is assumed. However, it is highly probable that the AFM cantilever will undergo certain level of plastic deformation. Thus the dynamic behavior will be different is plastic effects are considered. Depending on the material property of the AFM, the plastic deformation varies.

Also, some research suggested that some material exchange and chemical reaction happens between the AFM sensor tip and the sample surface, especially when the sample is a biological or volatile material. In this case, the contact interactions may not be accurately described by the contact mechanics theory.

7.3 Future Work

Due to the limited time and resources available, there is no sufficient experimental data at hand to verify the numerical results attained in this thesis. At the next stage of this research, experiments with AFM will be performed.

In this thesis, numerical results are attained for cantilevers with uniform rectangular cross section. There are AFM cantilevers of other shape such as triangular or V-shape. It is necessary to carry out further research into the different cantilever geometries.

Approximation methods like the harmonic balance method and the method of multiple scales are used to solve the nonlinear vibration problem. This problem can also be solved numerically from the partial differential equation. It will perhaps provide some useful information. Finite element analysis is one method for solving numerically this nonlinear vibration problem. The results from FEM can be used to attest the work in this thesis.

The Hertzian contact theory is used in this thesis to model the contact interaction between the AFM sensor tip and the specimen surface. This is a relatively simple model that does not take into consideration the surface forces. The contact interactions are very complicated and there are still intensive researches in this field. It will be greatly helpful if there are more sophisticated and accurate theoretical models to account for all the aspects of the contact forces.

References:

1. G. Binning, and C. F. Quate, "Atomic Force Microscope," *Physical Review Letters*, Vol. **56**, 930-933 (1986).
2. A. H. Nayfeh and D. T. Mook, *Nonlinear Oscillations*, Wiley, New York, (1979).
3. K. Johnson, *Contact Mechanics*, Cambridge University Press, (1985).
4. J. A. Turner, S. Hirsekorn, U. Rabe, and W.Arnold, "High-frequency response of atomic-force microscope cantilevers," *Journal of Applied Physics*, Vol. **82**, 966-979 (1997).
5. U. Rabe, K. Janser, and W. Arnold, "Vibrations of free and surface-coupled atomic force microscope cantilevers: Theory and experiment," *Review of Scientific Instruments*, Vol. **67**. 3281-3293 (1996).
6. U. Rabe, S. Amelio, E. Kester, V. Scherer, S. Hirsekorn, and W. Arnold, "Quantitative determination of contact stiffness using atomic force acoustic microscope," *Ultrasonics*, Vol. **38**, 430-437 (2000).
7. U. Rabe, E. Kester, and W. Arnold, "Probing Linear and Non-linear Tip-Sample Interaction Forces by Atomic Force Acoustic Microscopy," *Surface and Interface Analysis* Vol. **27**, 386-391 (1999).
8. L. Meirovitch, *Principles and Techniques of Vibrations*, Prentice Hall, New York (1997).
9. K. Yamanaka, H. Ogiso, and O. Kolosov, "Ultrasonic force microscopy for nanometer resoultion subsurface imaging," *Applied Physics Letters*, Vol. **64**, 178-180 (1994).
10. D. Sarid, *Scanning Force Microscopy*, Oxford University Press, New York, (1991).

11. P. Maivald, H. J. Butt, S. A. Gould, C. B. Prater, B. Drake, J. A. Gurley, V. B. Elings, and P. K. Hansma, "Using Force Modulation to Image Surface Elasticities with the Atomic Force Microscope," *Nanotechnology*, Vol. **2**, 103 (1991).
12. F. Oulevey, G. Gremaud, A. Semoroz, A. J. Kulik, N. A. Burnham, E. Dupas, and D. Gourdon, "Local mechanical spectroscopy with nanometer-scale lateral resolution," *Review of Scientific Instruments*, Vol. **69** 2085-2094 (1998).
13. H. U. Krotil, T. Stifter, H. Waschipky, K. Weishaupt, S. Hild, O. Marti, "Pulsed force mode: a new method for the investigation of surface properties," *Surface Interface Analysis*, Vol. **27**, 336-340 (1999).
14. P. Vairac, B. Certin, in: P. Tortoli, L. Masotti (Editors), *Acoustical Imaging*, Vol. **22**, 701, Plenum Press, New York (1996).
15. E. Chilla, T. Hesjedahl, H. J. Frohlich, "Scanning acoustic force detection of SAWs," *IEEE Ultrasonics Symposium Proceedings*, IEEE, 363-366 (1994).
16. K. Yamanaka, S. Nakano, "Quantitative elasticity evaluation by contact resonance in an atomic force microscope," *Applied Physics A* Vol. **66**, S313-S317 (1998).
17. K. L. Johnson, K. Kendall, and A. D. Roberts: *Proc. R. Soc. Lond. A*, Vol. **324**, 301 (1971).
18. S. Nakano, R. Maeda, K. Yamanaka, "Evaluation of the elastic properties of a cantilever using resonance frequencies," *Japanese Journal of Applied Physics*, Vol. **36**, 3265-3266 (1996).
19. K. Yamanaka, T.Tsuji, A. Noguchi, T. Koike and T. Mihara, "Nanoscale elasticity measurement with in situ tip shape estimation in atomic force microscopy," *Review of Scientific Instruments*, Vol. **71**, No. 6, 2403-2408 (2000)

20. O. Kolosov, and K. Yamanaka, "Nonlinear detection of ultrasonic vibration in an atomic force microscope," *Japanese Journal of Applied Physics*, Vol. **32**, L 1095- L 1098 (1993).
21. M. Pakdemirli, and A. H. Nayfeh, "Nonlinear Vibrations of a Beam-Spring-Mass System," *Journal of Vibration and Acoustics*, Vol. **116**, 433-439 (1994).
22. T. Watanabe, "Forced Vibration of Continuous System with Nonlinear Boundary Conditions," *Journal of Mechanical Design*, Vol. **100**, 487-491 (1978).
23. M. I. Qaisi, "Application of the Harmonic Balance Principle to the Nonlinear Free Vibration of Beams," *Applied Acoustics*, Vol. **40**, 141-151 (1993).
24. D. P. Hess, A. Soom, "Normal Vibrations and Friction Under Harmonic Loads: Part I – Hertzian Contacts," *Journal of Tribology*, Vol. **113**, 80-86 (1991).
25. M. D. Bryant, "Nonlinear Forced Oscillation of a Beam Coupled to an Actuator via Hertzian Contact," *Journal of Sound and Vibration*, Vol. **99**(3), 403-414 (1985).
26. H. J Butt, M. Jaschke, "Calculation of Thermal Noise in Atomic Force Microscopy," *Nanotechnology*, Vol. **6**, 1-7 (1995).
27. Park Scientific Instruments, *User's Guide to AutoProbe CP*, **Part I**, (1998).
28. Park Scientific Instruments, *User's Guide to AutoProbe CP*, **Part II**, (1998).
29. D. Maugis, *Contact, Adhesion and Rupture of Elastic Solids*, Springer, Berlin, New York, (2000).
30. J. A. Turner and J. S. Wiehn, "Sensitivity of atomic force microscope vibration modes to changes in surface stiffness," under review for *Nanotechnology* (to appear, 2001).

Modeling the Dynamics of Atomic Force Microscope Cantilevers

by

Joshua S. Wiehn

A THESIS

Presented to the Faculty of
The Graduate College of the University of Nebraska
In Partial Fulfillment of Requirements
For the Degree of Master of Science

Major: Engineering Mechanics

Under the Supervision of Joseph A. Turner

Lincoln, Nebraska

November, 2001

Modeling the Dynamics of Atomic Force Microscope Cantilevers

Joshua S. Wiehn, M.S.

University of Nebraska, 2001

Adviser: Joseph A. Turner

The atomic force microscope (AFM) was initially developed to provide topography information of a sample surface. Advancements have led to the development of new measurement techniques that exploit the dynamic properties of the AFM cantilevers (probes). In this thesis, models are developed for various AFM cantilevers. These models provide information about the flexural and torsional vibrations modes of the cantilevers and their sensitivity to changes in the stiffness of the sample surface. Closed-form expressions are derived for cantilevers with constant cross-sections. For nonuniform AFM cantilevers, such as those with a triangular shape, the Rayleigh-Ritz method is used to develop an approximate solution. The interaction between the cantilever and the sample surface is approximated as a linear spring, such that linear vibration theory may be used for the analysis. This simplification restricts the results to experiments involving low-amplitude excitations. Comparisons between the models and experimental results are made and the limitations of the models are discussed. It is anticipated that these models will aid in the selection of cantilevers and the specific vibration modes necessary for obtaining optimal measurements using the AFM. From the resonance frequency measurements, information regarding the material properties of the sample surface may also be obtained.

Acknowledgements

This research was sponsored by the Air Force Office of Scientific Research under Grant No. F49620-99-1-0254. The views and conclusions contained herein are those of the authors and should not be interpreted as necessarily representing the official policies or endorsements, either expressed or implied, of the Air Force Office of Scientific Research or the U.S. Government. Support of the Center for Electro-Optics at the University of Nebraska-Lincoln is also gratefully acknowledged.

First, I would like to thank my advisor Dr. Joseph A.Turner for his direction and support in this research. I would also thank my final exam committee members Dr. Ruqiang Feng and Dr. Jiashi Yang, Department of Engineering Mechanics, for their input and evaluation of this thesis. In addition, I would like to thank all the people who were involved in this research. Mr. Baowei Wei, Mr. Kangzhi Shen, and Ms. Roshanak Nilchiani, have offered many creative ideas and suggestions. I would also like to thank Dr. Y. Joe Zhou and Dr. Kit Lee at the Microscopy Core Research Facility for their assistance in examining the atomic force microscope cantilevers.

Most importantly, I would like to thank Rebecca for her love and understanding throughout this work. I would also like to thank our families for the support they provided.

Finally, I would like to dedicate this thesis to my late grandfather, Mr. Leonard J. Wiehn. His lasting memory inspired me to pursue and complete my Masters degree.

Contents

List of Figures

List of Tables

Chapter 1

Introduction

The atomic force microscope (AFM) was developed to provide high-resolution images of sample surface topography [1]. The topography is measured by scanning the AFM probe over the surface of the sample and then measuring the relative motion between the AFM probe and the sample surface. The displacement of the AFM probe, as it is scanned over the sample surface, is caused by the interaction between the tip of the probe and the sample surface. The probe used in an AFM is a cantilever beam with an attached tip. The AFM probes are typically rectangular or triangular in form. Throughout the rest of this thesis the probe used in the AFM will be referred to only as a cantilever.

Recent advancements with the AFM have utilized the dynamic properties of the AFM. These advancements have allowed the AFM to be used for material characterization. Standard commercial AFMs are able to operate in two primary dynamic modes, which are non-contact mode and "tapping" mode. In non-contact mode the AFM cantilever is excited slightly below a natural vibration frequency and in "tapping" mode the cantilever is excited above a natural vibration frequency. The advantages of the dynamic modes are that damage of the sample surface is greatly reduced, higher scanning speeds can be achieved, and noise associated with the cantilever displacement signal is reduced. Higher flexural vibration modes have also been shown to be more sensitive to force gradients between the AFM cantilever and the sample surface [2]. Modifications to commercial AFMs have led to the development of other dynamics methods, which include atomic force acoustic microscopy (AFAM) [3],[4] and ultrasonic force microscopy (UFM) [5]. AFAM and UFM can be used to measure the stiffness of the sample surface. These dynamic methods rely on the dynamic response of the AFM cantilevers. It has been demonstrated that the AFM cantilevers can be treated as continuous members with appropriate vibration modes [6].

The interaction between the AFM cantilever tip and the sample surface is nonlinear and difficult to model. The many flexural and torsional vibration modes experienced by the cantilever when in contact with a sample surface must be included in the dynamic analysis of the cantilever. To combat the nonlinear interaction between the cantilever and the sample the amplitude of the sample surface motion must be kept small. This allows the nonlinear interaction to be linearized about some equilibrium point. The dynamics of the AFM cantilever can then be modeled as a beam with a linear spring attached near the end of the beam. The measured natural frequencies of the beam in contact with the sample surface are then used to define the interaction stiffness between the AFM cantilever tip and the sample surface. Interaction models, such as the Hertzian model or the Maugis model [7], can then be used to relate the interaction stiffness to the Young's modulus of the sample surface.

The AFM cantilever plays an important role in measurements taken using dynamic AFM modes of operation. The information regarding the AFM cantilevers provided by the manufacturers is not always accurate. The parameters governing the dynamic response of the cantilevers can vary due to the conditions in which they are manufactured. Therefore, it is appropriate to calibrate the cantilevers before use. The plan view dimensions of the cantilevers can be measured using optical techniques, and the thickness of the cantilevers can be calculated from the free natural frequencies of the beam or measured by using an electron microscope. These measured parameters can then be used to determine the stiffness of the AFM cantilevers.

1.1 Objective

The objective of this research is to develop a model for various AFM cantilevers that provides information about the dynamics of the cantilevers and can also be used to determine material properties of different samples. Closed-form expressions are derived for cantilevers with constant cross-sections. For nonuniform AFM cantilevers, such as those with a triangular shape, the Rayleigh-Ritz method is used to develop an approximate solution. Flexural and torsional vibration modes are examined. The modal sensitivity, which defines the relative change in frequency of a vibration mode due to changes in the sample surface stiffness, is also derived for uniform and nonuniform AFM cantilevers.

The exact results for the uniform AFM cantilever provide a validation for the approximate method developed using the Rayleigh-Ritz method. The exact and approximate results show good comparison with previous methods developed to determine the stiffness of AFM cantilevers. The uniform and nonuniform cantilever models provide good results in comparison with frequencies measured in and out of contact with the sample surface. The stiffness of the sample surface will be calculated using the models and compared to results obtained form the Hertzian contact theory. The application of these models for evaluating the Young's modulus of elasticity for a sample surface will also be discussed. The modal sensitivity of different types of cantilevers will be discussed along with their usefulness for AFM measurements. Results using the dynamic AFM technique of atomic force acoustic microscopy (AFAM) will be presented to show how this technique can provide more information about the sample surface, other than topography information.

The remainder of this thesis is organized into five chapters. Chapter 2 provides an introduction to atomic force microscopy and an overview of the interactions between the AFM probe and the sample surface. Chapter 3 contains the equations governing the vibration response and modal sensitivity of the cantilevers. Chapter 4 contains the equations necessary to describe the approximate vibration response for uniform and nonuniform cantilevers using the Rayleigh-Ritz method. The approximate modal sensitivity is derived and example calculations are provided to aid in a comparison of the different cantilever shapes. Chapter 5 contains the experimental vibration response of four different cantilever shapes. Contact stiffness results are obtained from the experimental results and the use of the cantilever models for obtaining information about the material properties of the sample surface is discussed. Chapter 6 is the final chapter, in which the results of this thesis are discussed and future areas of study are addressed.

Chapter 2

Atomic Force Microscopy

2.1 Introduction

In this chapter, the origin of the atomic force microscope is introduced. A description of the different modes of operation for the AFM will be presented along with an overview of the interaction between the tip of the cantilever and the sample surface. Contact theories used to describe the tip-sample interaction will also be presented.

The AFM was developed by Binning, Quate, and Gerber in 1986 [1]. It is one of many scanning probe microscopes that were derived from the scanning tunneling microscope (STM), which was also developed by Binning and co-workers [8]. The STM was the first instrument able to produce images of surfaces with atomic resolution.

To better understand the motivation for the AFM, the STM must first be examined. To image a sample surface the STM uses a sharp tip made of a conductive material. A voltage is applied between the tip and sample. When the tip is brought close to the sample surface, typically within the range of about 10 Å, electrons from the sample begin to "tunnel" through the gap between the tip and sample into the tip or sample, depending on the polarity of the voltage applied between the tip and sample. This phenomenon is depicted in Figure 2.1. The image of the sample surface is created by monitoring the tunneling current between the tip and sample, which varies with tip-sample spacing. For this imaging method to work, the tip and sample must be made of either conductive or semiconductive materials [8]. Insulating materials can not be imaged with the STM. Due to this limitation, Binning, Quate, and Gerber developed the AFM.

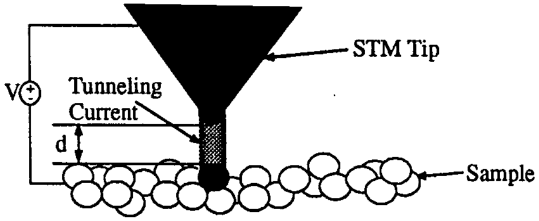

Figure 2.1: Tip and sample interaction for the STM. The voltage, *V*, applied between the tip and the sample creates a tunneling current. The variation in the current as the tip travels along the sample surface is used to produce an image of the sample surface [8].

In developing the AFM, ideas were taken from the STM and the stylus profilometer. The stylus profilometer is similar to the STM, in that it is used to generate images of a sample surface. The stylus profilometer uses a stylus mounted on a cantilever beam to scan along the surface of the sample. The main disadvantage of the stylus profilometer is that for rough surfaces the stylus can damage the sample as it is scanned over the surface. The cantilever beam used in the stylus profilometer is one of the most important components of the AFM. A tip mounted near the end of the cantilever beam will encounter forces as the tip nears the sample surface. These forces will cause the cantilever beam to deflect. Thus, it is important to use cantilever beams flexible enough to produce the maximum deflection for any force, but still stiff enough to minimize the sensitivity to vibrational noise from the surrounding area where the AFM is located [1]. The deflection of the cantilever beam was measured with an STM in the original AFM. The setup for the original AFM is shown in Figure 2.2.

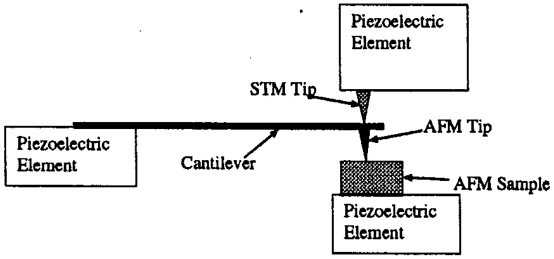

Figure 2.2: The schematic arrangement for the original AFM [1]. The displacement of the cantilever is measured with the STM. The piezoelectric elements can be used in different measurement techniques to control the movement of the AFM sample, STM tip, or the cantilever.

The STM tip, in Figure 2.2, is mounted on a piezoelectric element, which is used to move the tip in order to maintain a constant tunneling current while scanning over the sample surface. A feedback loop is used to control the STM tip, which is used to maintain a constant force acting on the AFM cantilever as the cantilever tip is in contact with the sample. Another arrangement involves the use of a feedback loop to control the position of the sample, which will enable the deflection of the cantilever to be kept constant. The signals from either of the feedback loops are plotted as a function of the scan directions to produce a constant force image of the sample surface [1],[9].

Advancements in the design of the AFM have led to new methods for measuring the deflection of the cantilevers, which include: the use of optical heterodyne interferometry, use of optical position-sensitive detectors, capacitance detection, and fiber optic interferometry [9]. Most commercial AFMs use the optical position-sensitive photodetectors (PSPD). The most common setup for commercial AFMs is shown in Figure 2.3(a). In this arrangement, a laser beam is reflected off the cantilever and onto a PSPD consisting of photodiodes divided into two halves or four quadrants. As the cantilever bends, the position of the reflected laser beam on the detector shifts. The difference between the signals of the photodiodes indicates the position of the laser spot on the detector and thus the angular deflection of the cantilever. The PSPD can measure displacements of light as small as 10 Å. The split PSPD, shown in Figure 2.3(b), can only measure the vertical deflection of the cantilever by monitoring the signals from each photodiode; the four quadrant PSPD, shown in Figure 2.3(c), can measure both the lateral and vertical deflections. The ratio of the distance between the cantilever and the detector to the length of the cantilever produces a magnification of the cantilever motion. The system can therefore measure sub-angstrom displacement of the cantilever tip [10].

2.2 AFM Cantilever Fabrication

The most important component of the AFM is the cantilever used to probe the sample surface. The cantilevers tend to be very small and are fabricated using microlitho-

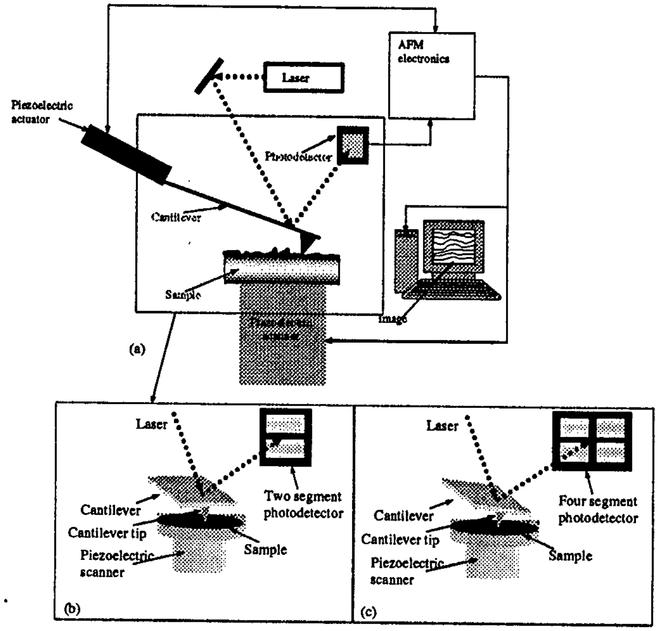

Figure 2.3: (a) Setup of AFM feedback electronics and optical detection scheme. (b) Detection setup for vertical cantilever displacements. (c) Detection setup for both vertical and lateral cantilever displacements.

graphy processes similar to those used to make computer chips. The tips protruding from the end of the cantilever are usually made of silicon nitride (Si_3N_4) or silicon (Si). The tip is typically a few microns long and less than 100 Å in diameter after fabrication. The cantilevers typically measure 100 to 300 μm in length, 10 to 50 μm in width, and 0.3 to 4 μm in thickness. Varying the dimensions of the cantilevers allows the effective stiffness of the cantilevers to vary within the range 0.01-50 N/m. Cantilevers with low stiffness are typically used to probe soft samples, while cantilevers with high stiffness are used to probe hard samples. Higher stiffness cantilevers are also used in dynamic AFM measurements for determining the nanomechanical properties of the sample surface. The shape of the tip and the effective stiffness of the cantilever are critical parameters in AFM measurements [11].

Conventional microfabrication methods have been used to create cantilevers suitable for use in the AFM. The cantilevers are generally formed from Si, SiO_2, and Si_3N_4 films. Figure 2.4 shows the steps needed to create cantilevers from thermally grown SiO_2 films and from Si_3N_4 films grown by low-pressure chemical vapor deposition (LPCVD). These materials are widely used because of their good mechanical properties and because techniques for working with these materials have been well established in industry[12].

The process starts with a deposition of the desired film (Si_3N_4 or SiO_2) on each side of a Si (100) wafer. The film is then patterned with photolithography to form openings on the top and bottom of the wafer, as shown in Figure 2.4(a-b). The layout of the cantilever is arranged so the openings are aligned with the (111) planes of the Si wafer. A self-terminating anisotropic Si etchant is then used to free the cantilever and remove the portion of the Si wafer up to the (111) planes, as shown in Figure 2.4(c). At this stage of the process,

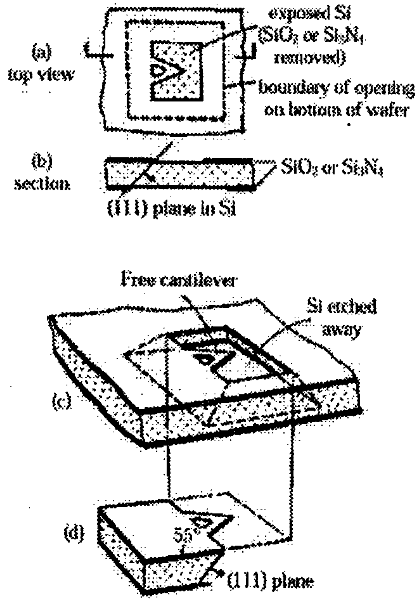

(a-b). The shape of the cantilever(s) and opening to remove the cantilever are patterned on either side of a Si (100) wafer using thin films of SiO_2 or Si_3N_4.

(c). Enchant that terminates at the (111) planes is used to undercut the cantilever(s).

(d). A small chip is cut from the Si wafer to aid in the handling and mounting of the cantilever in the AFM.

Figure 2.4: Steps for fabricating AFM cantilevers [12].

the freely suspended cantilever is coated with a thin metallic layer to increase its optical reflectivity. The final step involves cutting the Si wafer into manageable chips with a cantilever or array of cantilevers protruding from the end of the chip [12],[10]. It should be noted that the physical parameters of the cantilevers depend on the conditions in which the cantilevers are fabricated. These parameters can vary depending on a number of kinetic factors such as the gas ratio and temperature used in fabrication. The Young's modulus (E) for any given group of cantilevers can vary within the range of 150±30 GPa. An example of a commercial chip with cantilevers used in the AFM is shown in Figure 2.5. As shown in Figure 2.5, AFM cantilevers are made in two primary shapes, rectangular and triangular. The main advantage of the triangular cantilevers is that they are less susceptible to twisting as compared with the rectangular cantilevers. The rectangular cantilevers are easier to work with from a theoretical standpoint, because of their uniform cross-section.

Most cantilevers used with the AFM are fabricated with tips attached at the end of each cantilever, as depicted in Figure 2.5. The three most common tip shapes are pyramidal, conical, and tetrahedral. The tips are fabricated through processes involving the masking of the Si substrate with Si_3N_4 or SiO_2 films and then etching away the Si to create a post or pit, which will be used to form the tip. The remaining post material is etched to form conical or tetrahedral tips, and the pits are filed with the same cantilever material used to form pyramidal tips [12], [14]. When the tips have been formed, the cantilevers are then fabricated in the same process outlined in the preceding paragraph.

The tips of the cantilever play an important role in the imaging resolution obtainable with the AFM. Depending on the sample being examined, the appropriate tip must

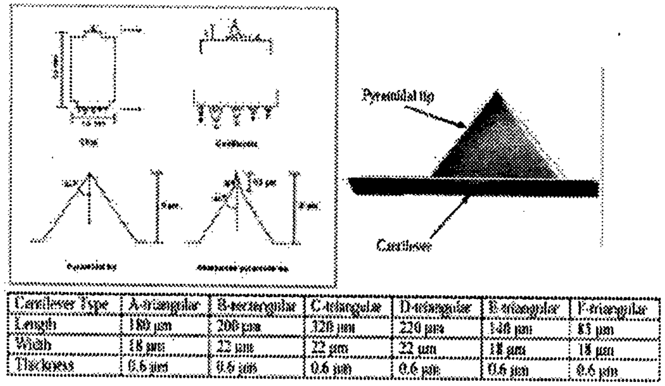

Cantilever Type	A-triangular	B-rectangular	C-triangular	D-triangular	E-triangular	F-triangular
Length	180 µm	200 µm	320 µm	220 µm	140 µm	85 µm
Width	18 µm	22 µm	22 µm	22 µm	18 µm	18 µm
Thickness	0.6 µm	0.6 µm	0.6 µm	0.6 µm	0.6 µm	0.6 µm

Figure 2.5: Specifications for AFM cantilevers called Microlevers fabricated by ThermoMicroscopes [13].

be used in order to be able to examine all the detail of a sample surface. Very sharp tips can be used to probe samples with high variations in topography, and less sharp tips can be used to probe flatter surfaces [15]. The interaction forces between the cantilever and sample surface are experienced through the tip of the cantilever. The tips of the cantilevers become dull with use in AFM measurements. Figure 2.6(a) shows a SEM image of an AFM cantilever tip that has been used in AFM measurements, and Figure 2.6(b) shows an unused AFM cantilever tip. The radius of the used AFM cantilever tip is approximately 250 nm, and the radius of the unused AFM cantilever tip is approximately 40 nm. The imaging resolution will be reduced as the tip becomes damaged and dull. Besides the decrease in imaging resolution, the increase in the tip radius also has an influence on the tip-sample interaction forces controlling the cantilever motion. These interaction forces can be repulsive with a sharp tip, but can become attractive with a dull tip [16]. It is therefore important to monitor the wear of the cantilever tip.

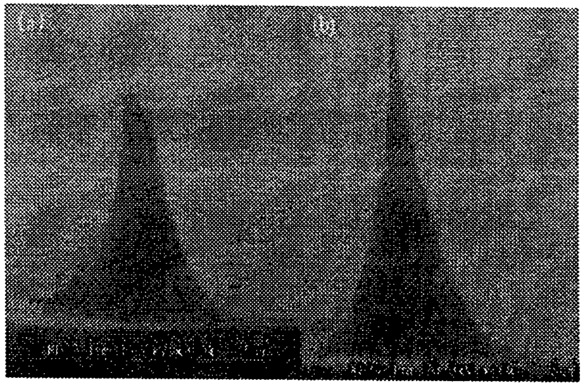

Figure 2.6: (a) AFM cantilever tip after a number of uses. (b) An unused AFM cantilever tip.

2.3 Tip-Sample Interaction Forces

The cantilever can be used to probe many different types of forces, depending on the mode in which the AFM is operated. Some forces that cause the cantilever to deflect include van der Waals, capillary, adhesive, frictional, capacitive, electrostatic, and magnetic forces. The tip-sample interaction forces can be classified as either attractive or repulsive, and either short or long range. At tip-sample spacings below 2 to 3 Å, the interaction forces are repulsive and short range. A representative plot of the tip-sample interaction force as a function of the tip-sample separation, for AFM experiments operated in ambient conditions,

is depicted in Figure 2.7.

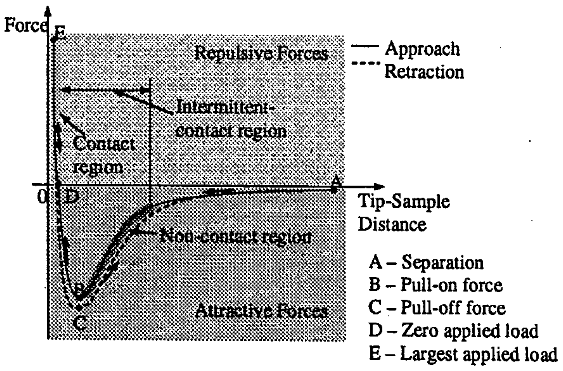

Figure 2.7: A typical force vs. tip-sample distance curved observed in AFM experiments [11],[17].

One parameter that must be defined before discussing the interaction forces experienced by the cantilever is the effective spring constant of the cantilever. The effective spring constant is the ratio of the applied force at the end of the cantilever to the maximum end deflection of the cantilever. The effective spring constant for a uniform cantilever can be defined as

$$k_c = \frac{3EI}{L^3},$$

where E is Young's modulus of elasticity, I is the area moment of inertia, and L is the total length of the cantilever [18].

Tip-sample interaction force measurements begin with the cantilever at a rest position (point A on Figure 2.7) far away from the sample surface. As the tip-sample separation is decreased, the cantilever bends toward the sample due to attractive surface forces. When the cantilever or sample is moved further, the attractive force gradient exceeds the effective spring constant of the cantilever and the cantilever jumps into contact with the sample, point B on Figure 2.7. This point is where the cantilever experiences a maximum deflection; this deflection multiplied by the effective spring constant of the cantilever is the pull-on force. As the cantilever and sample are brought even closer together, the attractive forces begin to weaken and the cantilever is deflected backward through a position of zero applied load (point D) at a distance of a few angstroms. Beyond this point, the force becomes repulsive and the atoms of the cantilever tip and the sample surface are in contact. The repulsive force balances any force that attempts to push the atoms together. This fact means that when the cantilever pushes the tip against the sample surface, the beam bends rather than forcing the tip atoms closer to the sample surface. It should be noted that besides bending, the tip and sample may experience local elastic or plastic deformations [17]. In the region on the curve where the force changes from attractive to repulsive, the atoms at the apex of the tip can experience a strong repulsive force, while the atoms further from the tip can experience an overall attractive force. This occurrence can lead to a deformation of the cantilever tip [19]. The tip-sample separation is decreased to a predetermined distance, corresponding to the maximum applied load (point E). At this position the cantilever tip or the sample surface is retracted. The tip-sample separation again reaches a position of zero applied load (point D); beyond this position the interaction forces become attractive. In this region of the curve, the forces are a short-range type. These forces are strongly repulsive at a short distance and slightly attractive at a long distance. Therefore, the short-range repulsive forces are more sensitive to changes in the tip-sample separations than the long-range attractive forces evident in the attractive (negative) region in Figure 2.7. The force experienced by the cantilever upon retraction reaches a maximum at point C on the curve. The maximum force is the pull-off force and is generally greater than the pull-on force. After this point the cantilever or sample are further retracted from each other to the position where separation occurs (point A) [17],[20]. The details of the force vs. tip-sample separation curve, as shown in Figure 2.7, can vary depending on the physical properties of the cantilever tip and sample and also on the medium in which the tip and sample are immersed. For instance, immersion of the tip and sample in polar liquids can reduce the van der Waals forces by more than two orders of magnitude, with respect to the value of the force in vacuum, at small tip-sample separation [21],[22]. The physical parameters of the tip and sample have a large influence in the repulsive (positive) region. In this region the mechanical response of the sample depends on the hardness of the sample and tip and also on the effective spring constant of the cantilever [10].

2.3.1 van der Waals Forces

The interatomic van der Waals force is dominate at large tip-sample separations [18],[19]. As the tip-sample separation decreases, the tip-sample interaction can be dominated by adhesive forces, capillary forces, frictional forces, or chemical interactions. The van der Waals forces are dispersion forces that act between atoms. They are caused by the instantaneous moments that occur between otherwise nonpolar atoms and molecules. These forces are called dispersion forces because they are associated with the dispersion of light in matter. The magnitude of these forces is in the range of 1-20 nN and can extend from 2 Å to more than 1000 Å [23].

2.3.2 Capillary Forces

The capillary force is the force exerted on the tip of the cantilever by the water layer present on the sample surface in ambient conditions. The tip of the cantilever is wetted by the liquid contamination layer, forming a capillary between the tip and the sample surface that holds the tip in contact with the sample surface. The capillary layer also increases the effective contact area between the cantilever tip and the sample surface, which decreases the imaging resolution of the AFM. The magnitude of this force is in the range of 10-100 nN. This force will remain constant as long as the tip is in contact with the sample surface because the tip-sample separation is virtually incompressible. The hysteresis present in Figure 2.7 can be partially attributed to the capillary force. Further separation of the tip from the sample surface is necessary to break the capillary and free the tip from the sample surface. The capillary force can be made negligible by operating the AFM in a vacuum, in a chamber filled with a dried gas, or by immersing the tip and sample in a liquid medium [10],[17].

2.3.3 Adhesive Forces

From Figure 2.7, the adhesive force is the maximum cantilever deflection (point C) during retraction multiplied by the effective spring constant of the cantilever. This force is proportional to the pull-off force needed to separate the cantilever tip from the sample surface [20]. The adhesion of two different materials and the cohesion of two similar materials can be examined by looking at the contact area between the two materials. In the case of the AFM, the contact area between the cantilever tip and the sample surface is examined. The adhesive force can be calculated by multiplying the contact area by the work needed to separate the tip from the sample surface. Measurements of the adhesive forces should be conducted in a vacuum, dried gas filled chamber, or immersed in a liquid medium. These conditions will help eliminate the effects of the capillary forces between the cantilever tip and sample surface present in most ambient conditions [22],[23].

2.3.4 Frictional Forces

Frictional forces are lateral forces experienced by the cantilever as it is scanned over the sample surface. These forces can be caused by any differences in the sample material and also by changes in the slope of the sample topography. The frictional forces cause the cantilever to deflect torsionally. Measurements of the twisting deflections of the cantilever can be used to determine the magnitude of the frictional forces. For moderate loads (in the range of 10-80 nN) the frictional force is proportional to the normal forces that the tip encounters. In the low load range, the relationship between the frictional force and the normal force is nonlinear. This nonlinearity is due to the adhesive and capillary forces present on the sample surface [10].

2.3.5 Capacitative Forces

The capacitative forces are attractive forces experienced by the cantilever tip due to changes in the capacitance between the tip and sample surface as the tip is scanned over the sample surface. The capacitance is measured by applying a voltage between the tip and sample. The capacitance depends on the dielectric constant of the medium between the tip and the sample surface. As the thickness of this medium varies with the topography of the sample surface the capacitance changes, which in turn causes the cantilever to deflect [17].

2.3.6 Electrostatic Forces

Electrostatic forces are attractive forces produced by static charges present on a sample surface. The electrostatic force is measured by applying a voltage between the cantilever tip and the sample surface, with both the cantilever and sample being made of conductive material. The applied voltage between the cantilever tip and the sample surface adds an attractive force between the tip and sample. As the cantilever tip is scanned over the sample surface, the cantilever deflects when it encounters a static charge on the sample surface [17],[24].

2.3.7 Magnetic Forces

The magnetic force is a material dependent force. Typically, a cantilever coated with a ferromagnetic film is used to probe magnetic surfaces. The attractive magnetic force causes the cantilever to deflect. At small tip-sample separations the deflections of the cantilever will be primarily due to the short range attractive forces between the tip and the sample. As the tip-sample separation is increased, the magnetic forces will have a greater effect on the deflection of the cantilever. The magnitude of the magnetic force is around a few hundred nanonewtons and very similar to other long range interaction forces [10],[17].

2.4 Primary Modes of Operation for the AFM

The standard commercial AFM can operate in three main modes: contact mode, non-contact mode, and intermittent-contact mode (or tapping mode). Information about the previously stated material properties can be obtained through these three main modes of operation, but to obtain quantitative measurements of material properties the AFM must be modified for use in different modes of operation. The main modes of operation will be discussed in the following sections along with other modes used to probe different material properties. The description of the following modes of operation is related to the Thermomicroscopes Autoprobe CP AFM [13] used in the Ultrasonics and Vibrations research facility [25].

2.4.1 Contact Mode

In contact mode the cantilever tip is held in contact with the sample surface. From Figure 2.7, it is shown that the contact mode operates in the repulsive (positive) region of the force vs. tip-sample separation curve. The sample being examined is mounted on a piezoelectric scanner, which traces the cantilever tip over the sample surface. The cantilever is brought into contact by selecting a set-point PSPD value that is higher than that for a cantilever in a rest position. The repulsive forces cause the cantilever to deflect. The deflection is measured by the position-sensitive photodetector (PSPD) and used to produce a map of the sample topography. There are two different techniques used to obtain sample surface images in contact mode: constant-height mode and constant-force mode.

For the constant-height technique, the height of the piezoelectric scanner is held constant while the cantilever is scanned over the sample surface. The topography of the sample surface is obtained by examining the spatial variation of the cantilever deflection. This technique is mainly used to image atomically flat surfaces. The main advantage of this technique is that it can scan surfaces very quickly. For this reason, the constant-height technique is used to obtain real time images of changing surfaces.

The constant-force technique is used to maintain a constant force on the sample surface. The constant force is implemented by using a feedback loop to control the movement of the piezoelectric scanner in the z-direction. The feedback loop takes the input from the PSPD and adjusts the piezoelectric scanner accordingly to maintain a set tip-sample separation. The image of the sample surface is generated from the movement of the piezoelectric scanner. Depending upon the conditions in which the AFM is operated, the forces exerted on the sample surface by the cantilever tip can vary from one to several hundred nanonewtons. The constant-height technique can scan a sample quicker than this technique, but this technique is the more widely used AFM technique [10],[11].

2.4.2 Non-contact mode

Non-contact AFM (NC-AFM) is a dynamic scanning mode in which the cantilever is oscillated near the sample surface. A feedback loop is used in the AFM electronics to maintain an amplitude ratio of A_{sp}/A_0, where A_0 is the free oscillation amplitude of the cantilever and A_{sp} is the set-point amplitude. During scanning, the oscillation amplitude of the cantilever is controlled by adjusting the vertical position of the sample. The cantilever is oscillated near its first resonance frequency with a small amplitude of 10-900 Å. The interaction forces between the cantilever tip and the sample surface cause changes in the

resonance frequency and oscillation amplitude of the cantilever. This mode operates in the attractive (negative) region on the force vs. tip-sample separation curve, as shown in Figure 2.7. The effective spring constant of the cantilever varies with the force gradient experienced by the cantilever as it is scanned over the sample surface. The force gradient is the derivative of the force vs. tip-sample separation curve. The attractive forces cause the resonance frequency to decrease while repulsive force interactions cause an increase in the resonance frequency. These changes in the resonance frequency of the cantilever provide information about the changes in the force gradient, which in turn provides information about the topography of the sample surface. The average total force between the cantilever tip and the sample surface is about 0.001 nN. This force is considerably smaller than that experienced in the contact mode. Depending on the sensitivity of the equipment used to measure the NC-AFM signal, sub-angstrom resolution can be achieved.

Another phenomenon experienced with this mode and other dynamic AFM modes is damping. Damping decreases the amplitude and phase of the cantilever displacement signal [26]. Damping is greatly dependent upon the environment in which the AFM is operated and the sample being examined. The shape of the cantilever and the distance between the cantilever and the sample surface also plays a role in damping [27]. Damping is comprised of forces acting along the length of the cantilever and at the cantilever tip. The forces may also be time dependent as the air below the cantilever is displaced with the oscillatory movement of the cantilever [28]. The transition between the attractive and repulsive force regimes is dependent upon damping. An increase in damping leads to an increase in the attractive tip-sample interaction forces which helps decrease the presence of hysteresis upon tip retraction from the sample surface. Damping can be a significant deterrent to the attainable imaging resolution with NC-AFM.

The main disadvantage of NC-AFM is that the low forces experienced in this mode are more difficult to measure as compared with those encountered in contact mode. In this mode stiffer cantilevers are used as opposed to those used in contact mode because stiffer cantilevers are less likely to be pulled into contact with the sample surface. The combination of the stiff cantilever and the weak interaction forces produce small signals which are difficult to measure. The tip or sample are less likely to degrade in this mode as opposed to contact mode because the tip contact with the sample surface is minimal as surfaces are scanned. The advantages of this mode over contact mode is that softer materials can be examined and better imaging resolution can be achieved because this mode is more sensitive to the force gradient experienced between the cantilever and sample surface [11].

2.4.3 Intermittent-contact Mode

The intermittent-contact mode (IC-AFM), also referred to as tapping mode, is similar to non-contact mode except that the cantilever is brought closer to the sample surface. The cantilever tip weakly comes into contact with the sample surface at the bottom of its oscillation cycle. The IC-AFM operates in the region between the contact mode and the non-contact mode on the force vs. tip-sample separation curve in Figure 2.7. Imaging of the sample surface is obtained by monitoring the change in the cantilever's oscillation amplitude as the tip-sample separation changes [11].

The contact of the cantilever tip and the sample surface is a very nonlinear interaction. For most of the cantilever's oscillation cycle the cantilever is not influenced by

external forces, but as the oscillating cantilever approaches the sample surface it is first influenced by a weak long-range attractive forces. The attractive forces will increase as the cantilever tip gets closer to the sample surface, which will cause a decrease in the free resonant frequency and oscillation amplitude of the cantilever. As the tip touches the sample surface an abrupt repulsive force is exerted on the cantilever. This repulsive force acts for a short period of the oscillation cycle. After impacting the sample surface, the cantilever bounces off the sample surface and continues its oscillation cycle [29],[30].

The main advantages of this mode over non-contact mode is that it is more useful for imaging larger scan areas that could include extreme variations in sample topography. IC-AFM eliminates some of the limitations experienced in using contact and non-contact modes [11].

2.5 Modes Used for Material Characterization

The AFM has been used to measure more than just the topography of a sample surface since it was first developed. Over the years the AFM has been used to measure materials properties like hardness, atomic-scale friction, elastic modulus, and adhesion. It can also be used to probe electrical, thermal, and magnetic properties of sample surfaces. It has become a useful tool for examining the nanoscale material properties of polymers, thin films, composite materials, and microelectromechanical systems (MEMS). For material property measurements, the primary modes of operation for the AFM have been adapted into new measurement techniques that allow the simultaneous collection of topography and material property information for a sample.

Specific AFM techniques have been developed to measure material properties other than elastic modulus and adhesion. Different techniques are needed to study the variations in surface friction and topology, the variations in magnetic and electrically charged surface structures, the thickness of dielectric materials, and the thermal properties of a sample. These AFM techniques are summarized in Table 2.1. Dynamic AFM techniques, which involve the oscillation of the cantilever or sample, have been used to examine the variations in elastic modulus and adhesion on a sample surface. These techniques can be used for material characterization and also for material evaluation. To fully utilize these techniques the nonlinear tip-sample interaction forces must be modeled. With an appropriate tip-sample interaction force model, the material parameters can be calculated from the measurements taken using the AFM. A description of the dynamic AFM techniques used for evaluating the elastic material characteristics and adhesion are summarized in Table 2.2.

2.6 Tip-sample Contact Theories

Different contact theories can be used to model the tip-sample interaction, which is very complex and generally nonlinear. Bodies in contact deform according to their elastic and inelastic properties. In general, it is difficult to describe these contact deformations because the stress distribution in the solids depends on the surface interaction, which in turn is dependent upon the exact shape of the deformation [7],[10]. The diameter of the tip-sample contact area present in some AFM measurements is in the range of several nanometers. Nanomechanical sample surface property information can be obtained through the use of a contact theory to model the tip-sample contact.

Table 2.1: AFM modes used to measure material properties such as surface friction, thermal conductivity, magnetism, capacitence, and the variation in elctrically charged domains.

AFM Modes	Description	Material Property Measured
Lateral Force Microscopy (LFM) or Friction Force Microscopy (FFM)	Operates in contact mode and uses a photodetector arrangement, as shown in Figure 2.3(b), to measure both the lateral and vertical cantilever deflections. Changes in surface friction or the slope of the sample surface will cause the cantilever to deflect laterally [10],[11].	Surface friction and slope.
Magnetic Force Microscopy (MFM)	Uses a ferromagnetic tip to probe the surface of a ferromagnetic or paramagnetic sample. This technique can be used with NC-AFM or IC-AFM modes to monitor the changes in the phase and resonant frequency of the cantilever vibrations [10],[11].	Magnetic properties.
Electrostatic Force Microscopy (EFM)	A voltage is applied between a conductive cantilever tip and sample. The cantilever is moved over the sample, not touching it, and deflects when the tip moves over static charges. The deflection is monitored to produce a map of the surface charge density [11],[24].	Electrical charge density.
Scanning Capacitance Microscopy (SCM)	Operates in NC-AFM mode to maintain a constant tip-sample separation. A voltage is applied between the cantilever tip and the sample surface. The cantilever deflects because of changes in the capacitance between the tip and sample surface [11].	Tip-sample capacitance, which depends on dielectric thickness.
Scanning Thermal Microscopy (SThM)	Operates in NC-AFM mode. The cantilever is made of two different metals or a resistive thermal element. The sample surface is probed and the cantilever deflects when changes in the material thermal conductivity are encountered [11].	Thermal conductivity.

Table 2.2: AFM modes used to measure elastic material properties and adhesion.

AFM Mode	Description
Atomic Force Acoustic Microscopy (AFAM)	The sample is oscillated at a frequency in the range of 1-15 MHz, chosen to be above the first flexural resonance frequency of the cantilever. The oscillation of the sample causes the cantilever to vibrate as the cantilever probes the sample surface. The amplitude of the cantilever deflection signal is monitored. Changes in the tip-sample interaction due to variations in the sample surface elastic and adhesive properties produce changes in the amplitude of the signal [3],[4].
Ultrasonic Force Microscopy (UFM)	Similar to AFAM, except the cantilever is oscillated instead of the sample. This allows for the large, heavy, or irregulary shaped samples to be examined. The cantilever is oscillated by a signal with a frequency in the range of 0.1-10 MHz. This signal excites the higher-order vibration modes of the cantilever. A high-frequency photodetector can be used to monitor the deflection of the cantilever or the detection electronics of a standard commercial AFM can be used by amplitude-modulating the driving signal for the cantilever at a frequency in the range 1-10 kHz. The amplitude and phase of the cantilever deflection signal are monitored to provide information about variations in the sample surface elastic properties and adhesion [31],[32].
Force Modulation Microscopy (FMM)	Operates in constant-force contact mode. The cantilever tip or sample is modulated with a low amplitude signal. The frequency of the signal is typically a few hundred kilohertz. Amplitude of the cantilever deflection is measured in order to detect the variation in the elastic properties of the sample. The phase shift of the signal is measured to provide information about the viscoelastic properties of the sample [10],[11].
Heterodyne Force Microscopy (HFM)	The sample and cantilever are both oscillated. The cantilever is oscillated at a frequency of ω_1 and the sample is oscillated at a frequency ω_2. The tip-sample separation is then modulated at a frequency $\omega_1 - \omega_2$. The cantilever deflection signal at this frequency is monitored. Changes due to variations in the tip-sample interaction produce changes in the phase and amplitude of the signal. The changes in the signal amplitude provide information about the elastic and adhesive properties of the sample surface, while changes in the phase provide information about the viscoelastic and also the adhesive properties of the sample surface [33].

The contact theories that will be discussed in the following sections include, the Hertzian contact model, the DMT model developed by Derjaguin, Muller, and Toporov, the BCP model developed by Burnham, Colton, and Pollock, the JKRS model developed by Johnson, Kendall, Roberts, and Sperling, and the Maugis model. The contact problem involving the AFM is depicted in Figure 2.8. The objective of these theories is to relate the applied load p to the indentation depth δ of the cantilever tip into the sample surface. Important variables used in the discussion of these theories are the radius of the tip-sample contact area a, the work of adhesion evaluated at the tip-sample contact ϖ, and the stress in the cohesive zone σ_0. The geometry important to this problem are shown in Figure 2.9.

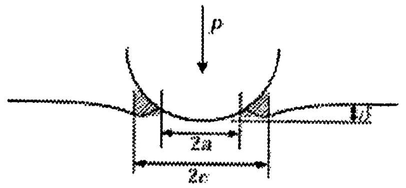

Figure 2.8: The arrangement for the contact problem. The applied load p results in an indentation depth of δ. The contact radius is a and the cohesive radius is c [34].

Some common notation for each of these theories is as follows:

The reduced tip-sample curvature is defined by

$$\frac{1}{R} = \frac{1}{R_t} + \frac{1}{R_s}, \tag{2.1}$$

which accounts for the radius of the tip R_t and the radius of the sample R_s. Generally the sample is assumed flat in AFM contact problems, such that $R = R_t$. The reduced elastic

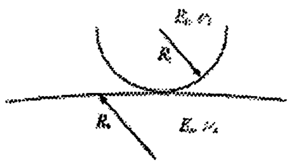

Figure 2.9: The geometry of the tip-sample contact problem. The tip parameters are represented by the subscript t and the sample parameters are represented by the subscript s.

modulus E^* for the tip-sample system is defined by

$$\frac{1}{E^*} = \left[\frac{1-\nu_t^2}{E_t} + \frac{1-\nu_s^2}{E_s}\right], \tag{2.2}$$

where E_t, ν_t, E_s, and ν_s are the Young's modulus and Poisson's ratio of the tip and sample, respectively. The contact models can also be defined in terms of the following nondimensional parameters [29]

$$\overline{A} = a\left(\frac{4E^*}{3\pi R^2\varpi}\right)^{\frac{1}{3}}, \quad \overline{P} = p\left(\frac{1}{\pi R\varpi}\right), \tag{2.3}$$

$$\overline{\Delta} = \delta\left(\frac{16E^{*2}}{9\pi^2 R\varpi^2}\right)^{\frac{1}{3}}, \quad \overline{\lambda} = 2\sigma_0\left(\frac{9R}{16\pi\varpi E^*}\right)^{\frac{1}{3}}, \tag{2.4}$$

where $\overline{A}$ represents the contact radius, $\overline{P}$ represents the applied load, $\overline{\Delta}$ represents the penetration depth, and $\overline{\lambda}$ represents the adhesion parameter.

2.6.1 Hertzian Contact Model

Hertz first analyzed the elastic contact between a sphere and a flat surface in 1888 [7],[35]. Hertz was able to relate the contact characteristics of the applied load, indentation

depth, and contact area, to the material properties of the interacting bodies, such as Young's moduli and Poisson's ratios. The Hertzian model assumes that there are no surface forces and no adhesion hysteresis ($\varpi = 0$). This model is not valid for low loads in the presence of surface forces. The relationship between the applied load, p, and the contact radius, a, is

$$p = \frac{4}{3}E^*\frac{a^3}{R}. \tag{2.5}$$

The indentation depth is related to the contact radius with the relation, $\delta = \frac{a^2}{R}$. The applied load can then be related to the indentation depth with the following [36],

$$p = \frac{4}{3}E^*\sqrt{R}\delta^{\frac{3}{2}} = K_0\delta^{\frac{3}{2}}, \tag{2.6}$$

where $K_0 = \frac{4}{3}E^*\sqrt{R}$ is defined as the Hertzian coefficient. In terms of the nondimensional parameters, Equation 2.5 and the equation relating the indentation depth to the contact radius become,

$$\overline{P}_H = \overline{A}^3, \text{ and } \overline{\Delta}_H = \overline{A}^2. \tag{2.7}$$

Equation 2.6 also becomes,

$$\overline{P}_H = \overline{\Delta}_H^{\frac{3}{2}}, \tag{2.8}$$

where the subscript, H, is used to indicate relations pertaining to the Hertzian contact model.

2.6.2 JKRS Contact Model

The JKRS model is an extension of the Hertzian model, which incorporates adhesion through the change in surface energy at the contact of the two spheres, as shown in 2.9. There are no forces between the spheres when they are not in contact [17],[37]. This model describes the short-range tip-sample interactions under the conditions of low elastic modulus and large radius of curvature. The model neglects the part of the attraction which acts outside of the periphery of the contact region. This model is appropriate for compliant samples, samples with high adhesion, and samples with large radii of curvature, but may underestimate surface forces [29].

The relationship between the applied load and the contact radius can be written as [34],

$$p = \frac{4}{3}E^{*}\frac{a^3}{R} - 2\sqrt{2\pi\varpi E^{*}a^3}. \tag{2.9}$$

The indentation depth is related to the contact radius with the relation, $\delta = \frac{a^2}{R} - 2\sqrt{\frac{\pi\varpi a}{2E^{*}}}$. In terms of the nondimensional parameters, the load and the indentation depth are related to the contact radius by,

$$\overline{P}_J = \overline{A}^3 - \overline{A}\sqrt{6\overline{A}} \text{ and } \overline{\Delta}_J = \overline{A}^2 - \frac{2}{3}\sqrt{6\overline{A}}, \tag{2.10}$$

where the subscript, J, is used to indicate relations pertaining to the JKRS model.

2.6.3 DMT Contact Model

The DMT model applies to the contact between a rigid tip and sample surface with small radii of curvature and low adhesion. This model allows surfaces to deform according to the Hertzian contact theory because the attractive forces are calculated outside the tip-sample contact area [20], [29]. The contact area may be underestimated due to the deformation having to conform to the Hertzian model.

The equation governing the applied load and contact radius is as follows [38],

$$p = \frac{4}{3}E^{*}\frac{a^3}{R} - 2\pi R\varpi. \tag{2.11}$$

The indentation depth is related to the contact radius in the same manner as in the Hertzian model, $\delta = \frac{a^2}{R}$. Therefore, the applied load is related to the indentation depth as,

$$p = K_0\delta^{\frac{3}{2}} - 2\pi R\varpi. \tag{2.12}$$

In terms of the nondimensional parameters, Equation 2.11 and the equation relating the indentation depth to the contact radius become,

$$\overline{P}_D = \overline{A}^3 - 2 \text{ and } \overline{\Delta}_D = \overline{A}^2. \tag{2.13}$$

Equation 2.12 becomes,

$$\overline{P}_D = \overline{\Delta}_D^{\frac{3}{2}} - 2, \tag{2.14}$$

where the subscript, D, is used to indicate the relations pertaining to the DMT contact model.

2.6.4 BCP Contact Model

The BCP model was developed through experimental work done with the AFM. It incorporates aspects of the Hertz, JKRS, and DMT models and is very representative of many combinations of tip-sample materials. The relationship between the applied load and the contact radius is [29],

$$p = \frac{4}{3}E^{*}\frac{a^3}{R} - \sqrt{2\varpi E^{*}a^3} - \pi R\varpi. \tag{2.15}$$

The second term in Equation 2.15 accounts for the contribution from attractive forces present between the tip and sample surface. The third term is similar to the second term in Equation 2.12 for the DMT model, except the factor of 2 is replaced with a factor of 1. The indentation depth is related to the contact radius with the relation, $\delta = \frac{a^2}{R} - \left[\frac{9\pi^2 R\varpi^2}{16E^{*2}}\right]^{\frac{1}{3}}$. In terms of the nondimensional parameters, Equation 2.15 and the equation relating the indentation depth to the contact radius become,

$$\overline{P}_B = \overline{A}^3 - \overline{A}\sqrt{\frac{3\overline{A}}{2}} - 1 \text{ and } \overline{\Delta}_B = \overline{A}^2 - 1, \tag{2.16}$$

where the subscript, B, is used to indicate the equations pertaining to the BCP contact model.

Figure 2.10 shows a comparison of the normalized applied load plotted as a function of the normalized indentation depth for the contact models summarized in the preceding sections. From Figure 2.10, it is evident that hysteresis is present in the JKRS model, while there is no hysteresis for the other models.

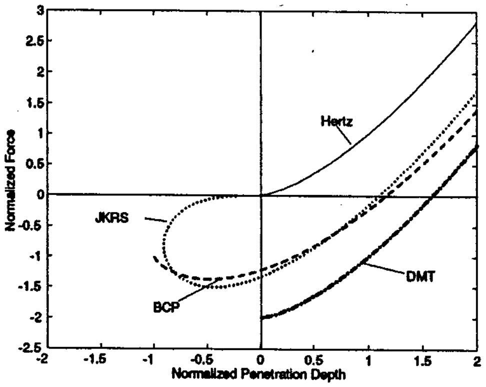

Figure 2.10: A comparison of the normalized force as a function of the normalized indentation depth for the Hertz, JKRS, DMT, and BCP contact models [7].

2.6.5 Maugis Contact Model

Maugis, in 1992, developed a more complete model for tip-sample interactions [39]. This model is applicable to systems involving high and low adhesion. The adhesion is represented by constant attractive stresses acting between the tip and the sample surface in an annular cohesive region that surrounds the contact area. This cohesive region is depicted in Figure 2.8. The relation between the applied load and the contact radius is [39]

$$p = \frac{4}{3}E^*\frac{a^3}{R} - \lambda a^2\left[\frac{16\pi\varpi E^{*2}}{9R}\right]^{\frac{1}{3}} M_1, \tag{2.17}$$

where $M_1 = \sqrt{m^2-1} + m^2\tan^{-1}\sqrt{m^2-1}$ and $m = \frac{c}{a}$. The parameter m is the ratio of the radius to the edge of the cohesive region to the radius of the contact area, as depicted in Figure 2.8. The indentation depth is related to the contact radius as,

$$\delta = \frac{a^2}{R} - \frac{4\lambda a}{3}\left[\frac{3\pi\varpi}{4E^*R}\right]^{\frac{1}{3}}\sqrt{m^2-1}. \tag{2.18}$$

A third equation is necessary to relate m, λ, and a. This third equation is the Griffith equilibrium equation, which is given by [39]

$$\frac{\lambda a^2}{2}\left[\frac{4E^*}{3\pi R^2\varpi}\right]^{\frac{2}{3}} M_2 + \frac{4\lambda a^2}{3}\left[\frac{4E^*}{3\pi R^2\varpi}\right]^{\frac{1}{3}} M_3 = 1, \tag{2.19}$$

where $M_2 = \sqrt{m^2-1} + (m^2-2)\tan^{-1}\sqrt{m^2-1}$ and $M_3 = 1 - m + \sqrt{m^2-1}\tan^{-1}\sqrt{m^2-1}$. In terms of the nondimensional parameters, Equation 2.17 and the equation relating the indentation depth to the contact radius become,

$$\overline{P}_M = \overline{A}^3 - \overline{\lambda}\overline{A}^2 M_1 \text{ and } \overline{\Delta}_M = \frac{4}{3}\overline{A}\overline{\lambda}\sqrt{m^2-1}, \tag{2.20}$$

where the subscript, M, is used in indicate the equations pertaining to the Maugis model. Equation 2.19 becomes,

$$\frac{\overline{\lambda}\overline{A}^2}{2} M_2 + \frac{4\overline{\lambda}^2\overline{A}}{3} M_3 = 1. \tag{2.21}$$

A comparison of the Maugis contact model for various values of λ is shown in Figure 2.11. A transition between the DMT model and the JKRS model is allowed through the use of λ in the Maugis contact model. As $\lambda \rightarrow 0$, the DMT limit is reached and $\overline{P} \rightarrow -2$. This limit occurs for systems with high moduli of elasticity, low adhesion, and small radius of curvature. As $\lambda \rightarrow \infty$, that is, for compliant systems with low adhesion and a large radius of curvature, the JKRS limit is reached and $\overline{P} \rightarrow 0$. Hysteresis is evident in Figure 2.11 from the curves that bend back on themselves. This behavior occurs for values of λ greater than 0.94. As this value for λ is exceeded, the cantilever tip loses contact with the sample surface because the stiffness of the cantilever exceeds the contact stiffness. When moving further on one of the curves, contact between the cantilever tip and the sample surface is reinitiated when the tensile stress in the cohesive region is greater than the compressive stress in the contact region.

2.7 Discussion

The development of the AFM as an instrument for obtaining detailed information about the topography of a sample surface was described along with the basic modes of operation and the dynamic techniques used for obtaining material property information about the sample surface in sections 2.4 and 2.5, respectively. A process for manufacturing an AFM cantilever was outlined and the possible reasons for variations in the physical parameters (i.e. modulus of elasticity and mass density) and the dimensions of the cantilever were discussed. The main reasons involve the conditions in which the cantilever is manufactured. Variations in the conditions allow the elastic modulus to vary within the

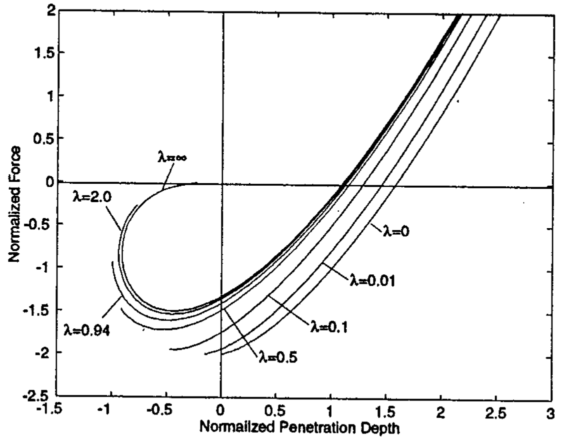

Figure 2.11: The applied load vs. penetration depth plot for various values of λ using the Maugis model [7].

range of 150±30 GPa. The different tip-sample interaction forces present in some AFM measurements was discussed and some of the different contact theories used to describe the tip-sample interaction were introduced.

Chapter 3

Governing Equations

AFM cantilevers can vibrate in four different types of modes: flexural, torsional, extensional, and Lamb. The main type of cantilever vibration mode experienced in most AFM studies is flexural. When the cantilever tip is in contact with the sample surface, flexural vibrations can be excited by oscillating the sample vertically. The contact between the cantilever tip and the sample can also cause the cantilever to vibrate torsionally when the cantilever is scanned over the sample surface. Extensional and Lamb modes can also be excited, but most methods used to detect the displacements of the cantilevers in the AFM can not detect these modes. These modes are not as significant for AFM vibration studies because their resonance frequencies are much higher than those for the flexural and torsional modes. Because of this reason, only the equations governing the flexural and torsional vibration modes will be presented in this chapter.

The AFM cantilevers can often be modeled as homogeneous, uniform beams with the assumptions of no applied distributed loads and no axial forces. This model is depicted

in Figure 3.1 [40]. A tip with a small radius is attached to the end of the cantilever. The mass of the tip is assumed to be negligible and it is assumed that the tip is located at the end of the cantilever.

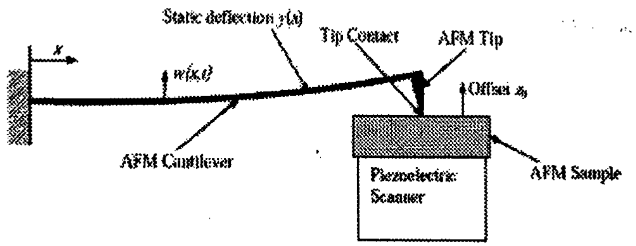

Figure 3.1: Model for flexural vibrations of AFM cantilevers. The cantilever tip is in contact with the sample surface. The static sample offset, z_0, causes a cantilever deflection of $y(x)$. The cantilever motion is defined by $w(x,t)$ relative to $y(x)$. The nonlinear tip-sample interactions can be approximated with different contact theories.

3.1 Flexural Vibrations

The Euler-Bernoulli beam theory for a beam in bending vibration will be used to model the flexural vibrations of the AFM cantilevers. This method will be used because it was recognized that the AFM cantilevers behave as continuous members with appropriate vibration modes [6]. The derivation can be carried out with the use of Figure 3.2(a), in which a beam in bending vibration under the distributed transverse force $f(x,t)$ is shown. Figure 3.2(b) shows a beam element subjected to an axial force $P(x)$.

The boundary-value problem is derived with the use of the extended Hamilton's

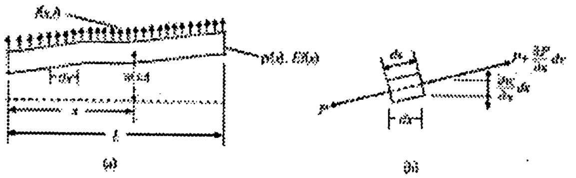

Figure 3.2: (a) A beam subject to distributed transverse force $f(x,t)$. (b) Axial forces acting on a beam element [41].

principle, which can be stated in the following form [41]

$$\int_{t_1}^{t_2} \delta(T(t) - V(t) + W_{nc}(t))dt = 0, \qquad \delta w(x,t) = 0, t = t_1, t_2, \tag{3.1}$$

where $T(t)$ is the kinetic energy of the system, $V(t)$ is the potential energy, $W_{nc}(t)$ is the work due to the nonconservative forces acting on the system, and $w(x,t)$ is the transverse displacement of the beam. Hamilton's principle states that the true motion of the system, within a certain arbitrary time interval, is characterized by the fact that the increment of the integral $\int_{t_1}^{t_2}(T(t) - V(t) + W_{nc}(t))dt$ vanishes for any continuously varying virtual displacement, provided that the displacement vanishes at the limits t_1 and t_2 of the chosen time interval. Assuming that the kinetic energy of the system is due to translation only, the kinetic energy can be expressed as

$$T(t) = \frac{1}{2}\int_0^L \rho A(x) \left[\frac{\partial x(x,t)}{\partial t}\right]^2 dx, \tag{3.2}$$

where ρ is the mass density of the beam, $A(x)$ is the cross-sectional area of the beam, and L is the total length of the beam.

The potential energy consists of two parts: one due to bending and one due to the axial force acting on the beam. The potential energy density due to the gravitational forces

can be neglected if displacements are defined from the equilibrium position. The potential energy density due to bending can be stated in the following form

$$V = \frac{EI(x)L}{2r^2}, \tag{3.3}$$

where r is the radius of curvature for the beam, E is Young's modulus of elasticity, and $I(x)$ is the area moment of inertia about an axis normal to the plane of x and the displacement w. The expression for the curvature of a plane curve is

$$\frac{1}{r} = \frac{\frac{\partial^2 w(x,t)}{\partial x^2}}{\left[1 + (\frac{\partial w(x,t)}{\partial x})^2\right]^{\frac{3}{2}}}. \tag{3.4}$$

By assuming $\partial w/\partial x << 1$ for small displacements, the curvature can then be written as $\frac{1}{r} = \frac{\partial^2 w(x,t)}{\partial x^2}$. By substituting the curvature expression into Equation 3.3 and integrating over the length of the beam, the potential energy due to bending is calculated as

$$V_{bend} = \frac{1}{2}\int_0^L EI(x) \left[\frac{\partial^2 w(x,t)}{\partial x^2}\right]^2 dx. \tag{3.5}$$

The potential energy due to the axial force is the sum of the work that must be performed by the force $P(x)$ to restore the beam to the original horizontal position. As depicted in Figure 3.2(b), the potential energy can be written as

$$V_{bond} = \int_0^L P(x)(dx - ds). \tag{3.6}$$

Equation 3.6 can be simplified by assuming that $\partial w/\partial x << 1$, such that

$$ds = \left[(dx)^2 + \left(\frac{\partial w}{\partial x}dx\right)^2\right]^{1/2} = \left[1 + \left(\frac{\partial w}{\partial x}\right)^2\right]^{1/2} dx \cong \left[1 + \frac{1}{2}\left(\frac{\partial w}{\partial x}\right)^2\right] dx, \tag{3.7}$$

where two terms are retained from the binomial expansion. Inserting Equation 3.7 into Equation 3.6, allows the combined potential energy due to bending and the axial force to be expressed as

$$V(t) = \frac{1}{2}\int_0^L \left\{ EI(x)\left[\frac{\partial^2 w(x,t)}{\partial x^2}\right]^2 + P(x)\left[\frac{\partial w(x,t)}{\partial x}\right]^2 \right\} dx. \tag{3.8}$$

The virtual work due to nonconservative forces is written as

$$\overline{\delta W}_{nc} = \int_0^L f(x,t)\delta w(x,t)dx. \tag{3.9}$$

Hamilton's principle, Equation 3.1, is applied and it is assumed that the variations and differentiations are interchangeable. The variation of the kinetic energy component, Equation 3.2, is

$$\delta T = \int_0^L \rho A \frac{\partial w}{\partial t}\delta\frac{\partial w}{\partial t}dx = \int_0^L \rho A \frac{\partial w}{\partial t}\frac{\partial}{\partial t}\delta w \; dx. \tag{3.10}$$

Integrating by parts, the first term in Equation 3.1 becomes

$$\begin{aligned}
\int_{t_1}^{t_2} \delta T dt &= \int_{t_1}^{t_2}\int_0^L \rho A(x)\frac{\partial w}{\partial t}\frac{\partial}{\partial t}\delta w \; dx \; dt = \int_0^L \int_{t_1}^{t_2} \rho A(x)\frac{\partial w}{\partial t}\frac{\partial}{\partial t}\delta w \; dt \; dx, \\
&= \int_0^L \rho A(x)\frac{\partial w}{\partial t}\delta w\Big|_{t_1}^{t_2} dx - \int_0^L\int_{t_1}^{t_2} \rho A(x)\frac{\partial^2 w}{\partial t^2}\delta w \; dt \; dx, \\
&= -\int_{t_1}^{t_2}\int_0^L \rho A(x)\frac{\partial^2 w}{\partial t^2}\delta w \; dx \; dt.
\end{aligned} \tag{3.11}$$

The variation of the potential energy, Equation 3.8, after integrating by parts has the following form

$$\begin{aligned}
\delta V &= \int_0^L \left(EI(x)\frac{\partial^2 w}{\partial x^2}\delta\frac{\partial^2 w}{\partial x^2} + P(x)\frac{\partial w}{\partial x}\delta\frac{\partial w}{\partial x}\right) dx, \\
&= \int_0^L \left(EI(x)\frac{\partial^2 w}{\partial x^2}\frac{\partial^2}{\partial x^2}\delta w + P(x)\frac{\partial w}{\partial x}\frac{\partial}{\partial x}\delta w\right) dx, \\
&= EI(x)\frac{\partial^2 w}{\partial x^2}\frac{\partial^2}{\partial x^2}\delta w\Big|_0^L - \frac{\partial}{\partial x}\left(EI(x)\frac{\partial^2 w}{\partial x^2}\right)\delta w\Big|_0^L + P(x)\frac{\partial w}{\partial x}\delta w\Big|_0^L \qquad (3.12) \\
&\quad + \int_0^L \left[\frac{\partial^2}{\partial x^2}\left(EI(x)\frac{\partial^2 w}{\partial x^2}\right) - \frac{\partial}{\partial x}\left(P(x)\frac{\partial w}{\partial x}\right)\right]\delta w \; dx.
\end{aligned}$$

Inserting Equations 3.9, 3.11, and 3.12 into Equation 3.1 and grouping terms, the following is obtained

$$\begin{aligned}
&-\int_{t_1}^{t_2}\left\{\left[-\frac{\partial}{\partial x}\left(EI(x)\frac{\partial^2 w}{\partial x^2}\right) + P(x)\frac{\partial w}{\partial x}\right]\delta w\Big|_0^L + EI(x)\frac{\partial^2 w}{\partial x^2}\delta\frac{\partial w}{\partial x}\Big|_0^L + \right. \\
&\left.\int_0^L \left[\rho A(x)\frac{\partial^2 w}{\partial t^2} + \frac{\partial^2}{\partial x^2}\left(EI(x)\frac{\partial^2 w}{\partial x^2}\right) - \frac{\partial}{\partial x}\left(P(x)\frac{\partial w}{\partial x}\right) - f\right]\delta w dx\right\} dt = 0.
\end{aligned} \tag{3.13}$$

It is assumed that the virtual displacements, δw, are arbitrary over the domain $0 < x < L$. Equation 3.13 shows that δw or its coefficient in the boundary term is zero at $x = 0$ and $x = L$ and that either $\delta(\partial w/\partial x)$ or its coefficient in the boundary term is zero at $x = 0$ and $x = L$. Equation 3.13 is satisfied if and only if

$$\rho A(x)\frac{\partial^2 w(x,t)}{\partial t^2} + \frac{\partial^2}{\partial x^2}\left(EI(x)\frac{\partial^2 w(x,t)}{\partial x^2}\right) - \frac{\partial}{\partial x}\left(P(x)\frac{\partial w(x,t)}{\partial x}\right) - f = 0, \quad 0 < x < L \tag{3.14}$$

and the boundary conditions

$$-\frac{\partial}{\partial x}\left(EI(x)\frac{\partial^2 w(x,t)}{\partial x^2}\right) + P(x)\frac{\partial w(x,t)}{\partial x} = 0 \quad \text{or} \quad w(x,t) = 0, \quad \text{at } x = 0, L \tag{3.15}$$

and

$$EI(x)\frac{\partial^2 w(x,t)}{\partial x^2} = 0 \quad \text{or} \quad \frac{\partial w(x,t)}{\partial x} = 0 \quad \text{at } x = 0, L. \tag{3.16}$$

Equation 3.14 is the equation of motion for the beam and Equations 3.15 and 3.16 are the boundary conditions. It is assumed here that $f(x) = P(x) = 0$. Therefore, the equation of motion simplifies to

$$\frac{\partial^2}{\partial x^2}\left(EI(x)\frac{\partial^2 w(x,t)}{\partial x^2}\right) + \rho A(x)\frac{\partial^2 w(x,t)}{\partial t^2} = 0. \quad 0 < x < L \tag{3.17}$$

Equation 3.17 is satisfied if and only if, either

$$\frac{\partial}{\partial x}\left(EI(x)\,\frac{\partial^2 w(x,t)}{\partial x^2}\right) = 0, \quad \text{at } x = 0, L \tag{3.18}$$

or

$$w(x,t) = 0, \quad \text{at } x = 0, L \tag{3.19}$$

and either

$$EI(x)\,\frac{\partial^2 w(x,t)}{\partial x^2} = 0, \quad \text{at } x = 0, L \tag{3.20}$$

or

$$\frac{\partial w(x,t)}{\partial x} = 0 \quad \text{at } x = 0, L. \tag{3.21}$$

The choice of which of the boundary conditions, from the sets in Equations 3.15 and 3.16, depends on the type of boundaries needed to model the beam. Equations 3.18, 3.19, 3.20, and 3.21 represent the shear force, displacement, bending moment, and slope of the displacement curve, respectively. The boundary conditions used to model AFM cantilevers are depicted in Figure 3.3. For the cantilevered end ($x = 0$), a *clamped end* boundary condition is used in which the bending moment and shear force are not zero. Therefore, Equations 3.19 and 3.21 are zero at the location of the clamped end. The *free* case, as depicted in Figure 3.3(a), has nonzero displacement and slope conditions. The remaining boundary conditions are Equations 3.18 and 3.20 which must be zero at the location of the free end. The *spring-coupled* end condition, as depicted in Figure 3.3(b), has nonzero displacement and slope. The remaining boundary conditions are Equation 3.20 and the following equation involving the shear force

$$\frac{\partial}{\partial x}\left(EI(x)\,\frac{\partial^2 w(x,t)}{\partial x^2}\right) = \kappa_n w(x,t), \tag{3.22}$$

where κ_n is the effective contact stiffness between the cantilever tip and the sample surface. The *pinned* end condition, as depicted in Figure 3.3, has nonzero slope and shear force. Therefore, the remaining boundary conditions are that Equations 3.19 and 3.20 are equal to zero[6].

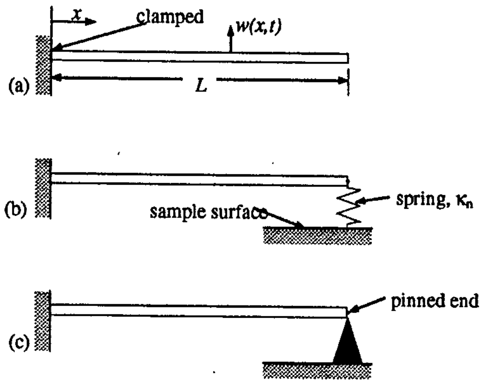

Figure 3.3: (a) Clamped-free case. (b) Clamped- spring coupled case. (c) Clamped-pinned case [6].

3.1.1 Free Case

The equations governing the dynamic behavior of a uniform cantilever that has a free end, as shown in Figure 3.3(a), can be derived with the use of the equation of motion, Equation 3.17, and the boundary conditions of Equations 3.19 and 3.21 at $x = 0$ and the boundary conditions of Equations 3.20 and 3.18 at $x = L$. For uniform cantilevers, $A(x) = I(x) =$ *constant.* The eigenvalue problem (EVP) for this condition is obtained by assuming harmonic solutions of the form, $w(x,t) = \psi(x)e^{i\omega t}$, which allows the equation of motion to be written as

$$EI\frac{\partial^4\psi(x)}{\partial x^4} - \omega^2\rho A\psi(x) = 0. \tag{3.23}$$

The geometric boundary conditions are

$$\psi(0) = 0, \qquad \psi'(0) = 0, \tag{3.24}$$

and the natural boundary conditions are

$$\psi''(L) = 0, \qquad \psi'''(L) = 0. \tag{3.25}$$

The general solution of Equation 3.23 is

$$\psi(x) = C_1\cos(\beta x) + C_2\sin(\beta x) + C_3\cosh(\beta x) + C_4\sinh(\beta x), \tag{3.26}$$

where $\beta = \left(\frac{\rho A\omega^2}{EI}\right)^{\frac{1}{4}}$. The mode shape $\psi(x)$, which is the shape the cantilever takes when it vibrates at different vibration modes, is determined by substituting Equation 3.26 into three of the boundary conditions from Equations 3.24 and 3.25 and solving in terms of one of the unknown coefficients. The mode shape can then be written as [41]

$$\psi(x) = C\left(\sin(\beta x) - \sinh(\beta x) - \left(\frac{\sin(\beta L) + \sinh(\beta L)}{\cos(\beta L) + \cosh(\beta L)}\right)(\cos(\beta x) - \cosh(\beta x))\right), \tag{3.27}$$

where C is the amplitude of the mode shape. By substituting Equation 3.26 into the boundary conditions, Equations 3.24 and 3.25, two simultaneous homogenous equations in terms of the unknown coefficients C_3 and C_4 can be obtained

$$\begin{aligned} C_3(\cos(\beta L) + \cosh(\beta L)) + C_4(\sin(\beta L) + \sinh(\beta L)) &= 0, \\ C_3(\sinh(\beta L) - \sin(\beta L)) + C_4(\cos(\beta L) + \cosh(\beta L)) &= 0. \end{aligned}$$

By equating the determinant of the coefficients to zero, the characteristic equation governing the eigenvalues for this case is

$$\cos(\beta L)\cosh(\beta L) + 1 = 0. \tag{3.28}$$

The eigenvalues, βL, along with the relation $\beta = \left(\frac{\rho A\omega^2}{EI}\right)^{\frac{1}{4}}$ can be used to provide the natural vibration frequencies, ω, of the free cantilever. The natural frequencies are given by the dispersion relation

$$\omega = (\beta L)^2\sqrt{\frac{EI}{\rho AL^4}}. \tag{3.29}$$

To further illustrate the shapes that the cantilevers take when vibrating at the natural frequencies, the first three nondimensional mode shapes are plotted in Figure 3.4. The eigenvalues corresponding to the first three natural frequencies from Equation 3.28 are substituted into Equation 3.27 to produce the mode shapes with $C = 1$. It is important to take note of the nodes, or points of zero amplitude, of the mode shapes because they must be avoided when trying to measure the displacement of the cantilevers.

3.1.2 Pinned Case

The equations governing the condition of the cantilever pinned at its free end, as shown in Figure 3.3(c), can be derived using the same method used in the derivation for the *free* case. The boundary conditions at the pinned end, at $x = L$, are Equations 3.19 and 3.20. The EVP has a similar form as that for the *free* case, except the natural boundary conditions are written as

$$\psi(L) = 0 \qquad \psi''(L) = 0. \tag{3.30}$$

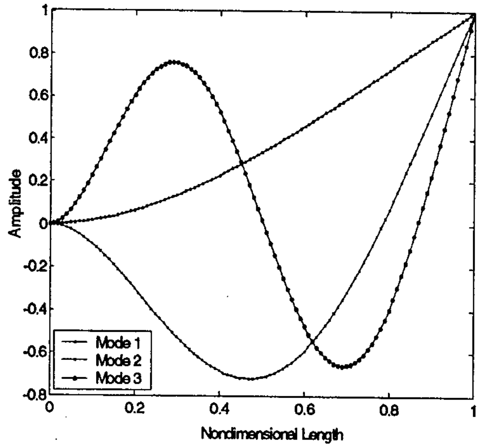

Figure 3.4: The first three mode shapes for the *free case.*

The mode shape $\psi(x)$ has the following form [41]

$$\psi(x) = C\left(\sin(\beta x) - \sinh(\beta x) + \left(\frac{\sinh(\beta L) - \sin(\beta L)}{\cos(\beta L) - \cosh(\beta L)}\right)(\cos(\beta x) - \cosh(\beta x))\right), \quad (3.31)$$

where C and β are defined similarly as for the *free* case. The characteristic equation can be derived by substituting Equation 3.26 into the boundary conditions of Equations 3.24 and 3.30. Two simultaneous homogeneous equations in terms of the unknown coefficients of C_3 and C_4 are obtained

$$\begin{aligned} C_3(\cosh(\beta L) - \cos(\beta L)) + C_4(\sinh(\beta L) - \sin(\beta L)) &= 0, \\ C_3(\cos(\beta L) + \cosh(\beta L)) + C_4(\sin(\beta L) + \sinh(\beta L)) &= 0. \end{aligned}$$

The characteristic equation is obtained by equating the determinant of the C coefficients to zero. The characteristic equation can then be written as

$$\cos(\beta L)\sinh(\beta L) - \cosh(\beta L)\sin(\beta L) = 0. \quad (3.33)$$

The mode shapes for the *pinned* case are determined by substituting the eigenvalues from Equation 3.33 into Equation 3.31. Figure 3.5 shows the first three mode shapes corresponding to the first three natural frequencies.

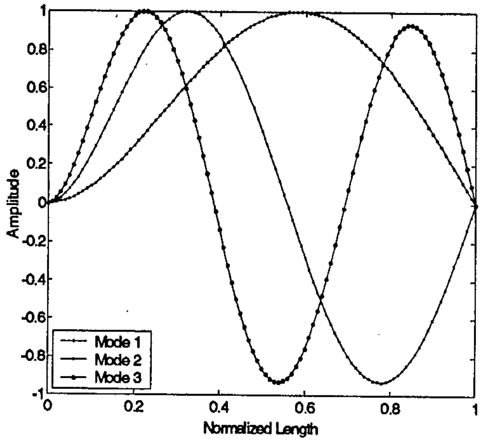

Figure 3.5: First three mode shapes for the *pinned* case.

3.1.3 Spring-coupled Case

The equations governing the dynamic response of the *spring-coupled* case, as shown in Figure 3.3(b), can be derived in the same manner as the *free* and the *pinned* cases. The linear spring coupled to the free end of the cantilever represents the stiffness between the cantilever tip and the sample surface. Due to the use of a linear spring, the cantilever is restricted to small displacements. The value of the linear spring depends on the contact theory used to model the tip-sample interaction. Any of the theories discussed in section 2.6 can be linearized about some initial equilibrium position to determine the value of the spring constant. The boundary conditions required at the spring-coupled end, at $x = L$, are Equations 3.20 and 3.22. The EVP is in the same form as the previous cases, except the natural boundary conditions can be written as

$$\psi''(L) = 0 \qquad EI\psi'''(L) = \kappa_n \psi(L). \tag{3.34}$$

The mode shape $\psi(x)$ has the following form [42]

$$\psi(x) = C\left(\sin(\beta x) - \sinh(\beta x) - \left(\frac{\sin(\beta L) + \sinh(\beta L)}{\cos(\beta L) + \cosh(\beta L)}\right)(\cos(\beta x) - \cosh(\beta x))\right), \tag{3.35}$$

where β and C are defined as previously stated for the *free* and *pinned* cases. The characteristic equation can be derived by substituting Equation 3.26 into the boundary conditions of Equations 3.24 and 3.34. Two simultaneous homogeneous equations in terms of the unknown coefficients of C_3 and C_4 are obtained

$$-C_3(\cosh(\beta L) + \cos(\beta L)) - C_4(\sinh(\beta L) + \sin(\beta L)) = 0,$$
$$C_3\left(\beta^3(\sin(\beta L) - \sinh(\beta L)) - \frac{\kappa_n}{EI}(\cos(\beta L) - \cosh(\beta L))\right) +$$
$$C_4\left(-\beta^3(\cos(\beta L) + \cosh(\beta L)) - \frac{\kappa_n}{EI}(\sin(\beta L) - \sinh(\beta L))\right) = 0.$$

The characteristic equation is obtained by equating the determinant of the C coefficients to zero. The characteristic equation can then be written as

$$\sinh(\beta L)\cos(\beta L) - \sin(\beta L)\cosh(\beta L) - \frac{(\beta L)^3 k_c}{3\kappa_n}(\cos(\beta L)\cosh(\beta L) + 1) = 0, \tag{3.36}$$

where $k_c = \frac{3EI}{L^3}$. Equation 3.36 covers the possible range of tip-sample interaction stiffness with the use of κ_n. The effect of the tip-sample interaction stiffness on the mode shapes is shown in Figure 3.6. The eigenvalues from Equation 3.36 for various values of $\frac{\kappa_n}{k_c}$ are substituted into Equation 3.35 to form the mode shapes. Figure 3.6 shows the mode shape for the first natural frequency. As $\frac{\kappa_n}{k_c} \to 0$, which represents the situation in which the cantilever is a great distance from the sample surface, the mode shape is that of the *free* case. As $\frac{\kappa_n}{k_c} \to \infty$, which represents the condition in which the cantilever is in contact with the sample surface under high load, the mode shape takes the form for the *pinned* case.

Offset Spring-coupled Case

In the previously mentioned *spring-coupled* case and the *pinned* case, the tip of the cantilever was assumed to be located at the end of the cantilever. In reality, many cantilevers are manufactured with the tips offset from the end of the cantilever. This situation can be modeled with a spring offset from the end of the cantilever, as shown in Figure 3.7. The cantilever is divided into two parts with length L_{tip} and L' and separate solutions $w(x)$ and $w'(x')$, respectively.

For the L_{tip} length the boundary conditions at $x = 0$ are Equations 3.24. For the L' length the boundary conditions at $x' = 0$ are Equations 3.25 in terms of $\psi'(x')$. The

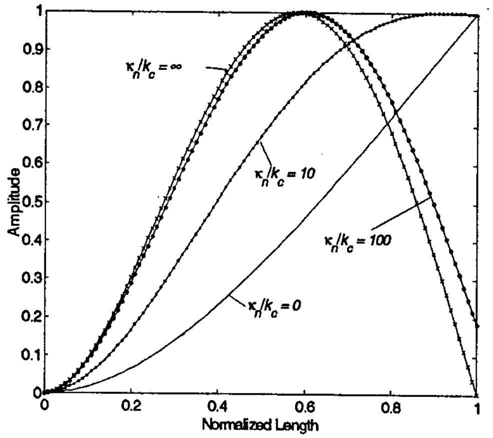

Figure 3.6: The first mode shape for the *spring-coupled* case plotted for various values of κ_n/k_c.

continuity conditions at $x' = L'$ and $x = L_{tip}$ are

$$\psi(L_{tip}) = \psi'(L'), \tag{3.37}$$

$$\frac{\partial\psi(L_{tip})}{\partial x} = -\frac{\partial\psi'(L')}{\partial x'}, \tag{3.38}$$

$$\frac{\partial^2\psi(L_{tip})}{\partial x^2} = \frac{\partial^2\psi'(L')}{\partial x'^2}, \tag{3.39}$$

and

$$-EI\frac{\partial^3\psi(L_{tip})}{\partial x^3} = EI\frac{\partial^3\psi'(L')}{\partial x'^3} - \kappa_n\psi'(L'). \tag{3.40}$$

To aid in the solution of the EVP, the general solution for $\psi'(x')$ and $\psi(x)$ can be written

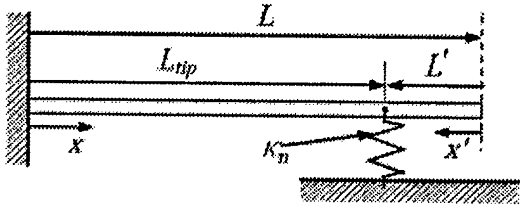

Figure 3.7: Model of cantilevers with tips offset from the free end of the cantilever. The cantilever is divided into two parts with length L_{tip} and L', respectively.

in the following form [6], shown here for $\psi(x)$,

$$\psi(x) = C_1(\cos(\beta x) + \cosh(\beta x)) + C_2(\cos(\beta x) - \cosh(\beta x)) + C_3(\sin(\beta x) + \sinh(\beta x)) + C_4(\sin(\beta x) - \sinh(\beta x)).$$

Inserting the general solution for $\psi(x)$ and $\psi'(x')$ into the boundary conditions, leads to four simultaneous homogeneous equations in terms of the unknown coefficients C_2, C_4, C_1', and C_3'. The equations can be written as

$$C_2(\cos(\beta L_{tip}) - \cosh(\beta L_{tip})) + C_4(\sin(\beta_{tip}) - \sinh(\beta L_{tip})) - C_1'(\cos(\beta L') + \cosh(\beta L')) - C_3'(\sin(\beta L') + \sinh(\beta L')) = 0,$$

$$C_2(-\sin(\beta L_{tip}) - \sinh(\beta L_{tip})) + C_4(\cos(\beta_{tip}) - \cosh(\beta L_{tip})) + C_1'(-\sin(\beta L') + \sinh(\beta L')) + C_3'(\cos(\beta L') + \cosh(\beta L')) = 0,$$

$$-C_2(\cos(\beta L_{tip}) + \cosh(\beta L_{tip})) - C_4(\sin(\beta_{tip}) + \sinh(\beta L_{tip})) - C_1'(-\cos(\beta L') + \cosh(\beta L')) - C_3'(-\sin(\beta L') + \sinh(\beta L')) = 0,$$

and

$$
\begin{aligned}
&-EI\left[C_2(\sin(\beta L_{tip})-\sinh(\beta L_{tip}))-C_4(\cos(\beta L_{tip})+\cosh(\beta L_{tip}))\right]-\\
&\qquad C_1'\left[EI\beta^3(\sin(\beta L')+\sinh(\beta L'))+\kappa_n(\cos(\beta L')+\cosh(\beta L'))\right]+\\
&\qquad\qquad C_3'\left[EI\beta^3(-\cos(\beta L')+\cosh(\beta L'))+\kappa_n(\sin(\beta L')+\sinh(\beta L'))\right]=0.
\end{aligned}
$$

The characteristic equation is obtained by equating the determinant of the C coefficients to zero. The characteristic equation can then be written as [6]

$$
\begin{aligned}
&(\cosh(\beta L_{tip})\sin(\beta L_{tip})-\cos(\beta L_{tip})\sinh(\beta L_{tip}))(1+\cos(\beta L')\cosh(\beta L'))-\\
&\qquad(\cosh(\beta L')\sin(\beta L')-\cos(\beta L')\sinh(\beta L'))(1-\cos(\beta L_{tip})\cosh(\beta L_{tip}))=\\
&\qquad\qquad-\frac{2EI\beta^3}{\kappa_n}\left[1+\cosh(\beta(L_{tip}+L'))\cos(\beta(L_{tip}+L'))\right].
\end{aligned}
\tag{3.41}
$$

Equation 3.41 can be written in a more convenient form by recognizing that $L=L_{tip}+L'$ and by using the definition $k_c=\frac{3EI}{L_{tip}^3}$. The characteristic equation for the *offset spring-coupled* case can now be written as [43]

$$
\begin{aligned}
&\frac{\kappa_n}{k_c}\left[(\cosh(\beta L_{tip})\sin(\beta L_{tip})-\cos(\beta L_{tip})\sinh(\beta L_{tip}))(1+\cos(\beta L')\cosh(\beta L'))-\right.\\
&\qquad\left.(\cosh(\beta L')\sin(\beta L')-\cos(\beta L')\sinh(\beta L'))\,(1-\cos(\beta L_{tip})\cosh(\beta L_{tip}))\right]=\\
&\qquad\qquad-\frac{2(\beta L_{tip})^3}{3}\left[1+\cosh(\beta L)\cos(\beta L)\right].
\end{aligned}
\tag{3.42}
$$

3.1.4 Tip-sample Stiffness (κ_n) Derivation

The values of κ_n used to model the tip-sample interaction stiffness can be calculated from tip-sample contact models, as summarized in section 2.6. The research for this thesis was directed toward hard materials with low adhesion and small radii of curvature. It is assumed that the cantilever tip and the sample surface deform elastically when in contact. Therefore, it is valid to apply the Hertzian contact model to describe the tip-sample contact interactions. For this reason, the Hertzian contact model will be applied throughout this thesis. From Equation 2.6, in section 2.6.1, the Hertzian contact force can be written as [36]

$$F_H=\frac{4}{3}E^*\sqrt{(-\delta)^3R}. \tag{3.43}$$

The load applied to the cantilever is represented by F_N. The summation of the forces between the tip and sample is used to obtain the equilibrium position, δ_c. With Equation 3.43, the summation of the tip-sample forces is

$$\frac{4}{3}E^*\sqrt{(-\delta)^3R}-F_N=0.$$

Therefore,

$$\delta_c=-\left(\frac{3F_N}{4E^*}\right)^{\frac{2}{3}}R^{-\frac{1}{3}}. \tag{3.44}$$

Taking the derivative of Equation 3.43 about the equilibrium position, δ_c, leads to

$$\left.\frac{\partial F_H}{\partial\delta}\right|_{\delta=\delta_c}=-\sqrt[3]{6\,(E^*)^2\,RF_N}.$$

This relation means that

$$\kappa_n=\sqrt[3]{6\,(E^*)^2\,RF_N}. \tag{3.45}$$

3.2 Torsional Vibrations

The derivation of the equations governing the torsional vibrations of the cantilevers is carried out in the same manner as that used for flexural vibrations. The cantilever is modeled as a beam with a spring attached laterally to the cantilever tip, as shown in Figure 3.8. Torsional vibrations of a uniform beam can be described by [41]

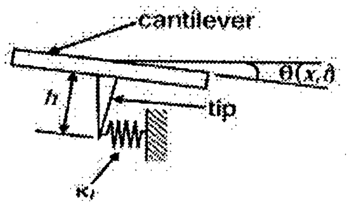

Figure 3.8: Model for the torsional vibrations of the AFM cantilever. The cross-section of a rectangular cantilever is shown with a spring, κ_l, attached to the tip.

$$\frac{\partial}{\partial x}\left(\frac{Gc_T(x)}{\rho J(x)}\frac{\partial\theta(x,t)}{\partial x}\right)=\frac{\partial^2\theta(x,t)}{\partial t^2}, \tag{3.46}$$

where G is the shear modulus, J is the polar moment of area, ρ is the mass density, and c_T is a torsional constant related to the warping of the beam cross-section. Warping occurs in noncircular cross-sections under torsion. c_T is obtained from a warping function, which describes the displacement of each section in the direction parallel to the length of the beam, independent of the position along the twisted axis running down the center of the beam. For a rectangular cross-section, the constant can be written as [44]

$$c_T=\frac{1}{3}t^4\left[\frac{w}{t}-\frac{192}{\pi^5}\sum_{n-0}^{\infty}\frac{\tanh(k_n(w/2))}{(2n+1)^5}\right], \tag{3.47}$$

where w and t are the width and thickness of the rectangular cross-section, respectively. The values for k_n are given by the relation

$$k_n=\frac{(2n+1)\pi}{t}.$$

For narrow cross-sections, where $w > t$, Equation 3.47 can be approximated as

$$c_T=\frac{1}{3}t^4\left[\frac{w}{t}-\frac{192}{\pi^5}\right]. \tag{3.48}$$

This approximation is valid for most AFM cantilevers. The torsional constant, c_T, for cross-sections other than rectangular can be found in most texts on elasticity or mechanics of materials.

The boundary conditions for the problem are [45],[46]

$$\theta(0,t)=0 \quad \text{and} \quad Gc_T(x)\frac{\partial\theta(L,t)}{\partial x}=-\kappa_l h^2\theta(L,t), \tag{3.49}$$

where L is the length of the cantilever, h is the length of the cantilever tip, and κ_l is the value for the lateral spring. The first boundary condition is due to the clamped condition at $x = 0$ and the second boundary condition is due to the tip-sample interaction, which is represented by the lateral spring, κ_l. For a uniform cantilever, $c_T(x) = J(x) =$ *constant*.

The EVP can be written by looking for harmonic solutions of the form $\theta(x,t) = \Theta(x)e^{i\omega t}$, which allows Equation 3.46 to be written as

$$\frac{Gc_T}{\rho J}\Theta''(x)+\omega^2\Theta(x)=0, \tag{3.50}$$

and the boundary conditions, Equation 3.49, to be written as

$$\Theta(0)=0 \quad \text{and} \quad \Theta'(L)=-\frac{\kappa_l h^2}{Gc_T}\Theta(L). \tag{3.51}$$

The general solution for the EVP is given by

$$\Theta(x)=C_1\sin(\gamma x)+C_2\cos(\gamma x), \tag{3.52}$$

where the torsional wave number, γ, is given by

$$\gamma^2=\frac{\omega^2\rho J}{Gc_T}.$$

Substituting Equation 3.52 in the first boundary condition of Equation 3.51 gives $C_2 = 0$. The second boundary condition of Equation 3.51 gives

$$\gamma \cos(\gamma L) = -\frac{\kappa_l h^2}{G c_T} \sin(\gamma L).$$

The characteristic equation governing the torsional frequencies, ω, of the cantilever can then be written as

$$\gamma L \cos(\gamma L) + \eta_l \sin(\gamma L) = 0, \tag{3.53}$$

where $\eta_l = \frac{\kappa_l h^2 L}{G c_T}$, which defines the lateral stiffness of the sample surface relative to the torsional spring constant of the cantilever, $\frac{G c_T}{L}$.

3.3 Modal Sensitivity

In each of the vibration models discussed in the previous sections, equations governing the vibration frequencies and mode shapes were derived. For each mode, the tip-sample interactions have a unique effect [40],[42]. This is because each mode has a different shape, which is affected by damping and surface loading in a different way. It has been shown that at higher modes, damping is decreased [2]. Therefore, each mode has a different sensitivity to variations in surface stiffness and damping [40],[42],[43],[47]. Sensitivity is defined as the relative change in frequency of a mode due to changes in surface stiffness. The most sensitive modes should be exploited for imaging because their response will provide the highest contrast [45].

3.3.1 Flexural Modal Sensitivity

The characteristic equation for the *spring-coupled* case, Equation 3.36, derived in section 3.1.3 is used to derive the flexural modal sensitivity because of all the possible tip-sample interactions available through the use of κ_n. Starting with the definitions of $\lambda = \beta L$ and $\eta_n = \frac{3\kappa_n}{k_c}$, the frequencies governed by the zeros of the characteristic equation, Equation 3.36, can be defined by

$$S(\lambda, \eta_n) \equiv \eta_n(\sinh(\lambda)\cos(\lambda) - \sin(\lambda)\cosh(\lambda)) - \lambda^3(\cos(\lambda)\cosh(\lambda) + 1) = 0. \tag{3.54}$$

The modes which change the most for small variations in surface stiffness for a given sample are of great interest. Therefore, with regard to Equation 3.54, this means the interest lies in the change of λ with respect to η_n. Differentiation of Equation 3.54 with respect to η_n implies that

$$\frac{dS(\lambda, \eta_n)}{d\eta_n} = 0,$$

$$\frac{\partial S(\lambda, \eta_n)}{\partial \eta_n} + \frac{\partial S(\lambda, \eta_n)}{\partial \lambda}\frac{d\lambda}{d\eta_n} = 0.$$

Rearranging these equations gives

$$\frac{d\lambda}{d\eta_n} = -\frac{\partial S/\partial \eta_n}{\partial S/\partial \lambda}. \tag{3.55}$$

Using Equation 3.54, gives

$$\frac{d\lambda}{d\eta_n} = (\sinh(\lambda)\cos(\lambda) - \sin(\lambda)\cosh(\lambda)) \times \{3\lambda^2(\cos(\lambda)\cosh(\lambda) + 1) + \tag{3.56}$$
$$2\eta_n(\sin(\lambda)\sinh(\lambda)) + \lambda^3(\cos(\lambda)\sinh(\lambda) - \sin(\lambda)\cosh(\lambda))\}^{-1}.$$

Equation 3.56 is the wave number sensitivity to changes in surface stiffness. Experimentally, the change in frequency is measured. Therefore, in terms of frequency, further expansion gives

$$\frac{\partial f}{\partial \eta_n} = \frac{\partial f}{\partial \lambda}\frac{d\lambda}{d\eta_n}. \tag{3.57}$$

The dispersion relation between the wave number and the frequency, Equation 3.29, written in terms of frequency is

$$f^2 = \frac{EI}{4\pi^2 \rho A L^4}\lambda^4. \tag{3.58}$$

Differentiating Equation 3.58 with respect to λ gives

$$\frac{\partial f}{\partial \lambda} = \lambda \frac{1}{\pi}\sqrt{\frac{EI}{\rho A L^4}}.$$

Substituting this expression into Equation 3.57 allows the change in frequency relative to the change in surface stiffness to be expressed as

$$\frac{df}{d\eta_n} = \frac{1}{2\pi}\sqrt{\frac{EI}{\rho A L^4}}\,(2\lambda\,(\sinh(\lambda)\cos(\lambda) - \sin(\lambda)\cosh(\lambda))) \times \{3\lambda^2(\cos(\lambda)\cosh(\lambda)+1) +$$

$$2\eta_n(\sin(\lambda)\sinh(\lambda)) + \lambda^3(\cos(\lambda)\sinh(\lambda) - \sin(\lambda)\cosh(\lambda))\}^{-1}. \tag{3.59}$$

This equation is solved for a given normal stiffness, η_n, by substituting the wave numbers, λ, obtained from Equation 3.54 for the given normal stiffness.

In dimensionless form, Equation 3.59 can be written as [45]

$$\sigma_f = \frac{df/d\eta_n}{\frac{1}{2\pi}\sqrt{\frac{EI}{\rho A L^4}}} = (2\lambda\,(\sinh(\lambda)\cos(\lambda) - \sin(\lambda)\cosh(\lambda))) \times \{3\lambda^2(\cos(\lambda)\cosh(\lambda)+1) +$$

$$2\eta_n(\sin(\lambda)\sinh(\lambda)) + \lambda^3(\cos(\lambda)\sinh(\lambda) - \sin(\lambda)\cosh(\lambda))\}^{-1}. \tag{3.60}$$

This relation may be thought of as the ratio of the frequency measurement resolution, $df/d\eta_n$, relative to a characteristic frequency for the cantilever, $\frac{1}{2\pi}\sqrt{\frac{EI}{\rho A L^4}}$.

3.3.2 Torsional Modal Sensitivity

The modal sensitivity for torsional vibrations can be derived by first defining the characteristic equation for the *spring-coupled* case, Equation 3.53, as

$$S(\lambda, \eta_t) \equiv \lambda\cos(\lambda) + \eta_t \sin(\lambda) = 0, \tag{3.61}$$

where $\lambda = \gamma L$. The modes which change the most for small variations in surface stiffness for a given sample are of great interest. With regard to Equation 3.61, this means the interest lies in the change of λ with respect to η_t. Using the same procedure as for flexural vibrations, differentiation of Equation 3.61 with respect to η_t implies

$$\frac{d\lambda}{d\eta_t} = -\frac{\partial S/\partial \eta_t}{\partial S/\partial \lambda} = \frac{\sin(\lambda)}{\lambda\sin(\lambda) - (1+\eta_t)\cos(\lambda)}. \tag{3.62}$$

In terms of frequency, Equation 3.55 can be written as

$$\frac{\partial f}{\partial \eta_t} = \frac{\partial f}{\partial \lambda}\frac{d\lambda}{d\eta_t}. \tag{3.63}$$

The dispersion relation between the frequency and wave number for torsional vibrations is

$$\lambda = 2\pi f\sqrt{\frac{\rho J L^2}{G\sigma_T}}. \tag{3.64}$$

Solving equation 3.64 for f and then differentiating with respect to λ gives

$$\frac{\partial f}{\partial \lambda} = \frac{1}{2\pi}\sqrt{\frac{G\sigma_T}{\rho J L^2}}. \tag{3.65}$$

Combining Equations 3.65 and 3.62, produces the torsional modal sensitivity,

$$\frac{\partial f}{\partial \eta_t} = \frac{1}{2\pi}\sqrt{\frac{G\sigma_T}{\rho J L^2}}\frac{\sin(\lambda)}{\lambda\sin(\lambda) - (1+\eta_t)\cos(\lambda)}. \tag{3.66}$$

In dimensionless form, Equation 3.66 becomes

$$\sigma_t = \frac{\partial f / \partial \eta_l}{\frac{1}{2\pi}\sqrt{\frac{Gc_T}{\rho J L^2}}} = \frac{\sin(\lambda)}{\lambda \sin(\lambda) - (1 + \eta_l)\cos(\lambda)}. \tag{3.67}$$

This relation may be thought of as the ratio of the frequency measurement resolution, $df/d\eta_l$, relative to a characteristic frequency for the cantilever, $\frac{1}{2\pi}\sqrt{\frac{Gc_T}{\rho J L^2}}$.

3.4 Discussion

A linear spring was used to approximate the tip-sample interactions and the equations governing the flexural and torsional vibration modes for this *spring-coupled* case were derived. The derivation for this case was then used to obtain the flexural and torsional modal sensitivities of the AFM cantilevers.

Chapter 4

Approximate Methods

The analysis presented in chapter 3 was directed toward cantilevers with a uniform cross-section. This analysis technique is adequate to model some of the AFM cantilevers used in research, but it is not adequate for modeling the majority of the cantilevers that have a nonuniform cross-section. An example of a nonuniform cantilever is the triangular cantilever, as shown in Figure 2.5. To analyze the cantilevers with a nonuniform cross-section, the Rayleigh-Ritz method is used here. The equations necessary to approximate the flexural and torsional vibration response of the cantilevers, using this method, will be presented in this chapter.

The Rayleigh-Ritz method is an extension of Rayleigh's method, which is a technique used for calculating the fundamental natural frequencies of continuous systems. The calculations are carried out by using functions to approximate the mode shapes of the systems. A single assumed function is used for Rayleigh's method and many functions are used to approximate the natural mode shapes for the Rayleigh-Ritz method. The number of frequencies that can be calculated is equal to the number of functions used.

Part of the motivation for choosing the Rayleigh-Ritz method is in its ease of use for developing programs to perform the calculations. *Matlab* [48] was used to create the programs to perform the calculations using the Rayleigh-Ritz method, which in turn are made available over the internet at http://em-jaturner.unl.edu/calcs.htm.

The Rayleigh-Ritz method is based on Rayleigh's quotient [41]. The flexural and torsional EVPs can be represented by

$$\mathcal{L}\left[\psi_r\right] = \omega_r^2 \mathcal{M}\left[\psi_r\right], \tag{4.1}$$

where $\mathcal{L}$ and $\mathcal{M}$ are linear operators on eigenfunction ψ_r with corresponding frequency ω_r. $\mathcal{L}$ is of even order $(2q)$ for flexural and torsional problems. Multiplying both sides of Equation 4.1 by ψ_r and then integrating over the domain Ω of the system, gives

$$\omega_r^2 = \frac{\int_\Omega \psi_r \mathcal{L}\left[\psi_r\right] d\Omega}{\int_\Omega \psi_r \mathcal{M}\left[\psi_r\right] d\Omega} = \frac{N\left[\psi_r\right]}{D\left[\psi_r\right]}, \qquad \text{for } r = 1, 2..\infty. \tag{4.2}$$

Equation 4.2 defines the numerator, $N\left[\psi_r\right]$, and the denominator, $D\left[\psi_r\right]$, of Rayleigh's quotient, $R[\psi] = N[\psi]/D[\psi]$.

The eigenfunctions are approximated with a set of admissible functions, u. These functions are defined as being q times differentiable over the domain of the system. They must also satisfy the geometric boundary conditions, but are not required to satisfy the natural boundary conditions. The eigenfunctions, ψ_r, can be expanded in terms of the admissible functions as

$$\psi_r(x) = \sum_{i=1}^{r} a_i u_i(x). \tag{4.3}$$

The stationarity of Rayleigh's quotient is then exploited by attempting to minimize the ratio in Equation 4.2. Carrying out the minimization allows the EVP to be written in

discretized form as [41]

$$\mathbf{Ka} = \lambda^2 \mathbf{Ma}, \tag{4.4}$$

where $\mathbf{a} = \{a_1, a_2, \ldots a_r\}^{\mathrm{T}}$. This eigenvector has components which are the coefficients of the expansion, Equation 4.3, for the rth eigenfunction, $\psi_r(x)$. The eigenvalue, λ^2, is the approximation of the exact eigenvalue, ω^2. The stiffness, $\mathbf{K}$, and the mass, $\mathbf{M}$, matrices in Equation 4.4 are defined in terms of the admissible functions and linear operators by

$$K_{ij} = \int_\Omega u_i \mathcal{L}\left[u_j\right] d\Omega, \tag{4.5}$$

$$M_{ij} = \int_\Omega u_i \mathcal{M}\left[u_j\right] d\Omega. \tag{4.6}$$

4.1 Flexural Vibrations

The equations governing the dynamic behavior of a nonuniform cantilever that has a spring-coupled end, as shown in Figure 3.3(a), are the equations of motion, Equation 3.17, and the boundary conditions of Equations 3.19 and 3.21 at $x = 0$ and the boundary conditions of Equations 3.20 and 3.22 at $x = L$. For this analysis, the tip of the cantilever is assumed to be located at the end of the cantilever. The boundary value problem (BVP) is written as

$$\frac{\partial^2}{\partial x^2}\left(EI(x)\frac{\partial^2 \psi(x)}{\partial x^2}\right) - \omega^2 \rho A(x)\psi(x) = 0, \tag{4.7}$$

$$\psi(0) = 0, \qquad \frac{\partial \psi(0)}{\partial x} = 0, \tag{4.8}$$

$$EI(L)\frac{\partial^2 \psi(L)}{\partial x^2} = 0, \qquad \frac{\partial}{\partial x}\left(EI(L)\frac{\partial^2 \psi(L)}{\partial x^2}\right) = \kappa_n \psi(L). \tag{4.9}$$

The linear operators become [41]

$$\mathcal{L}[\psi] = \frac{\partial^2}{\partial x^2}\left[EI(x)\frac{\partial^2 \psi(x)}{\partial x^2}\right], \tag{4.10}$$

$$\mathcal{M}[\psi] = \rho A(x)\,\psi(x)\,. \tag{4.11}$$

The linear operators are now used to derive the numerator and denominator of Rayleigh's quotient. The numerator, in terms of admissible functions, $u_i(x)$, can be written as

$$N[u] = \int_\Omega u\mathcal{L}[u]\,d\Omega = \int_0^L u\frac{\partial^2}{\partial x^2}\left(EI(x)\frac{\partial^2 u}{\partial x^2}\right)dx.$$

Integration by parts gives

$$N[u] = u\frac{\partial}{\partial x}\left(EI(x)\frac{\partial^2 u}{\partial x^2}\right)\Big|_L - u\frac{\partial}{\partial x}\left(EI(x)\frac{\partial^2 u}{\partial x^2}\right)\Big|_0 - \int_0^L\left(\frac{\partial u}{\partial x}\right)\frac{\partial}{\partial x}\left(EI(x)\frac{\partial^2 u}{\partial x^2}\right)dx.$$

The first and second terms are found from the boundary conditions. The first term becomes $\kappa_n u^2(L)$ and the second term becomes zero. Integrating by parts a second time gives

$$N[u] = \kappa_n u^2(L) - \frac{\partial u}{\partial x}\left(EI(x)\frac{\partial^2 u}{\partial x^2}\right)\Big|_L + \frac{\partial u}{\partial x}\left(EI(x)\frac{\partial^2 u}{\partial x^2}\right)\Big|_0 + \int_0^L EI(x)\left(\frac{\partial^2 u}{\partial x^2}\right)^2 dx. \tag{4.12}$$

The second and third terms of Equation 4.12 are zero by implementation of the boundary conditions, such that

$$N[u] = \kappa_n u^2(L) + \int_0^L EI(x)\left(\frac{\partial^2 u}{\partial x^2}\right)^2 dx. \tag{4.13}$$

The denominator of Rayleigh's quotient for this problem is given by

$$D[u] = \int_\Omega u\mathcal{M}[u]\,d\Omega = \int_0^L \rho A(x)\,u^2 dx. \tag{4.14}$$

The equations for the stiffness and mass matrices are then given by

$$K_{ij} = \int_0^L EI(x)\left(\frac{\partial^2 u_i(x)}{\partial x^2}\right)\left(\frac{\partial^2 u_j(x)}{\partial x^2}\right)dx + \kappa_n u_i(L)\,u_j(L)\,, \tag{4.15}$$

$$M_{ij} = \int_0^L \rho A(x)\,u_i(x)\,u_j(x)\,dx. \tag{4.16}$$

These equations can be normalized for comparison with the exact results derived in section 3.1.3. In normalized form, the Equations 4.15 and 4.16 become

$$\widetilde{K}_{ij} = \frac{K_{ij}}{EI_0/L^3} = \int_0^1 \frac{EI(\widetilde{x})}{EI_0}\left(\frac{\partial^2 u_i(\widetilde{x})}{\partial \widetilde{x}^2}\right)\left(\frac{\partial^2 u_j(\widetilde{x})}{\partial \widetilde{x}^2}\right)d\widetilde{x} + \eta_n u_i(1)\,u_j(1)\,, \tag{4.17}$$

$$\widetilde{M}_{ij} = \frac{M_{ij}}{\rho A_0 L} = \int_0^1 \frac{\rho A(\widetilde{x})}{\rho A_0}u_i(\widetilde{x})\,u_j(\widetilde{x})\,d\widetilde{x}, \tag{4.18}$$

where EI_0 and ρA_0 are the bending stiffness and mass density at $x = 0$, respectively. Also, $\eta_n = \frac{3\kappa_n}{k_{c0}}$, where $k_{c0} = \frac{3EI_0}{L^3}$, and $\widetilde{x} = \frac{x}{L}$. If the cantilever tip were offset from the end of the cantilever, then the last term in Equation 4.17 must be modified to accommodate the offset tip location, such that

$$\widetilde{K}_{ij} = \int_0^1 \frac{EI(\widetilde{x})}{EI_0}\left(\frac{\partial^2 u_i(\widetilde{x})}{\partial \widetilde{x}^2}\right)\left(\frac{\partial^2 u_j(\widetilde{x})}{\partial \widetilde{x}^2}\right)d\widetilde{x} + \eta_n u_i\left(\frac{L_{tip}}{L}\right)u_j\left(\frac{L_{tip}}{L}\right).$$

In terms of the normalized matrices, $\widetilde{\mathbf{K}}$ and $\widetilde{\mathbf{M}}$, the EVP is given by

$$\widetilde{\mathbf{K}}\mathbf{a} = \Omega^2\widetilde{\mathbf{M}}\mathbf{a}, \tag{4.19}$$

where $\mathbf{a}$ is the eigenvector of expansion coefficients and the normalized frequency is

$$\Omega = \frac{\lambda}{\sqrt{EI_0/\rho A_0 L^4}}. \tag{4.20}$$

4.1.1 Approximate Flexural Modal Sensitivity

To derive the equation governing the sensitivity of the cantilever to changes in the surface stiffness, the derivative of Equation 4.19 is taken with respect to η_n. This result is written as

$$\frac{\partial\widetilde{\mathbf{K}}}{\partial\eta_n}\mathbf{a} + \widetilde{\mathbf{K}}\frac{\partial\mathbf{a}}{\partial\eta_n} = 2\Omega\frac{\partial\Omega}{\partial\eta_n}\widetilde{\mathbf{M}}\mathbf{a} + \Omega^2\frac{\partial\widetilde{\mathbf{M}}}{\partial\eta_n}\mathbf{a} + \Omega^2\widetilde{\mathbf{M}}\frac{\partial\mathbf{a}}{\partial\eta_n}. \tag{4.21}$$

Noticing that $\widetilde{\mathbf{M}}$ does not depend explicitly on η_n and assuming that the change in the eigenvector to small stiffness changes is negligible, allows Equation 4.21 to be simplified as

$$\frac{\partial \widetilde{\mathbf{K}}}{\partial \eta_n}\mathbf{a} = 2\Omega \frac{\partial \Omega}{\partial \eta_n}\widetilde{\mathbf{M}}\mathbf{a}. \tag{4.22}$$

The normalization condition, $\mathbf{a}^{\mathrm{T}}\widetilde{\mathbf{M}}\mathbf{a} = 1$, is used to simplify Equation 4.22 by multiplying the right side by $\mathbf{a}^{\mathrm{T}}$. Equation 4.22 can then be further simplified as

$$\frac{\partial \Omega}{\partial \eta_n} = \frac{1}{2\Omega}\mathbf{a}^{\mathrm{T}}\frac{\partial \widetilde{\mathbf{K}}}{\partial \eta_n}\mathbf{a}. \tag{4.23}$$

Comparison of Equation 4.23 with the definition of the normalized flexural sensitivity from Equation 3.60 gives

$$\frac{\partial \Omega}{\partial \eta_n} = \sigma_f.$$

The approximate form of the flexural sensitivity is then given by [45]

$$\sigma_f = \frac{1}{2\Omega}\mathbf{a}^{\mathrm{T}}\frac{\partial \widetilde{\mathbf{K}}}{\partial \eta_n}\mathbf{a}. \tag{4.24}$$

This expression for the approximate modal sensitivity is governed by Equation 4.19. For a given stiffness, η_n, the eigenvalues, Ω, and eigenvectors, $\mathbf{a}$, are calculated. The sensitivity for each mode is then found using Equation 4.24.

The flexural sensitivity, σ_f, of the first five vibration modes, calculated using the Equation 4.24 and the exact solution from Equation 3.60, is plotted in Figure 4.1. The approximate solution is represented by the symbols and the exact solution is represented by the solid curves. A ten-term polynomial expansion was used for the approximate solution. Both solution agree well with each other. From Figure 4.1, it can be concluded that when the cantilever is much more compliant than the sample surface, the first mode is the most sensitive to changes in the stiffness of the sample surface. The maximum value of σ_f for all modes is found from the limit of $\eta_n \to 0$ of Equation 3.60. In this limit the wave numbers, λ, approach those for the free vibration case (i.e. 1.8751, 4.694, 7.854 etc). Thus, the maximum sensitivities for the first three modes are $\sigma_f = 0.57,\ 0.091,\ 0.032$. When η_n is greater than about 30, the sensitivity of the first mode becomes smaller than that of the second mode. Thus, it is expected that the second mode will experience the largest shifts in frequency of all the modes. At the same time, the overall sensitivity of all the modes is reduced to a maximum around 0.1. When the stiffness ratio, η_n, is about 160, the first mode is less sensitive than modes two through five. The sensitivity of all modes scales with $1/\eta_n^2$ for large η_n.

4.2 Torsional Vibrations

The torsional EVP can be derived with the use of the Equation 3.46 and the boundary conditions from Equation 3.49. By looking for solutions of the form $\theta(x,t) = \Theta(x)\,e^{i\omega t}$, the EVP can be written as

$$\frac{\partial}{\partial x}\left(\frac{G\sigma_T(x)}{\rho J(x)}\frac{\partial \Theta(x)}{\partial x}\right) = -\omega^2\Theta(x), \tag{4.25}$$

$$\Theta(0) = 0, \qquad \text{and} \qquad G\sigma_T(L)\frac{\partial \Theta(L)}{\partial x} = -\kappa_t h^2\Theta(L). \tag{4.26}$$

The linear operators are given by [45]

$$\mathcal{L}[\Theta] = \frac{\partial}{\partial x}\left[G\sigma_T(x)\frac{\partial \Theta(x)}{\partial x}\right], \tag{4.27}$$

$$\mathcal{M}[\Theta] = \rho J(x)\,\Theta(x). \tag{4.28}$$

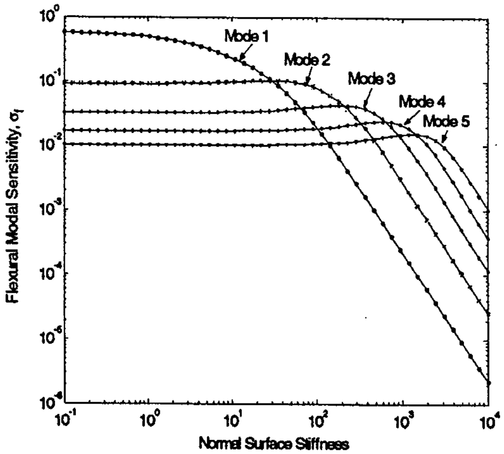

Figure 4.1: Exact and approximate solutions of the flexural modal sensitivity, σ_f, for a uniform cantilever. The solid curves represent the exact solution calculated from Equation 3.60 and the symbols represent the approximate solution calculated from Equation 4.24.

The linear operators are now used to derive the numerator and denominator of Rayleigh's quotient. The numerator of Rayleigh's quotient, in terms of admissible functions, $u_i(x)$, can be written as

$$N[u] = \int_\Omega u\mathcal{L}[u]\,d\Omega = -\int_0^L u\frac{\partial}{\partial x}\left(G\sigma_T(x)\frac{\partial u}{\partial x}\right)dx.$$

Integration by parts gives

$$N[u] = u\left(G\sigma_T(x)\frac{\partial u}{\partial x}\right)\Big|_L - u\left(G\sigma_T(x)\frac{\partial u}{\partial x}\right)\Big|_0 + \int_0^L\left(\frac{\partial u}{\partial x}\right)\left(G\sigma_T(x)\frac{\partial u}{\partial x}\right)dx.$$

The first and second terms are found from the boundary conditions, Equations 4.26. The first term becomes $\kappa_l h^2 u^2(L)$ and the second term becomes zero. The numerator is then

written as

$$N[u] = \kappa_l h^2 u^2(L) + \int_0^L G\sigma_T(x)\left(\frac{\partial u}{\partial x}\right)^2 dx. \tag{4.29}$$

The denominator of Rayleigh's quotient is given by

$$D[u] = \int_\Omega u\mathcal{M}[u]\,d\Omega = \int_0^L \rho J(x)\,u^2 dx. \tag{4.30}$$

The equations for the stiffness and mass matrices may then be defined as

$$K_{ij} = \int_0^L G\sigma_T(x)\left(\frac{\partial u_i(x)}{\partial x}\right)\left(\frac{\partial u_j(x)}{\partial x}\right)dx + \kappa_l h^2 u_i(L)\,u_j(L)\,, \tag{4.31}$$

$$M_{ij} = \int_0^L \rho J(x)\,u_i(x)\,u_j(x)\,dx. \tag{4.32}$$

These equations can be normalized for comparison with the exact results derived in section 3.2. In normalized form, Equations 4.31 and 4.32 become

$$\widetilde{K}_{ij} = \frac{K_{ij}}{G\sigma_{T_0}/L} = \int_0^1 \frac{G\sigma_T(\widetilde{x})}{G\sigma_{T_0}}\left(\frac{\partial u_i(\widetilde{x})}{\partial \widetilde{x}}\right)\left(\frac{\partial u_j(\widetilde{x})}{\partial \widetilde{x}}\right)d\widetilde{x} + \eta_l u_i(1)\,u_j(1)\,, \tag{4.33}$$

$$\widetilde{M}_{ij} = \frac{M_{ij}}{\rho J_0 L} = \int_0^1 \frac{\rho J(\widetilde{x})}{\rho J_0}u_i(\widetilde{x})\,u_j(\widetilde{x})\,d\widetilde{x}, \tag{4.34}$$

where $E\sigma_{T_0}$ and ρJ_0 are the bending stiffness and mass density at $x = 0$, respectively. Also, $\eta_l = \frac{\kappa_l h^2 L}{G\sigma_{T_0}}$ and $\widetilde{x} = \frac{x}{L}$. If the cantilever tip were offset from the end of the cantilever, then the last term in Equation 4.33 must be modified to accommodate the offset tip location, such that

$$\widetilde{K}_{ij} = \int_0^1 \frac{G\sigma_T(\widetilde{x})}{G\sigma_{T_0}}\left(\frac{\partial u_i(\widetilde{x})}{\partial \widetilde{x}}\right)\left(\frac{\partial u_j(\widetilde{x})}{\partial \widetilde{x}}\right)d\widetilde{x} + \eta_l u_i\left(\frac{L_{tip}}{L}\right)u_j\left(\frac{L_{tip}}{L}\right).$$

In terms of the normalized matrices, $\widetilde{\mathbf{K}}$ and $\widetilde{\mathbf{M}}$, the EVP is given by

$$\widetilde{\mathbf{K}}\mathbf{a} = \Omega^2\widetilde{\mathbf{M}}\mathbf{a}, \tag{4.35}$$

where $\mathbf{a}$ is the eigenvector of expansion coefficients and the normalized frequency is

$$\Omega = \frac{\lambda}{\sqrt{Gc_{T_0}/\rho J_0 L^2}}. \tag{4.36}$$

4.2.1 Approximate Torsional Modal Sensitivity

To derive the equations governing the sensitivity of the cantilever to changes in the surface stiffness, the derivative of Equation 4.35 is taken with respect to η_l. This result is written as

$$\frac{\partial \widetilde{\mathbf{K}}}{\partial \eta_l}\mathbf{a} + \widetilde{\mathbf{K}}\frac{\partial \mathbf{a}}{\partial \eta_l} = 2\Omega\frac{\partial \Omega}{\partial \eta_l}\widetilde{\mathbf{M}}\mathbf{a} + \Omega^2\frac{\partial \widetilde{\mathbf{M}}}{\partial \eta_l}\mathbf{a} + \Omega^2\widetilde{\mathbf{M}}\frac{\partial \mathbf{a}}{\partial \eta_l}. \tag{4.37}$$

Noticing that $\widetilde{\mathbf{M}}$ does not depend explicitly on η_l and assuming that the change in the eigenvector to small stiffness changes is negligible, allows Equation 4.37 to be simplified as

$$\frac{\partial \widetilde{\mathbf{K}}}{\partial \eta_l}\mathbf{a} = 2\Omega\frac{\partial \Omega}{\partial \eta_l}\widetilde{\mathbf{M}}\mathbf{a}. \tag{4.38}$$

The normalization condition, $\mathbf{a}^{\mathrm{T}}\widetilde{\mathbf{M}}\mathbf{a} = 1$, is used to simplify Equation 4.38 by multiplying the right side by $\mathbf{a}^{\mathrm{T}}$. This enables Equation 4.38 to be further simplified as

$$\frac{\partial \Omega}{\partial \eta_l} = \frac{1}{2\Omega}\mathbf{a}^{\mathrm{T}}\frac{\partial \widetilde{\mathbf{K}}}{\partial \eta_l}\mathbf{a}. \tag{4.39}$$

Comparison of Equation 4.39 with the definition of the normalized torsional sensitivity from Equation 3.67 gives

$$\frac{\partial \Omega}{\partial \eta_l} = \sigma_t.$$

The approximate form of the torsional sensitivity is then given by [45]

$$\sigma_t = \frac{1}{2\Omega}\mathbf{a}^{\mathrm{T}}\frac{\partial \widetilde{\mathbf{K}}}{\partial \eta_l}\mathbf{a}. \tag{4.40}$$

This expression for the approximate modal sensitivity is governed by Equation 4.35. For a give stiffness, η_l, the eigenvalues, Ω, and eigenvectors, $\mathbf{a}$, are calculated from Equation 4.35. The sensitivity for each mode is then found using Equation 4.40.

The torsional modal sensitivity, σ_t, for the first five modes is plotted in Figure 4.2 for the case of a cantilever with a constant cross-section. The exact results from Equation 3.67 are represented by the solid curves and the approximate results from Equation 4.40 are represented by the symbols. There is good agreement between the solutions. The error between the solutions is less than 0.021% for the first four modes with the largest error in the highest mode. The error for the fifth mode is less than 0.65% for the entire range of η_l.

The torsional modal sensitivity has manner similar features to the flexural. The first mode is the most sensitive for small η_l. For stiffer samples, the sensitivity begins to decrease, finally dropping like $1/\eta_l$ for large η_l. In contrast with the flexural sensitivity, the torsional sensitivities are more compact, meaning that the sensitivities of the modes is about the same for $\eta_l > 4$. The transition region for the torsional sensitivity occurs at about the same level of the lateral stiffness for all modes.

4.3 Cantilever Models

Four different models have been developed for the different kinds of cantilevers used in AFM research. A uniform rectangular cantilever will be modeled and three nonuniform cantilevers will be modeled. The equations used for the cross-sectional area, A, the area moment of inertia, I, the torsional constant, c_T, and the area polar moment of inertia, J, will be presented for each model. These equations will then be used with the Rayleigh-Ritz

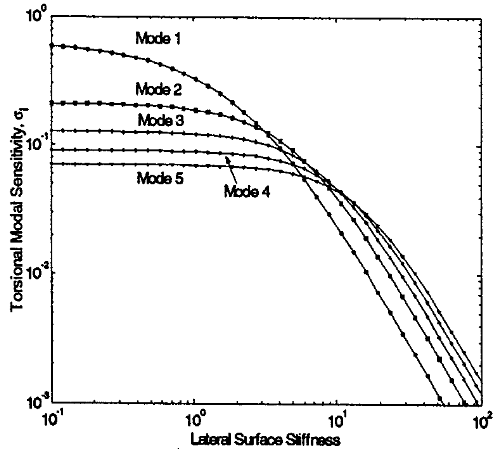

Figure 4.2: The exact and approximate results for the torsional modal sensitivity for a cantilever with a uniform cross-section. The solid curves are the exact solution from Equation 3.67 and the symbols represent the approximate solution from Equation 4.40.

method to model the dynamics of the different cantilevers.

4.3.1 Rectangular Cantilever Model

The uniform rectangular cantilever can easily be modeled with the Rayleigh-Ritz method. The results from this approximate method compare well with the exact results obtained from the equations presented in chapter 3. The expressions for I and A used for flexural vibration modes are as follows

$$A = tW \quad \text{and} \quad I = \frac{Wt^3}{12}, \tag{4.41}$$

where t is the thickness of the cantilever and W is the width of the cantilever. For torsional vibration modes, the polar moment of area, J, and the torsional constant, c_T, are

$$J = \frac{Wt^3 + tW^3}{12} \quad \text{and} \quad c_T = \frac{t^4}{3}\left[\frac{W}{t} - 0.63\right]. \tag{4.42}$$

The expressions for Equation 4.41 are substituted into Equations 4.15 and 4.16 to calculate the $\widetilde{\mathbf{K}}$ and $\widetilde{\mathbf{M}}$ matrices for flexural vibrations and the expressions from Equation 4.42 are substituted into Equations 4.31 and 4.32 to calculate the $\widetilde{\mathbf{K}}$ and $\widetilde{\mathbf{M}}$ matrices for torsional vibrations. The use of the Rayleigh-Ritz method is validated by comparing the results from the Rayleigh-Ritz method with the results obtained in chapter 3. Table 4.1 show the first five flexural eigenvalues for the *free* case. The exact eigenvalues were calculated from Equation 3.28 or from Equation 3.36 with $\kappa_n = 0$. The approximate eigenvalues were calculated by solving the EVP given by Equation 4.19 with admissible functions of the form

$$u_i(\bar{x}) = \left(\frac{x}{L}\right)^{i+1}. \tag{4.43}$$

These admissible functions are differentiable over the domain of the system and they satisfy the geometric boundary conditions. Another possible choice for admissible functions would be the exact mode shapes calculated from Equation 3.27. The number of terms used for the admissible functions must be chosen with caution. Figure 4.3 shows the first three calculated eigenvalues for the *free* flexural vibration case with three to twelve terms used for the admissible functions. Using too many terms can lead to numerical instabilities as evident by the decrease in the eigenvalues as shown Figure 4.3 for terms greater than eleven. Using too few terms will lead to poor approximations of the eigenvalues and will limit the number of eigenvalues that can be sufficiently approximated. The eigenvalues converge well with six terms, but for higher modes, more terms are needed. A good compromise for this analysis was found to be ten terms.

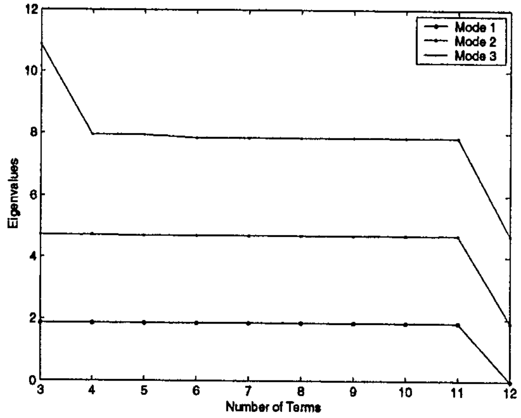

Figure 4.3: The convergence of the calculated flexural eigenvalues for the *free* case based on the number of terms used for the admissible functions.

Table 4.1 shows a comparison of exact and approximate flexural eigenvalues for the *free* case. The approximate results were calculated with ten terms used for the admissible functions. The difference between the exact and approximate results is insignificant. The two results begins to deviate at the third mode, with the largest error occurring at the fifth mode.

A similar comparison of the torsional eigenvalues for the *free* case is shown is Table 4.2. The approximate eigenvalues were calculated by solving Equation 4.35 with admissible

Table 4.1: Comparison of flexural eigenvalues calcualted from the exact result and from the Rayleigh-Ritz method.

Mode	Exact	Rayleigh-Ritz Method
1	1.875104069	1.875104069
2	4.694091133	4.694091133
3	7.854757438	7.854757444
4	10.99554073	10.99563854
5	14.13716839	14.13813563

functions of the form

$$u_i(\bar{x}) = \left(\frac{x}{L}\right)^i. \tag{4.44}$$

Ten terms were used for the expansion. The exact eigenvalues were calculated using Equation 3.53 with $\eta_l = 0$. The largest error between the exact and approximate results is with the fifth mode, but overall the difference between the results is insignificant.

Table 4.2: Comparison of torsional eigenvalues calcualted from the exact result and from the Rayleigh-Ritz method.

Mode	Exact	Rayleigh-Ritz Method
1	1.570796327	1.570796327
2	4.712388980	4.712388980
3	7.853981634	7.8543981794
4	10.99557429	10.995665903
5	14.13716694	14.143600842

4.3.2 Triangular Cantilever Model

One of the triangular cantilevers, common to the AFM, can be represented by the geometry given in Figure 4.4. The triangular cantilever is modeled as a beam with a nonuniform cross-section. Some models for these triangular cantilevers have approximated the geometry of the cantilever as two parallel beams with a triangular section attached to the end of the beams [28],[49]. It was determined that approximating the geometry of the cantilever is not appropriate for analyzing the vibrational response of the cantilevers because the true shape of the cantilever is not maintained. This affects the mode shapes of the cantilevers. Using the approximated geometry will not adequately model the dynamics of the triangular cantilever.

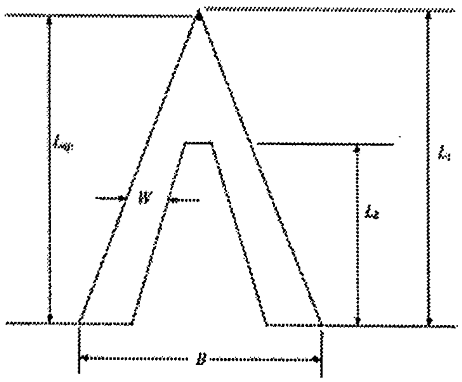

Figure 4.4: Geometry for the nonuniform triangular cantilever.

The cantilever is divided into two parts to aid in developing the model. The first part is the length $0 \le x \le L_2$ and the second part is the length $L_2 \le x \le L_1$, where x represents the direction parallel to the cantilever. The expressions used for calculating I and A for $0 \le x \le L_2$ for flexural vibrations are given by

$$A = \left(\frac{Dt}{U}(4W - BR) - \frac{Bt}{L_1}\right)x + t(4QB - 6W) \tag{4.45}$$

and

$$I = \left(\frac{Dt^3}{12U}(4W - BR) - \frac{Bt^3}{12L_1}\right)x + \frac{t^3}{12}(4QBR - 6W), \tag{4.46}$$

where $D = \frac{(Q-1)}{R}$, and $U = L_1(R - 2Q)$. In these relations $R = \frac{L_2}{L_1}$ and $Q = \frac{2W}{B}$. The expressions for $L_2 \le x \le L_1$ are

$$A = Bt\left(1 - \frac{x}{L_1}\right) \tag{4.47}$$

and

$$I = \frac{Bt^3}{12}\left(1 - \frac{x}{L_1}\right). \tag{4.48}$$

The torsional vibrations of the triangular cantilever can be examined by defining c_T and J for $0 \le x \le L_2$ as

$$c_T = c_{T_0}\left[\left(\frac{D}{U}\left(2 - \frac{R}{Q}\right) - \frac{1}{QL_1}\right)x + 1\right], \tag{4.49}$$

and

$$J = J_0\left[\left(\frac{D}{U}\left(2 - \frac{R}{Q}\right) - \frac{1}{QL_1}\right)x + 1\right], \tag{4.50}$$

where $c_{T_0} = 2\left[\frac{t^4}{3}\left(\frac{W}{t} - 0.63\right)\right]$. and $J_0 = 2\left[\frac{Wt^3 + tW^3}{12}\right]$. The subscript 0 is used to indicate values for c_T, J, A, and I calculated at $x = 0$. For $L_2 \le x \le L_1$ the expressions for c_T and J can be written as

$$c_T = \frac{c_{T_0}}{Q}\left(1 - \frac{x}{L_1}\right), \tag{4.51}$$

and

$$J = \frac{J_0}{Q}\left(1 - \frac{x}{L_1}\right). \tag{4.52}$$

These expressions are used to solve the EVPs derived from the Rayleigh-Ritz method with admissible functions given by Equation 4.43 for flexural vibrations and Equation 4.44 for torsional vibrations.

4.3.3 V-shaped Cantilever Model

Another common AFM cantilever is the V-shaped cantilever, which can be modeled in a similar fashion as the triangular cantilever. The geometry for the V-shaped cantilever is shown in Figure 4.5. Other models for the V-shaped cantilever have approximated the geometry as two parallel beams [12],[49]. When examining the dynamics of the cantilever, the true geometry must be maintained as close as possible.

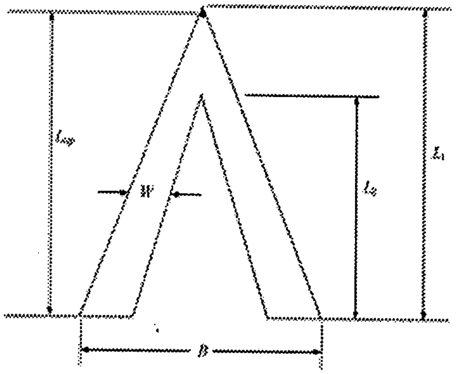

Figure 4.5: The geometry for the v-shaped AFM cantilever.

The cantilever is divided into two parts, as was done for the triangular cantilever. The expressions used for calculating I and A for $0 \le x \le L_2$ are given by

$$A = 2Wt\left[\left(\frac{S}{L_1}\left(\frac{1}{R}-1\right)-\frac{1}{RL_1}\right)x+1\right], \qquad (4.53)$$

and

$$I = \frac{2Wt^3}{12}\left[\left(\frac{S}{L_1}\left(\frac{1}{R}-1\right)-\frac{1}{RL_1}\right)x+1\right], \qquad (4.54)$$

where $S = \frac{1}{(1-R)}$. For $L_2 \le x \le L_1$ the relations are

$$A = 2WtS\left(1-\frac{x}{L_1}\right), \qquad (4.55)$$

and

$$I = \frac{2Wt^3S}{12}\left(1-\frac{x}{L_1}\right). \qquad (4.56)$$

The torsional vibrations of the triangular cantilever can be examined by defining c_T and J for $0 \le x \le L_2$ as

$$c_T = c_{T_0}\left[\left(\frac{S}{L_1}\left(\frac{1}{R}-1\right)-\frac{1}{RL_1}\right)x+1\right], \qquad (4.57)$$

and

$$J = J_0\left[\left(\frac{S}{L_1}\left(\frac{1}{R}-1\right)-\frac{1}{RL_1}\right)x+1\right], \qquad (4.58)$$

where c_{T_0} and J_0 are defined similarly as in the previous section for the triangular cantilever. For $L_2 \le x \le L_1$, c_T and J are defined as

$$c_T = c_{T_0}S\left(1-\frac{x}{L_1}\right), \qquad (4.59)$$

and

$$J = J_0S\left(1-\frac{x}{L_1}\right). \qquad (4.60)$$

These expressions are used to solve the EVPs derived from the Rayleigh-Ritz method with admissible functions given by Equation 4.43 for flexural vibrations and Equation 4.44 for torsional vibrations.

4.3.4 Olympus Cantilever Model

The final type of nonuniform cantilever modeled is the OMCL-AC cantilever manufactured by the Olympus Optical Company [50]. This cantilever has a rectangular body and a triangular section at the end of the cantilever. The geometry for this cantilever model is shown in Figure 4.6. Other cantilevers used in AFM research have a similar form, such as the dLevers manufactured by Thermomicroscopes [13]. This model, developed for the Olympus cantilever, will be applied to cantilevers with a similar form, and will be referred to as the "Olympus" model.

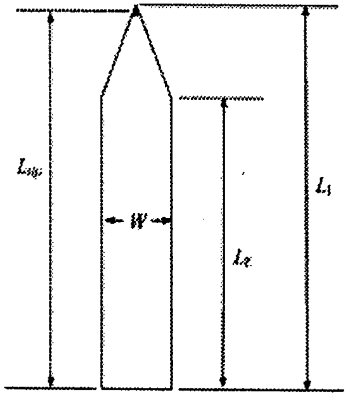

Figure 4.6: Geometry for the Olympus cantilever model.

The model for the cantilever shown in Figure 4.6 is divided into two parts, one for the rectangular body and one for the triangular section. For flexural vibrations, A and I

for the rectangular section, $0 \leq x \leq L_2$, can be written as

$$A = A_0 \tag{4.61}$$

and

$$I = I_0, \tag{4.62}$$

where $A_0 = Wt$ and $I_0 = \frac{Wt^3}{12}$. For the triangular section, $L_2 \leq x \leq L_1$, the expressions for A and I are

$$A = A_0 U \left(1 - \frac{x}{L_1}\right), \tag{4.63}$$

and

$$I = I_0 U \left(1 - \frac{x}{L_1}\right), \tag{4.64}$$

where $U = \frac{1}{(1-R)}$.

To examine the torsional vibration response of the Olympus cantilevers, expressions for c_T and J are needed. The expressions for $0 \leq x \leq L_2$ are

$$c_T = c_{T_0}, \tag{4.65}$$

and

$$J = J_0, \tag{4.66}$$

where $c_{T_0} = \frac{t^4}{3}\left[\frac{W}{t} - 0.63\right]$ and $J_0 = \frac{Wt^3+tW^3}{12}$. For the triangular section, $L_2 \leq x \leq L_1$, the expressions for A and I are

$$c_T = c_{T_0} U \left(1 - \frac{x}{L_1}\right), \tag{4.67}$$

and

$$J = J_0 U \left(1 - \frac{x}{L_1}\right). \tag{4.68}$$

Some cantilevers have a trapezoidal cross-section, which was discovered when examining a few cantilevers with the scanning electron microscope (SEM). Looking only at the expressions needed for a flexural vibration analysis, A_0 and I_0 become

$$A_0 = \frac{t}{2}(W_1 + W_2) \tag{4.69}$$

and

$$I_0 = t^3 \left[\frac{W_1^2 + 4W_1W_2 + W_2^2}{36(W_1 + W_2)}\right], \tag{4.70}$$

where W_1 and W_2 are the width dimensions defined in Figure 4.7.

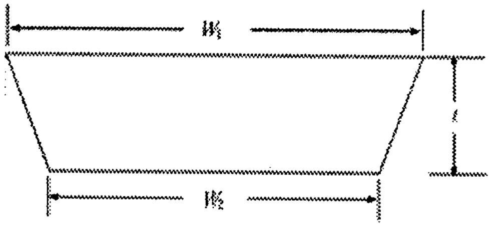

Figure 4.7: Geometry for a trapezoidal cross-section.

4.4 Example Modal Sensitivity Calculations

To compare the four cantilever models outlined in section 4.3, example flexural and torsional modal sensitivities were calculated using Equations 4.24 and 4.40, respectively. These calculations were carried out for cantilevers defined by the geometric properties given in table 4.3. The material properties for each cantilever are E = 179 GPa, ν = 0.28, and ρ = 2330 kg/m^3. A ten-term polynomial expansion was used for the approximate method. The polynomial functions are defined by Equations 4.43 and 4.44 for the flexural and torsional modal sensitivities, respectively.

Table 4.3: The geometric dimensions used for modal sensitivity calculations of the four cantilever models defined in section 4.3. All dimensions are in μm.

Cantilever	L_1	L_2	L_{tip}	W	B	t
Rectangular	200	—	200	40	—	1
Olympus	200	160	200	40	—	1
Triangular	200	160	200	20	164	1
V-shaped	200	160	200	20	164	1

A plot of the flexural modal sensitivity vs. normal surface stiffness, η_n, for the Olympus and rectangular cantilever models is shown in Figure 4.8. The first three modes for each cantilever are depicted. In comparison of the Olympus cantilever and the rectangular cantilever, the flexural modal sensitivity for the rectangular cantilever is greater than that of the Olympus cantilever. This is especially evident when the cantilever is more compliant than the sample surface. The first three modes of the rectangular cantilever are greater than those of the Olympus cantilever, except for when $\eta_n \approx 63$. For this surface stiffness, the sensitivity of the second mode for the Olympus cantilever is greater than the sensitivity for the first mode of the rectangular cantilever. The maximum sensitivity of the first mode for the rectangular cantilever is 6.44 kHz and the maximum sensitivity of the first mode for the Olympus cantilever is 0.54 kHz. The sensitivity begins to change more sharply when $\eta_n \approx 28$ for the rectangular cantilever and when $\eta_n \approx 60$ for the Olympus cantilever. Therefore, the Olympus cantilever will maintain a greater sensitivity, as compared to the rectangular cantilever, for samples with larger stiffness variations.

The torsional modal sensitivity for these two cantilevers is shown in Figure 4.9. The

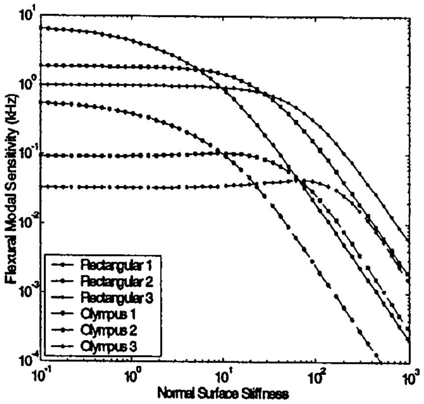

Figure 4.8: The flexural modal sensitivity for a rectangular and Olympus cantilever. The first three modes for each cantilever are depicted. The numbers next to the cantilever names correspond to vibration modes.

torsional modal sensitivities are closely spaced as those shown in Figure 4.2 for the uniform cantilever. The sensitivity for the Olympus cantilever is greater than that of the rectangular cantilever. The maximum sensitivity for the first mode of the Olympus cantilever is 126 kHz and the maximum sensitivity for the rectangular cantilever is 115 kHz. The sensitivity begins to change more sharply when $\eta_l \approx 3.63$ for the Olympus cantilever and when $\eta_l \approx 0.15$ for the rectangular cantilever. Therefore, the Olympus cantilever will again maintain a greater sensitivity for samples with large stiffness variations.

In Figure 4.10, the flexural modal sensitivity of a triangular and V-shaped cantilever are depicted. The difference in sensitivity between the two cantilevers is very small. This is expected since there is very little difference in the shapes of the cantilevers. The ratio of the first mode to the third mode is about 6 for the V-shaped cantilever and about 6.5 for the triangular cantilever. The sensitivity begins to change more sharply when $\eta_n \approx 25$ for each cantilever. Therefore, either cantilever would be suitable for examining samples with large variations in stiffness.

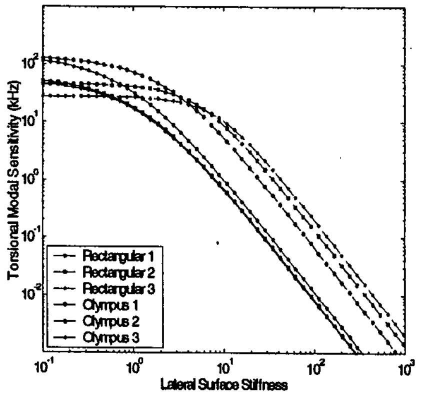

Figure 4.9: The torsional modal sensitivity for a rectangular and Olympus cantilevers. The numbers next to the cantilever names correspond to a specific mode.

The torsional modal sensitivity for the triangular and V-shaped cantilevers is shown in Figure 4.11. The difference in modal sensitivity for each cantilever is very small. The maximum sensitivity for the first mode of the V-shaped cantilever is about 79 kHz and the maximum sensitivity for the triangular cantilever is about 72 kHz. For $\eta_l < 0.45$, the sensitivity for the first mode of the triangular cantilever is slightly greater than that of the V-shaped cantilever. For $\eta_l > 0.45$, the sensitivity for the first mode of the V-shaped

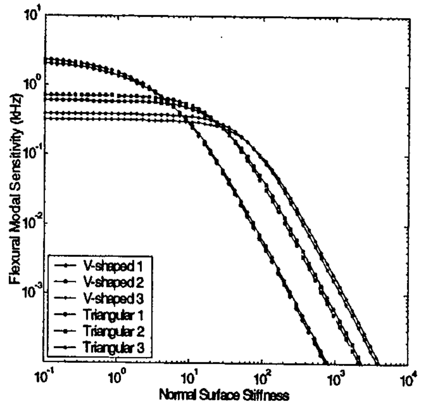

Figure 4.10: The flexural modal sensitivity of the first three modes for a triangular and V-shaped cantilevers. The numbers next to the cantilever names correspond to a specific mode.

cantilever becomes greater than that for the triangular. This transition between cantilevers also happens for modes 2 and 3, except that it occurs at $\eta_l \approx 1$.

4.5 Discussion

The Rayleigh-Ritz method was used to approximate the vibration response for the AFM cantilevers. This method was used to describe both flexural and torsional vibration modes. The torsional and modal sensitivity was also derived using this method. The equations used to approximate four different cantilever shapes were presented in section 4.3. Example modal sensitivity calculations were presented to demonstrate the usefulness of

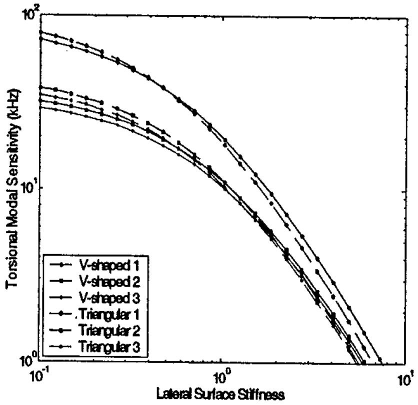

Figure 4.11: The torsional modal sensitivity of the first three modes for a V-shaped and triangular cantilevers. Thge numbers next to the cantilever names correspond to specific vibration modes.

this technique for selecting the proper cantilever or vibration mode for use in measurements conducted with the AFM.

Chapter 5

Analysis and Results

The results obtained using the cantilever models presented in section 4.3 will be compared with experimental results. The models will be used to determine the tip-sample contact stiffness and their usefulness for measuring the Young's modulus of a sample surface will be discussed. Example calculations of the modal sensitivity for each cantilever model will be presented to show a comparison of the different models. AFAM results will be presented to demonstrate the improved imaging capabilities available with this dynamic AFM technique.

5.1 The Spring Constants of AFM Cantilevers

The spring constant of AFM cantilevers is an important parameter used in measurements taken with the AFM. The spring constant limits the force exerted on the sample surface during measurements and also limits the speed at which measurements can be taken. When measuring tip-sample interaction forces, an accurate value for the spring constant is

needed. Accurate determination of cantilever spring constants will also aid in the quantitative interpretation of images.

A few different approaches have been taken to determine the spring constants of AFM cantilevers. A common parameter used in each of these methods is the measured first resonance frequency of the cantilever out of contact with the sample surface. Cleveland *et al.* developed a method in which the spring constant is determined by measuring the first resonance frequency with different masses attached to the end of the cantilever [51]. The resonance frequency measurement without a mass and with just one mass will provide enough information to determine the spring constant. The expression for the spring constant, relating the added mass and the loaded and unloaded resonance frequencies, using the Cleveland method, is

$$k_{clev} = \frac{4\pi^2 m}{(1/f_1^2) - (1/f_2^2)}, \tag{5.1}$$

where m is the added mass, f_1 is the unloaded resonance frequency, and f_2 is the loaded resonance frequency.

Sader *et al.* also developed a method for determining the cantilever spring constants in which the measured dimensions of the cantilevers and the measured resonance frequency in vacuum are used [52],[53]. The Sader method was developed by modeling the cantilevers as plates and then performing a finite element analysis to provide the necessary results for calculating the spring constant for any type of cantilever [54]. This method requires the dimensions of the cantilever to be known, which will allow the mass of the cantilever to calculated using the mass density of the cantilever. The spring constant determined from the Sader method is given by

$$k_{sad} = M_c m 4\pi^2 f^2, \tag{5.2}$$

where m is the mass of the cantilever, M_c is the normalized effective mass, which relates the resonance frequency for the cantilever to the spring constant, and f is the resonance frequency of the cantilever measured in vacuum. M_c is determined from the finite element results provided by Sader *et al.* [52]. The M_c results are given for cantilevers with different aspect ratios, $\frac{B}{L}$, and width ratios, $\frac{W}{B}$. Sader *et al.* compared their method with the Cleveland method for rectangular and V-shaped cantilevers [52].

The Rayleigh-Ritz method was used with the area, A, and area moment of inertia, I, relations from section 4.3.1 for the rectangular cantilevers and section 4.3.3 for the V-shaped cantilevers to calculate the spring constants for the same cantilevers that Sader examined using his method and the Cleveland method [54]. The spring constant calculated with the Rayleigh-Ritz method is given by

$$k_{cm} = \left(\frac{EI_0}{L^3}\right)\frac{1}{U}, \tag{5.3}$$

where U is the vector summation of the product $\tilde{\mathbf{K}}^{-1}\tilde{\mathbf{u}}$. The values for $\tilde{\mathbf{K}}$ are given by Equation 4.17 and $\tilde{\mathbf{u}}$ is a dimensionless vector of admissible functions.

The comparison of the methods used to determine the cantilever spring constants is shown in Table 5.1. The cantilevers were made of Si_3N_4 under closely monitored conditions. A density of $\rho = 2800$ kg/m^3, a Young's modulus of $E = 130$ GPa, and a thickness of $t = 0.61$ μm were used in the calculations.

The results given in Table 5.1 show good agreement for each method. The largest differences between the three methods is for the method using the Rayleigh-Ritz method, specifically for cantilevers 1 and 3. The difference is insignificant and the results demonstrate that the method utilizing the Rayleigh-Ritz method is adequate to determine the cantilever spring constants, provided that the measured cantilever dimensions are available.

Table 5.1: Comparison of cantilever spring constant calculation methods. Cantilevers 3 and 6 are rectangular cantilevers and the remainder are V-shaped. The spring constants were determined using the Cleveland method [51], k_{clev}, the Sader method [52], k_{sad}, and the Rayleigh-Ritz method outlined in the previous chapter with the appropriate functions from section 4.3, k_{cm}. All dimensions are in μm unless otherwise noted.

cantilever	B	W	L_1	L_2	f_{free} (kHz)	k_{clev} $(\frac{N}{m})$	k_{sad} $(\frac{N}{m})$	k_{cm} $(\frac{N}{m})$
1	182	37.4	182	107.2	29.5	0.091	0.092	0.090
2	178	16.4	176	143.57	24.6	0.044	0.044	0.044
3	—	11.9	101	—	66.3	0.092	0.091	0.087
4	90.3	14.1	89.2	61.34	109	0.28	0.29	0.29
5	90.4	24.2	89.4	41.54	135	0.46	0.47	0.47
6	—	21.7	101	—	66.3	0.16	0.16	0.16

Manufacturers of AFM cantilevers provide the length, width, thickness, and spring constants for each of their cantilevers. The spring constants are usually determined from resonance frequency measurements and approximations of the cantilever geometry. The resonance frequency measurements are done on sample cantilevers manufactured from a given group of cantilevers. Table 5.2 shows a comparison of the calculated, k_{calc}, manufacturer provided by the manufacturer, k_{man}, spring constants for dLevers [13]. The Olympus model outlined in section 4.3.4 was used to calculate the spring constants using the Rayleigh-Ritz method. The dLevers are made of Si_3N_4. The values of $E = 150$ GPa and $\rho = 3100$ kg/m^3 for bulk Si_3N_4, and a thickness $t = 2.35$ μm were used in the calculations. The thickness of the dLevers was calculated using the first resonance frequency, f_1, measured in air.

Table 5.2: Comparison of manufacuterer provided, k_{man}, and calculated, k_{cm}, spring constants for dLever cantilevers [13].

type	L_1	L_2	L_{tip}	W	f_1 (kHz)	k_{man} $(\frac{N}{m})$	k_{cm} $(\frac{N}{m})$
A	178	145.22	168.9	38.33	99.04	1.3	4.3
B	177.33	143.78	169.45	56.88	101.82	2.2	6.7

As shown in Table 5.2, the difference between k_{man} and k_{cm} is large. The calculated k_{cm} is nearly three times larger than the spring constant provided by the manufacturer. The reason for this large discrepancy can be attributed to variations in the thickness of the cantilevers and variations in Young's modulus and the mass density [22]. The variations in Young's modulus and the mass density for the cantilevers are mainly due to the conditions in which the cantilevers are manufactured. Variations in the length and width are negligible because the photolithography techniques used to manufacture the cantilevers allow for submicrometer resolution in these dimensions [12]. Because of the large differences between the spring constants provided by the manufacturer and those determined using the Olympus model, individual cantilevers should be calibrated before being used for precise measurements.

5.2 Atomic Force Acoustic Microscope Setup

An AFM modified for Atomic Force Acoustic Microscopy (AFAM) was used to measure the resonance frequencies of AFM cantilevers, in and out of contact with a sample surface. The AFAM arrangement shown in Figure 5.1 is similar to that developed by Rabe *et al.* [3], except the built-in cantilever deflection measurement system is used. The AFM used is an Autoprobe CP manufactured by Thermomicroscopes [13]. A transducer, used to excite the flexural vibrations of the cantilever, is placed between the sample and the three-axis piezoelectric scanner. The transducer used has a center frequency of 2.25 MHz [55]. A sine wave signal produced by a HP 33120A[56] waveform generator or a NI 5411[57] waveform generator is used to drive the transducer. The HP 33120A is capable of producing signals greater than 50 mV and the NI 5411 can cover the range of 0-50 mV. The measured displacement signal of the excited cantilever is input into a SR844 Lock-in Amplifier[58] along with the reference excitation signal from the waveform generator. The lock-in amplifier is used to measure the amplitude and phase of the cantilever displacement signal at the excitation frequency. A LabVIEW[57] program was developed to perform frequency sweeps by incrementally changing the excitation frequency of the waveform generator and recording the amplitude and phase output from the lock-in amplifier. The amplitude of the excitation signal needs to be monitored to avoid nonlinear vibration spectra associated with a high excitation amplitude. Only linear vibration spectra is suitable for accurate resonance frequency measurements [59].

To measure the free frequencies of the cantilever, the cantilever is lowered to a position of 1-2 μm from the sample surface. The transducer is then excited with a sine wave. The vibrations of the transducer are transmitted to the cantilever through the air gap between the sample surface and the cantilever. This method has been proven sufficient for exciting the free vibration frequencies of the cantilevers [3]. The contact frequencies of the cantilever are measured by first using the AFM control software to automatically lower the cantilever to a set distance above the sample surface. In an approach, the cantilever is lowered to a set distance above the sample surface. This set distance is related to the load applied to the cantilever through the spring constant of the cantilever. To reduce the movement of the cantilever on the sample surface, the scan size is set to zero or the scanner is turned off. A frequency sweep similar to that done to measure the free frequencies is then performed to measure the contact frequencies.

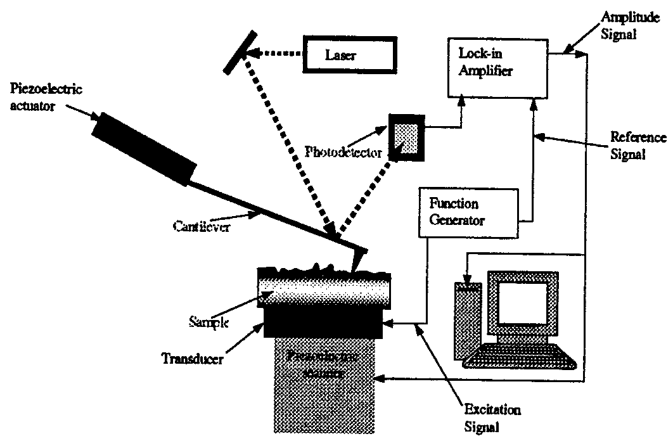

Figure 5.1: Experimental setup for the Atomic Force Acoustic Microsope (AFAM).

5.3 Frequency Response of AFM Cantilevers

The frequency response of AFM cantilevers changes as the tip-sample separation is reduced. The tip-sample interaction is highly nonlinear and changes with the load applied to the cantilever [60]. As the cantilever goes through the transition from free to surface-coupled, the resonance frequencies of the cantilevers shift. An example of this shift in frequency is shown in Figure 5.2, which shows the frequency shift of the first resonance frequency of a dLever B[13] cantilever in contact with a Si(111) sample. As the applied load increases, the attractive force interaction between the cantilever tip and the sample

surface decreases. The attractive forces can mainly be attributed to adhesion effects between the cantilever tip and the sample surface, which causes damping of the vibrating cantilevers [42],[61]. The damping influences the cantilevers in a manner that effectively reduces their spring constants, and thus reduces their resonance frequencies. When the tip experiences repulsive forces, the amplitude of the resonance frequency increases and the frequency shifts to a higher frequency [62]. As the load applied to the cantilever is increased, the contact area between the cantilever tip and the sample surface increases, which causes a higher contact stiffness. This higher contact stiffness subsequently leads to an increase in the resonance frequencies [63]. It should also be noted that the frequency shift for higher modes is smaller in comparison to lower resonance frequencies [64].

Experimental results will be presented for two different rectangular cantilevers and two different triangular cantilevers. The experimental free and contact frequencies will be compared with the models presented in section 4.3.

5.3.1 Flexural Free Vibrations

Each of the four cantilever models, as presented in section 4.3, will first be used in a comparison with experimental frequency measurements taken for the case of the cantilever free from contact with a sample surface.

Rectangular Model

The first three free resonance frequencies of a model NSC16 [65] rectangular cantilever are shown in Figure 5.3. The cantilever is made of Si with bulk properties of $E = 169$ GPa and $\rho = 2330$ kg/m^3. The dimensions of the cantilever, measured optically,

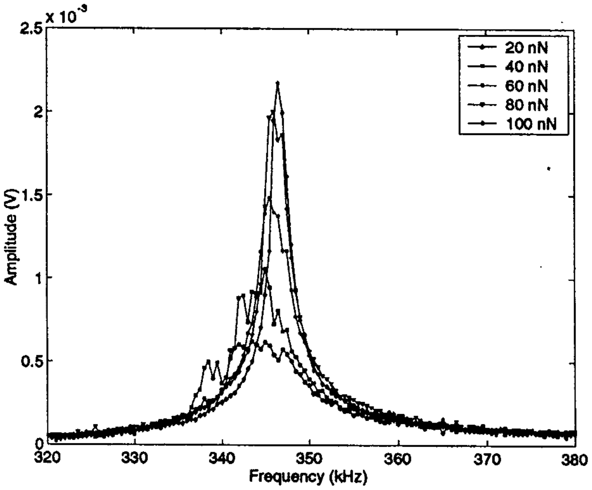

Figure 5.2: First resonance frequency shift for a model B dLever [13] in contact with Si(111).

are $L_1 = 236.43$ μm and $L_{tip} = 225.35$ μm. The cantilever has a trapezoidal cross-section, as measured with an SEM, with $W_1 = 51.24$ μm and $W_2 = 42.45$ μm. The thickness of the cantilever was calculated using the measured free frequencies with the relation, derived for a trapezoidal cross-section,

$$t = \sqrt{\frac{\rho}{E}\left(\frac{4\pi^2 f^2 L^4}{(\lambda)^4}\right)\left(\frac{18\,(W_1+W_2)^2}{W_1^2+4W_1W_2+W_2^2}\right)}, \tag{5.4}$$

where f is the measured free frequency and λ is the eigenvalue calculated from Equation 4.4. The thickness calculated using the first frequency is $t = 7.24$ μm, from the second $t = 7.14$ μm, and from the third $t = 6.85$ μm. The thickness calculated using the second resonance frequency was chosen to be used in the model for this cantilever. The reason for

---

this selection is because the calculated contact resonance frequencies more closely match the measured contact frequencies, which will be shown in section 5.3.3.

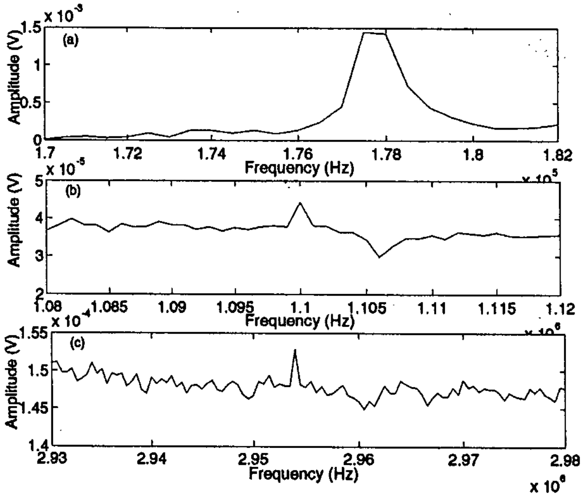

Figure 5.3: First three free resonance frequencies of a model NSC16 [65] rectangular cantilever. (a) First resonance frequency. (b) Second resonance frequency. (c) Third resonance frequency.

The measured and calculated free resonance frequencies are shown in Table 5.3. There is a noticeable difference between the measured and calculated frequencies for the first and third modes, with the largest error of 4.27% for the third mode. The difference between the measured and calculated frequencies can more than likely be attributed to variations in the thickness of the cantilever.

Table 5.3: The measured, f_{exp}, and the calculated, f_{calc}, free frequencies for the rectangular NCS16 cantilever.

mode	f_{exp} (kHz)	f_{calc} (kHz)
1	178.0	175.5
2	1100.0	1100.0
3	2954.0	3080.0

Olympus Model

The Olympus model, outlined in section 4.3.4, will be used to model the dynamics of a model dLever A [13] cantilever. The free resonance frequencies were calculated using this model and compared with the first two measured resonance frequencies shown in Figure 5.4. The cantilever is made of Si_3N_4 with bulk properties of $E = 150$ GPa and $\rho = 3100$ kg/m^3. The dimensions of the cantilever, measured optically, are $L_1 = 178.0$ μm, $L_2 = 145.22$ μm, $L_{tip} = 168.9$ μm, and $W = 38.33$ μm. The thickness of the cantilever was calculated using the measured free resonance frequencies and Equation 5.4, with $W_1 = W_2 = W$ for a rectangular cross-section. The thickness calculated using the first measured frequency is $t = 2.0905$ μm and the thickness calculated from the second is $t = 2.0638$ μm. The thickness calculated from the first resonance frequency was chosen to be used in the model for this cantilever. The reason for this selection is because the calculated contact resonance frequencies more closely match the measured contact frequencies, which will be shown in section 5.3.3.

The measured and calculated free resonance frequencies are shown in Table 5.4. The largest error between the measured and calculated frequencies is with the second mode, which is 1.3%.

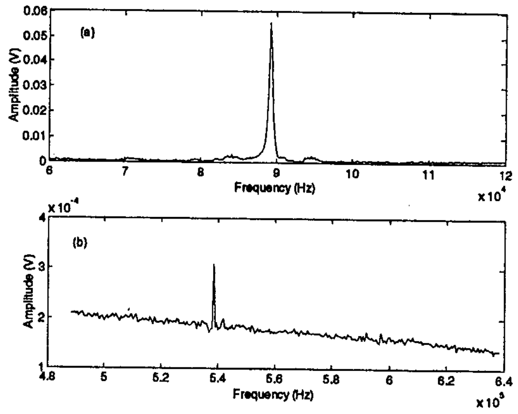

Figure 5.4: The first two free resonance frequencies for the model dLever A cantilever [13]. (a) First resonance frequency. (b) Second resonance frequency.

Table 5.4: The measured, f_{exp}, and the calculated, f_{calc}, free frequencies for the dLever A cantilever.

mode	f_{exp} (kHz)	f_{calc} (kHz)
1	89.1	89.1
2	538.9	545.9

Triangular Model

The triangular model, outlined in section 4.3.2, will be used to model the dynamics of a model NCS11 A [65] cantilever. The free resonance frequencies will be calculated using this model and compared with the first two measured resonance frequencies shown in Figure 5.5. The cantilever is made of Si with bulk properties of $E = 169$ GPa and $\rho = 2330$ kg/m^3. The dimensions of the cantilever, measured optically, are $L_1 = 197.84$ μm, $L_2 = 141.63$ μm,

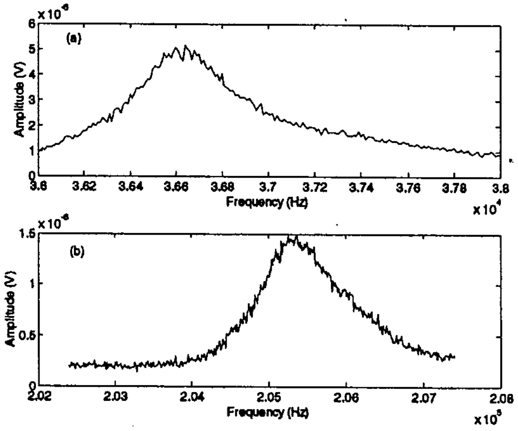

Figure 5.5: The first two free resonance frequencies for the NCS11 A [65] triangular cantilever. (a) First resonance frequency. (b) Second resonance frequency.

$L_{tip} = 190.39$ μm, $B = 409.57$ μm, and $W = 44.02$ μm. A thickness of $t = 0.79$ μm was measured using a SEM.

The measured and calculated free resonance frequencies are shown in Table 5.5. The error between the measured and calculated frequencies for the first mode is 8.84% and the error for the second mode is 2.86%. An adjustment could be made to improve the results for the free resonance frequencies calculated using the triangular model by using a cantilever thickness calculated from the measured frequencies. An adjustment in the thickness could also cause the calculated contact resonance frequencies to differ greatly from the measured frequencies.

Table 5.5: The measured, f_{exp}, and the calculated, f_{calc}, free frequencies for the NCS11 A cantilever.

mode	f_{exp} (kHz)	f_{calc} (kHz)
1	36.64	33.4
2	205.37	211.24

V-shaped Model

The V-shaped cantilever model, outlined in section 4.3.3, will be used to model the dynamics of a model Si_3N_4 V-shaped cantilever manufactured by Advanced Surface Microscopy [66]. The free resonance frequencies will be calculated using this model and compared with the first two measured resonance frequencies shown in Figure 5.6. The cantilever is made of Si_3N_4 with bulk properties of $E = 150$ GPa and $\rho = 3100$ kg/m^3. The dimensions of the cantilever, measured optically, are $L_1 = 184.0$ μm, $L_2 = 104.88$ μm, $L_{tip} = 180.0$ μm, $B = 194.45$ μm, and $W = 41.43$ μm. A thickness of $t = 0.40$ μm was measured using a SEM.

The measured and calculated free resonance frequencies are shown in Table 5.6. The largest error between the measured and calculated frequencies is with the second mode, which is 1.56%.

Table 5.6: The measured, f_{exp}, and the calculated, f_{calc}, free frequencies for a Si_3N_4 V-shaped cantilever.

mode	f_{exp} (kHz)	f_{calc} (kHz)
1	19.72	19.68
2	105.79	107.44

5.3.2 Torsional Free Vibrations

The AFM used for this research has a split photodetector, which is used for measuring the vertical displacements of the cantilever. It is not adequate for lateral displacement

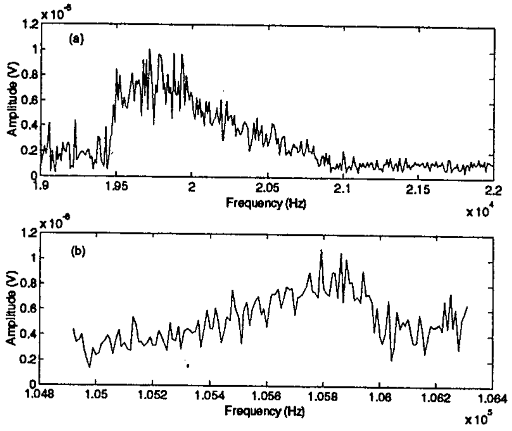

Figure 5.6: First two free resonance frequencies for a V-shaped Si_3N_4 cantilever. (a) First resonance frequency. (b) Second resonance frequency.

measurements. For this reason, torsional measurements were not conducted with the four cantilevers that were analyzed in the previous sections. Instead, the torsional vibrations of a rectangular cantilever will only be examined. The experimental results for a rectangular cantilever were obtained from the Frawnhofer Institute for Nondestructive Testing (IZFP) [67]. The cantilever used in the measurements was a rectangular Si cantilever manufactured by Nanosensors [68]. The bulk properties of $E = 169$ GPa and $\rho = 2330$ kg/m^3 for Si were used in calculations. The measured dimensions of the cantilever are: $L_1 = 477.9\ \mu$m, $L_{tip} = 447.3\ \mu$m, $W_1 = 52.3\ \mu$m, and $W_2 = 40.7\ \mu$m. A thickness of $t = 1.94\ \mu$m for the cantilever was calculated from the measured free flexural resonance frequencies.

The measured and calculated free torsional resonance frequencies are shown in Table 5.7. The largest error between the measured and calculated frequencies is with the first mode, which is 21.2%. This large error with the first mode could be attributed to an error in the measurement of the resonance frequency. A peak frequency at 226.0 kHz was measured along with the peak at 265.5 kHz, and it should also be noted that the third flexural mode is located at 204 kHz. This error could also be due to the use of the rectangular model because, in looking at the cantilever, the Olympus model may be a more appropriate choice.

Table 5.7: The measured, f_{exp}, and the calculated, f_{calc}, free frequencies for a rectangular nanosensor.

mode	f_{exp} (kHz)	f_{calc} (kHz)
1	265.5	209.3
2	626.5	627.8
3	1063.0	1046.4

5.3.3 Flexural Contact Vibrations

The measured contact resonance frequencies will be presented for each of the four cantilevers. As the tip of the cantilever contacts the sample surface and the load applied to the cantilever is increased, the resonance frequency shifts. The shift in the resonance frequency is related to changes in the sample surface stiffness. A plot of the change in frequency vs. change in surface stiffness will also be presented for each cantilever.

Rectangular Model

The first two resonance frequency shifts for the rectangular NCS16 cantilever are shown in Figure 5.7. The sample that the cantilever tip is in contact with is Si(111). In Figure 5.7(a) the first resonance frequency for an applied load of 1000 nN is 663.5 kHz and shifts to a frequency of 664.0 kHz for an applied load of 2000 nN. In Figure 5.7(b) the second resonance frequency for an applied load of 1000 nN is 1374.0 kHz and shifts to a frequency of 1374.5 kHz for an applied load of 2000 nN.

Figure 5.8 shows the change in frequency that occurs when the stiffness of the sample increases. The first two flexural vibration modes are plotted. The plot is created be calculating the eigenvalues, λ, from Equation 4.4, for changes in the surface stiffness, which is defined as κ_n/k_c. The eigenvalues are substitute into the dispersive relation

$$f = \frac{\lambda}{2\pi}\sqrt{\frac{EI}{\rho A L_1^4}}, \tag{5.5}$$

to obtain frequency values. The measured resonance frequencies for the two applied loads are also plotted in Figure 5.8. The intersection of the measured frequencies with the curves for modes 1 and 2 correspond to values for the surface stiffness, which are given in table 5.8.

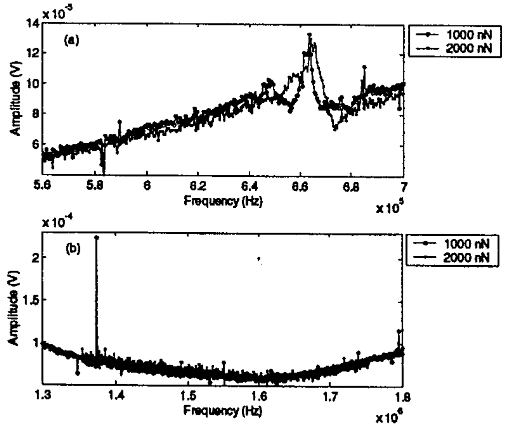

Figure 5.7: The first two contact resonance frequencies for the rectangular NCS16 cantilever. (a) First resonance frequency. (b) Second resonance frequency.

There is relatively good agreement between the calculated stiffness values for each mode at the given applied loads. The differences between the values can be attributed to variations in the physical dimensions of the cantilever and also to possible errors in measuring the contact resonance frequencies.

Table 5.8: The normal surface stiffness values, κ_n/k_c, calculated from the plot of the change in frequency vs. change in surface stiffness for the applied loads of 1000 nN and 2000 nN for the NCS16 rectangular cantilever. Frequencies f_1 and f_2 correspond to the measured vibration modes 1 and 2, respectively.

Applied Load (nN)	f_1 (kHz)	f_2 (kHz)	κ_n/k_c mode 1	κ_n/k_c mode 2
1000	663.5	1374.0	25.671	25.755
2000	664.0	1374.5	25.753	25.789

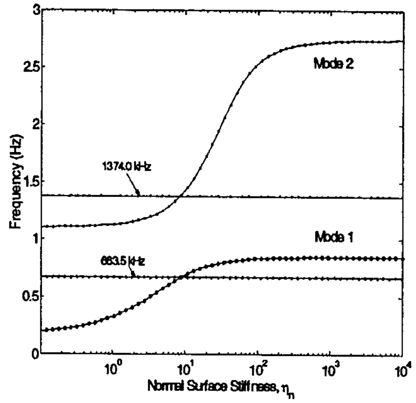

Figure 5.8: The change in resonance frequency due to an increase in the surface stiffness, κ_n/k_c, for the first two modes of the NCS16 rectangular cantilever.

Olympus Model

The first two resonance frequency shifts are shown in Figure 5.9 for the dLever A cantilever. In Figure 5.9(a) the first resonance frequency for an applied load of 30 nN is 355.58 kHz and shifts to a frequency of 356.08 kHz for an applied load of 90 nN. In Figure 5.9(b) the second resonance frequency for an applied load of 30 nN is 1112.7 kHz and shifts to a frequency of 1117.55 kHz for an applied load of 90 nN.

Figure 5.10 shows the change in frequency that occurs when the stiffness of the sample increases. The first two flexural vibration modes are plotted. The measured resonance frequencies for the two applied loads are also plotted in Figure 5.10. The intersection of the measured frequencies with the curves for modes 1 and 2 correspond to values for the

---

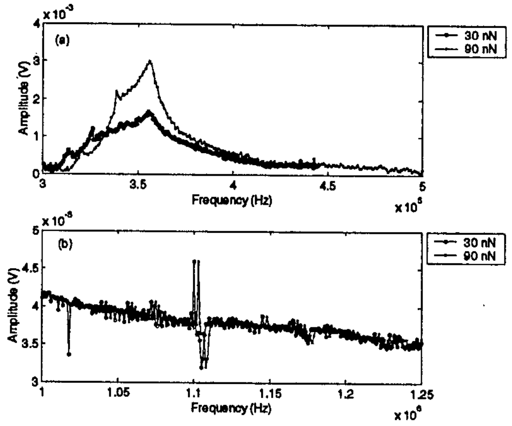

Figure 5.9: The first two measured contact resonance frequencies for the dLever A cantilever at applied loads of 30 nN and 90 nN. (a) First resonance frequency. (b) Second resonance frequency.

surface stiffness, which are given in table 5.9. There is relatively good agreement between the calculated stiffness values for each mode at the given applied loads, especially with the first mode.

Table 5.9: The normal surface stiffness values, κ_n/k_c, calculated from the plot of the change in frequency vs. change in surface stiffness for the applied loads of 30 nN and 90 nN for the dLever A cantilever. Frequencies f_1 and f_2 correspond to the measured resonance frequency of vibration modes 1 and 2, respectively.

Applied Load (nN)	f_1 (kHz)	f_2 (kHz)	κ_n/k_c mode 1	κ_n/k_c mode 2
30	355.58	1112.7	361.64	399.44
90	356.08	1117.6	361.66	396.18

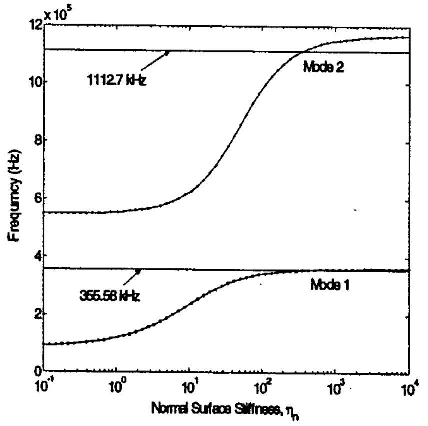

Figure 5.10: The change in resonance frequency due to an increase in the surface stiffness, κ_n/k_c, for the first two modes of the dLever A cantilever.

Triangular Model

The first two resonance frequency shifts are shown in Figure 5.11 for the NCS11 A triangular cantilever. In Figure 5.11(a) the first resonance frequency for an applied load of 60 nN is 62.2 kHz and shifts to a frequency of 62.1 kHz for an applied load of 100 nN. In Figure 5.11(b) the second resonance frequency for an applied load of 60 nN is 223.6 kHz and shifts to a frequency of 224.7 kHz for an applied load of 100 nN.

Figure 5.12 shows the change in frequency that occurs when the stiffness of the sample increases. The first two flexural vibration modes are plotted. The measured resonance frequencies for the two applied loads are also plotted in Figure 5.12. The intersection of the measured frequencies with the curves for modes 1 and 2 correspond to values for the

---

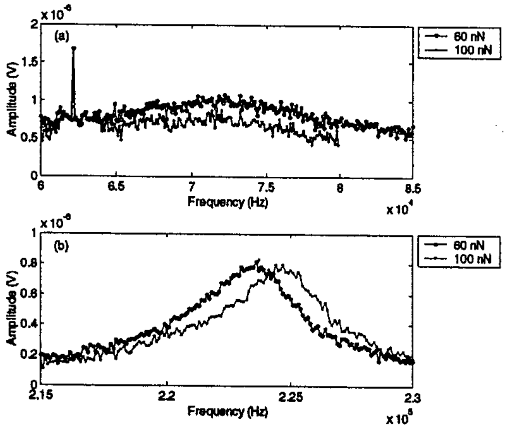

Figure 5.11: The first two contact resonance frequencies of the NCS11 A triangular cantilever at applied loads of 60 nN and 100 nN. (a) First resonance frequency. (b) Second resonance frequency.

surface stiffness, which are given in table 5.10. There is relatively good agreement between the calculated stiffness values for each mode at the given applied loads. The largest difference occurs with the stiffness values for an applied load of 100 nN. The difference between the first and second modes for the 100 nN applied load is 0.4467. This is due to the decrease in the resonance frequency as the load is increased from 60 nN to 100 nN.

Table 5.10: The normal surface stiffness values, κ_n/k_c, calculated from the plot of the change in frequency vs. change in surface stiffness for the applied loads of 60 nN and 100 nN for the NCS11 A triangular cantilever. Frequencies f_1 and f_2 correspond to the measured resonance frequency of vibration modes 1 and 2, respectively.

Applied Load (nN)	f_1 (kHz)	f_2 (kHz)	κ_n/k_c mode 1	κ_n/k_c mode 2
60	62.2	223.6	3.6762	3.8191
100	62.1	224.7	3.7151	4.1618

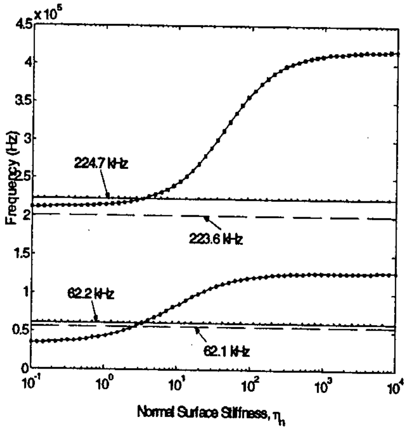

Figure 5.12: The change in resonance frequency due to an increase in the surface stiffness, κ_n/k_c, for the first two modes of the NCS11 A triangular cantilever.

V-shaped Model

The first two resonance frequency shifts are shown in Figure 5.13 for the Si_3N_4 V-shaped cantilever. In Figure 5.13(a) the first resonance frequency for an applied load of 2.2 nN is 47.78 kHz and shifts to a frequency of 47.79 kHz for an applied load of 2.5 nN. In Figure 5.13(b) the second resonance frequency for an applied load of 2.5 nN is 137.54 kHz and shifts to a frequency of 137.75 kHz for an applied load of 4 nN.

Figure 5.14 shows the change in frequency that occurs when the stiffness of the sample increases. The first two flexural vibration modes are plotted. The measured resonance frequencies for the two applied loads are also plotted in Figure 5.14. The intersection of the measured frequencies with the curves for modes 1 and 2 correspond to values for

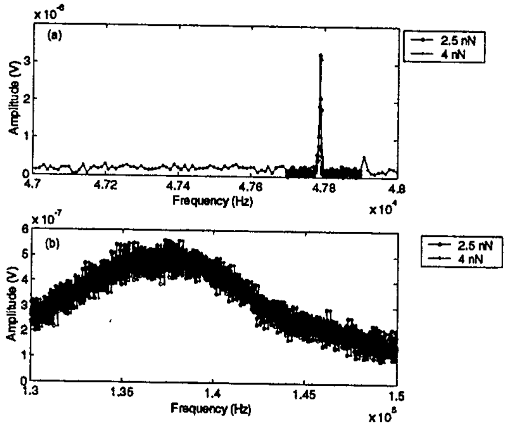

Figure 5.13: The first two contact resonance frequencies for the v-shaped cantilever. The loads applied are 2.5 nN and 4 nN. (a) First resonance frequency. (b) Second resonance frequency.

the surface stiffness, which are given in table 5.11. The difference between the calculated stiffness values for modes 1 and 2 for each applied load is quite large. For the applied load of 2.5 nN the difference is 0.678 and the difference for the 4 nN load is 0.563. These differences can be attributed to errors in the measurement of the contact resonance frequencies and variations in the physical parameters of the cantilever.

Table 5.11: The normal surface stiffness values, κ_n/k_c, calculated from the plot of the change in frequency vs. change in surface stiffness for the applied loads of 2.5 nN and 4 nN for the V-shaped cantilever. Frequencies f_1 and f_2 correspond to the measured resonance frequency of vibration modes 1 and 2, respectively.

Applied Load (nN)	f_1 (kHz)	f_2 (kHz)	κ_n/k_c mode 1	κ_n/k_c mode 2
2.5	47.78	137.54	12.494	11.816
4	47.79	137.75	12.495	11.932

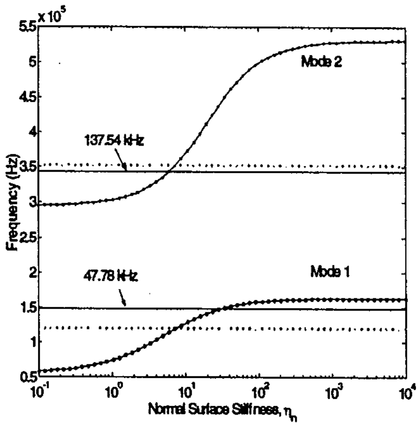

Figure 5.14: The change in resonance frequency due to an increase in the surface stiffness, κ_n/k_c, for the first two modes of the V-shaped cantilever

5.3.4 Torsional Contact Vibrations

The first three torsional contact resonance frequencies for the rectangular Nanosensor are plotted in Figure 5.15 along with curves showing the variation in the resonance frequencies associated with an increase in the lateral surface stiffness, η_l, which is defined as $\eta_l = \frac{\kappa_l h^3 L}{G c_T}$. The calculated lateral surface stiffness for each resonance frequency is presented in table 5.12. A normal load of 9 nN and a lateral load of 26 nN is applied to the cantilever. The resulting values of the lateral surface stiffness, from table 5.12, vary a great deal for each mode. The difference between each mode can be attributed to errors in the measurement of the contact resonance frequencies and the model used to model the Nanosensor. More data would be necessary to fully develop a model that matches the measured contact

resonance frequencies more closely.

Table 5.12: The lateral stiffness values, η_l, calculated for the first three torsional vibration modes of the rectangular Nanosensor.

Mode	f (kHz)	η_l
1	330	2.633
2	646	0.699
3	1070.5	1.734

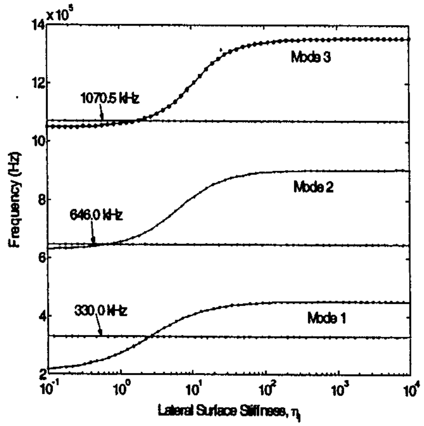

Figure 5.15: The change in the first three torsional vibration modes due to an increase in the lateral surface stiffness, η_l. The measured torsional contact resonance frequencies are also shown.

5.4 Contact Stiffness Calculations

Information about the contact stiffness will be obtained from the flexural vibration results presented in sections 5.3.1 and 5.3.3. The exact solution for the *offset spring-coupled* *case*, from section 3.1.3, will be used to compare the exact solution with the results obtained using the rectangular model for the NCS16 rectangular cantilever and the Olympus model for the dLever A cantilever. To use the exact solution, a characteristic cantilever constant relating the Young's modulus E, mass density ρ, and the dimensions of the cantilever is defined as [43]

$$c_B = \sqrt{4\pi^2 \frac{\rho A}{EI}} = \frac{\beta_n^2}{f_n}, \tag{5.6}$$

where β_n is the wave number and f_n is the frequency. The eigenvalue, $\beta_n L$, can then be written as

$$\beta_n L = c_B L \sqrt{f_n}. \tag{5.7}$$

The characteristic equation for the *offset spring-coupled case*, Equation 3.42, is defined in terms of L_{tip} and the ratio $R = \frac{L_{tip}}{L}$. It can then be written as

$$\begin{aligned} \frac{\kappa_n}{k_c} \big[&(\cosh(\beta L_{tip}) \sin(\beta L_{tip}) - \cos(\beta L_{tip}) \sinh(\beta L_{tip})) \times \\ &(1 + \cos(\beta L_{tip}(\frac{1}{R} - 1)) \cosh(\beta L_{tip}(\frac{1}{R} - 1)) - (\cosh(\beta L_{tip}(\frac{1}{R} - 1)) \sin(\beta L_{tip}(\frac{1}{R} - 1)) - \\ &\cos(\beta L_{tip}(\frac{1}{R} - 1)) \sinh(\beta L_{tip}(\frac{1}{R} - 1)))(1 - \cos(\beta L_{tip}) \cosh(\beta L_{tip})) \big] \\ &= -\frac{2(\beta L_{tip})^3}{3} \left[1 + \cosh\left(\frac{\beta L_{tip}}{R}\right) \cos\left(\frac{\beta L_{tip}}{R}\right) \right]. \end{aligned} \tag{5.8}$$

It should be noted that since everything is defined in terms of L_{tip}, then $k_c = \frac{3EI}{L_{tip}^3}$. Equation 5.8 is solved for κ_n/k_c in terms of R by calculating βL_{tip} from the measured resonance frequencies. The measured free frequencies along with the known values of βL_{tip} (i.e.1.875, 4.694, etc for the free case) are used to calculate $c_B L_{tip}$ for each value of R. The measured contact resonance frequencies are then used along with $c_B L_{tip}$ to calculate the new values for βL_{tip}. The new βL_{tip} values are finally substituted into Equation 5.8 to determine κ_n/k_c

in terms of R.

A plot of the result calculated for the NCS16 rectangular cantilever at an applied load of 1000 nN is shown in Figure 5.16. The calculated stiffness values, for the applied loads of 1000 nN and 2000 nN, from Equation 5.8 and the results from table 5.8 are shown in table 5.13. The results for the rectangular model compare well with the results from Equation 5.8. The length ratio of 0.958 is close to the measured ratio of 0.953. The differences between the κ_n/k_c values can be attributed to variations in the physical cantilever dimensions, which would lead to errors in the model used for the cantilever.

Table 5.13: κ_n/k_c results calcualted using the rectangular model and Equation 5.8 for the NCS16 rectangular cantilever..

Applied Load (nN)	κ_n/k_c mode 1	κ_n/k_c mode 2	κ_n/k_c from Equation 5.8	R
1000	25.671	25.755	21.727	0.958
2000	25.753	25.789	21.777	0.958

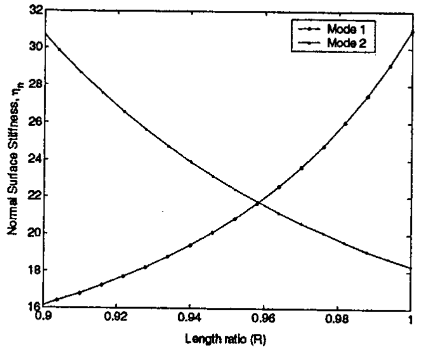

Figure 5.16: Results for κ_n/k_c from Equation 5.8 for the NCS16 rectangular cantilever at an applied load of 1000 nN.

Equation 5.8 is used to calculate stiffness values for the dLever A cantilever. A plot of the κ_n/k_c result for an applied load of 30 nN is shown in Figure ??. The marked intersection point is used to determine the κ_n/k_c value for the given applied load. The calculated stiffness values, for the applied loads of 30 nN and 90 nN, from Equation 5.8 and the results from table 5.9 are shown in table 5.14. The results for the Olympus model don't compare well with the results from Equation 5.8. The values for κ_n/k_c determined from the Olympus model are approximately two times greater than the values determined from Equation 5.8. The length ratio of 0.619 is much smaller than the ratio of 0.949 from the measured dimensions. The difference in the length ratios and κ_n/k_c values clearly shows that the Olympus model is more appropriate for modeling cantilevers similar in shape to the cantilever depicted in Figure 4.6.

Table 5.14: κ_n/k_c results calculated using the rectangular model and Equation 5.8 for the dLever A cantilever.

Applied Load (nN)	κ_n/k_c mode 1	κ_n/k_c mode 2	κ_n/k_c from Equation 5.8	R
30	361.64	399.44	170.77	0.619
90	361.66	396.18	179.16	0.619

The κ_n/k_c results calculated using the rectangular model for the NCS16 cantilever will be now used to compare the contact stiffness, κ_n, values with those calculated using Equation 3.45, derived using the Hertzian contact theory. The selection of this cantilever for this comparison is due the available information regarding the cantilever tip. The tip of the NCS16 cantilever has the properties of: $E_t = 130.4$ GPa and $\nu_t = 0.181$. The flexural contact resonance frequency results presented in section 5.3.3 were measured on a Si(111) sample with the properties of: $E_s = 187$ GPa and $\nu_s = 0.36$. The reduced elastic modulus for the tip-sample interaction is calculated from Equation 2.2 as $E^* = 82.836$ GPa. The radius if the

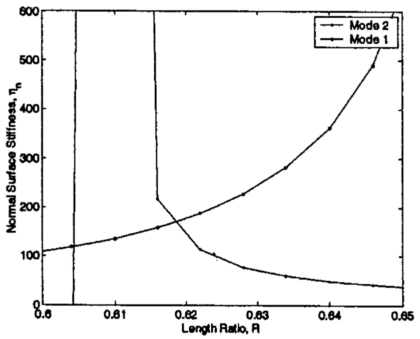

Figure 5.17: Results for κ_n/k_c from Equation 5.8 for the dLever A cantilever at an applied load of 30 nN.

cantilever tip is assumed to be 100 nm. The contact stiffness is calculated using Equation 3.45. The spring constant of the NCS16 cantilever was calculated using the rectangular model as $k_c = 56.53$ N/m. A comparison of results calculated using the two methods is shown in table 5.15. The difference in the results for κ_n is due to the assumption made about the tip radius. In order to measure the Young's modulus of a sample, the results calculated here for contact with the Si(111) sample should be used to calibrate the cantilevers. The tip radius can be calculated using the contact stiffness, κ_n, obtained from the cantilever model and Equation 3.45. This should be done for each resonance frequency and applied load. Once the tip radius has been determined, then Young's modulus measurements can be made on other samples at the same contact resonance frequencies and applied loads. This method is only appropriate for measuring samples with cantilevers calibrated on material with a similar stiffness as compared to the sample. At the present stage of the development of this measurement technique the error in calculating E_s is around 20% [43],[63]. This error is mostly due to the model not matching the true dimensions of the cantilever.

Table 5.15: The contact stiffness, κ_n, results calculated for the NCS16 rectangular cantilever using the rectangular cantilever model and Equation 3.45. A cantilever tip radius of 100 nm was assumed. All dimension are in N/m unless otherwise noted.

Applied Load (nN)	κ_n mode 1	κ_n mode 2	κ_n from Equation 3.45
1000	1451.11	1455.85	1602.74
2000	1455.74	1457.77	2019.33

5.5 AFAM Measurement

Results obtained using the dynamic AFM technique of atomic force acoustic microscopy will now be provided to show how imaging the elastic properties of a sample surface can provided enhanced contrast of different regions on the sample surface not seen with standard AFM techniques. A polysilicon microelectromechanical system (MEMS) material was examined with the AFAM. The topography image of the sample surface is shown in Figure 5.18. A dLever A cantilever, with dimensions given in section 5.3.1, was used for the measurements. A contact resonance frequency of 415.20 kHz was found for an applied load of 300 nN. The voltage supplied to the transducer coupled to the sample was 800 mV. The voltage was selected in order to produce a linear resonance peak with sufficient amplitude to use for AFAM imaging. Higher voltages would cause the peak to be nonlinear and unstable for imaging [31],[32]. The AFAM image of the sample MEMS sample was taken at a frequency of 412.15 kHz, which is on the low frequency side of the resonance peak. The

is shown in Figure 5.19. The darker regions in the AFAM image represent

ompliant regions. This contrast is reversed if a

frequency on the high side of the resonance peak is used for the measurements [43],[69]. If the frequency is increased far beyond the resonance frequency, then the contrast is lost.

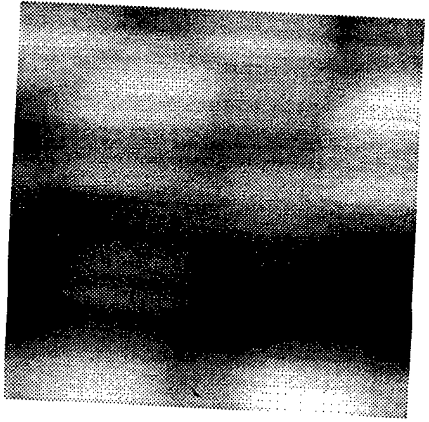

Figure 5.18: Topography image of a polysilicon MEMS sample taken with a dLever A cantilever. The scan size is 1 $\mu m \times 1$ μm.

In looking at the AFAM image, it is clear that higher contrast images can be obtained with this dynamic technique. The topography image shows a few of the polysilicon grains. The AFAM image shows details about the grains that can not be seen from the topography image. Some of the individual grains have large variations in stiffness.

These images were taken using the first contact resonance frequency. The use of higher modes with greater sensitivities to changes in the sample surface stiffness can provide more information about the stiffness features of the sample surface [2],[59]. However, taking AFAM images with higher modes is difficult. There are limitations in measuring resonance frequencies with high enough amplitudes using the standard cantilever measurement

Figure 5.19: An AFAM image taken of a polysilicon MEMS sample. The scan size is 1 μm × 1 μm.

techniques of the AFM used for this research. Using different measurement techniques to measure the displacement of the AFM cantilever or improving the standard measurement techniques will allow the higher modes to be used to provide more information about the sample surface using dynamic AFM techniques.

5.6 Discussion

In this chapter, the vibration response of AFM cantilevers in and out of contact with a sample surface were examined. Also, the spring constants for of AFM cantilevers, calculated using the approximate method, compared well with the results obtained using established experimental techniques. The experimental setup was presented and its use for

measuring the vibration response of the AFM cantilevers was explained. The measured free resonance frequencies showed good agreement with the approximate results. The contact stiffness was determined from the measured contact resonance frequencies and the best results were obtained for the rectangular cantilever. A technique for determining the local Young's modulus of a sample surface, using the cantilever model and the measured contact frequencies, was outlined. AFAM results were provided to demonstrate the improved imaging contrast available with the use of this dynamic AFM technique.

Chapter 6

Conclusions

In this thesis, the dynamics of AFM cantilevers has been modeled for flexural and torsional vibration modes. Closed-form expressions for cantilevers with uniform cross-sections have been derived. For cantilevers with nonuniform cross-sections, the Rayleigh-Ritz method was used to develop an approximate solution. The cantilevers with nonuniform cross-sections (i.e. triangular and V-shaped) are modeled as beams with variable cross-sections. The exact closed-form expressions served to validate the approximate solution method.

Four different types of AFM cantilevers were modeled using the approximate method, two of a rectangular shape and two of a triangular shape. To model the interaction between the cantilever tip and the sample, a linear spring was used. This approximation is valid as long as the motion of the sample surface is kept small. The change in frequency and modal sensitivity associated with changes in the tip-sample interaction stiffness was examined. As expected, the results showed that the first mode is the most sensitive for

materials that are compliant relative to the cantilever. The usefulness of higher-order vibration modes for examining surfaces with high stiffness was also addressed for each type of cantilever. Using the approximate formulae derived for the different types of cantilevers, predictions of the modal sensitivity may be made such that specific modes or cantilevers with optimum sensitivity may be chosen for specific measurement applications.

The approximate solutions were also used to determine the spring constants of the cantilevers. The results were in good agreement with spring constants determined from other experimental techniques. The spring constant is an important parameter in AFM measurement techniques, especially those techniques that exploit the dynamic properties of the cantilevers.

The frequency response of cantilevers in and out of contact with the sample surface were measured and compared with results obtained from the approximate method. There was reasonably good agreement between the measured and calculated results. One of the major sources of error in the results can be attributed to the models not matching the true geometry of the cantilevers. In particular, the thickness of the cantilever. The thickness, for some cantilevers, can vary along the entire length of the cantilever.

The measured contact resonance frequencies were used to determine the contact stiffness between the cantilever tip and sample surface. The stiffness results calculated from the approximate method were in good agreement with results calculated using the analytic solution of the spring-coupled beam for the rectangular cantilever. The method for determining the elastic modulus of the sample surface, using results calculated from the approximate method, was outlined. In order to make quantitative measurements of the elastic modulus of a sample surface, the cantilever used for the measurements must be calibrated.

Results from the dynamic AFAM technique were presented to show the type of image contrast possible with this technique. Exploiting the contact resonances of the cantilever has allowed the elastic properties of the sample surface to be examined. This technique can provide information about the sample surface that is not available from topography measurements.

In order to make use of the AFM for material property measurements, more information about the true geometry of the cantilevers must be known. This would eliminate some of the error encountered with measurements done at this time. Accurate models of the cantilevers would allow other features of the tip-sample interaction to be explored, such as the effects of the surface forces on the cantilever and the contact between the cantilever tip and sample surface. With continued advancements in these areas, the dynamic AFM measurement techniques could prove to be valuable tools for measuring the material properties of sample surfaces.

Bibliography

[1] G. Binning, C. F. Quate, and C. Gerber, “Atomic Force Microscope,” Physical Review Letters **56**, 930–933 (1986).

[2] M. Hoummady and E. Farnault, “Enhanced Sensitivity to Force Gradients by Using Higher Felxural Modes of the Atomic Force Microscope Cantilever,” Applied Physics A. **66**, S361–S364 (1998).

[3] U. Rabe and W. Arnold, “Atomic Force Microscopy at Ultrasonic Frequencies,” 1994 Proceedings of IEEE Ultrasonics Symposium **94**, 367–370 (1994).

[4] U. Rabe and W. Arnold, “Acoustic Microscopy by Atomic Force Microscopy,” Applied Physics Letters **64**, 1493–1495 (1994).

[5] K. Yamanaka, H. Ogiso, and O. Kolosov, “Ultrasonic Force Microscopy for Nanometer Resolution Subsurface Imaging,” Applied Physics Letters **64**, 178–180 (1994).

[6] U. Rabe, K. Janser, and W. Arnold, “Vibrations of Free and Surface-Coupled Atomic Force Microscope Cantilevers: Theory and Experiment,” Review of Scientific Instruments **67**, 3281–3293 (1996).

[7] D. Maugis, *Contact, Adhesion, and Rupture of Elastic Solids* (Springer-Verlag, Berlin, 2000).

[8] G. Binning, H. Rohrer, C. Gerber, and E. Weibel, "Tunneling Through a Controllable Vacuum Gap," Applied Physics Letters **40**, 178–180 (1982).

[9] N. A. Burnham and R. J. Colton, "Measuring the Nanomechanical Properties and Surface Forces of Materials Using an Atomic Force Microscope," Journal of Vacuum Scince Technology B **7**, 2906–2913 (1989).

[10] S. Magonov and M. Whangbo, *Surface Analysis with STM and AFM* (VCH Publishers, Inc., 1996).

[11] ThermoMicroscopes, *A Practical Guide to Scanning Probe Microscopy* (ThermoMicroscopes, 2000).

[12] T. R. Albrecht, S. Akamine, T. E. Carver, and C. F. Quate, "Microfabrication of Cantilever Styli for the Atomic Force Microscope," Journal of Vacuum Science Technology A **8**, 3386–3396 (1990).

[13] ThermoMicroscopes, Sunnyvale, CA.

[14] A. Folch, M. S. Wrighton, and M. A. Schmidt, "Microfabrication of Oxidation-Sharpened Silicon Tips on Silicon Nitride Cantilevers for Atomic Force Microscopy," Journal of Micromechanical Systems **6**, 303–306 (1997).

[15] T. P. Weihs, Z. Nawaz, S. P. Jarvis, and J. B. Pethica, "Limits of Imaging Resolution for Atomic Force Microscopy of Molecules," Applied Physics Letters **59**, 3536–3538 (1991).

[16] G. Bar, R. Brandsch, and M. H. Whangbo, "Effect of Tip Sharpness on the Relative Contributions of Attractive and Repulsive Forces in the Phase Imaging of Tapping Mode Atomic Force Microscopy," Surface Science **422**, L192–L199 (1999).

[17] N. A. Burnham, R. J. Colton, and H. M. Pollock, "Interpretation of Force Curves in Force Microscopy," Nanotechnology **4**, 64–80 (1993).

[18] D. Sarid, *Scanning Force Microscopy* (Oxford University Press, New York, 1991).

[19] S. Ciraci, E. Tekman, A. Baratoff, and I. P. Batra, "Theoretical Study of Short- and Long-Range Forces and Atom Transfer in Scanning Force Microscopy," Physical Review B **46**, 10411–10422 (1992).

[20] N. A. Burnham, D. D. Dominguez, R. L. Mowery, and R. J. Colton, "Probing the Surface Forces of Monolayer Films with an Atomic-Force Microscope," Physical Review Letters **64**, 1931–1934 (1990).

[21] U. Hartmann, "Van der Waals Interactions Between Sharp Probes and Flat Sample Surfaces," Physical Review B **43**, 2404–2407 (1991).

[22] A. L. Weisenhorn, P. Maivald, H.-J. Butt, and P. K. Hansma, "Measuring Adhesion, Attraction, and Repulsion Between Surfaces in Liquids with an Atomic-Force Microscope," Physical Review B **45**, 11226–11232 (1992).

[23] J. N. Israelachvili, *Intermolecular and Surface Forces* (Academic Press Inc., London, 1985).

[24] S. Belaidi, P. Girard, and G. Leveque, "Electrostatic Forces Acting on the Tip in a Atomic Force Microscopy: Modelization and Comparison with Analytic Expressions," Journal of Applied Physics **81,** 1023–1030 (1997).

[25] Engineering Mechanics Department, University of Nebraska-Lincoln.

[26] L. Wang, "The Role of Damping in Phase Imaging in Tapping Mode Atomic Force Microscopy," Surface Science **429,** 178–185 (1999).

[27] G. Lévêque, P. Girard, S. Belaidi, and G. Solal, "Effects of Air Damping in Noncontact Resonant Force Microscopy," Review of Scientific Instruments **68,** 4137–4144 (1997).

[28] G. Y. Chen, R. J. Warmack, T. Thundat, D. P. Allison, and A. Huang, "Resonance Response of Scanning Force Microscopy Cantilevers," Review of Scientific Instruments **65,** 2532–2537 (1994).

[29] N. A. Burnham, O. P. Behrend, F. Oulevey, G. Gremaud, P. J. Gallo, D. Dupas, A. J. Kulik, H. M. Pollock, and G. A. D. Briggs, "How Does a Tip Tap?," Nanotechnology **8,** 67–75 (1997).

[30] O. P. Behrend, F. Oulevey, D. Gourdon, E. Dupas, A. J. Kulik, G. Gremaud, and N. A. Burnham, "Intermittent Contact: Tapping or Hammering?," Applied Physics A. **66,** S219–S221 (1998).

[31] K. Yamanaka and S. Nakano, "Ultrasonic Atomic Force Microscope with Overtone Excitation of Cantilever," Japanese Journal of Applied Physics **35,** 3787–3792 (1996).

[32] K. Yamanaka, A. Noguchi, T. Tsuji, T. Koike, and T. Goto, "Quantitative Material Characterization by Ultrasonic AFM," Surface and Interface Analysis **27,** 600–606 (1999).

[33] M. T. Cuberes, H. E. Assender, G. A. D. Briggs, and O. V. Kolosov, "Heterodyne Force Microscopy of PMMA/rubber Nanocomposites: Nanomapping of Viscoelastic Response at Ultrasonic Frequencies," Journal of Physics D: Applied Physics **33,** 2347–2355 (2000).

[34] K. L. Johnson, K. Kendall, and A. D. Roberts, "Surface Energy and the Contact of Elastic Solids," Proceedings of the Royal Society of London, A. **324,** 301–313 (1971).

[35] K. L. Johnson, *Contact Mechanics* (Cambridge University Press, 1985).

[36] M. Pärssinen, "Hertzian Contact Vibrations under Random External Excitation and Surface Roughness," Journal of Sound and Vibration **214,** 779–783 (1998).

[37] A. Fogden and L. R. White, "Contact Elasticity in the Presence of Capillary Condensation," Journal of Colloid and Interface Science **138,** 414–430 (1990).

[38] V. M. Muller, V. S. Yushchenko, and B. V. Derjaguin, "On the Influence of Molecular Forces on the Deformation of an Elastic Sphere and its Sticking to the Rigid Plane," Journal of Colloid and Interface Science **77,** 91–101 (1980).

[39] D. Maugis, "Adhesion of Spheres: The JKR-DMT Transition Using a Dugdale Model," Journal of Colloid and Interface Science **150**, 243–269 (1992).

[40] U. Rabe, J. Turner, and W. Arnold, "Analysis of the High-Frequency Response of Atomic Force Microscope Cantilevers," Applied Physics A. **66**, S277–S282 (1998).

[41] L. Meirovitch, *Principles and Techniques of Vibrations* (Prentice-Hall, Inc., Upper Saddle River, New Jersey 07458, 1997).

[42] J. A. Turner, S. Hirsekorn, U. Rabe, and W. Arnold, "High-Frequency Response of Atomic-Force Microscope Cantilevers," Journal of Applied Physics **82**, 966–979 (1997).

[43] U. Rabe, S. Amelio, E. Kester, V. Scherer, S. Hirsekorn, and W. Arnold, "Quantitative Determination of Contact Stiffness Using Atomic Force Acoustic Microscopy," Ultrasonics **38**, 430–437 (2000).

[44] C. Wang, *Applied Elasticity* (McGraw-Hill Book Company, Inc., New York, 1953).

[45] J. A. Turner. and J. S. Wiehn, "Sensitivity of Flexural and Torsional Vibration Modes of Atomic Force Microscope Cantilevers to Surface Stiffness Variations," Nanotechnology **12**, 322–330 (2001).

[46] V. Scherer, W. Arnold, and B. Bhushan, "Lateral Force Microscopy Using Acoustic Friction Force Microscopy," Surface and Inerface Science **27**, 578–587 (1999).

[47] T. Drobek, R. W. Stark, M. Gräber, and W. M. Heckl, "Overtone Atomic Force Microscopy Studies of Decagonal Quasicrystal Surfaces," New Journalof Physics **1**, 15.1–15.11 (1999).

[48] The Mathworks, Inc., Natick, MA.

[49] J. E. Sader, "Parallel Beam Approximation for V-Shaped Atomic Force Microscope Cantilevers," Review of scientific Instruments **66**, 4583–4587 (1995).

[50] Olympus Optical Co., LTD., Tokyo, Japan.

[51] J. Cleveland, S. Manne, D. Bocek, and P. Hansma, "A Nondestructive Method for Determining the Spring Constant of Cantilevers for Scanning Force Microscopy," Review of Scientific Instruments **64**, 403–405 (1993).

[52] J. E. Sader, I. Larson, P. Mulvaney, and L. R. White, "Method for the Calibration of Atomic Force Microscope Cantilevers," Review of Scientific Instruments **66**, 3789–3798 (1995).

[53] J. E. Sader, J. W. M. Chon, and P. Mulvaney, "Calibration of Rectangular Atomic Force Microscope Cantilevers," Review of Scientific Instruments **70**, 3967–3969 (1999).

[54] J. E. Sader and L. White, "Theoretical Analysis of the Static Deflection of Plates for Atomic Force Microscope Applications," Jouranl of Applied Physics **74**, 1–9 (1993).

[55] Panametrics, Waltham, MA.

[56] Agilent Technologies, Palo Alto, CA.

[57] National Instruments, Austin, TX.

[58] Stanford Research Systems, Sunnyvale, CA.

[59] K. Yamanaka and S. Nakano, "Quantitative Evaluation by Contact Resonance in an Atomic Force Micoscope," Applied Physics A. **66**, S313–S317 (1998).

[60] N. A. Burnham, A. J. Kulik, and G. Gremaud, "Nanosubharmonics: The Dynamics of Small Nonlinear Contacts," Physical Review Letters **74**, 5092–5095 (1995).

[61] L. Wang, "Analytical Description of the Tapping-Mode Atomic Force Microscopy Response," Applied Physics Letters **72**, 3781–3783 (1998).

[62] A. Kühle, A. H. Sørensen, and J. Bohr, "Role of Attractive Forces in Tapping Force Microscopy," Journal of Applied Physics **81**, 6562–6569 (1997).

[63] U. Rabe, E. Kester, and W. Arnold, "Probing Linear and Non-Linear Tip-Sample Interaction Forces by Atomic Force Acoustic Microscopy," Surface and Interface Analysis **27**, 386–391 (1999).

[64] O. Pfeiffer, C. Loppacher, C. Wattinger, M. Bammerlin, U. Gysin, M. Guggisberg, S. Rast, R. Bennewitz, E. Meyer, and H. J. Güntherodt, "Using Higher Flexural Modes in Non-Contact Force Microscopy," Applied Surface Science **157**, 337–342 (2000).

[65] MikroMasch, Tallinn, Estonia.

[66] Advanced Surface Microscopy, Inc., Indianapolis, IN.

[67] Frawnhofer Institute for Nondestructive Testing (IZFP), Saarbrücken, Germany.

[68] Nanosensors, Wetzlar-Blankenfeld, Germany.

[69] D. DeVecchio and B. Bhushan, "Localized Surface Elasticity Measurements Using an Atomic Force Microscope," Review of Scientific Instruments **68**, 4498–4505 (1997).

Atomic Force Acoustic Microscopy for Materials Characterization of Microelectromechanical Systems

by

Roshanak Nilchiani

A THESIS

Presented to the Faculty of
The Graduate College of the University of Nebraska
In Partial Fulfillment of Requirements
For the Degree of Master of Science

Major: Engineering Mechanics

Under the Supervision of Professor Joseph A. Turner

Lincoln, Nebraska

May, 2002

Atomic Force Acoustic Microscopy for Materials Characterization of Microelectromechanical Systems

Roshanak Nilchiani, M.S.
University of Nebraska, 2002

Adviser: Professor Joseph A. Turner

The atomic force microscope (AFM) has traditionally been used for providing data on surface topography of materials. However, interest in the potential of the AFM to provide quantitative information about surface properties has recently increased. When in contact with a sample vibrating at ultrasonic frequencies, the natural frequencies of the cantilever shift to higher frequencies. Using appropriate tip-sample contact theories, it is possible to derive the Young's modulus for the surface from these shifts. The resulting AFM technique, often called the atomic force acoustic microscope (AFAM), can be used to determine the surface stiffness of a variety of samples. This study focused on the experimental development of an AFAM system using an existing commercial AFM. The resulting system was then used to study the surface stiffness for polysilicon microelectromechanical systems (MEMS). Hertzian contact theory was used to calculate the surface stiffness from the frequency shift data. Silicon <100> was used as a calibration material, and then some additional experiments were done on a silicon <111> sample and polysilicon MEMS device. Using the AFAM method, surface stiffnesses of these samples were determined and some images of the stiffness of the samples were taken, the results of which are discussed and analyzed.

Acknowledgements

I would like to thank my committee members, Dr. Suzanne Rohde and Dr. FLorin Bobaru, for vigorously evaluating my thesis with objectivity and fairness. I am grateful to Dr. Joseph A. Turner for supervising my research during my graduate studies at UNL. I would also like to acknowledge the support of the Air Force Office of Scientific Research under Grant No. F49620-99-1-0254 and the center for Electro-optics at the University of Nebraska-Lincoln.

Contents

List of Figures

Chapter 1

Introduction

Since its development in 1986 by Binning, et al. [1], the atomic force microscope (AFM) has been used to solve processing and materials problems in a wide range of technologies affecting the electronics, telecommunications, biomedical, chemical, automotive, aerospace, and energy industries. The materials under investigation include thin and thick film coatings, ceramics, composites, glasses, synthetic and biological membranes, metals, polymers, and semiconductors. The AFM has been applied to studies of phenomena such as abrasion, adhesion, cleaning, corrosion, etching, friction, lubrication, plating, and polishing. At present, the potential using of the AFM for material properties characterization has not been fully exploited. However, studies dealing with modifications of the AFM to expand its analysis capabilities are gradually emerging [2], [3].

One possible modification involves using the dynamic aspects of the AFM, in which ultrasonic excitations are induced in the sample or base of the cantilever. In this case, the contact between the cantilever tip and the specimen causes the natural frequencies of

the cantilever to shift. Using appropriate contact theories, it is possible to relate these frequency shifts to sample surface stiffness [4]. In this way, it is possible to observe the changes in elastic modulus when scanning the surface of the specimen. The modified AFM, often called an atomic force acoustic microscope (AFAM) due to its ultrasonic component, can be used to analyze a variety of materials on the nanoscale, including but not limited to mixtures of polymers, composite materials, semiconductors and microelectromechanical systems (MEMS). The research in this field is in its initial stages and the AFAM is not commercially available. Most contributions in this field have been made by European and Japanese researchers [3]-[10]. Only recently have research groups across the U.S. started to study the potentials of this modified AFM.

The current research has focused on the development of an AFAM system by coupling a commercial AFM with an ultrasonic transducer. Using contact theories previously developed in the literature [5], the Young's modulus of the surface grains of a polysilicon MEMS have been analyzed.

This thesis begins with a literature review covering the basics of the atomic force microscope, modified AFMs, contact theories and current developments in the field of atomic force acoustic microscopy. The experimental methods used in the research are outlined next. Results, data and image analysis, discussions and recommendations for future work conclude the thesis.

Chapter 2

Background

Since this research is based on standard AFM technology, it is important to illustrate the basics of the atomic force microscope. Therefore, the initial section of this chapter focuses on the principles behind the AFM, its range of applications and the underlying theories for the AFM in both its static- and dynamic mode.

2.1 Atomic Force Microscopy (AFM)

The AFM was first discussed in a research paper by Binning, et al. in 1986 [1]. It is a scanned-proximity probe microscope. These microscopes are routinely used to measure local properties like height, optical absorption, or magnetism using a tip placed very close to the specimen. The small tip-sample separation makes taking measurements over nanoscale areas possible. To acquire an image, the microscope raster-scans the tip over the sample surface while measuring the local property in question. Since these systems do not use lenses, their resolution is generally limited by the size of the tip rather than diffraction

effects. AFMs can achieve a resolution of up to 1 nm, and unlike electron microscopes, can image samples even in air or immersed in liquids.

The AFM (as shown schematically in Figure 2.1) measures attractive or repulsive forces between a tip and the sample (Binning et al. [1]). In its repulsive (or "contact") mode, the instrument touches the sample with a cantilever tip using a small force. As a raster-scan drags the tip over the sample, a detection apparatus measures the vertical deflection of the cantilever, which indicates the local sample height. Thus, in contact mode the AFM measures hard-sphere repulsion forces (where the force fields of the molecules touch but do not overlap) between the tip and sample.

In the attractive (or "noncontact") mode, the AFM produces topographic images from measurements of attractive forces. In this case, the tip does not touch the sample. As seen in Figure 2.2, an optical detector then determines the displacement of the cantilever position. In the following sections the mechanism of the feedback control loop, AFM imaging modes and cantilever displacement detection are discussed in more detail.

Figure 2.1: Concept of the AFM, a cantilever touching a sample. The red line denotes the laser, which reflects from the cantilever. (D. Baselt, Ph.D thesis, California Institute of Technology, 1993).

Figure 2.2: The AFM optical lever and the photodetector (D. Baselt, Ph.D thesis, California Institute of Technology, 1993).

2.1.1 AFM feedback control loop

The presence of a feedback control loop is one of the more subtle differences between AFMs and older stylus-based instruments such as stylus profilometers. Using its feedback control loop, the AFM measures and regulates the force on the sample, allowing image acquisition at very low forces. Figure 2.3 shows the feedback loop of the AFM. The feedback loop (Figure 2.3) consists of a piezoelectric scanner that controls the distance between the cantilever tip and the sample, the cantilever, the laser and photodetector system, which measures the deflection of the cantilever, and a feedback circuit that tries to keep the cantilever deflection constant by adjusting the voltage applied to the scanner. The bandwidth of AFM feedback loops is about 10 kHz. The scanner can move in the X or Y direction with frequencies which can be varied between 0.1 Hz to 10 Hz. Depending on the chosen scan rate and number of scanned lines, image acquisition can take a wide range of

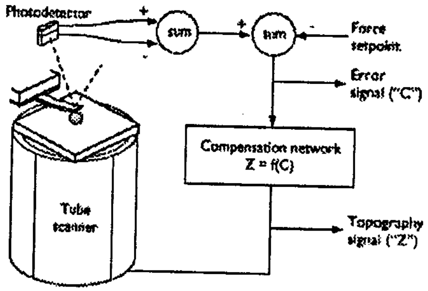

Figure 2.3: Schematic of the AFM feedback loop. Software monitors the cantilever deflection and keeps it constant by adjusting the height of the sample (or cantilever) (D. Baselt, Ph.D thesis, California Institute of Technology, 1993).

time spans. If the chosen resolution is high, it takes more time than low resolution mode to take an AFM image. Two- and three-dimensional images taken by the AFM from a CrBN sample are shown in Figures 2.4 and 2.5, respectively as examples of AFM topography images.

2.1.2 AFM and surface forces

Surface forces are categorized into two main categories on the basis of their range. Short-range surface forces are those due to chemical or metallic bonding. These are not discussed here, since they have little relevance to the forces encountered in atomic force acoustic microscopy. Long-range surface forces can be categorized in three different categories [6], including:

Electrostatic forces are due to charges, image charges, and dipoles. Since molecules and atoms are polarized by electric fields, forces exist that act between these two. Electric

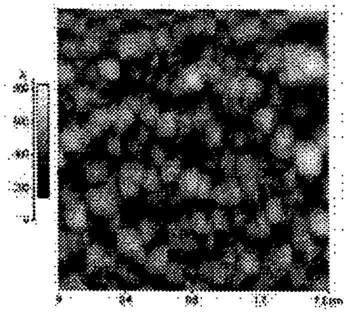

Figure 2.4: AFM 2D topography image of a CrBN thin film.

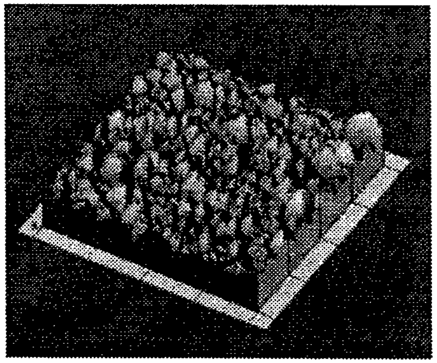

Figure 2.5: AFM 3D topography image of a CrBN thin film.

fields may also be applied intentionally between the tip and the sample.

Electrodynamic forces may also be present. Oscillating electrons generate a fluctuating dipole field, which interacts with nearby atoms, inducing attractive instantaneous dipole moments. This phenomenon is known as the dispersion force because the frequencies correspond to ultraviolet and visible light, which are dispersed by the fluctuations. Other electrodynamic forces include the van der Waals forces.

Electromagnetic forces are less important in atomic force acoustic microscopy. They are most pronounced when using magnetic force microscopy. Forces due to liquids become important when the sample is immersed in water or surrounded by a thicker layer of water. Such forces are especially important for imaging biological materials, but they are not so important for this research.

2.1.3 AFM imaging modes

As discussed in Section 2.1.1, the AFM tip makes physical contact with the sample in contact mode. As the scanner gradually follows the tip across the specimen, the contact forces cause a deflection in the cantilever to accommodate for changes in the surface topography of the specimen. A typical force-distance curve for this interaction is shown in Figure 2.6.

As we go towards the right of the curve, interatomic distances grow, and repulsive forces give way to attractive ones. When the interatomic separation decreases, the repulsion gradually weakens the attractive force. The force goes to zero when the distance between the atoms reaches an equilibrium distance, which is about a couple of angstroms. If the atoms are forced slightly closer, the total force becomes positive, and the atoms are considered to

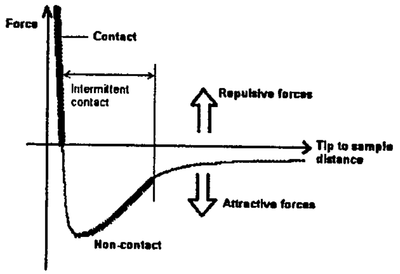

Figure 2.6: Typical force distance curve. In contact mode, the distance between the tip and the sample is very small and the repulsive forces are dominant. In noncontact mode, attractive forces pull the cantilever tip toward the sample.

be in contact. In taking a topographical image of the sample, there should be a repulsive force between the tip and the sample. Once the cantilever deflection is determined, the AFM generates the topographic data set by operating in one of two modes, constant height mode or constant force mode.

In the constant height mode, the spatial variation of the cantilever deflection can be used directly to generate the topographic information because the height of the scanner is fixed as it scans. Constant-height mode is often used for taking atomic-scale images of atomically flat surfaces, where the cantilever deflections and thus variations in applied force are small. Constant-height mode is also essential for recording real-time images of changing surfaces, where a high scan speed is desired.

In constant-force mode, the deflection of the cantilever is used as input to the feedback circuit that moves the scanner up and down in z. The scanner responds to the topography by keeping the cantilever deflection constant. In this case, the image is generated from the scanner's motion. With the cantilever deflection held constant, the total force applied to the sample is constant. The scanning speed in this mode is limited by the response time of the feedback circuit, but the total force exerted on the sample by the tip is well controlled. Since the exerted force on the sample is an essential element of the tip-sample contact theories, this mode is considered most suitable for surface material characterization purposes, such as the ones studied here.

Non-contact mode AFM is one of several vibrating cantilever techniques in which an AFM cantilever is vibrated near the surface of a sample. As explained in Section 2.1.1, in this mode the tip is not directly touching the sample and the AFM measures the attractive force between the cantilever and the sample. The spacing between the tip and the sample for non-contact AFM is on the order of tens to hundreds of angstroms. Non-contact mode imaging is mostly used in biological applications or in applications when the tip is to be immersed in a liquid or in the air. Since this research is focused only on the contact mode, non-contact methods are not discussed in further detail.

2.1.4 AFM cantilever vibrations

The dynamic modes of the AFM can be modeled in different ways. The basic equations of the AFM vibrations are described here. The AFM cantilever as portrayed in Figure 2.7 can be modeled as an Euler-Bernoulli beam. The beam is assumed uniform and homogenous with constant cross-section, cantilevered at one end, with a tip at the end of the cantilever. The equation of motion can be obtained from Hamilton's principle, which states that the motion of a system can be such that the value of the line integral is equal to zero. In reality, the cross section of most cantilevers can deviate from a perfect rectangular shape and the cross section of the cantilever may vary as a function of position along the cantilever. For simplicity, these variations are neglected. The kinetic and potential energy are thus defined, respectively, as [7]

$$\begin{aligned} KE &= \int_0^L (\frac{1}{2}\rho A(\frac{\partial w}{\partial t})^2 + \frac{1}{2}kw_L^2)dx, \\ PE &= \int_0^L \frac{1}{2}EI(\frac{\partial^2 w}{\partial x^2})^2 dx, \end{aligned} \tag{2.1}$$

where

$w =$ transverse displacement of the cantilever beam,

$w_L =$ transverse displacement of the cantilever beam at its end ($x = L$),

$\rho =$ linear mass density,

$k =$ linear spring constant from the contact,

$E =$ the modulus of the cantilever beam,

$I =$ the area moment of inertia, and

$A =$ cross section of the cantilever.

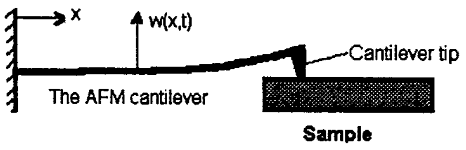

Figure 2.7: A schematic of the cantilever in contact with a sample.

The deflection $w(x,t)$ is defined as the cantilever position relative to its initial static deflection, $y(x)$. The Lagrangian is defined as

$$\pounds = \int_0^L \{\frac{1}{2}\rho A(\frac{\partial w}{\partial t})^2 + \frac{1}{2}kw_L^2 - \frac{1}{2}EI(\frac{\partial^2 w}{\partial x^2})^2\}dx. \tag{2.2}$$

Hamilton's principle states that

$$\delta A = \delta \int_{t_1}^{t_2} \pounds dt = 0. \tag{2.3}$$

In this case, Eq.2.3 can be written as

$$\begin{aligned} \delta A &= \int_{t_1}^{t_2}\int_0^L \{\frac{1}{2}\rho A(\dot{w} + \delta\dot{w})^2 + \frac{1}{2}k(w_L + \delta(w_L))^2 - \frac{1}{2}EI(w'' + \delta w'')^2 - \frac{1}{2}\rho A(\dot{w})^2 \\ & -\frac{1}{2}kw_L^2 + \frac{1}{2}EI(w'')^2\}dxdt = 0, \end{aligned} \tag{2.4}$$

or in other notation

$$\begin{aligned} \delta A &= \int_{t_1}^{t_2}\int_0^L \{\frac{1}{2}\rho A(\dot{w} + \frac{d}{dt}\delta w)^2 + \frac{1}{2}k(w_L + \delta(w_L))^2 - \frac{1}{2}EI(w'' + \frac{d^2}{dx^2}\delta w)^2 - \frac{1}{2}\rho A(\dot{w})^2 \\ & -\frac{1}{2}kw_L^2 + \frac{1}{2}EI(w'')^2\}dxdt = 0. \end{aligned} \tag{2.5}$$

Neglecting very small terms, we have

$$\delta A = \int_{t_1}^{t_2}\int_0^L \{\rho A\dot{w}\frac{d}{dt}\delta w + kw_L\delta w_L - EIw''\frac{d^2}{dx^2}\delta w\}dxdt = 0. \tag{2.6}$$

Integration by parts gives

$$\begin{aligned} \delta A &= \int_0^L \rho A\dot{w}\delta w dx]_{t_1}^{t_2} - \int_{t_1}^{t_2}\int_0^L \rho A\ddot{w}\delta w dxdt + \int_{t_1}^{t_2} kw_L\delta w_L - \int_{t_1}^{t_2} EIw''\frac{d}{dx}(\delta w)dt]_0^L \\ & + \int_{t_1}^{t_2} EIw'''\delta w dt]_0^L - \int_{t_1}^{t_2}\int_0^L EIw''''\delta w dxdt = 0. \end{aligned} \tag{2.7}$$

$$\begin{aligned} \delta A &= -\int_{t_1}^{t_2}\int_0^L (\rho A\ddot{w} + EIw'''')\delta w dxdt + \int_{t_1}^{t_2}(kw_L - EIw_L''')\delta w_L - \int_{t_1}^{t_2} EIw_0'''\delta w_0 dt \\ & -\int_{t_1}^{t_2} EIw''\frac{d}{dx}(\delta\dot{w})dt]_0^L = 0. \end{aligned} \tag{2.8}$$

It is possible to find the equation of motion for the cantilever beam from the equation above, because δw is arbitrary throughout the domain. The linearized boundary value problem of this system is then expressed as

$$EI\frac{\partial^4 w(x,t)}{\partial x^4} + \rho A\frac{\partial^2 w(x,t)}{\partial t^2} = 0, \quad (2.9)$$

$$w(x = 0,t) = 0, \quad (2.10)$$

$$w'(x = 0,t) = 0, \quad (2.11)$$

$$w''(x = L,t) = 0, \quad (2.12)$$

$$EIw'''(x = L,t) = kw(x = L,t). \quad (2.13)$$

The boundary conditions expressed in Equations 2.10 and 2.11 correspond to the conditions of zero displacement and zero slope when $x = 0$. The boundary condition in 2.12 refers to the moment at $x = L$. The force balance between the beam and the linear tip-sample stiffness is expressed by Equation 2.13. For the linearized model to hold true, tip displacements must be very small. Such a condition can be maintained experimentally. The actual value of the linear spring constant k in terms of the tip-sample parameters depends on the contact theory chosen. The contact theory used here to determine k is the simple Hertzian theory [8]. Linearization of the contact model about equilibrium leads to the value of k.

Equations 2.9-2.13 completely define the linearized flexural vibration problem. The natural frequencies of the cantilever vibrations are dependent on k. In order to solve Equation 2.9, separation of variables is used. In this case, w is defined as $w(x,t) = \psi(x)T(t)$.

The eigenvalue problem is then given by

$$\psi(x)'''' = \frac{\rho A\omega^2}{EI}\psi(x), \quad (2.14)$$

$$\psi(0) = 0, \quad (2.15)$$

$$\psi'(0) = 0, \quad (2.16)$$

$$\psi''(L) = 0, \quad (2.17)$$

$$EI\psi'''(L) = k\psi(L). \quad (2.18)$$

The general solution is of the form

$$\psi(x) = a\cosh\gamma x + b\sinh\gamma x + c\cos\gamma x + d\sin\gamma x. \quad (2.19)$$

Using the boundary conditions Equations 2.15-2.17, the constants in Equation 2.19 will have the following relations:

$$c = -a,$$

$$d = -b,$$

$$b = -a\frac{\cosh\gamma L + \cos\gamma L}{\sinh\gamma L + \sin\gamma L}. \quad (2.20)$$

Solution of the related eigenvalue problem gives the characteristic equation that governs all the allowable frequencies. Using the last boundary condition, the characteristic equation is given as follows:

$$\gamma^3(\cos\gamma L\cosh\gamma L + 1) - \frac{kL^3}{EI}(\sinh\gamma L\cos\gamma L - \sin\gamma L\cosh\gamma L) = 0. \quad (2.21)$$

where γ is the wave number.

Equation 2.21 must be solved numerically for the values of γ. The relation

$$f = \gamma^2\frac{1}{2\pi}\sqrt{\frac{EI}{L^3\rho AL}}, \quad (2.22)$$

can then be used to determine the natural frequencies in terms of the wave numbers γ. Thus, the linear vibrations of the cantilever may be used to study the material properties of samples. The coupling stiffness k can be determined using natural frequency data. Usually the value given for k from the manufacturing company has variations from the real value of the spring constant. The tip-sample mechanics are then used to calculate the local Young's modulus of the sample.

2.1.5 Hertzian contact theory

In order to illustrate the contact theory used in these calculations, the most general contact mechanics model is discussed. The mechanics of the AFM tip-sample interaction are generally nonlinear. The contact is assumed frictionless and the contact force is assumed to act normal to the tip. In order to account for both the tip and sample curvatures, the reduced tip-sample curvature is defined as

$$\frac{1}{R} = \frac{1}{R_t} + \frac{1}{R_s}, \qquad (2.23)$$

where R_t is the radius of the AFM cantilever tip and R_s is the radius of the sample. If the sample is flat, which is often the case, then $R = R_t$. In the experiments here, R is calculated using Equation 2.23, because the MEMS surface is not flat.

The reduced elastic modulus K is expressed as[9]

$$\frac{1}{K} = \frac{3}{4}[\frac{1-\nu_t^2}{E_t} + \frac{1-\nu_s^2}{E_s}], \qquad (2.24)$$

where E_t, ν_t, E_s, ν_s are the Young's modulus and Poisson's ratio of the tip and sample, respectively. In order to determine the Young's modulus of the sample, K has to be measured.

Assuming the material properties of the tip are known, it is only necessary to calculate the tip radius by SEM or by a calibration procedure.

One of the assumptions of the Hertzian contact theory is that the cantilever tip and the sample surface are deformed elastically in contact mode. For deflections of the cantilever tip, which are much smaller than the tip radius, the tip can be considered a sphere. Neglecting friction between the tip and the sample, the tip sphere radius can be expressed as [10]

$$r^3 = \frac{F_H R}{K}, \qquad (2.25)$$

where F_H is the force, R is the reduced tip radius 2.23 and, K is the reduced elastic modulus 2.24.

In the Hertzian model adhesion is neglected, so that an attractive force is not associated with loss of contact. The initial AFM cantilever deflection $y(x)$ is determined by the force balance on the tip. When the cantilever or sample are vibrated using small displacements, a linearization of the above mentioned contact theories can be used to determine the appropriate spring stiffness.

Using the Hertzian contact theory, it is possible to calculate the surface stiffness of materials. For this purpose, the first step is to relate the natural frequency shift to a relative stiffness. It is then possible to calculate the actual surface stiffness from the relative stiffness data obtained. The relative stiffness is found in the same manner discussed in the silicon calibration section. An example surface stiffness calculation is presented for the MEMS sample.

For the surface stiffness calculation, the tip radius is assumed known from the silicon calibration. The surface stiffness is determined using the Hertzian contact model. Using the frequency shift for the cantilever, the relative stiffness is first found. This value corresponds to a dimensionless relative stiffness obtained from the modal frequency table presented in Appendix A. For a cantilever with rectangular cross section, $I = \frac{ab^3}{12}$, where a and b are the width and the thickness of the cantilever respectively. The actual contact stiffness is then calculated from the relative stiffness using Eq. 2.2.

The reduced elasticity modulus is related to the contact stiffness from the Hertz model as given before,

$$K = \frac{(\frac{2}{3}\kappa)^{1.5}}{\sqrt{RF}}. \tag{2.26}$$

The reduced modulus is related to the surface stiffness by

$$K = \frac{1}{\frac{4}{3}(\frac{1-\nu_s^2}{E_s} - \frac{1-\nu_t^2}{E_t})}. \tag{2.27}$$

For tip radius calculations, the surface stiffness is known, and thus K can be calculated. Then using Equation 2.26 the tip radius can be calculated, when the applied force and the relative stiffness are known.

2.2 Atomic Force Acoustic Microscopy (AFAM)

Recent developments in the aerospace and electronic industries demand new materials with complex microstructures on a wide range of scales as small as the nanoscale. These demands necessitates the determination of mechanical properties on these scales, including thin surface and thin interfacial layers. Therefore, nondestructive methods for characterization on these scales is also necessary.

High-resolution acoustic imaging can be a powerful tool for materials research. Using these techniques it is possible to determine elastic properties and defects in materials with a resolution given by wavelengths. In order to exploit the commercially available AFM for this purpose, the sample is coupled with an ultrasonic transducer. The resulting system is calibrated to measure the tip displacements due to this excitation.

Several displacement-detecting methods have been developed based on the excitation signal. Kolosov and Yamanaka [11] detected the nonlinear response of the tip-sample interaction force by propagating an amplitude modulated longitudinal wave through the sample. Rabe and Arnold [12] utilized a beam splitter and a knife-edge detection system to investigate cantilever deflections by generating amplitude images using broadband needle impulse MHz frequencies. Burnham, et al. [13] have investigated three different ultrasonic modes of operation: contact, mechanical diode, and sub-harmonic. In the contact mode, a small amplitude continuous longitudinal wave is propagated through the sample. The probing tip remains in constant contact with the sample due to the small amplitude of the excitation signal throughout the cycle. Larger amplitudes cause the tip to lose contact sporadically and bounce chaotically.

As discussed before, the motivation for studying the hardness of the material in nanoscale led to modifying the original AFM. This modified AFM, often called an atomic force acoustic microscope (AFAM), has been found useful in many applications in the field of materials research. The dynamic properties of the cantilever change during scanning due to changes in surface stiffness. Contact with the sample causes the natural frequency of the cantilever to shift. The stiffer the material surface scanned by the tip, the higher the frequency shift. Using the contact theories discussed previously it is possible to calculate the stiffness of the sample surface.

2.2.1 Recent research in AFAM

In the last decade the literature on dynamic modes of the AFM, and applying an ultrasonic excitation to Atomic Force Microscope specimens (cantilever) to map surface stiffness has grown tremendously.

Rabe and Arnold performed one of the earliest studies in this field in 1994 [14]. They report applying ultrasonic excitations in the range of (5-20 MHz) to a sample. A part of the position-sensing light beam reflected from the cantilever is directed to an external knife-edge detector in order to detect the distribution of the ultrasonic vibration amplitude. The lateral resolution of the acoustic images taken on the surface of a wafer is about 100 nm at an ultrasonic frequency of 20 MHz .

At nearly the same time, Kolosov and Yamanaka [15] published a paper on the nonlinear detection of ultrasonic vibrations with the atomic force microscope. They proposed a new method which uses the average cantilever displacement and makes detection of small amplitude ultrasonic vibrations (less than 0.2 nm) possible. Dubbing the technique as ultrasonic force microscopy (UFM), they successfully detected ultrasonic frequencies up to the GHz range, using an AFM cantilever, which had a resonant frequency of less than 100 kHz. They also found that after the ultrasonic amplitude threshold is crossed, a strong repulsive force acts on the cantilever. The amplitude of this threshold was found to depend on the average force applied to the cantilever tip.

In another article in the same year, Kolosov and Yamanaka [5] studied UFM for applications in nanometer resolution subsurface imaging. According to the method presented, the sample is vertically vibrated at ultrasonic frequencies, which are much higher than the natural resonance frequency of the AFM cantilever. Modulating the ultrasonic vibration amplitude, it is then possible to image subsurface features from the cantilever deflection vibration at the modulation frequency. Adding low-frequency lateral vibrations to the ultrasonic vibration, it is possible to image subsurface features with different shear rigidity from the torsional vibrations of the cantilever. According to their findings, it is possible to distinguish subsurface features of different elastic properties, when directions of the vibrational forces are controlled.

In their research of free- and surface-coupled vibration of AFM cantilevers, Rabe, et al. [16] focused on both the theoretical, as well as the experimental aspects of these vibrations. In order to measure the free vibration spectra and the local vibration amplitude of four rectangular AFM cantilevers made of silicon, they used an optical interferometer in the frequency range of 100 kHz to 10 MHz. They found a good agreement between the experimental results obtained in this manner and the flexural wave theory of elastic beams. According to their observations, when the cantilever tip is in contact with the specimen surface, the resonance frequencies shift. The vibration amplitudes throughout the cantilever are also changed during contact. Using a linear approximation method for the tip-sample interaction forces, they propose a method to calculate the frequency shift caused by contact, from the point-mass model. They note that the results obtained from this method do not agree well with the ones measured experimentally. They speculate that the different geometry of commercial cantilevers and the over simplification of the linearity assumption of the tip-sample interaction forces might explain the disagreements with experimental values.

Turner, et al. [10] studied high-frequency responses of atomic force microscope cantilevers. They used the flexural vibrations to show the limitations of a one-degree of freedom system. This approach, called a first mode approximation (FMA) or point-mass model, was compared with the complete flexural equation using both linear and nonlinear examples. Using analytical and finite difference techniques, the two systems were observed to have differences in drive-point impedance and it was also observed that they were influenced differently by the interaction damping. It was shown that in order for both the low and high frequency dynamics to be modeled in an accurate manner, the higher modes must be included for excitations above the first resonance.

Rabe and Arnold [12] studied the linear and nonlinear tip-sample interaction forces by atomic force acoustic microscopy. The cantilever-sample system of a commercial atomic force microscope was excited in the frequency range reaching from 10 kHz to 3 MHz. The mechanical system under study consisted of a flexural beam clamped at one end and the sensor tip at the other end. They obtained information about the stiffness and the damping of the whole mechanical system, by analyzing the cantilever vibration in the frequency domain, in forced interaction with the specimen surface. According to their observations, the range of the tip-sample distance covered during the vibration cycles changes with variations of the cantilever sample distance or of the excitation amplitude. They also observed that with increased excitation amplitude or decreased static cantilever load the contact resonance frequencies shift to lower values.

In their study of quantitative material characterization by ultrasonic force microscopy, Yamanaka, et al. [17] observed that the cantilever vibration spectra depend strongly on the excitation power. When a small enough excitation power was used, the resonance peak width decreased and the peak frequency increased to a limiting value. They assumed that if lateral stiffness would also be taken into consideration, the linearity assumption would be valid.

Rabe, et al. [18] studied the measurement of mechanical properties of nanoscale ferrites using atomic force acoustic microscopy. They proposed a quantitative model based on linear tip-sample force which shows that the stiffness of the specimen can be derived from the shift of the contact resonance frequencies relative to resonance frequencies of the free cantilever. They used a silicon <100> single-crystal to prove that the local measurement of modulus was consistent. Using this result as a basis, they determined the influence of the deviation from the stoichiometry on the modulus for a given grain size.

Iwata, et al. [19] used the UFM method developed by Yamanaka and Kolosov [20] to perform local stiffness measurements of nanobundle structure of polycarbonate surface. They describe the process of changing modulus during bundle formation, using UFM imaging.

Rabe, et al. [21] have studied the application of the principles of AFAM to measure the Young's modulus of nanocrystalline ferrites with spinel structures as a function of the oxidation temperature on a nanoscale. They observed an overall decrease in the Young's modulus with increasing oxidation temperature. The measurements strengthen the argument for the existence of chemicals gradients in the γ-phase from the surface layer to the interior of the films, which occurs during the oxidation process.

Stahl and Bourquin [22] have used the experimental AFAM setup by Rabe and Arnold [14] to characterize mechanical resonators. They evaluated the normal components of the surface vibrations of a 10 MHz quartz crystal resonator and a tuning fork. The cartography of the local characteristics of the resonator material was thus obtained.

Yamanaka, et al. [23] have studied nanoscale elasticity measurements with in situ tip shape estimation using UFM. The contact radius is a parameter for determining the contact stiffness. They present an in situ model, with the assumption of axial symmetry along the tip, whose parameters are clearly determined from a contact force dependence of the cantilever resonance frequency. The method was shown to provide an accurate prediction of the cantilever thickness, the tip shape and the effective stiffness of soft and hard samples. However, one of the limitations of their model is identified as the necessity of a reference point on the tip profile, since the estimated tip profile depends directly on the selection of the reference point.

Yamanaka and Nakamato [11] later developed an improved ultrasonic atomic force microscopy for mapping the resonance frequency and the Q factor of a cantilever, where the tip is in linear contact with the sample. Assuming the vibration amplitude at resonance to be linearly proportional to the Q factor, it was possible to measure the resonance frequency and Q factor in the resonance-tracking mode by scanning the sample in the constant force mode.

2.2.2 AFAM setup

The experimental setup for the AFAM used here is shown in Figure 2.8. As shown, a modified commercial AFM is used for the AFAM experiments. An ultrasonic excitation is produced in the frequency generator and induced in the sample by a transducer. The cantilever tip is pressed on the vibrating sample, which is adhesively mounted. The tip deflection is captured by the photodetector. The signal is routed through a lock-in amplifier and the results are analyzed by the software.

The amplitudes of the cantilever vibrations are evaluated by a lock-in amplifier. For spectroscopy, the excitation frequency is changed in a stepwise manner, and the corresponding response by the cantilever is recorded. For imaging, on the other hand, the excitation frequency is fixed and the sample surface is scanned in contact mode.

When the sensor tip is brought into contact with the sample surface, vertical and lateral elastic forces act between the sensor tip and the sample surface. There is a nonlinear relationship between the tip-sample distance and the interaction forces. In order to be able to interpret AFAM data in a convenient manner, simplifying assumptions have to be made. Therefore, the Hertzian contact model is used in the stiffness calculation. The assumptions in the Hertzian contact model are important. First of all, we assume that the resonance shift is solely a consequence of the tip-sample interaction and can therefore be directly related to the Young's modulus. We also assume that the cantilever tip has the equivalent diameter of a Hertzian sphere. While over simplified, we will use this model to analyze AFAM images and shift data to calculate surface stiffness. A typical AFAM image, along with its corresponding AFM topography image can be seen in Figure 2.9. Figure 2.10 shows

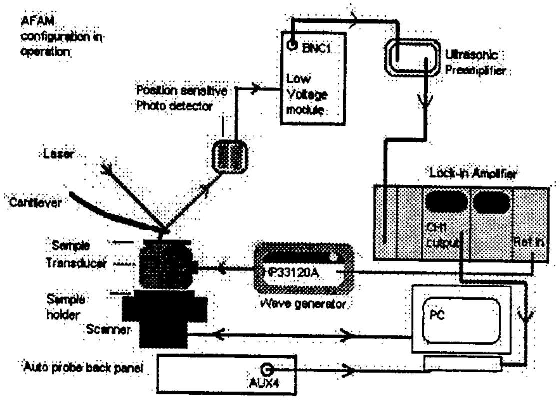

Figure 2.8: Schematic of the AFAM equipment.

a typical frequency shift due to sample excitation.

2.3 Microelectromechanical systems (MEMS)

Microelectromechanical systems, or MEMS, are integrated micro devices or systems that combine electrical and mechanical components on a very fine scale. They are fabricated using integrated circuit batch processing techniques and their size can range from micrometers to millimeters. In the most general form, MEMS are a set of mechanical microstructures, microsensors, microactuators and electronics integrated in the same environment (normally on a silicon chip). Microfabrication technology enables fabrication of large arrays of devices that individually perform simple tasks, but in combination these

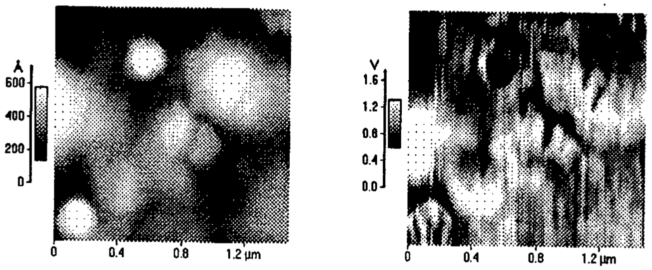

Figure 2.9: An AFM topography image of a polysilicon sample (left image) and an AFAM image of the same sample (right image).

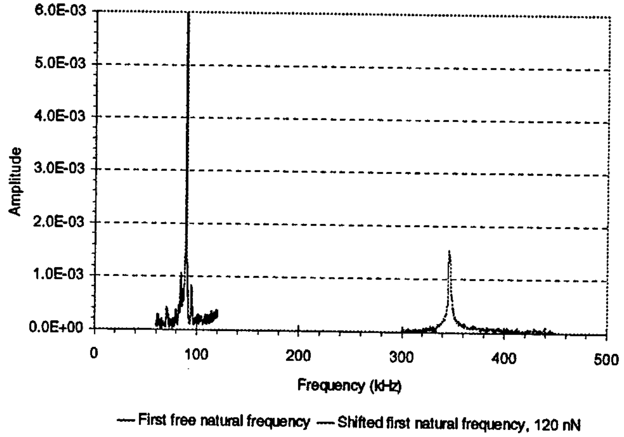

Figure 2.10: First free natural frequency and its shift due to sample contact for a d-lever B cantilever.

devices can accomplish complicated functions. Current MEMS applications include, but are not limited to pressure, chemical and flow sensors, accelerometers, micro-optics, optical scanners, and fluid pumps [24].

MEMS have many advantages over traditional mechanical and electronic devices that perform the similar tasks. Their small size allows hundreds of them to take the same space as a similar macro-device. The integration of the electrical and mechanical components on the same wafer also has the advantage of picking up less electrical noise, thus improving the precision and sensitivity of sensors. Using integrated circuit processing, these devices can be mass produced on a single wafer. This processing reduces the price of each MEMS device dramatically. Thus, MEMS devices can also be less expensive than their macroscale counterparts [24]. Other production methods include the stress-controlled thin film polysilicon process for the production of polysilicon resonator transducers, high energy photon light sources and electrodeposition techniques for the production of high aspect ratio electrostatic resonator and deep x-ray lithography and electrodeposition process for the production of magnetic micro motors and precision engineered gears [25].

The MEMS samples used in this research have columnar grains and a strong <110> out-of-plane texture. They have thicknesses on the order of a few microns, with finer features on the order of one micron [26]. They have been fabricated using low pressure chemical vapor deposition (LPCVD) processes by Cronos. Co [27].

Chapter 3

Experimental Methods

In the experimental part of the research, different steps were taken. In the first section of this chapter, some information about our atomic force microscope and the additional necessary equipment for setting up the AFAM is described. In the second section of the chapter, three different configurations used for this research are described in detail. In the third section, the focus is on the experiments done in order to determine the cantilever tip radius, which is another crucial parameter in this research. In the fourth section, the stiffness calculation which uses the data from the experimental configuration and the cantilever tip radius is presented. To conclude this chapter, the experimental stiffness of several samples is calculated.

3.1 AFAM Setup

In this chapter, the experimental setup developed is discussed in detail.

3.1.1 AFAM components and settings

The basic components used for constructing an atomic force acoustic microscope are the following:

- AFM, Thermomicroscopes Autoprobe CP
- HP 33120A, function generator/arbitrary waveform generator
- Transducer V125, Panametrics, central frequency 2.25 MHz
- Cantilevers (NSC-16 and d-lever B, both rectangular)
- Model SR 844 RF lock-in amplifier
- Ultrasonic preamplifier, Panametrics model 5676
- Low voltage module, APSA-1000, Thermomicroscopes

Each of these components is now briefly described and the connections between all components is outlined.

3.1.2 AFM

The main component of the atomic force acoustic microscope is a standard AFM, which in this case is a Thermomicroscopes Auto Probe CP. The specifications of this AFM are as follows:

Scanner: 5 μm piezoelectric scanner

Scan range: Maximum lateral scan range=5 μm

Maximum vertical scan range=2.5 μm

Control resolution: Maximum lateral resolution=0.0013 μm

Maximum vertical resolution=0.009 μm

Sample size: 50 mm 50 mm 25 mm

The main components of the AFM are the probe head, the manual XY stage, the motorized Z stage, and the scanner. The probe head consists of a deflection sensor, which contains a laser diode, a mirror, and a position-sensitive photo detector (PSPD). The probe head holds a probe cartridge, which contains a removable chip carrier with a cantilever chip mounted on it. The probe cartridge can slide in and out on side rails and click into the exact position. A probe head is shown in Figure 3.1.

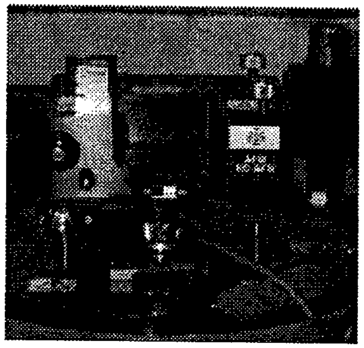

Figure 3.1: AFM head, Thermomicroscopes Co.

Using an XY translation stage, the probe head can translate in the X and Y directions. The XY translation makes it possible to position the cantilever tip in a desirable place for scanning using the two screws as shown in Figure 3.1. The displacements using these screws are large in comparison with the scanning area of the AFM.

The probe head can move up and down in Z direction. Up and down movements of the probe make it possible to increase or decrease the distance between the sample and cantilever. This motion is controlled using tools in the Proscan data acquisition software. The Z-axis step increments are very fine and can be changed from 0.0005 μm to 0.4 μm.

The scanner is a piezoelectric ceramic tube. It is installed below the probe head. A sample holder exists on the top of the scanner. The scanner can move the sample in X, Y and Z directions. However the range of these movements is very limited. The scanner is used for moving the sample only when the cantilever is used for imaging the sample. Large displacements in the X or Y directions may harm the cantilever and cantilever tip. The range of movements of scanner is limited to 5 μm in both X and Y directions.

The AFM used here has two different modes, contact mode and non-contact mode. For each of these modes, a specific procedure should be followed. In this specific research, the contact mode is the one most frequently used. The non-contact mode is used only for determining the free natural frequencies of the cantilever. The basics of contact and non-contact mode have been discussed in the literature review (Section 2.1.3).

Proscan data acquisition software controls the AFM and collects data. It has two main modes, move mode and image mode. Move mode involves software driven stage control. Image mode includes scan and feedback controls for setting parameters as well as a virtual oscilloscope display.

3.1.3 Function generator/arbitrary waveform generator

The HP 33120A is a high performance 15 MHz wave generator. The peak-to-peak output voltage range is from 50 mV to 10 V. This function generator is able to produce ten standard waveforms although the sine wave form is the primary output wave form used here. The HP 33120 is controlled with a GPIB interface and Labview software.

3.1.4 Transducer V 125

The Panametrics V 125 transducer is a standard longitudinal transducer, and therefore vibrates out of the plane of the transducer. The diameter of this transducer is 0.375 in and the central frequency is 2.25 MHz. The signal waveform and the frequency spectrum for the transducer used is shown in Figure 3.2. These plots are published by the manufacturer for calibration purposes. It is possible to observe the frequency range in which this transducer has a sufficient amplitude response. This transducer is not suitable for frequency ranges above 4.5 MHz. For the frequency range used in this research in which a very low voltage sine wave is applied, it provides a low amplitude vibration that is appropriate for linear vibration of the cantilever. One limitation in using different transducers in this research is their size and weight. A suitable transducer should fit on the top of the scanner and leave enough space for probe head. It also should not be too heavy, since it could damage the scanner or impede the response of the scanner. In addition, it should have enough surface area to mount the sample. Finally, it should be responsive over the frequency ranges which are used in the research.

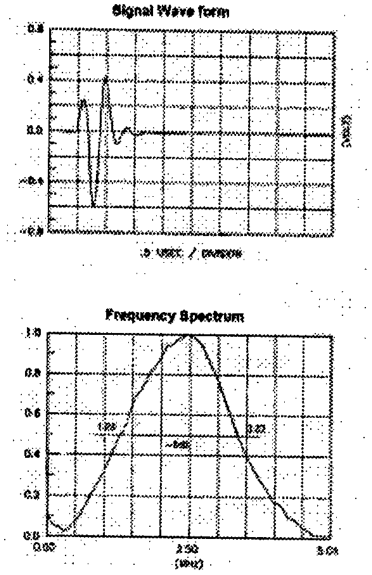

Figure 3.2: Typical response of Panametrics transducer V 125 provided by manufacturer.

3.1.5 Cantilevers

In this research, several different cantilevers were used. Cantilevers are usually made of silicon or silicon nitride using micromachining techniques. Cantilevers are usually coated on the back with a thin reflective layer that improves the laser reflection. Reflective coatings are thin aluminum or gold that also prevent magnetization of the tip with the direction usually along the tip axis. It is also possible to coat the cantilever tip. The reason for coating the cantilever tip is to protect the tip from early erosion. The coating for the tip is usually polycrystalline diamond or another wear-resistant coating. Two types of cantilevers were found to be the most suitable cantilevers found for calibrating the AFM and obtaining AFAM vibrational data. The first is the d-lever B cantilever from Thermomicroscopes Co. [28] and the second one is cantilever NSC-16 from MikroMasch Co. [29]. Both of these cantilevers have a basic rectangular shape and the nominal specifications of both of these cantilevers are shown in Table 3.1.

Table 3.1: Specifications of cantilevers NSC 16 and d-lever B.

Cantilever type	d-lever B	NSC-16
Cantilever length	180 μm	230 μm
Cantilever width	55 μm	40 μm
Cantilever thickness	2 μm	7 μm
Force constant	2.2 N/m	40 N/m
First resonant frequency	80 kHz	170 kHz

The force constant of commercial cantilevers varies from 0.01 N/m to 60 N/m and for most cantilevers, the force constant is less than 1 N/m. Cantilevers may be divided into two categories, either soft or hard, in terms of their force constant. Soft cantilevers which have a force constant less than 1 N/m are usually used for experiments on soft samples (e.g., biological samples). Soft cantilevers are not suitable for stiff samples and specifically in AFAM research because the effect of adhesive forces between tip and sample are not negligible. Hard cantilevers usually have a force constant of more than 1 N/m and both cantilevers used in this research are in this class. Hard cantilevers are more suitable for scanning stiff surfaces.

The exact cantilever stiffness varies from the nominal values provided by the manufacturer. Although current production methods are able to control the length and the width of the cantilever reasonably well, thickness is known with the least precision. The variations in geometry cause variations in the cantilever force and natural frequencies of the cantilevers. Values of the free natural frequencies measured in the non-contact mode are used to adjust the thickness parameter to match the experimental data.

3.1.6 Lock-in amplifier

A lock-in amplifier is used to monitor the signal output from the photodetector. The SR844 lock-in amplifier which is used in this research can operate in a range of 25 kHz to 200 MHz. This instrument has very good gain stability and have zero drift. It also has output filters which make it possible to filter the amplitude signal and remove a significant part of noise. The sensitivity and filters may be adjusted to obtain an optimum signal which does not have too much noise and at the same time, resonance peaks are clear and distinguishable.

3.1.7 Ultrasonic preamplifier

A Panametrics 5676 ultrasonic preamplifier was used to amplify the photodetector signal. This ultrasonic preamplifier has ultra low noise, high gain and has broadband performance. This specific preamplifier is designed to operate in a bandwidth of 50 kHz-20 MHz which covers the frequency range of the present AFAM experiments.

3.1.8 Low voltage module

The low voltage module makes it possible to monitor any signal passing through the low voltage I/O cable. The BNC1 channel is the signal output from the photodetector.

3.2 Experimental Configurations

Three different connection configurations are used for the AFAM experiments. The first configuration is used for obtaining free vibration data using an external transducer and is called the air-coupled method. The second configuration uses an internal transducer and may also be used for obtaining free vibration data. The difference between the two is the amplitude of vibrations they can induce. The third configuration is used for obtaining contact spectra of the vibrating cantilever and for taking an AFAM image of the material.

3.2.1 Free vibrations with air coupling

Free vibrations data are needed as a baseline to measure the shift due to excitation, when in contact with the sample. There are two ways to measure free vibrations: air coupling and using the built-in transducer.

In the air coupling method, a vibrating transducer, which is located on the sample holder, transfers its vibration through the air to the cantilever located on the head of the probe. The configuration of the equipment and all connections are shown in Figure 3.3. A photograph of the equipment is shown in Figure 3.4. With this technique, it is possible to determine the free natural frequencies of the cantilever beam. Experimental results with cantilevers of different stiffness have shown that this technique is suitable for detecting only the first free natural frequency for high stiffness cantilevers. However, it can be used to detect several free natural frequencies of soft cantilevers.

Labview software is used to control these measurements. Using this software, a sweep of frequencies is made. As the transducer vibrates, the motion is coupled to the free cantilever above the transducer. The cantilever starts to vibrate at the driving frequency. The laser and position sensitive photodetector can detect very small vibration amplitudes. The signal from the position sensitive photodetector is transferred through low voltage module output BNC1. The signal is first amplified using the preamplifier and then amplified further by the lock-in amplifier.

In order to be able to operate this system, some adjustments are necessary to the system and software and the correct connections between equipment should be established. Two different sets of adjustments are necessary for the AFM. First, it is necessary to adjust the mechanical parameters and laser position on the cantilever. Software adjustments include deactivating the z-control mechanism, which would otherwise prevent cantilever deflection.

After mounting the desired cantilever on the probe cartridge, the head of the AFM

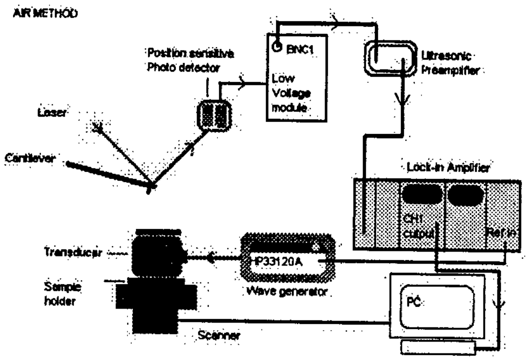

Figure 3.3: AFAM configuration for the air method.

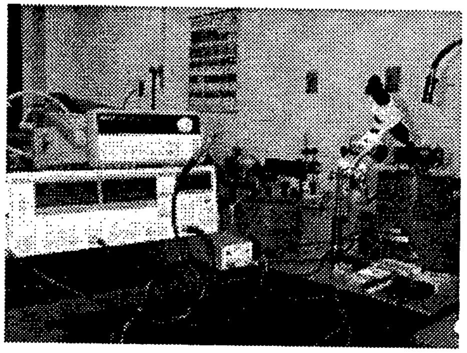

Figure 3.4: Photograph of the AFAM setup described here.

should be turned on. The laser should be positioned at the end of the cantilever tip using the laser beam steering screws shown in Figure 3.5. In the Proscan software, with the voltmeter option, the A-B and A+B voltages should be checked. For the optimum laser adjustment, the A+B voltage should be more than 1 V and the A-B voltage should be in the range of -300 mV to 300 mV. It is also possible to check the adjustment of the signal using the prism located on the top of the head. The best adjustment is when the green middle light is on and there is no red light in the prism panel.

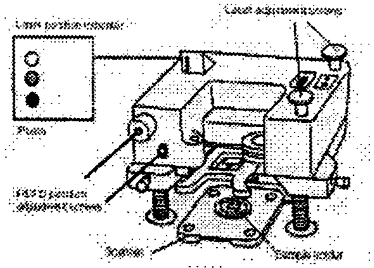

Figure 3.5: Laser adjustment (Park Scientific Instrument User Guide to Autoprobe CP, 1997).

After all the AFM adjustments are made, the Labview software is activated. It controls both the waveform generator and the lock-in amplifier using an IEEE GPIB interface card in the AFM computer. The transducer is attached to an AFM sample holder using carbon conductive tape and it is placed on the sample holder. The range and the step of the scan is selected within the Labview software. This program receives the amplitude

of the vibration from the lock-in amplifier while changing the frequency on the waveform generator.

By choosing large steps (e.g., 2 kHz) it is possible to sweep a wide range of frequencies to find the natural frequency peaks. After locating the coarse natural frequency peak position within the spectrum, a higher resolution scan (e.g., 10 Hz) over a smaller range is made in order to obtain a highly resolved peak. The data from the Labview program are then stored in text files for later analysis.

3.2.2 Free vibrations with built-in transducer

In this method, instead of using an external transducer, as in the air method, the built-in transducer (a piezoelectric actuator) of the AFM is used. The experimental setup is shown schematically in Figure 3.6. The position of the built-in transducer is in the probe cartridge. It is a very thin transducer sandwiched between the cartridge and the cartridge mount. The excitation signal is connected to the piezoelectric actuator through the back panel of the AFM. The AC signal from the waveform generator enters the AFM system through NC Clock input. All other connections are the same as in the air-coupled method. Using the built-in transducer method, it is possible to detect numerous natural frequencies up to 3 MHz. This limit on detecting frequencies more than 3 MHz is the frequency limit of the photodetector on this specific AFM. In order to detect the higher resonance frequencies, an alternative photodetector with higher frequency detection limit should be used.

The non-contact mode of the PSI Proscan software should be used when applying an excitation to the built-in transducer. The AFM head must be turned off and the Proscan database configuration opened. It is necessary to change the head mode in the dialog box

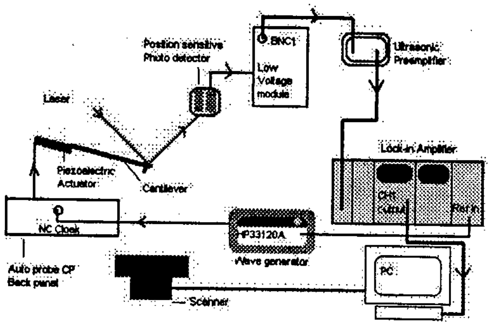

Figure 3.6: Schematic of the experimental setup for the piezoelectric actuator technique.

to NCM (Non Contact Mode). After this change, the head should be turned on and the software switched to non-contact mode. A parameter dialog box appears automatically on the screen. The drive % (or drive amplitude), controls the gain of the AC signal, input from the wave generator. This gain must be set large enough for detection, but small enough to avoid nonlinear behavior. The exact range has to be determined on a case to case basis.

3.2.3 Contact vibrations

The procedure for determining the natural frequencies while in contact are described here. In this method, the external transducer (the experimental setup is shown schematically in Figure 2.8) is used to vibrate the sample and cantilever at the same time. An AC signal produced using the waveform generator is used to drive the transducer. Using the image mode in the control panel, the desired force is set in the set point dialog box. The applied force is selected using the Proscan software. After setting the force, an auto approach is done and the cantilever makes contact with the sample. At this point, the scanner is turned off such that the cantilever stays at one point on the sample. Next, the contact natural frequencies are determined using the same frequency sweep technique outlined in Section 3.2.1. For this purpose, the Labview program is used to control the wave generator and lock-in amplifier simultaneously.

In order to be able to create a surface stiffness image, a frequency in the range of the peak and slightly smaller or larger than the peak itself should be selected. The frequency should be in the range of the peak. Otherwise, the image will not represent the surface stiffness image, but will show the background noise instead. The difference between choosing either right side or left side slope of the peak is in the contrast of the stiffness of the image which is being produced. For two frequencies on opposite sides of the peak, two images would be produced which would be opposite in contrast.

After choosing the driving frequency, the Labview program is stopped and the waveform generator is fixed on this frequency. The amplitude output signal from the lock-in amplifier is connected to the AUX 4 at the back of the AFM. The AUX 4 signal can be monitored using Proscan software. This signal can be mapped similar to the surface topography image. The topography and AUX 4 signals are then activated and an image is taken from the sample. The result is two images, one of which is the ordinary topography of the sample and the other which is the surface stiffness map of the sample.

3.3 Tip Radius Evaluation

Evaluation of the tip radius is important for calculation of the surface modulus as discussed in Section 2.2.4. Because of different techniques and methods used to produce cantilevers, the tip radius will vary between cantilevers. The tip radius also changes due to wear from prolonged use. Three methods for evaluating the tip radius are used in this research. The first method uses calibration gratings. The second method uses single crystal silicon as a material with known stiffness such that the tip radius may be determined. The last method uses a scanning electron microscope to measure the tip radius. In following sections, these methods are described in detail.

3.3.1 Calibration gratings

The use of calibration gratings from MikroMasch Co. and SPIP software (Image metrology Co.) are used to evaluate the tip radius. Gratings are typically an array of tips or other physical shapes which have dimensions and scales that are well known. They are usually made of etched single crystal silicon and can fit in the sample holder of the AFM. Using these geometric patterns, it is possible to take an atomic force microscopy image of these gratings. Because the dimensions and scales for gratings are known with precision, the resulting AFM topography image may be compared with the known geometry. The tip radius is then estimated using SPIP software, which uses blind tip reconstruction and a deconvolution technique [30],[31]. Several types of gratings may be used. Some grating images are shown in Figures 3.7-3.8. As can be seen, the finite geometry of the imaging tip can distort the image data and complicate metrological investigations of the surface features. These images are mixtures of the tip and gratings shape. In order to correct the grating images to the known grating geometry, it is necessary to have an estimation of tip geometry. After taking images, the image is loaded into the SPIP software. The software uses a blind tip reconstruction technique which has been discussed in detail by Williams, et al. [30] and Villarubia [31].

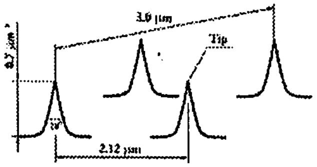

Figure 3.7: Schematic of the silicon calibration grating TGT01. This grating is an array of sharp tips characterized by strict symmetry of tip sides, small cone angles and small curvature radius (K-TEK International Inc. Mikromasch grating catalog, 2000).

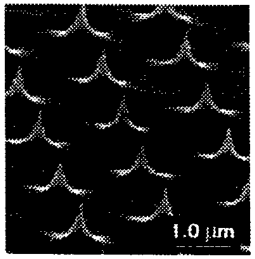

Figure 3.8: SEM image of silicon calibration grating TGT01 of an array of sharp tips characterized by strict symmetry of tip sides, small cone angles and small curvature radius (K-TEK International Inc. Mikromasch grating catalog, 2000).

Gratings are not only used to estimate tip radius. They can also be used to perform vertical and lateral calibration of the AFM scanner, detect vertical and lateral nonlinearity and angular distortions, detect hysteresis, and detect the creep effect.

In this research, a TGT01 model grating was used to evaluate tip radius. The TGT01 grating was placed on sample holder of the scanner of the AFM and several images were taken. As shown in Figures 3.9-3.12, using blind tip reconstruction technique, it is possible to reconstruct the real tip shape and evaluate the tip radius as well as correct the grating images. In Figure 3.9, an AFM image of the TGT01 grating is shown. It has been taken using a new d-lever B. Using the tip estimation in SPIP software, tip radius and dimensions are given in images 3.10, 3.11 and 3.12.

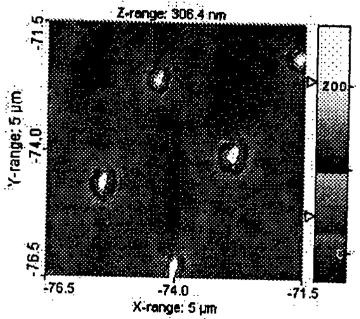

Figure 3.9: An image of grating TGT01 using a sharp dlever B tip (Scanning Probe Image Processor Software, SPIP, © Image Metrology Co., 2001).

In Figure 3.9, a topographical image of the grating surface is shown. This image is an input to the SPIP software for calculation of the tip radius. Several grating tips are shown in this Figure.

A 3-dimensional image of the tip reconstructed from the topographical image is shown in Figure 3.10. The SPIP software makes it possible to visualize the tip shape. The tip shown is not symmetric. As can be seen in Figures 3.11 and 3.12, SPIP software makes it possible to draw a profile of the tip from two different views from the side. Using clear profiles, the cone angle of the cantilever tip and the tip radius is calculated by the software. As shown, the tip is not necessarily symmetric and the profiles in X and Y do not overlap each other. This result is due to the deformed and irregular shape of the tip. Current micro machining techniques for producing tips are not accurate enough to control all the dimensions of the tip.

Figure 3.10: A 3D image of the sharp d-lever B tip (Scanning Probe Image Processor Software, SPIP, © Image Metrology Co., 2001).

Figure 3.13 is an example of topography of the grating surface using a worn tip. Comparison of the color indicator of the grating image in Figure 3.13 with that shown in Figure 3.9, it can be observed that the height of the worn grating tips is much less than

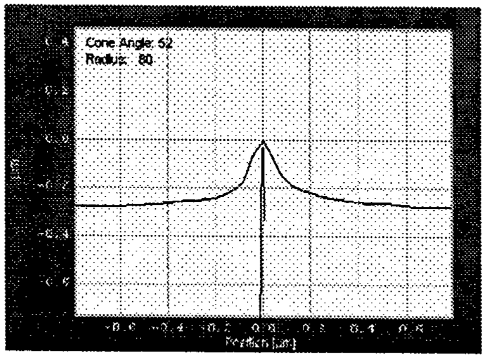

Figure 3.11: X profile of a new d-lever B tip (Scanning Probe Image Processor Software, SPIP, © Image Metrology Co., 2001)

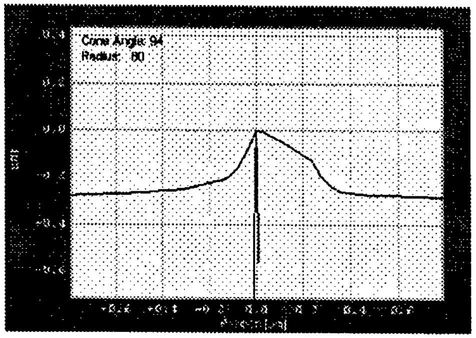

Figure 3.12: Y Profile of a new d-lever B tip (Scanning Probe Image Processor Software, SPIP, © Image Metrology Co., 2001).

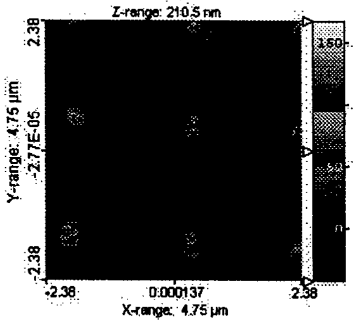

Figure 3.13: An image of a d-lever B tip with wear from prolonged use (Scanning Probe Image Processor Software, SPIP , © Image Metrology Co., 2001).

the new tip grating image. When a tip loses its sharpness, it is unable to detect the details of features smaller than the worn tip. Several grating tips are shown on the surface. The three dimensional shape of the worn out tip is shown in Figure 3.14. As can be seen in the three dimensional visualization, the tip is very dull and the tip radius has increased immensely. As shown in Figure 3.15, the deconvolution allows the known grating geometry to be reconstructed. This image shows the reconstructed topography of the grating surface used in this research for determining the tip shape and dimensions. The tip radius can be estimated within a very small error range as shown in Figure 3.16. The accuracy of these calculations is estimated to be 97.5% using the SPIP software. If a grating surface is used instead of an arbitrary AFM image, a more accurate determination of the tip radius is possible, because the dimensions and geometrical values of the grating are well known.

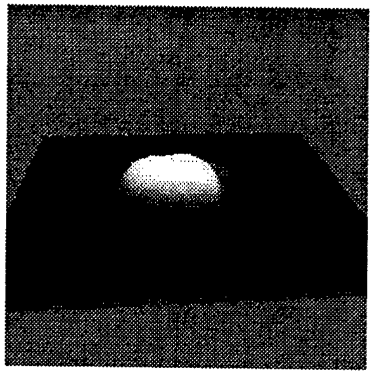

Figure 3.14: A 3D Image of the worn tip (Scanning Probe Image Processor Software, SPIP , © Image Metrology Co., 2001).

Figure 3.15: The image of grating TGT01 after deconvolution (Scanning Probe Image Processor Software, SPIP, © Image Metrology Co., 2001).

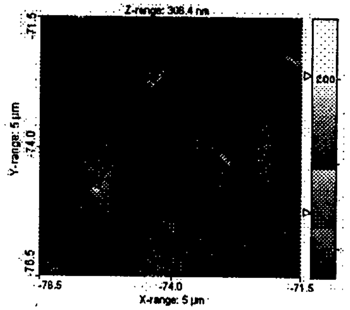

Figure 3.16: Uncertainty map of the grating (Scanning Probe Image Processor Software, SPIP, © Image Metrology Co., 2001).

3.3.2 Silicon calibration

In this method, vibration theory and the Hertzian model are used to estimate the tip radius. Several frequency spectra of cantilevers on Si <111> and Si <100> samples with different applied loads were measured and the first shifted natural frequency was determined. Using a method developed by J. A. Turner and J. S. Wiehn, it is possible to calculate the first five natural frequencies of a cantilever at a specific relative stiffness. Given the dimensions of the cantilever, the density, and the cantilever stiffness, a MATLAB® (Mathworks Corp.) program written by Turner and Wiehn in the Department of Engineering Mechanics of the University of Nebraska-Lincoln can be used to produce an output containing the relative stiffness and the corresponding natural frequencies for the different modes of vibration. For the two cantilevers used in this research, (i.e. the d-lever cantilever and the NSC-16 cantilever), the program outputs are presented in Appendix A.

Using the first column of the output, it is possible to find (directly or by interpolation) the corresponding relative stiffness for a given shifted frequency. The stiffness and Poisson's ratio of the sample and tip are assumed to be known, and the reduced elastic modulus can then be calculated. All other parameters of calculation are known except the tip radius, so it is possible to find the tip radius. In order to investigate the tip radius change as a function of use, a frequency scan on one of the calibration materials (Si <111> or Si <100>) can be repeated. It is possible then to evaluate the tip radius at that specific time. The position of the tip on the cantilever beam is also important in calculations for this technique as it determines the effective length of the cantilever that enters in the vibration calculations. Scanning electron microscopy (SEM) images of the NSC-16 and d-lever B cantilevers were used to determine the position of the tip along the cantilever. Some SEM images of NSC-16 cantilevers and d-lever B are shown in Figures 3.17, 3.18, 3.19 and 3.20. As shown in Figure 3.17, the tip position can be measured using scales at the bottom of the Figure. The tip position is located at 96% of the total length of the d-lever B. As shown in Figures 3.19 and 3.20, the tip radius is located near the end of the cantilever. Using the scales on the SEM images (error <3%, the tip position is calculated to be at 97% of the total cantilever length. A detail of the peak shape is shown in Figure 3.20. An example of this procedure for Si <111> is now given. Assuming the surface stiffness to be known, the tip radius can be estimated with the following procedure.

Using the procedure described in Section 2.1.4, the tip radius can be estimated using the following data. With the frequency shift for the cantilever known, the relative stiffness is found. For the case of Si <111> in contact with the NSC-16 cantilever, the

Figure 3.17: An SEM image of d-lever B.

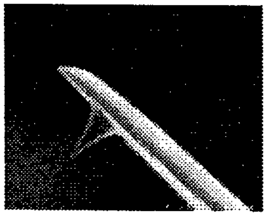

Figure 3.18: Partial SEM image of d-lever B and its tip.

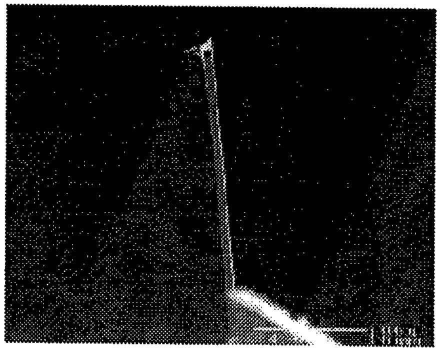

Figure 3.19: An SEM image of the NSC-16 cantilever and its tip.

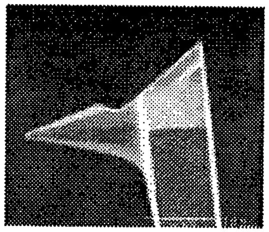

Figure 3.20: Scanning electron microscopy image of cantilever NSC-16.

natural frequency shifts from 173 kHz to 803.7 kHz, when a force of $F = 600$ nN is applied. This result corresponds to a dimensionless relative stiffness of $\Gamma = 31750.9$ obtained from modal frequency table in Appendix A.

Given that for a rectangular cantilever, $I = \frac{ab^3}{12}$, where a and b are the width and the thickness of the cantilever respectively, for the NSC-16 cantilever we have $I = 9.802(10)^{-22}\mathrm{m}^4$.

The actual contact stiffness is calculated from the relative stiffness using Eq. 2.2. With the elastic modulus for the cantilever taken to be $E = 169$ GPa, and using the effective length of $L_{\mathrm{eff}} = 0.969L$, we have $\kappa = \frac{EI\Gamma}{L_{eff}^3} = 58312$.

The reduced elasticity modulus is determined using Equation 2.24. The tip radius is calculated using Equation 2.27, is $R = 76.45(10)^{-9}$m= 76.45 nm. This calculation is used as a basis for the tip radius estimation required in the surface stiffness calculation for the MEMS sample.

3.3.3 Scanning electron microscopy

Scanning electron microscopes are very useful for estimating the dimensions of the cantilever, as well as the tip radius. In this research, several studies on cantilevers have been done using the Hitachi 3000 and JEOL JSM-840A scanning electron microscopes. After taking an image, the scanning electron microscope software is used to determine the dimensions of the tip. This method is not very accurate in comparison with the grating and calibration methods. Some examples of scanning electron microscope images are presented in Figures 3.21, 3.22 and 3.23. Even using the highest resolution possible for the SEM, it is difficult to take a clear image of the tip in order to estimate the tip radius. Especially when the tip is very sharp and new, taking a high resolution SEM image for determining tip radius is a problem. Even with highest resolution possible, many possible errors may arise with the measurement of the tip radius via SEM (e.g., astigmatism of the microscope, movement of the tip because of high concentration of electric discharge). Also, many technical limitations, such as the accumulation of a high concentration of electric charges on cantilever tip during SEM imaging, restrict the resolution and magnification of the SEM.

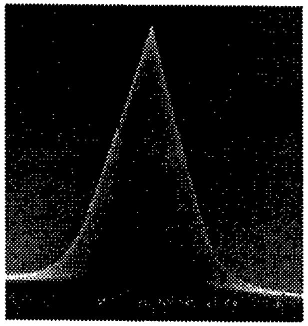

Figure 3.21: An SEM image of the tip of cantilever NSC-16.

Using Figure 3.23 and its scale, the estimated tip radius for this worn tip is around 200 nm; however, it is not possible to calculate the tip radius accurately. The profile of the tip is not accurate in these images and the curvature of the end of the tip is neither symmetric nor clear.

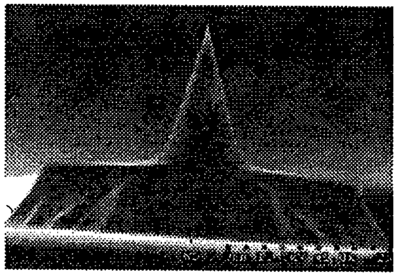

Figure 3.22: An SEM image of the tip of a NSC-16 cantilever.

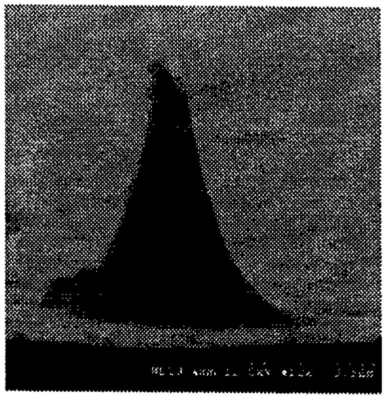

Figure 3.23: An SEM image the tip of a d-lever B cantilever.

3.4 Surface stiffness calculation

Using the Hertzian contact theory described earlier in Section 2.2.4, it is possible to calculate the surface stiffness of materials. An example of the surface stiffness calculation is presented for the MEMS sample.

The tip radius is assumed known from the silicon calibration. The surface stiffness is determined using the procedure described in Section 2.4.1. For the case of the MEMS sample in contact with the NSC-16 cantilever, the natural frequency shifts from 173 kHz to 767 kHz when a force of $F = 1000$ nN is applied. This value corresponds to a dimensionless relative stiffness of $\Gamma = 2351.3$, a value obtained from the modal frequency table presented in Appendix A. For a cantilever with rectangular cross section, $I = \frac{ab^3}{12}$, where a and b are the width and the thickness of the cantilever respectively. For the NSC-16 cantilever data given in Table 3.2, $I = 9.802(10)^{-22}\text{m}^4$. The actual contact stiffness is then calculated from the relative stiffness using Eq. 2.2. With the elastic modulus for the cantilever $E = 169$ GPa, and using the effective length of $L_{eff} = 0.969L$, we have $\kappa = \frac{EIT}{L_{eff}^3} = 5.83122(10)^6$.

Table 3.2: Poisson coefficient and the elastic modulus for the NSC-16 tip and the sample.

ν_s	0.266 Poisson coefficient for the sample
ν_t	0.181 Poisson coefficient for the tip
E_t	$130.4(10)^9$ Pa Elastic modulus for the tip
E_s	$129(10)^9$ Pa

With the tip-radius previously estimated at $R = 76.4$ nN and the applied force known to be $F = 1000$ nN, K can be calculated using Equation 2.26. The reduced modulus is related to the surface stiffness by Equation 2.27, where ν_s, ν_t and E_t are known from Table 3.3. The surface stiffness is then $E_s = 128.63$ GPa.

Table 3.3: Some mechanical properties of the tip and the sample.

ν_s	0.180 Poisson coefficient for the sample
ν_t	0.181 Poisson coefficient for the tip
E_t	$130.4(10)^9$ Pa Elastic modulus for the tip

The same principle can be applied to different applied loads, which result in different frequency shifts. The following example shows the variation in the stiffness calculation for different applied loads. Using the frequency shift for the cantilever, the relative stiffness is found. For the case of the MEMS sample in contact with the NSC-16 cantilever, the natural frequency shifts from 173 kHz to 787 kHz when a force of $F = 1500$ nN is applied. This frequency corresponds to a dimensionless relative stiffness of $\Gamma = 3123.4$, which is obtained by interpolation of the modal frequency table presented in Appendix A. Using the same values for I, E, and L_{eff} gives $\kappa = \frac{EI\Gamma}{L_{eff}^3} = 5.8434(10)^6$. Assuming the same tip radius gives $E_s = 128.99$ GPa. This example shows that for different applied forces there is only a slight difference in the calculated surface stiffness.

Chapter 4

Results and Discussion

In this chapter, results of the AFAM experiments are described in detail. In the first section of this chapter, the result of the free vibration measurements of the selected cantilevers are shown. This section is critical for the calculations that follow because all the stiffness calculations based on this method rely on the amount of the shift from its initial free vibration case. In the second section, the shift of the first natural frequency of the NSC-16 cantilever in contact with a single crystal silicon <111> is measured and their shift due to varying applied forces are measured. In the next section, shifts of natural frequencies on the single crystal silicon <100> are measured as a function of varying applied forces. These two different orientations of single crystal silicon are mainly used for calibration of the equipment. In the fourth section of the chapter, the MEMS material is investigated and the shifted spectrum is obtained for this polysilicon material. Then, in fifth section, the calculations related to polysilicon MEMS are presented. In the following section, the AFAM images of the surface of polysilicon MEMS samples are presented, as is the related surface stiffness map of the image is presented. In the last section, some nonlinear effects related to the amplitude of the vibration and its relationship to calculation of the stiffness and shift of the peaks are presented and discussed.

4.1 Free Vibration Analysis

In order to determine the natural frequencies of the cantilever prior to contact with the sample, the natural frequency of the sample is measured when vibrating in the air. The free vibration data for two types of cantilevers, the NSC-16 Cantilever from SPM tips Co. and the d-lever B cantilever from Thermomicroscopes have been analyzed using the setup described in Section 3.1.

4.1.1 NSC-16 cantilever

The first natural frequency for the NSC-16 cantilever can be found using the air method as described in Section 3.2.1. In this research it was determined that the air method is not suitable for determining the second and third natural frequencies, for stiff cantilevers such as the NSC-16, since the amplitude of the vibrations it could induce was insignificant. Figure 4.1 illustrates the result of this experiment. While not accurate for stiff cantilevers, this method can still be useful for soft cantilevers, because the wave energy is still powerful enough to vibrate the softer cantilever for second or higher modes. The first smaller peak is considered a non linear effect. The real peak is outstanding in comparison with this nonlinear effect. As can be seen, the first free natural frequency is 173.86 kHz. The sharpness of the peak is related to the damping of the vibrations. Since all the experiments in this thesis were done in air, it was logical to observe the damping effect of the air on the vibrating cantilever. The damping can be measured using the peak width, where a wider peak indicates a larger damping effect.

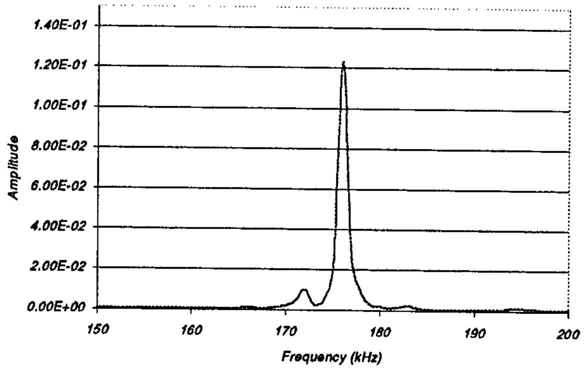

Figure 4.1: First free natural frequency for cantilever NSC-16 using the air method.

For the second and third natural frequencies the built in piezoelectric transducer is used. As shown in Figures 4.2 and 4.3, the second and third natural frequencies are found to be 1.06 MHz and 2.643 MHz, respectively. Figure 4.2 also shows the effect of using different voltages for exciting the built-in piezoelectric transducer. It is observed that for an excitation signal with amplitude of 1 V, the peak is not observable. Our experience with the built-in transducer shows that it is sensitive to voltages higher than 1.5 V only. Applied voltages less than 1.5 V give no measurable response to the photo detector. Only for applied voltages of 2 V and 3 V, is a peak observed.

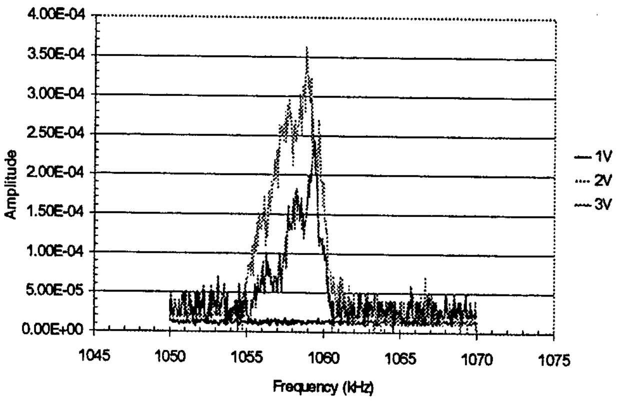

Figure 4.2: Second free natural frequency for cantilever NSC-16 using the built in piezoelectric actuator in the AFM, for different applied voltages to the built in transducer.

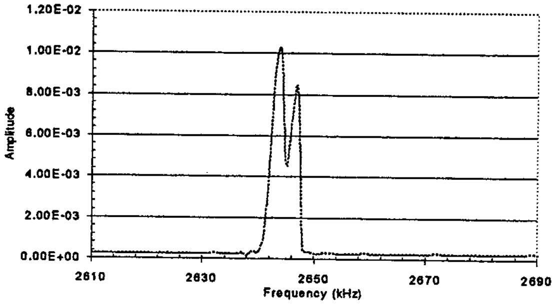

Figure 4.3: Third free natural frequency for cantilever NSC-16 using the built in piezoelectric transducer in the AFM.

4.1.2 d-lever B cantilever

As with the NSC-16 cantilever, the first natural frequency for the d-lever B cantilever (Thermomicroscopes Co.) was measured using the air-coupling method. The result, is illustrated in Figure 4.4. It can be observed that the first free natural frequency of the d-lever B cantilever is lower than that of the NSC-16 cantilever. This result is expected because of the smaller dimensions of the d-lever cantilever. It is specifically related to the ratio of the length to thickness of the cantilever as discussed in Section 2.1.5. Thus, the first free natural frequency of this cantilever is 88.2 kHz.

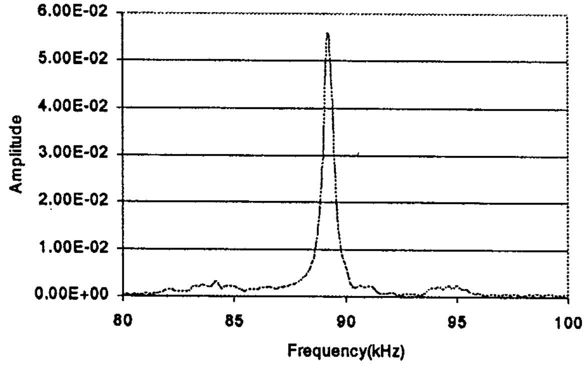

Figure 4.4: d-lever B, first free natural frequency.

For the second natural frequency the built in piezoelectric transducer was used. The two sets of data taken for Figure 4.5, overlap almost completely which indicates the

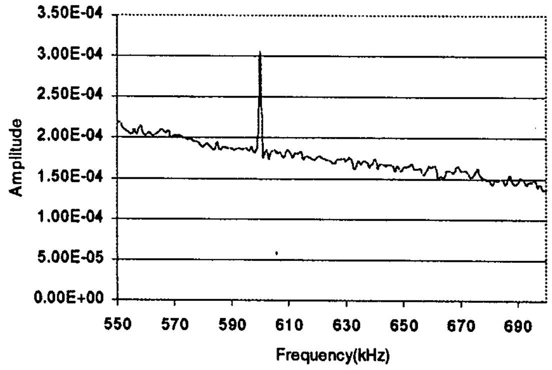

Figure 4.5: d-lever B, second free peak.

repeatability of the measurements. The second natural frequency for the d-lever B cantilever is 593 kHz and the third natural frequency is 2.64 MHz. Because this cantilever is softer than cantilever NSC-16, the higher natural frequencies can be detected without difficulty. If necessary, it is possible to detect all the natural frequencies up to 3 MHz.

With the natural free frequencies for both cantilevers determined, it is possible to determine the frequency shift for the cantilevers in contact with different material surfaces. In the following sections, the frequency shift results for these two cantilevers in contact with the surface of silicon <111>, silicon <100> and polysilicon MEMS materials are discussed. Using the Hertzian model described in Section 2.2.4, the natural frequency shifts are used to determine surface stiffness.

4.2 Contact Resonances on Silicon <111>

Silicon wafers are produced with different crystalline structures. In this section, the frequency shift response of silicon <111> for varying applied forces and at varying transducer voltages are studied for the NSC-16 and the d-lever B cantilevers.

d-lever B cantilever frequency shift response The frequency shift was measured at different applied forces (1 V) for the d-lever B cantilever. The results are shown in Figure 4.6. It can be seen that as expected, although the peak amplitudes are different, the peak shift falls within a narrow range of frequencies. As shown, with higher applied forces, the peak shifts to higher frequencies as expected by theory.

As can be seen in Figure 4.6, the peak shifts due to different applied forces. In these sets of experiments a sine wave with a low actuating voltage amplitude equal to 1 V is used. The reason for using such a low amplitude is for confining the major vibrations of the cantilever in a linear range. As can be seen, with increasing the applied force between cantilever tip and the sample, the peak shifts to a higher frequency. This effect is predicted by theory and according to this set of experiments, matches the theoretical predictions.

From Figure 4.6, it can be also noted that when the applied force is lower, the amplitude of the peak is lower and the width greater. As we apply higher forces, the peak gradually becomes sharper and the amplitude of the peak becomes larger. This effect can also be important for obtaining AFAM images of the surface of different samples. If a constant actuating voltage is used, with applying higher forces for taking an image, the contrast of the image would be higher, and a sharp image is obtained.

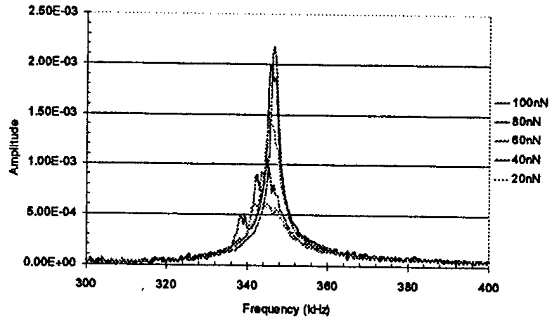

Figure 4.6: First peak shift due to different applied loads for d-lever B, applied transducer voltage 1V.

The first peak shift for the d-lever B cantilever in contact with silicon <111> is determined to be in the range of 340-348 kHz depending on the force applied. In addition, the repeatability of the above results were examined to determine the reliability of the acquired data sets. Different data sets were acquired for different applied forces, and the results show that the experiments are relatively accurate, and that the data sets are reliable and repeatable. The results are shown in Figures 4.7, 4.8, 4.9, 4.10 and 4.11. These data were taken with one hour elapsed time between each subsequent trial.

Figure 4.7 shows the natural frequency shift for an applied force of 20 nN, Figure 4.8 for an applied force of 40 nN, Figure 4.9 for an applied force of 60 nN, Figure 4.10 for an applied force of 80 nN, Figure 4.11 for an applied force of 100 nN and Figure 4.12 for an applied force of 120 nN.

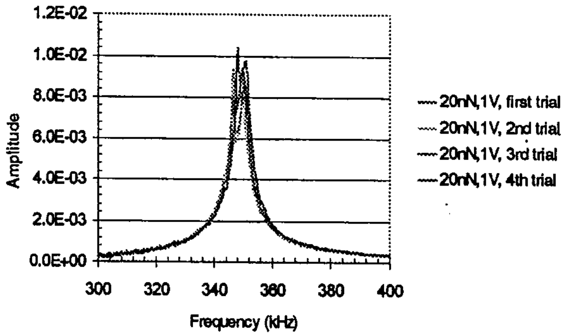

Figure 4.7: d-lever B, repeatablilty of the data for applied force 20 nN.

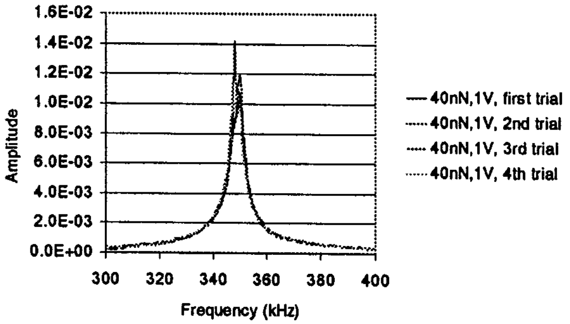

Figure 4.8: d-lever B, repeatablilty of the data for applied force 40 nN.

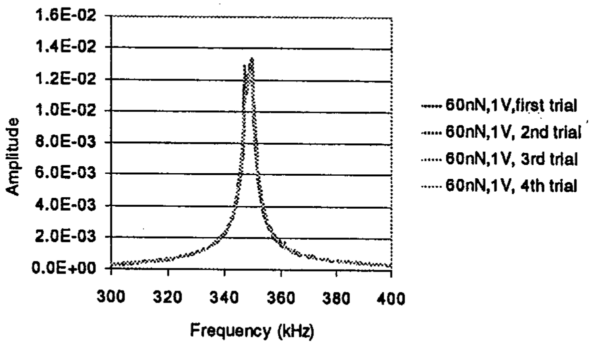

Figure 4.9: d-lever B, repeatablilty of the data for applied force 60 nN.

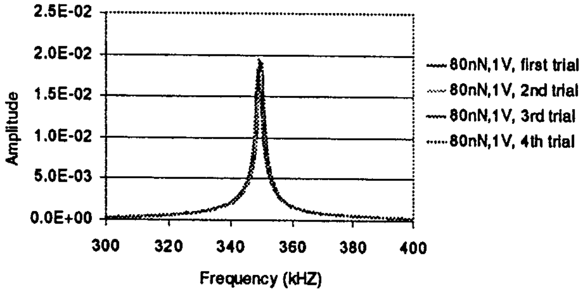

Figure 4.10: d-lever B, repeatablilty of the data for applied force 80 nN.

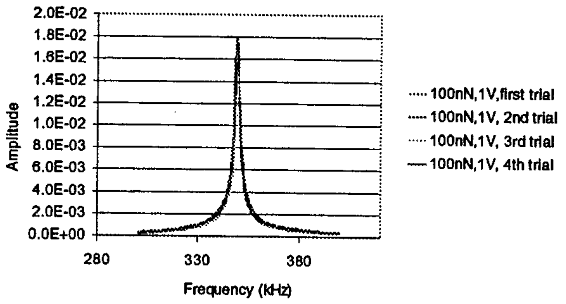

Figure 4.11: d-lever B, repeatability of the data for applied force 100 nN.

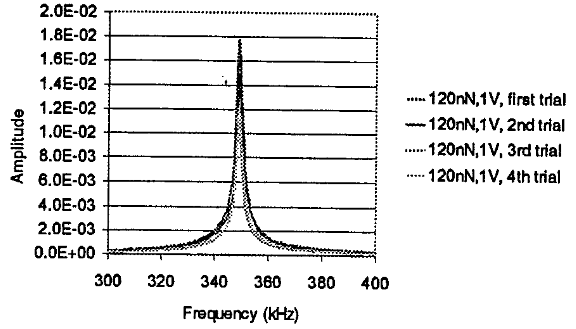

Figure 4.12: d-lever B, repeatablilty of the data for applied force 120 nN.

Cantilever NSC-16 frequency shift response For the NSC-16 cantilever the frequency response was also measured at different applied forces. In this case, the frequency shift for the different applied forces falls in the range of 835-865 kHz.

Figure 4.13 shows the frequency shift under different applied forces, with the actuating voltage held at 1 V. With lower applied voltages to the transducer, more clear peaks can be obtained. The effect of shifting peaks to higher frequencies with increasing applied forces can be observed in Figure 4.14. Also shown in Figure 4.14, increasing actuating voltage to the transducer (e.g., 5V), causes the peaks become more nonlinear and less sharp. However, they still show the appropriate peak shift due to different applied forces.

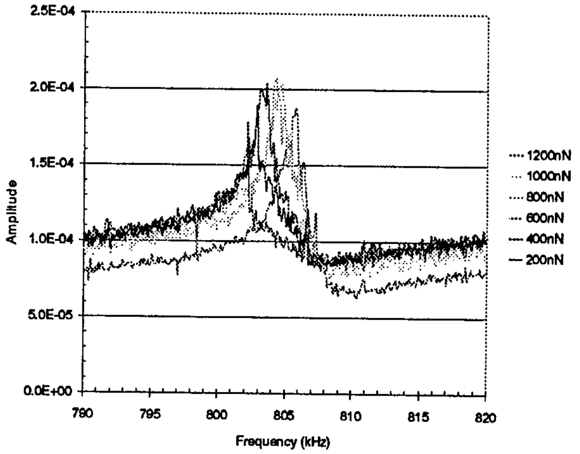

Figure 4.13: Frequency shift due to different applied loads for cantilever NSC-16 on sample Si<111>, voltage amplitude 1V.

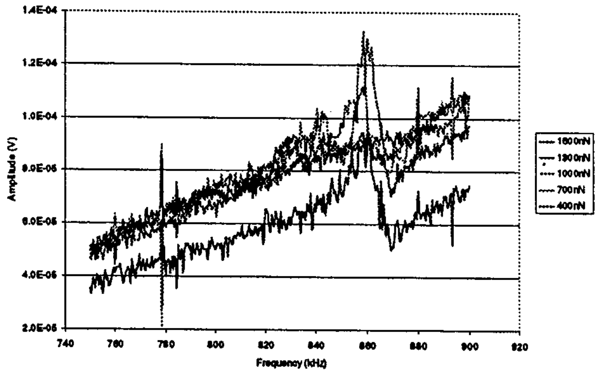

Figure 4.14: First peak shift due to different applied loads on Si <111>, applied voltage 5 V.

Figure 4.15 shows the results of the first natural frequency shift under higher applied forces. For studying the linear peak shift, a range for applied forces can be defined. This limit can be determined with automatic force measurement of the AFM. For each cantilever, a specific deflection is permitted in order to stay in linear zone. This is the threshold by which no non-linear behavior is observed from vibrational data. Although it is possible to control the deflection manually and increase the deflection which results in increasing the applied force, the results would not be reliable, since non-linear behavior could be mistaken as peak shifts.

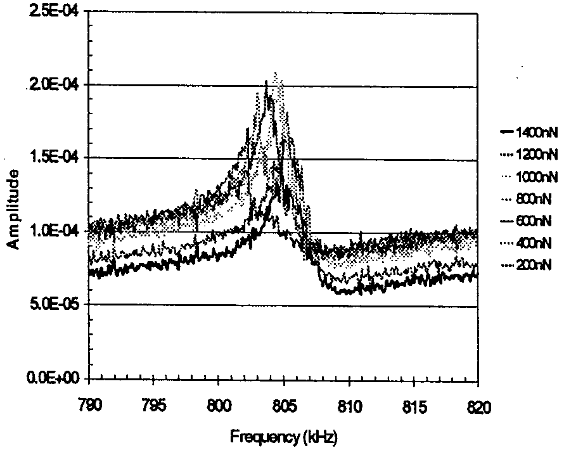

Figure 4.15: Frequency shift due to different applied forces, Si <111>, actuating voltage 1V.

4.3 Contact Resonances on Silicon <100>

4.3.1 NSC-16 frequency shift response

For silicon <100> the NSC-16 cantilever was used exclusively. Similar to the previous section, the frequency shift was measured for different applied forces with constant voltage. Figure 4.16 shows the results of the first natural frequency shift for different applied forces, at 1 V. As before it can be observed that the peak shifts to higher frequencies with increasing applied forces to the cantilever. According to Figure 4.16, the first natural frequency shifts from the free vibration value of 173 kHz to 840-860 kHz for different applied forces for the NSC-16 cantilever.

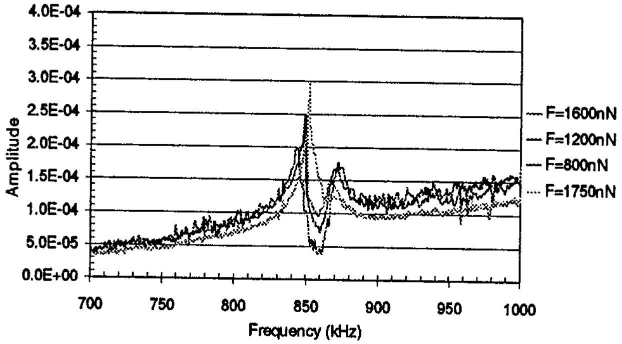

Figure 4.16: Frequency shift due to different applied forces on Si <100> for cantilever NSC-16, applied voltage 1 V.

4.4 Contact Resonances on Polysilicon

4.4.1 Cantilever NSC-16 and d-lever B

The MEMS specimen was analyzed using both the NSC-16 and the d-lever B cantilevers. The frequency shift response of the NSC-16 cantilever in contact with the polysilicon microelectromechanical system specimen was measured for two different applied forces. The first natural frequency shift (as illustrated in Figure 4.17) lies between 750-780 kHz. The spike which can be observed at lower frequencies is again a nonlinearity effect and

can be distinguished from a resonance peak, by the fact that it is unaffected by changes in applied force.

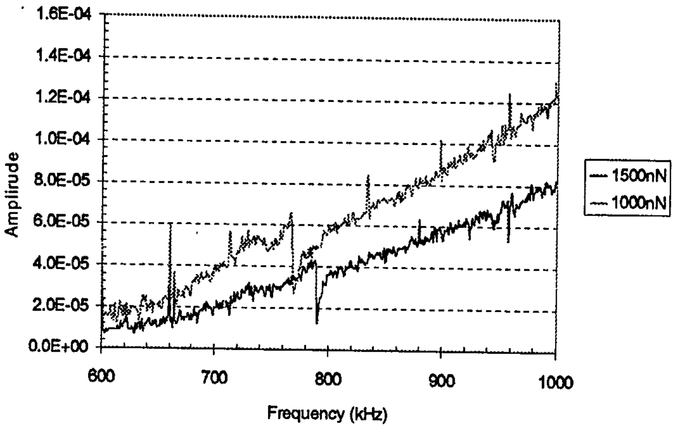

Figure 4.17: Frequency shift on MEMS due to different applied forces for cantilever NSC-16.

The frequency shift response of the d-lever B cantilever in contact with the MEMS specimen at 5 V is shown in Figure 4.18. Wide peaks and sometimes two peaks can be observed. This effect is possibly due to the nonhomogeneous sample because of the possible small movements of the cantilever tip on the sample. MEMS materials are made of polysilicon with numerous small grains. In microscopic dimension, the sample is made of different regions with different moduli due to effects such as grain boundaries. The possibility of small motion of the cantilever on the X or Y direction on the sample is not negligible. Random movements of tips from the middle of a grain to its boundary or to the grain next to it will slightly change the measurements and result in wide peaks or dual peaks.

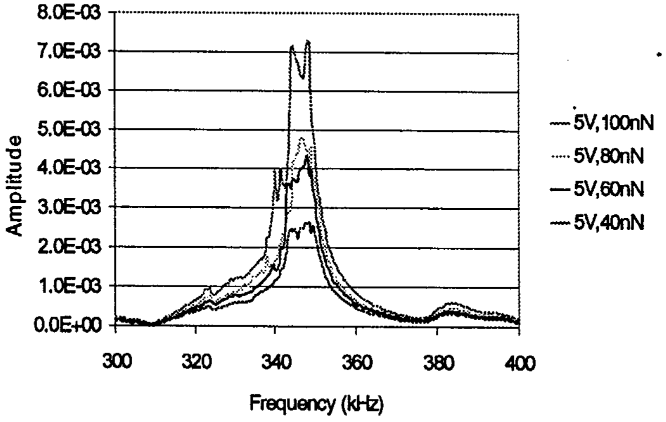

Figure 4.18: First peak shift due to different applied forces on MEMS for d-lever B, applied voltage 5V.

As can be observed from Figure 4.18 the first natural frequency shifts from 82.8 kHz to the range of 340-350 kHz. This result is very similar to the range for silicon <111>, which is to be expected, since the polysilicon MEMS material used in this research has a stiffness close to single crystal silicon <111>. As can be seen, the peaks are not very sharp due to the non-homogenous material structure.

4.5 Surface Stiffness Estimation: calculated vs. actual values

Based on the frequency shift data discussed above, the Table 4.1 shows the calculated and actual values (manufacturer data) for surface stiffness of the samples, and the corresponding errors. The surface stiffness calculations are presented in Section 3.4.

As can be seen from the Table 4.1, the estimation for silicon <100> is very close to the accepted value of surface stiffness (less than 3% error), whereas the value for the silicon <111> sample exhibits an error of 31.5%.

It was demonstrated by the repeatability experiments for silicon <111> that the frequency shift data was repeatable and relatively accurate. The resulting error can be attributed to the following sources:

1) Incorrect Poisson coefficient data for the tip and the sample

2) Inadequacy of the applied surface stiffness calculation method resulting from neglecting the nonlinear effects.

3) Incorrect tip stiffness estimation.

Table 4.1: Surface stiffness calculation for several samples.

Sample	Calculated stiffness	Stiffness data (manufacturer)	% error
Si <100>	125.2 GPa	129 GPa	2.9
Si <111>	128.0 GPa	187 GPa	31.5
MEMS	128.6 GPa	N/A	N/A

4.6 AFAM Imaging of Polysilicon

In addition to the natural frequency shift which enables us to calculate the surface stiffness, the topography image and mapping photodetector signal taken at an operating frequency near to the actual shifted natural frequency also provides us with visual data on relative stiffness of different parts of the surface material. In the following pages, normal AFM topography images and AFAM images are displayed side-by-side for a number of different applied forces and operating frequencies. The contrast of the AFAM images can be reversed using an operating frequency on the left side of the peak. If an operating frequency is not in the range of the peak, it is impossible to take an AFAM image of the sample and only a noise signal is observed.

As shown in Figure 4.19, in the ordinary AFM topography images which can be observed at the left side, the contrast between grains and their background is not large. However, in AFAM images on the right side, a large contrast is observed. This contrast is due to the changes in surface stiffness of the sample in different parts of the scanning area. The boundary of the grain is well defined and some features within the grain can be observed which is due to the change of stiffness. The indicator color bar in AFM images shows the change in height of the sample. The indicator color bar in AFAM images shows the changes in voltage amplitude. The voltage contrast in AFAM can be interpreted as the change in surface stiffness on the surface of the sample. The AFAM images are simply the map of the signal which is the output from the lock-in amplifier. When the cantilever is sweeping the sample, it moves from the top of grains to the grain boundaries and the different region on the sample. Using the original free spectrum of the cantilever and the

spectrum of the cantilever with specific applied load, it is possible to calculate the changes in modulus on the sample.

As shown in Figure 4.20, in AFAM images many variations in background of the grains can be detected. The corresponding AFM topography, does not show these variations. It leads to the conclusion that these changes of the voltage in background are not due to topographical variation of height, but related to the stiffness or softness of the background.

Adjustment of the signal which is coming from the photodetector, plays an important role in the quality of the AFAM image. For taking the best possible image, filter parameters and sensitivity of the lock-in amplifier should be adjusted. Unsuitable adjustment can result in a very noisy image. In this case, sensitivity should be high, otherwise the small changes in voltage amplitude, and respectively, the small changes in surface stiffness can not be distinguished. Figures 4.20-4.23 represent the AFM topography and the AFAM images of the MEMS sample at varying force constants.

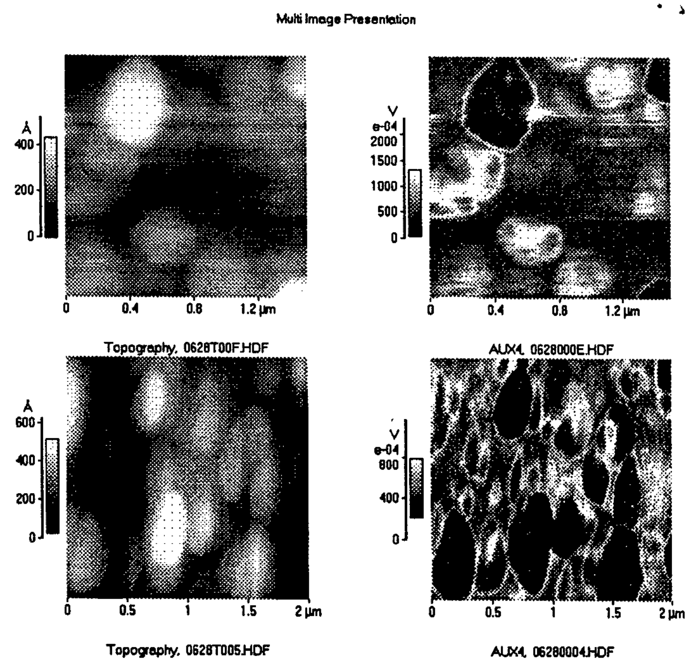

Figure 4.19: AFAM images of MEMS using cantilever NSC-16 with force constant 43 N/m, applied force 1200 nN, applied voltage to the transducer 1V. These images were taken using the first mode $f = 837$ kHz.

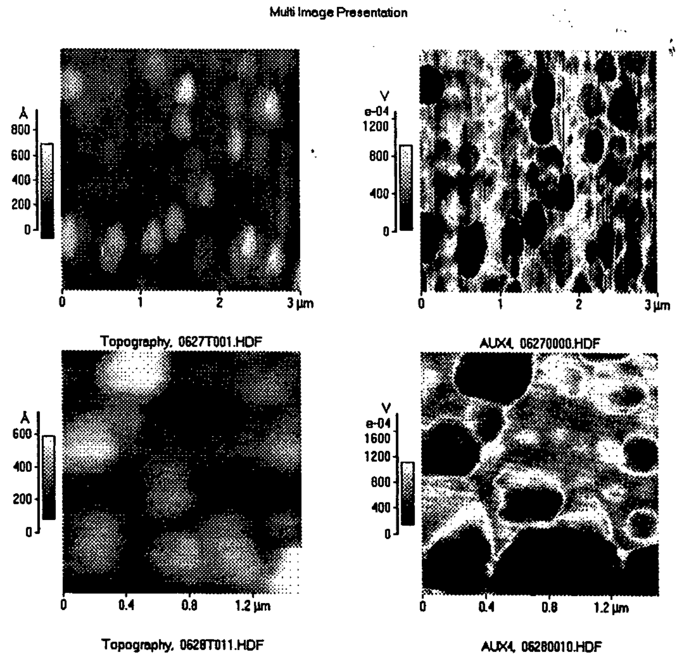

Figure 4.20: AFAM images of MEMS using cantilever NSC-16 with force constant 43 N/m, applied force 1000 nN, applied voltage to the transducer 1V. These images were taken using the first mode $f = 837$ kHz.

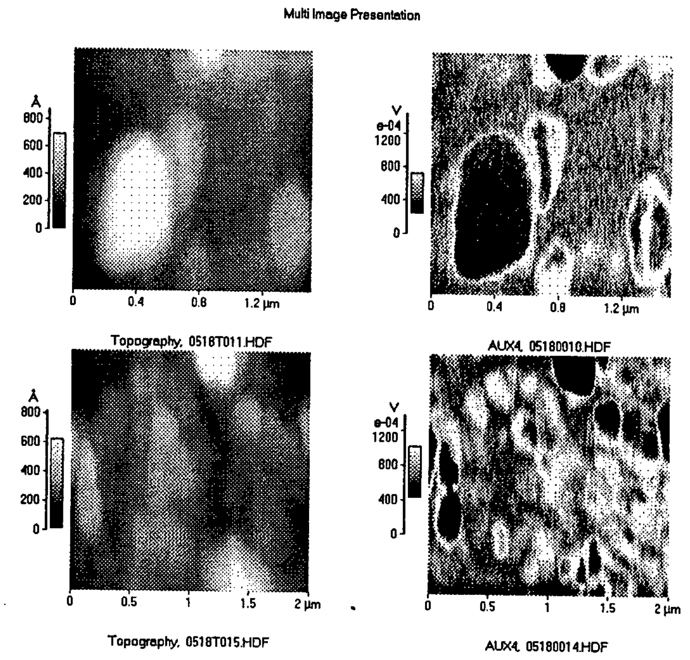

Figure 4.21: AFAM images of MEMS using cantilever NSC-16 with force constant 43 N/m, using non linear peaks. These images were taken using the first mode f= 740 kHz.

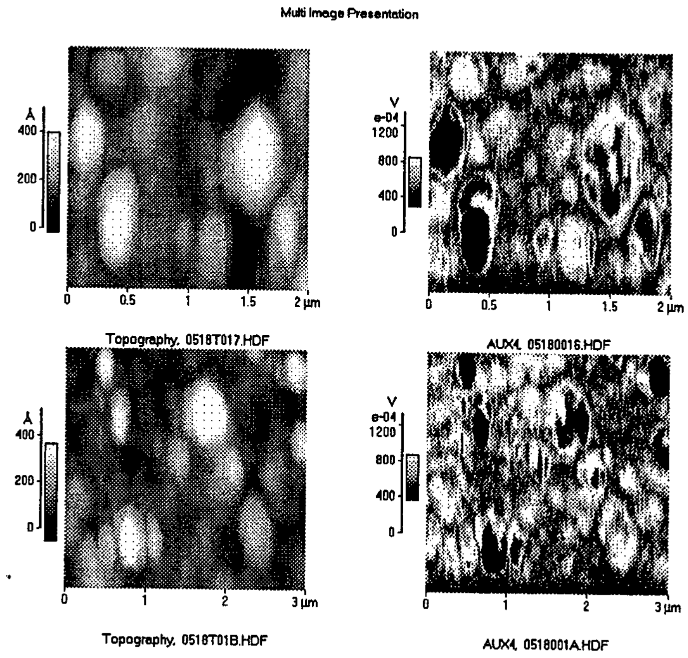

Figure 4.22: AFM and AFAM images of MEMS using cantilever NSC-16 with force constant 43 N/m, applied force 1000 nN, applied voltage to the transducer 1V. These images were taken using the first mode f= 837 kHz.

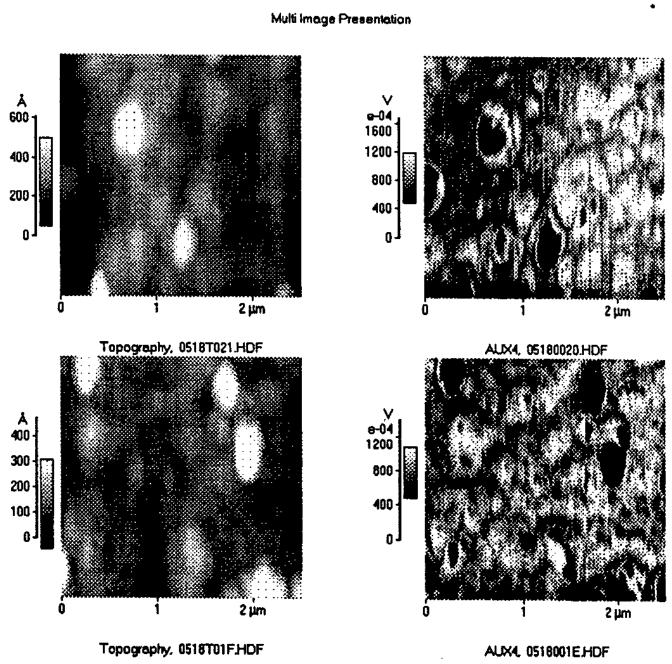

Figure 4.23: AFM and AFAM images of MEMS using cantilever d-lever B with force constant 3.148 N/m, applied force 1200 nN, applied voltage to the transducer 1 V. These images were taken using the first mode $f = 355.5$ kHz.

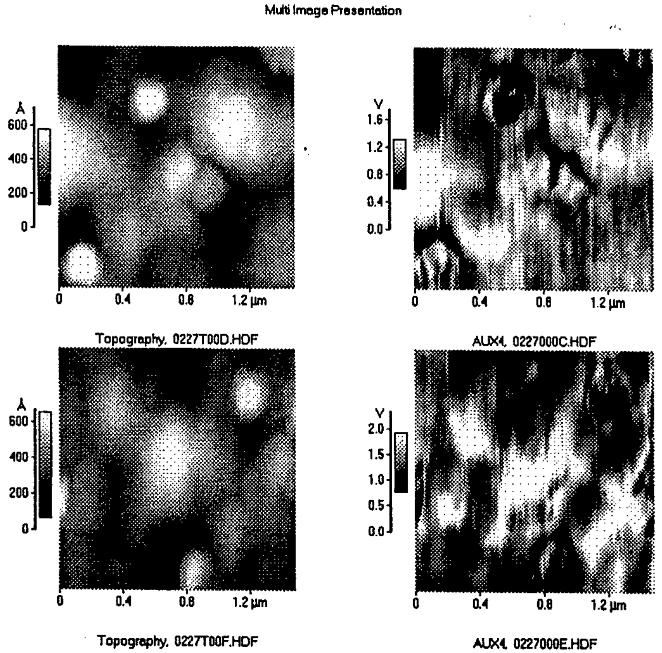

Figure 4.24: AFM and AFAM images of MEMS using cantilever d-lever B with force constant 3.148 N/m, applied force 1200 nN, applied voltage to the transducer 1 V. These images were taken using the first mode $f = 355.5$ kHz.

4.7 Nonlinearity Effects

The primary focus of this thesis is on the linear AFM vibrations for determining surface stiffness images. In the course of these investigations, many nonlinear vibration characteristics were observed. As a small part of this thesis, several nonlinear experiments were conducted. These results may be used for comparison with nonlinear AFM models.

4.7.1 Nonlinearity effect on vibrations of the d-lever B cantilever

When higher voltages are applied to the transducer, the peaks of the natural frequency diagram become wider and less sharp. An example of nonlinear effect is observed in Figure 4.25. Because the applied driving voltage amplitude to the transducer is high, the amplitude of the vibration is high and it forces the cantilever to vibrate in a nonlinear fashion. As can be observed, instead of shifting the peak to higher frequencies with higher applied forces, a reverse effect is created. This effect is a characteristic of a softening nonlinearity.

4.7.2 Nonlinearity effect on vibrations of cantilever NSC-16

As with the d-lever B cantilever, the frequency response shows nonlinearity at higher voltages. The voltages were varied from 1 V to 10 V to observe the effect on the frequency shift of the first natural frequency. In this case, the applied force remains constant. For low actuating voltages to the transducer, the peak is sharp and narrow. With increasing the actuating voltage, the peaks become wider and they lose their sharpness. Peaks also shift to a lower frequency which is less than the linear value of the shift which shows the

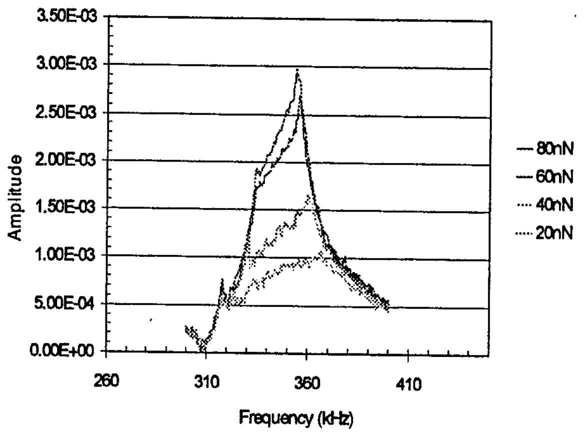

Figure 4.25: First peak shift for different applied loads for d-lever B, applied voltage 9V.

softening effect. This effect can be observed in Figure 4.26, where the frequency shift at higher voltages is highly nonlinear.

The nonlinearity effect at larger voltages was studied by varying the input voltage and holding the applied force constant. Figure 4.26 illustrates the results of this experiment. As can be seen, the peak shifts to lower frequencies with increasing applied voltage. Figure 4.27 shows the natural frequency shift for an applied force of 40 nN for the nonlinear region (5 V). These peaks shows the repeatability of the nonlinearity effect. Figure 4.28 shows the natural frequency shift for an applied force of 60 nN for the nonlinear region (5 V). As shown, they show a high reliability of the data. Figure 4.29 shows the natural frequency

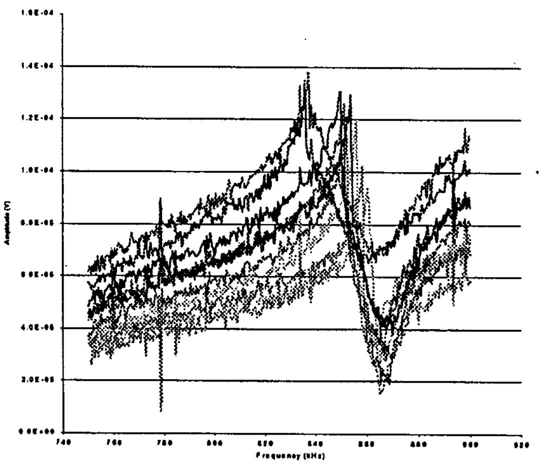

Figure 4.26: First peak shift and nonlinearity effect: different applied voltages to the transducer to observe nonlinear behavior. An applied force of 1200 nN was used for each measurement.

shift for an applied force of 80 nN for the nonlinear region (5 V). For the repeatability experiments, after each scan, the head is raised and applied force and voltmeter parameters adjusted. Then an approach to the sample surface with the same force takes place. Figure 4.30 shows the natural frequency shift for an applied force of 100 nN for the nonlinear region (5 V) and Figure 4.31 shows the natural frequency shift for an applied force of 120 nN for the nonlinear region (5 V).

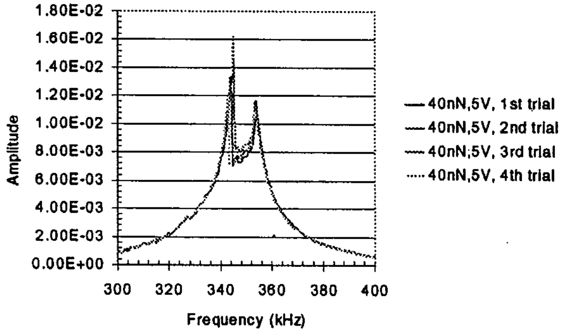

Figure 4.27: Nonlinear repeatability on d-lever B, applied force 40 nN, applied voltage to the transducer 5V.

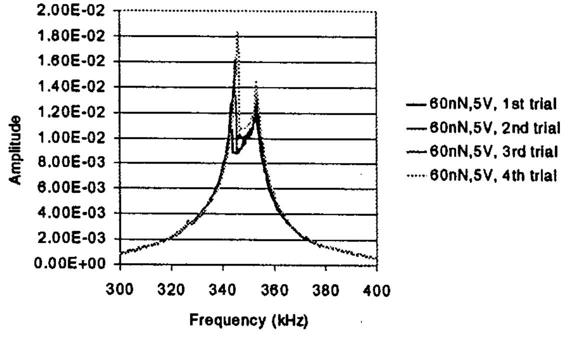

Figure 4.28: Nonlinear repeatability on d-lever B, applied force 60 nN, applied voltage to the transducer 5V.

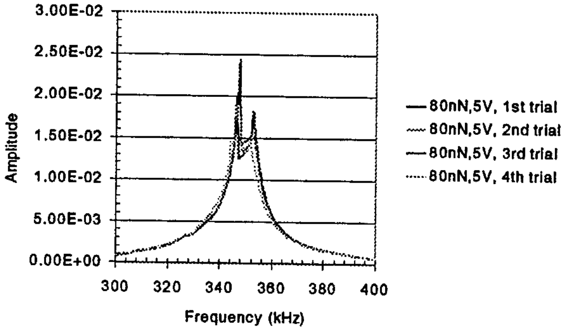

Figure 4.29: Nonlinear repeatability on d-lever B, applied force 80 nN, applied voltage to the transducer 5V.

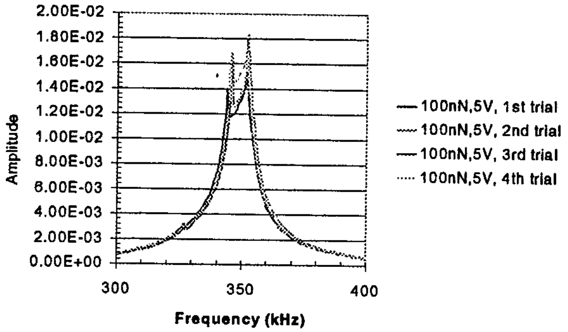

Figure 4.30: Nonlinear repeatability on d-lever B, applied force 100 nN, applied voltage to the transducer 5V.

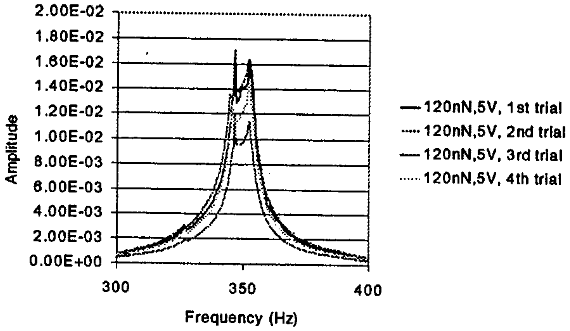

Figure 4.31: Nonlinear repeatability on d-lever B, applied force 120 nN, applied voltage to the transducer 5V.

Chapter 5

Conclusion and Summary

The focus of this research was the development of an atomic force acoustic microscopy system from a commercial atomic force microscope. In order to verify the functionality of this setup, the atomic force acoustic microscope was used to study the surface properties of silicon <111>, silicon <100> and polysilicon MEMS samples. Overall, the experimental setup was successfully implemented, and the results for the surface stiffness calculation are promising. In the following section, the results are compared to actual surface stiffness values and error sources are explored. Subsequently, an outline of future work to be performed is presented.

5.1 Conclusions

The following table shows the calculated and actual values for surface stiffness of the above materials, and the corresponding errors.

Table 5.1: The calculated stiffness for MEMS using AFAM.

Sample	Calculated stiffness	Actual Stiffness	% error
Si <100>	125.2 GPa	129 GPa	2.9
Si <111>	128.0 GPa	187 GPa	31.5
MEMS	128.6 GPa	N/A	N/A

As can be seen from Table 5.1, the estimation for silicon <100> is very close to the actual surface stiffness (less than 3% error), whereas the value for the silicon <111> sample exhibits an error of 31.5%. The reason for this discrepancy is the fact that the surface calculation method used in this research can only be applied to materials which are less stiff than the cantilever tip itself. Also, the difference with the surface stiffness obtained from bulk methods can be explained by observations made by Sharpe, et al. [26], which indicates that the size of the sample influences the surface stiffness measurements. They found that larger specimens had larger surface stiffness values, indicating that the flaws in these samples were greater than that of smaller samples. They reported a surface stiffness value of 121 GPa for a MEMS sample comparable in size to the one used in this research.

In general, the atomic force acoustic microscope can be considered a useful tool for surface stiffness evaluations on the nanoscale. Many of the results based on this method can be improved by improvements in the contact theories used. In addition, like any normal AFM it can provide topographical data at the same time.

5.2 Future Work

The work to be performed in future research may be categorized as instrument related, sample related and theory related. In this research, only two cantilevers were used for analysis purposes. Considering the abundance of different cantilevers with different sensitivities using other cantilevers seems a logical next step. Specially, in order to find the second and third mode frequency shifts, using cantilevers with high tip stiffness (e.g. diamond tip cantilevers), different cantilever cross-sections and dimensions will be helpful.

Also in order for the cantilever to be reflective, they are coated with gold, aluminum and other reflective metals. It would be useful to determine how much these coatings affect the free natural frequencies of the cantilever.

As discussed in Chapter 2, different transducers have different ranges of sensitivity. Extending the results of this research to other transducers should provide valuable information. In order to measure frequencies higher than 3 MHz, higher speed position sensitive photo detectors should be used.

Materials with different grains can be studied effectively using the atomic force acoustic microscope. Composite materials for example, which have stiff fibers and soft matrices, are one example of complex materials samples which could be studied using AFAM. AFAM is also suitable for the study of hard coatings which are composed of several phases, like CrBN.

As discussed earlier, there are two parts for surface stiffness calculation using frequency shift data. The first part is to relate the frequency shift to a dimensionless relative stiffness. The second part is to relate the relative stiffness to surface stiffness. Both parts need improvement, if the AFAM is to be a reliable method for surface stiffness estimation. The use of more complex contact models, such as Maugis may increase the accuracy of the calculated stiffness values.

Bibliography

[1] G. Binning, C. F. Quate, and C. Gerber, "Atomic Force Microscope," Physical Review Letters **56**, 930–933 (1986).

[2] K. Inagaki, O. V. Kolosov, G. A. D. Briggs, and O. B. Wright, "Waveguide Ultrasonic Force Microscopy at 60 MHz," Applied Physics Letters **76**, 1836–1838 (2000).

[3] K. Inagaki, O. V. Kolosov, G. A. D. Briggs, S. Muto, Y. Horisaki, and O. B. Wright, "Ultrasonic Force Microscopy in Waveguide Mode Up to 100 MHz," 1998 Proceedings of IEEE Ultrasonics Symposium **98**, 1255–1259 (1998).

[4] U. Rabe and W. Arnold, "Acoustic Microscopy by Atomic Force Microscopy," Applied Physics Letters **64**, 1493–1495 (1994).

[5] K. Yamanaka, H. Ogiso, and O. Kolosov, "Ultrasonic Force Microscopy for Nanometer Resolution Subsurface Imaging," Applied Physics Letters **64**, 178–180 (1994).

[6] N. A. Burnham, R. J. Colton, and H. M. Pollock, "Interpretation of Force Curves in Force Microscopy," Nanotechnology **4**, 64–80 (1993).

[7] L. Meirovitch, *Analytical Methods in Vibrations* (The Macmillan Company, 1975).

[8] N. A. Burnham and O. P. Behrend, "How Does a Tip Tap?," Nanotechnology **8**, 67–75 (1997).

[9] A. Fisher-Cripps, *Introduction to Contact Mechanics* (Springer Verlag, 2000).

[10] J. A. Turner, S. Hirsekorn, U. Rabe, and W. Arnold, "High-Frequency Response of Atomic-Force Microscope Cantilevers," Journal of Applied Physics **82**, 966–979 (1997).

[11] K. Yamanaka, Y. Maruyama, T. Tsuji, and K. Nakamoto, "Resonance Frequency and Q Factor Mapping by Ultrasonic Atomic Force Microscopy," Applied Physics Letters **78**, 1939–1941 (2001).

[12] U. Rabe, E. Kester, and W. Arnold, "Probing Linear and Non-Linear Tip-Sample Interaction Forces by Atomic Force Acoustic Microscopy," Surface and Interface Analysis **27**, 386–391 (1999).

[13] N. A. Burnham, A. J. Kulik, G. Gremaud, P.-J. Gallo, and F. Oulevey, "Scanning Local-Acceleration Microscopy," Journal of Vacuum Science Technology B **14**, 794–799 (1996).

[14] U. Rabe and W. Arnold, "Atomic Force Microscopy at Ultrasonic Frequencies," 1994 Proceedings of IEEE Ultrasonics Symposium **94**, 367–370 (1994).

[15] O. Kolosov and K. Yamanaka, "Nonlinear Detection of Ultrasonic Vibrations in an Atomic Force Microscope," Japanese Journal of Applied Physics **32**, L1095–L1098 (1993).

[16] U. Rabe, K. Janser, and W. Arnold, "Vibrations of Free and Surface-Coupled Atomic

Force Microscope Cantilevers: Theory and Experiment," Review of Scientific Instruments **67**, 3281–3293 (1996).

[17] K. Yamanaka, A. Noguchi, T. Tsuji, T. Koike, and T. Goto, "Quantitative Material Characterization by Ultrasonic AFM," Surface and Interface Analysis **27**, 600–606 (1999).

[18] U. Rabe, M. Dvorak, and W. Arnold, "The Atomic Force Microscope as a Near-Field Probe for Ultrasound," Thin Solid Films **264**, 165–168 (1998).

[19] T. M. F. Iwata and A. Sasaki, "Local Elasticity Imaging of Nanobundle Structure of Polycarbonate Surface Using Atomic Force Microscopy," Nanotechnology **11**, 10–15 (2000).

[20] K. Yamanaka and S. Nakano, "Ultrasonic Atomic Force Microscope with Overtone Excitation of Cantilever," Japanese Journal of Applied Physics **35**, 3787–3792 (1996).

[21] U. Rabe, S. Amelio, E. Kester, V. Scherer, S. Hirsekorn, and W. Arnold, "Quantitative Determination of Contact Stiffness Using Atomic Force Acoustic Microscopy," Ultrasonics **38**, 430–437 (2000).

[22] R. B. F. Stahl and R. Bourquin, "Characterizing Mechanical Resonators by Means of a Scanning Acoustic Force Microscope," Applied Physics Letters **77**, 1792–1794 (2000).

[23] K. Yamanaka, T. Tsuji, A. Noguchi, T. Koike, and T. Mihara, "Nanoscale Elasticity Measurement with in Situ Tip Shape Estimation in Atomic Force Microscopy," Review of Scientific Instruments **71**, 2403–2408 (2000).

[24] L. Howell, "What is MEMS?,", 2000, integrated Microelectronics Laboratory Website.

[25] H. Guckel, "What is MEMS?,", 2001, educational Web-page http/mems.engr.wisc.edu/MEMS.html.

[26] W. N. Sharpe, K. M. Jackson, K. J. Hemker, and Z. Xie, "Effect of Specimen Size on YoungŠs Modulus and Fracture Strength of Polysilicon," Journal Of Microelectromechanical Systems **10**, 317–327 (September 2001).

[27] "Cronos. Co,", 2001, webpage http://www.memsrus.com.

[28] P. S. Instruments, *User's Guide to Autoprobe CP* (Park Scientific Instrument, TM Microscopes 1171 Borregas Avenue Sunnyvale, CA 94089, 1997), http://www.tmmicro.com/.

[29] *MicroMasch Gratings Catalog*, K-TEK International, Inc., Portland, Oregon, 2000.

[30] P. M. Williams and K. M. Sherkesheff, "Blind Reconstruction of Scanning Probe Image Data," Journal of Vacuum Science and Technology B pp. 1557–1562 (1996).

[31] J. S. Villarubia, "Scanning Probe Microscope Tip Characterization Without Calibrated Tip Characterizers," Journal of Vacuum Science and Technology B **14**, 1518–1521 (1996).

Appendix A – First Modal Frequency
For NSC-16 cantilever

Stiffness	Mode 1(Hz)	Stiffness	Mode 1(Hz)
0.016	193989	50.057	270494
0.022	194154	66.026	291270
0.028	194319	87.089	313642
0.037	194484	114.872	337732
0.049	194650	151.519	363672
0.065	194815	199.856	391604
0.086	194981	263.613	421682
0.113	195147	347.711	454070
0.149	195313	458.637	488946
0.197	195479	604.951	526500
0.260	195645	797.941	566939
0.343	195811	1052.499	610484
0.452	195978	1388.266	620951
0.596	196144	1831.148	631597
0.787	196311	2415.318	642426
1.037	196478	3185.849	653440
1.368	196645	4202.194	664644
1.805	196812	5542.771	676039
2.381	198393	7311.017	687630
3.140	201997	9643.366	699420
4.142	205666	12719.778	711412
5.463	209401	16777.621	723609
7.206	213204	22129.991	736016
9.505	217077	29189.865	748635
12.537	221020	38501.970	761471
16.537	225034	50784.806	774526
21.813	229121	66986.094	787806
28.771	233283	88355.891	801313
37.950	251201	116543.047	815052

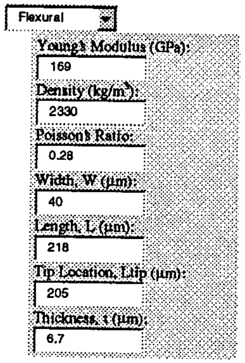

Young's Modulus (GPa): 169

Density (kg/m³): 2330

Poisson's Ratio: 0.28

Width, W (μm): 40

Length, L (μm): 218

Tip Location, Ltip (μm): 205

Thickness, t (μm): 6.7